THE IMPACT OF SAHARAN DUST ON ATLANTIC CONVECTIVE SYSTEMS: A CASE STUDY

JIANYU LIANG

A DISSERTATION SUBMITTED TO

THE FACULTY OF GRADUATE STUDIES

IN PARTIAL FULFILLMENT OF THE REQUIREMENTS

FOR THE DEGREE OF

DOCTOR OF PHILOSOPHY

GRADUATE PROGRAM IN EARTH AND SPACE SCIENCE

YORK UNIVERSITY

TORONTO, ONTARIO

August 2018

Abstract

Tropical weather systems such as the African Easterly Waves (AEWs), the African Easterly Jet (AEJ), and tropical cyclones usually interact with the Saharan Air Layer (SAL) and mineral dust aerosols embedded in the SAL. Previous studies have debates about the strength and even the direction of the impact from the dust and SAL on the development of the tropical systems. In this study, the sole impact from the dust on a hurricane is quantified using carefully designed numerical experiments.

Hurricane Earl (2010) was originated from an AEW disturbance over Africa. It was influenced by the dusty SAL especially in its early development stage. We conduct numerical experiments using the Weather Research and Forecasting model coupled with Chemistry (WRF-Chem) to simulate Hurricane Earl (2010) starting from a weak disturbance.

Experiments with 36-km resolution show that without moist convection, dust slightly weakens the low-pressure system in North Africa by cooling the atmosphere. This scenario mainly results from a reduction of the boundary layer heating during the daytime and from the enhancement of the outgoing longwave radiative cooling during the nighttime. The zonal mean of the AEJ is intensified slightly (less than 1m/s) in its southern part and weakened in its northern part when dust is included in the model. Adding dust weakens the AEWs at 850 hPa and 600 hPa levels and the tropical cyclone.

High-resolution (4-km) cloud-resolving model experiments show that dust deepens the system slightly but does not affect the track. In the tropical low stage, dust increases the low-level cloud at 1-2 km height. It reduces rainfall in the outer edge of SAL region between 250 km to 350 km radii while it increases rainfall in the inner edge at around 200 km. The associated latent heat

release shifts the updraft radially inward. The dynamical consequence is the acceleration of the tangential wind and the mid-level circulation. In the tropical depression stage, adding dust increases the number of cloud droplets in most of the regions and enhances the convection around the center, which generates more ice, snow, and rain. Overall, the impact of dust aerosols on Earl is small, the center minimum sea-level pressures only differ by less than 1 hPa at the end of the simulation. This suggests that pure meteorological model may be sufficiently accurate to forecast hurricanes if the dynamical and thermodynamical features of the SAL are properly described.

In order to predict aerosols, one can use a simple chemistry model such as GOCART which only has aerosol direct effects. Using the Ensemble Kalman Filter (EnKF) to assimilate conventional observations and MODIS aerosol optical depth (AOD) data, both forecasts of the track of the storm and the aerosol can be improved.

Acknowledgments

- Professor Yongsheng Chen gave me the opportunity to conduct this research. He guided me throughout the whole project. He also offered to fund for my living and study in Toronto. During the difficult time, he gave me emotional support and encouraged me not to give up.
- Professor Gary Klaassen and Professor Leiming Zhang served on the committee and gave me useful feedback on the research.
- Professor Avelino F. Areliano from the University of Arizona kindly shared his code and have given me helpful advice about the project.
- My colleagues: Dr. Abdulla Mamun, Dr. Mahtab Majdzadeh, Dr. Sangay Bhutia, Mr. Zhengqi Wang, they edited and proofread my thesis. They also gave me emotional support during my difficult time.
- Dr. Zhiquan Liu supported my visit to the National Center for Atmospheric Research (NCAR) in the USA to conduct this project. He and other people in NCAR gave me many supports.
- Ms. Marcia Gaynor helped me with many administration processes during my study.
- Professor Mark Gorden guided my TA work and helped me with the defense process.
- Professor Baoxin Hu and Professor George Zhu spent their time examining my thesis and served in the defense committee.
- Many friends believe in me and encourage me.
- Finally, the biggest thanks to my parent. My mother is always with me. During her visit to Toronto, she took care of me and inspired me to finish the thesis.

Table of Contents

List of Abbreviation

AEW: African Easterly Waves

AEJ: African Easterly Jet

CCN: Cloud Condensation Nuclei

EnKF: Ensemble Kalman Filter

FNL: NCEP Final Operational Global Analysis

GCCN: Giant Cloud Condensation Nuclei

LW: Longwave Radiation

NCEP: National Center for Environmental

NCAR: National Center for Atmospheric Research

n mi: Nautical Mile

SAL: Saharan Air Layer

SW: Shortwave Radiation

TOA: Top of the Atmosphere

TC: Tropical Cyclone

WRF-Chem: Weather Research and Forecasting model coupled with Chemistry

List of Tables

List of Figures

1. Introduction

Tropical cyclone (TC) is a rotating system with low-pressure center and organized thunderstorms. Under some favorable conditions, it can evolve into a hurricane with maximum sustained wind speeds of at least 119 km/h (74 mph). Since tropical cyclones can severely interrupt people's lives by bringing heavy rain, flood and high winds to the coastal region, it is essential to improve the accuracy of the tropical cyclone forecast. Over the years, the forecasts have been significantly improved due to the increased scientific understanding of the tropical convective systems and the development of forecast techniques. Tropical cyclones developed on the eastern Atlantic Ocean may be impacted by many factors such as the African Easterly Jet (AEJ), African Easterly Waves (AEWs), the Saharan Air Layer (SAL), and aerosols inside the SAL (Figure 1-1 and Figure 1-2). Many studies have investigated how these factors involved in the development of tropical cyclones. An overview of them will be given in the following sections.

(a) (b)

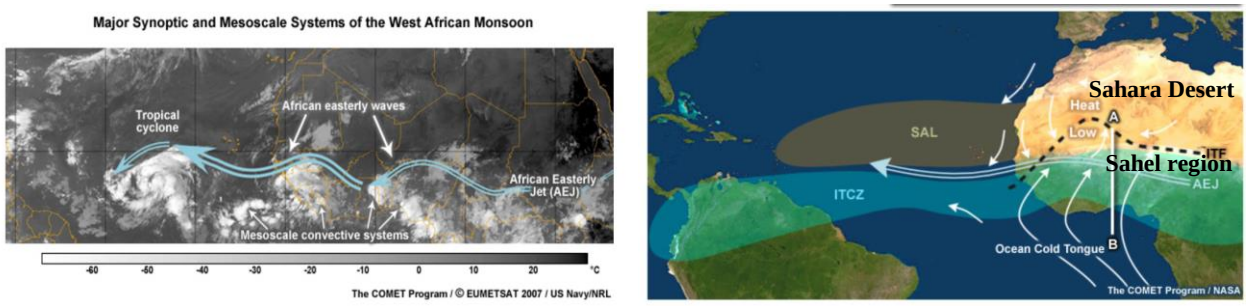

Figure 1-1. (a) Satellite image and (b) schematic diagram of major synoptic and mesoscale systems in tropics and subtropics. (The COMET program/ UCAR 2017).

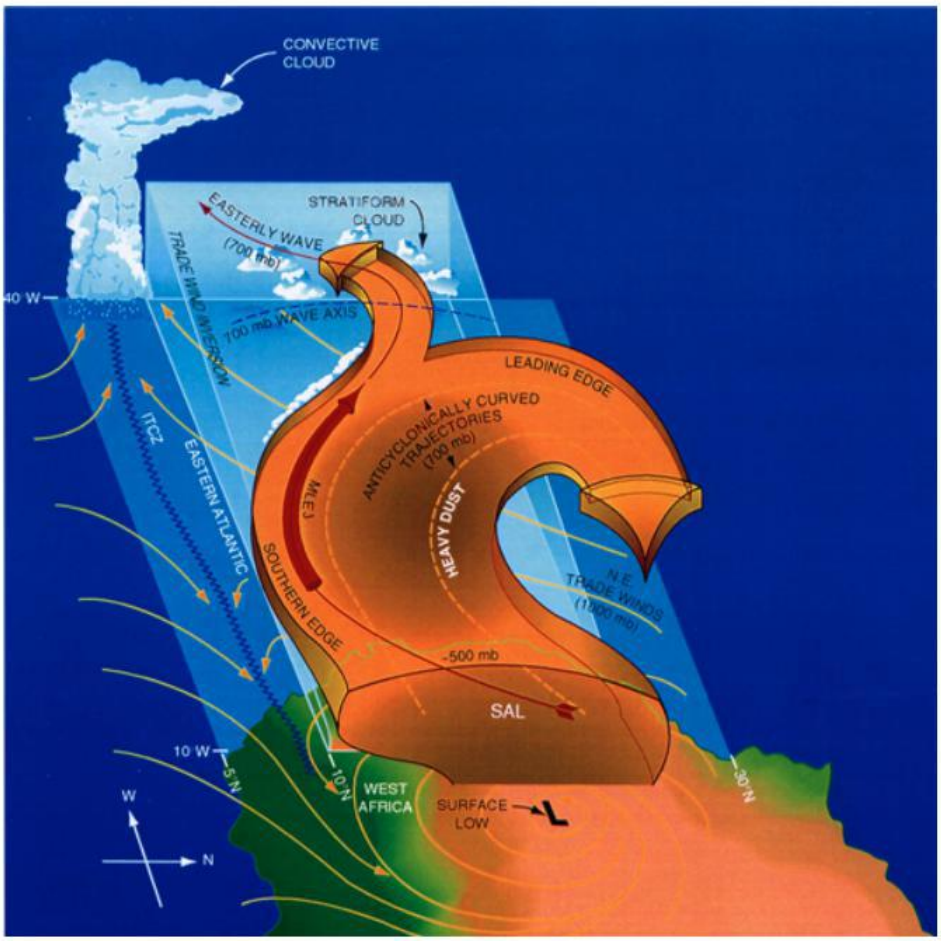

Figure 1-2. SAL conceptual model illustrates the following properties: geographic location of the African continent, ITCZ, dust plume, surface flow (solid yellow arrows), particle trajectories (dashed yellow arrows), mid-level easterly jet (thick red arrow), 700 hPa wave axis (thin red arrow), regions of convection, and the rise of the SAL base to the west (Karyampudi et al. 1999).

1.1 African Easterly Jet and African Easterly Waves

In North Africa, on the poleward side of Sahel region (~15^{o}N), the atmosphere over the Sahara Desert is dry, hot, and well mixed in the boundary layer. A thermal low is usually located

over this region. On the other hand, on the equatorial side of the Sahel region, the air is relatively cool and moist. Therefore, there is a positive meridional temperature gradient below the 600-700 hPa level. The temperature gradient is opposite above that level. Due to the thermal wind balance, a maximum easterly wind, i.e. AEJ, is located in the lower troposphere at 600-700 hPa layer and over 15-17^{o}N region (Figure 1-3). AEJ normally confines to the area between 15^{o}E and 20^{o}W because the meridional temperature gradient is weaker on the west coast of Africa. The wind speed of AEJ can reach up to 12-15 m/s (Carlson 1969a; Burpee 1972; Thorncroft and Blackburn 1999).

Many factors can affect the maintenance of AEJ. For example:

(1) AEJ is sensitive to the radiation, surface temperature, humidity gradient (Thorncroft and Blackburn 1999), orography, and soil moisture (Wu et al. 2009).

(2) The presence of Saharan dust may impact the location and the intensity of AEJ because dust can change the temperature gradient due to its direct radiative effect (Reale et al. 2011a; Tompkins et al. 2005). The basic state (zonal mean) of AEJ can move vertically or meridionally under different temperature profiles over the Saharan dry region.

(3) Convective systems such as squall lines can intensify AEJ by the rear-to-front flow below the trailing stratiform (Diongue et al. 2002).

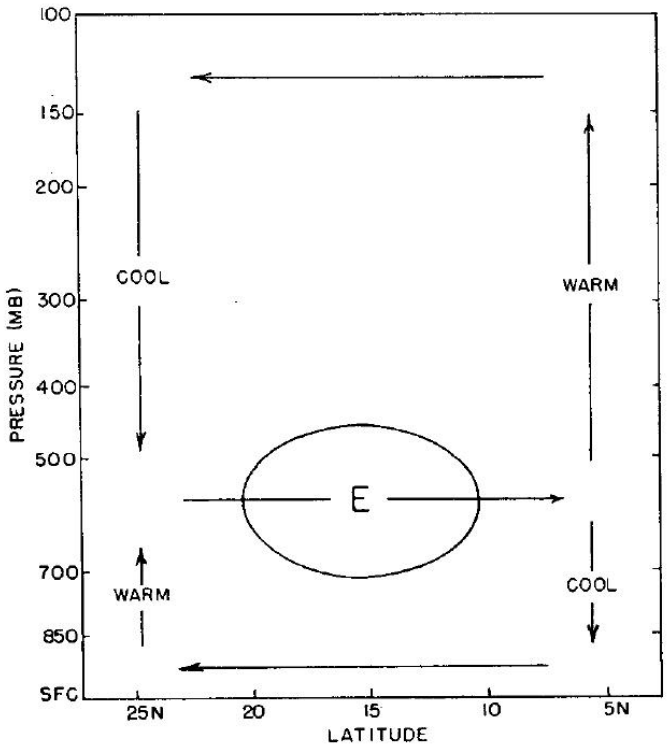

Figure 1-3. Idealized cross section of thermally direct, ageostrophic meridional circulation and its position relative to the mid-tropospheric easterly jet, adapted from Burpee (1972).

AEWs are westward propagating synoptic-scale disturbances that develop over North Africa from June to October with a period of 3-4 days and wavelength of 2000-4000 km (Burpee 1972; Thorncroft et al. 1994). They reach maximum intensity at about 600-700 hPa (Carlson 1969a; Burpee 1972). AEWs are often first observed in the east of Africa, and they then propagate to the west at a speed of around 8 m/s. Convective activities sometimes occur ahead of the AEW trough or its maximum vorticity region (Redelsperger et al. 2002; Brammer and Thorncroft 2017; Carlson 1969b; Diongue et al. 2002). Some waves experience decay once they move further to the west coast of Africa because they encounter the relatively cool temperature over the ocean (Burpee 1972; Thorncroft and Hodges 2001). However, some waves can develop into tropical cyclones under

favorable conditions. AEWs can be responsible for half of the cyclone activities in the eastern Atlantic Ocean (Burpee 1972; Thorncroft et al. 1994).

AEWs are triggered convectively and grow through the mixed baroclinic and barotropic instability mechanism associated with AEJ (Burpee 1972; Thorncroft et al. 1994; Thorncroft and Hodges 2001). "Charney-Stern instability criterion" is the necessary condition for barotropic and baroclinic instability. The criterion states that for an unstable flow to occur, either: (a) potential vorticity gradient on a constant pressure surface changes sign in the fluid interior while the temperature gradient is close to zero at the lower boundary, or (b) the potential vorticity gradient everywhere and the temperature gradient at the lower boundary have opposite signs (Charney and Stern 1962; Thorncroft et al. 1994; Burpee 1972).

AEWs typically have two circulation centers, one to the south of AEJ around 600 hPa and one to the north around 850 hPa (Pytharoulis and Thorncroft 1999) (Figure 1-4). To the south of AEJ, there is positive potential vorticity gradient at 600 hPa resulting from ITCZ heating (Thorncroft and Blackburn 1999). Together with a negative potential vorticity gradient at the jet core and the zero temperature gradient at the lower boundary, the "Charney-stern instability criterion" is satisfied. AEWs grow significantly at this level (Figure 1-5). Disturbances at this level may form over as far as Ethiopian highlands or in the region west of 20^{o}E. Waves grow due to barotropic and baroclinic instability as they move westward. Clouds are formed and organized once they reach the region between 10^{o}E and the west coast of Africa, where they encounter the moist air from the ocean (Carlson 1969b; Burpee 1972). AEWs can also be amplified by latent heat release over the sea just off the west coast of Africa. But they may also decay further to the west due to relatively cool SST or wave dispersion (Carlson 1969b; Thorncroft and Hodges 2001).

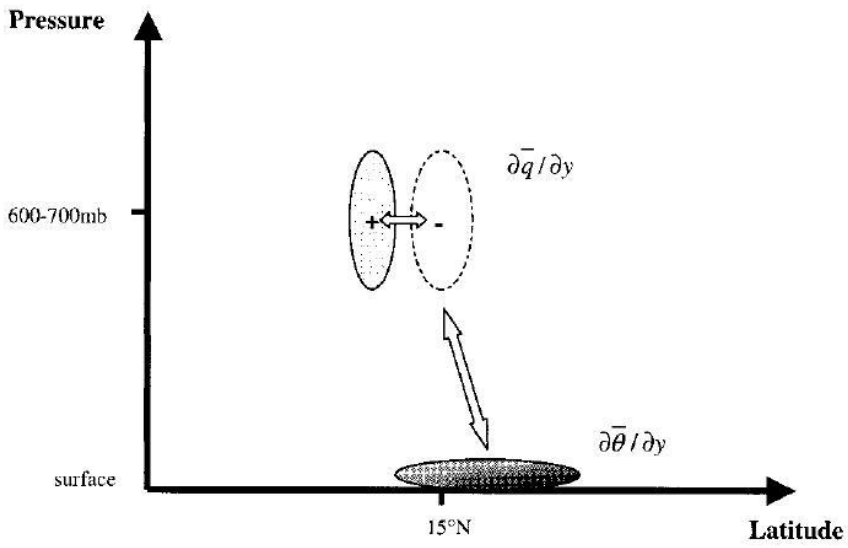

Figure 1-4. Schematic of the meridional gradients of PV ($\partial\overline{q}/\partial y$), the low-level meridional gradient of potential temperature ($\partial\overline{\theta}/\partial y$), and their interactions (indicated by the arrows) over North Africa. The plus (+) and minus (-) signs denote positive and negative values. Adapted from Pytharoulis and Thorncroft (1999).

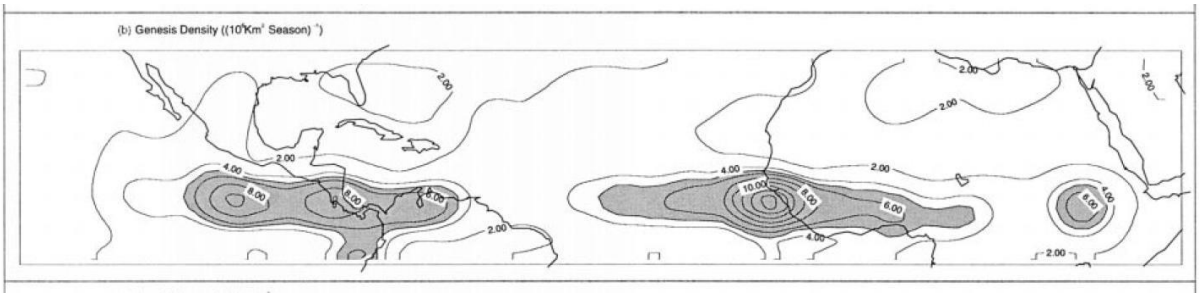

Figure 1-5. Climatological tracking statistics at 600 hPa based on the ERA data (1979–93) and the ECMWF analyses (1994–98). Genesis density per unit area (~10^6 km^2) per season (MJJASO), shading for values greater than 5. Adapted from Thorncroft and Hodges (2001).

In the core of the AEJ and on its poleward side, the meridional gradient of potential vorticity is negative while the temperature gradient at the lower boundary is positive (Figure 1-4). This configuration also satisfies “Charney-Stern instability criterion”. The northern AEW circulations may grow due to baroclinic instability and orographic process in the region (Pytharoulis and Thorncroft 1999; Thorncroft and Hodges 2001; Thorncroft et al. 1994). Genesis density plot shows that AEWs in this region reach maximum intensity around 850 hPa (Figure 1-6). AEWs in this region generally start to decay before they reach the coast while some waves can move across AEJ to the south (Ross and Krishnamurti 2007).

Despite often being part of the same AEW structure, they impact the weather and climate differently. The southern circulations form and move to the west. With moist convection, they are more responsible for tropical cyclogenesis. While the northern circulations are mainly associated with dry convective processes in Sahara area. When they propagate westward into the ocean, they bring dry and dusty Saharan air, known as SAL, that may influence AEW and TC development. AEWs can merge, split and dissipate when they reach the ocean (Reed et al. 1988; Ross and Krishnamurti 2007).

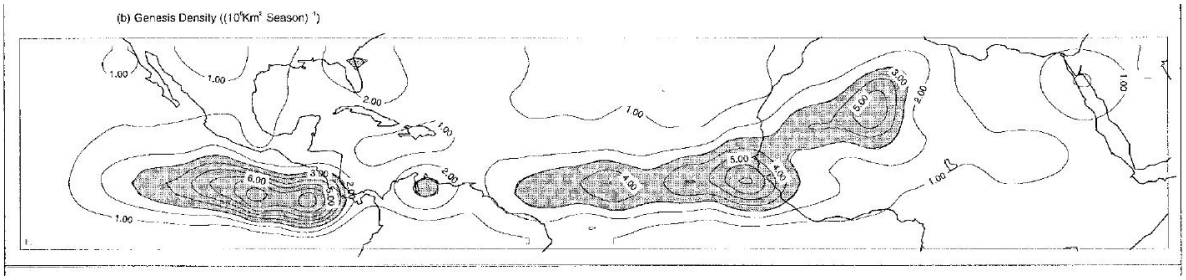

Figure 1-6. Climatological tracking statistics at 850 hPa based on the ERA data (1979–93) and the ECMWF analyses (1994–98). Genesis density per unit area (~10^6 km^2) per season (MJJASO), shading for values greater than 5. Adapted from Thorncroft and Hodges (2001).

1.2 Saharan Air Layer Impacts Tropical Weather Systems

Originated from North Africa, Saharan Air Layer (SAL) is an elevated layer of warm, dry and dusty air. Under the influence of easterly wind, the air mass moves westward off the North African coast and it covers a large region in the North Atlantic Ocean (Figure 1-7) (Dunion and Velden 2004; Burpee 1972). SAL usually forms from late spring to early fall. When its active period overlaps with the hurricane season, it potentially influences the evolution of Atlantic tropical cyclones.

SAL usually contains small dust particles with size ranging from 0.1 to 5 μm. They can be carried away for a very long distance along with the warm air by the easterly wind (Satheesh and Moorthy 2005). Dust affects the characteristic of the SAL by radiative effect and microphysical effect which we will discuss later.

Previous observational and modeling studies show that SAL or dust aerosols can impose positive or negative, or unclear impacts on the development of tropical convective systems. Table 1-1 summarizes some studies. Detailed discussions will follow.

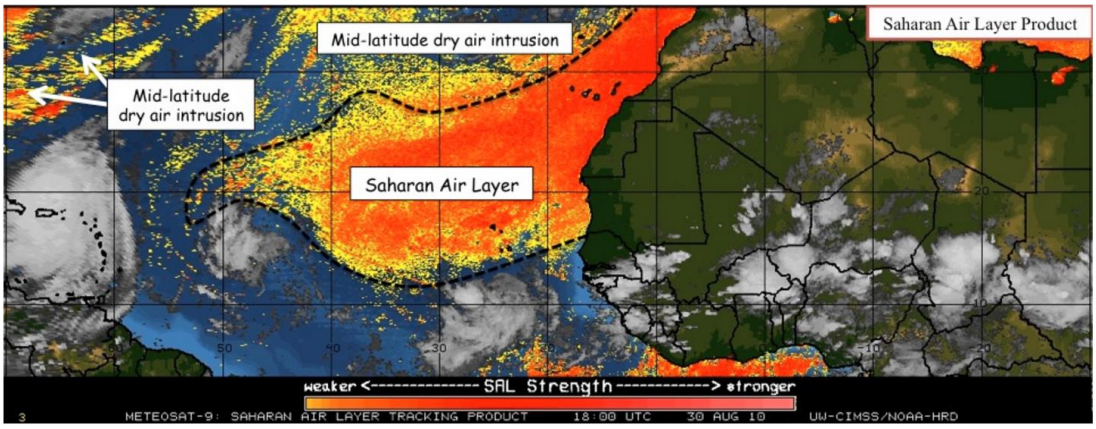

Figure 1-7. Example of a split window "SAL" image (CIMSS/ University of Wisconsin-Madison).

Table 1-1. Summary of previous studies on the impact of SAL and/or dust on AEWs or tropical convective systems.

Method	**Positive impact**	**Negative impact**	**Unclear or little impact**
Observation and re-analysis	SAL has a positive impact on AEWs (Burpee 1972) Dust has a positive impact on AEWs (Jones et al. 2004; Hosseinpour and Wilcox 2014)	SAL has a negative impact on TCs (Dunion and Velden 2004a; Sun et al. 2008) SAL has a negative impact on convections (Wong and Dessler 2005; Ismail et al. 2010; Sun et al. 2008) Dust has a negative impact on AEWs (Jury and Santiago 2010) Dust has a negative impact on TCs (Sun et al. 2008; Evan et al. 2006)	Positive or negative (Shu and Wu 2009) SAL has a negative impact on TCs at the early stage, but no impact later (Braun and Sippel 2013) Unclear (Braun 2010)
Idealized Simulation	Dust has a positive impact on AEW (Grogan et al. 2016; Ma et al. 2012)	Dust has a negative impact on TC (Zhang et al. 2007a)	

Real case simulation	SAL has a positive impact on AEW, but dust has a negative impact on AEW (Karyampudi and Carlson 1988) Dust has a positive impact on AEW (Lavaysse et al. 2011)	SAL has a negative impact on AEW (Vizy and Cook 2009; Reale et al. 2009) SAL has negative impact on TC (Wu et al. 2006; Jones et al. 2007; Sun et al. 2009) Dust has a negative impact on TC (Reale et al. 2014; Chen et al. 2010)	SAL has a negative impact on TCs at the early stage, but no impact later (Sippel et al. 2011; Braun and Sippel 2013)

1.2.1 Negative impact

The mechanisms that the SAL suppresses the development of convective systems are:

a) Enhanced low-level temperature inversion (Dunion and Velden 2004; Wong and Dessler 2005; Jury and Santiago 2010; Ismail et al. 2010; Sun et al. 2009): The temperature in the SAL is warmer than the average tropical sounding. This temperature anomaly enhances the trade wind inversion and suppresses vertical motion in AEWs. These are unfavorable to the development of TCs.

b) Dryer layer (Dunion and Velden 2004; Wong and Dessler 2005; Wu et al. 2006; Vizy and Cook 2009; Ismail et al. 2010; Jones et al. 2007; Sun et al. 2009): Dryness associated with the SAL increases evaporation. This will generate negative buoyancy and create the downdraft. It also

reduces convective available potential energy (CAPE). Numerical simulations show that dry air from the SAL slows down the intensification of a TC at its early stage (Sippel 2011).

c) Stronger vertical wind shear (Dunion and Velden 2004; Wu et al. 2006; Vizy and Cook 2009; Jury and Santiago 2010; Jones et al. 2007; Sun et al. 2009; Chen et al. 2010): The AEJ is usually located at the southern edge of the SAL. Its intensity is determined by the horizontal temperature gradient between the warm SAL and cool tropical air to the south. Stronger AEJ brings stronger vertical wind shear in this region, which is unfavorable for TC development.

d) Dust direct radiative effect: Dust aerosols inside the SAL absorbing shortwave radiation enhances the warm temperature anomaly. The low-level temperature inversion in enhanced. The increased stability is less favorable to TC development. The warm temperature anomaly also increases the vertical wind shear which suppresses TC development (Chen et al. 2010). Sea-surface temperature (SST) is cooler because dust reduces solar insolation at the ocean surface (Foltz and McPhaden 2008; Yoshioka et al. 2007; Evan et al. 2012; Jury and Santiago 2010).

e) Dust indirect effect: Dust act as cloud condensation nuclei (CCNs) which decrease the average size of cloud droplets and increase their number. The precipitation is reduced (Jury and Santiago 2010).

1.2.2 Positive impact

a) The SAL promotes convection on its southern edge and enhances AEWs. More prominent SAL leads to larger differential heating that is more favorable to the growth of AEWs. Numerical

model studies indicate that representation of the SAL in the initial conditions is important for the development of AEWs (Karyampudi and Carlson 1988).

b) Dust enhances AEWs. Using 12 years of satellite data, Hosseinpour and Wilcox (2014) found that dust AOD is positively correlated with AEW activities in the downstream offshore region. Model simulations also show that dust strengthens the AEJ and AEWs because dust increases baroclinicity by absorbing solar radiation (Lavaysse et al. 2011). Idealized model experiments indicate that AEW is intensified when dust radiative process is included in the model, which increases the barotropic and baroclinic energy conversion (Ma et al. 2012; Grogan et al. 2016). After analyzing statistically 22 years of dust data from a global transport model and NCEP/NCAR analysis increment data, Jones et al., (2004) suggested that dust modulates the amplification of AEWs.

1.2.3 Positive/negative or unclear

a) SAL can have both positive or negative effects on TC development depending on its relative location and time to the TC. Observational studies show that the SAL favors TC development when it is located in the northwest quadrant of TC, but it negatively impacts TC when the dry air intrudes within 360 km of the TC center. The SAL may intensify TCs in their earlier stage, but weaken them later (Shu and Wu 2009).

b) Warm temperature associated with the SAL may not change the convection south of its border (Braun 2010). Although the warm temperature within the SAL increases the stability of the region (Dunion and Velden 2004), it may have limited impact on the convection developed south of the SAL (Braun 2010).

c) Dry air from the SAL does not necessarily inhibit hurricane. The dry air can be associated with the strongest hurricane which is less susceptible to entrainment of dry air (Sippel 2011). In addition, dry air does not necessarily only come from SAL, it can come from the air above SAL (Braun 2010; Hopsch et al. 2010; Brammer and Thorncroft 2017). Dry air from Sahara is only confined in the low level (below 700-600 hPa). In the mid-level between 600 and 400 hPa, the humidity is increased due to deep convection over this region. In the subtropical and eastern Atlantic regions, the low relative humidity in the mid-level and upper-level can come from the large-scale descent.

d) The AEJ does not necessarily strengthen or weaken TC development (Braun 2010). The AEJ intensities in the developing TC and non-developing TC scenarios are similar although the AEJ in the developing TC can be 2 m/s larger than that in the non-developing TC case after the cyclogenesis. The vertical wind shear brought by the AEJ may only negatively impact its underlying region. But it can be favorable to TC development to its south by providing positive vorticity (Braun 2010). This might be the reason why different conclusions are made by different studies based on the relative position of the TC development and the SAL.

e) There are no significant differences in SAL features for strengthening and weakening storms (Braun 2010)

f) The SAL may only have impacts on TC development at the early stage. Dryness from the SAL slows down the development of TC in its pre-depression and depression stages, but it has no effect later (Sippel 2011; Braun and Sippel 2013). Other factors such as SST have more influence on the development of TC.

1.3 Aerosol, Cloud, and Precipitation

Discussions in the previous section focus on how the dynamic and thermal dynamic features of the SAL and the associated dust aerosols might change the development of tropical convective systems. In this section, how dust and other types of aerosols impact the microphysical processes in the atmosphere is specifically discussed.

1.3.1 Aerosols in Cloud Physics

Aerosols can act as cloud condensation nuclei (CCN) (Jones et al. 1994; Twohy et al. 2009). The effectiveness of aerosols as CCN depends on their size, composition, mixing state, and ambient environment (IPCC 2007). Aerosols can be categorized into soluble aerosols (such as sulfate, sea salt) and insoluble aerosol (such as dust).

(1) For soluble aerosols, Köhler theory explains the growth process of a particle. The Köhler equation is

$$ln(\frac{p_w(D_p)}{p^0}) = \frac{4M_w\sigma_w}{RT\rho_w D_p} - \frac{6n_s M_w}{\pi\rho_w D_p^3} \quad (1.1)$$

where p_w is the droplet water vapor pressure, p^0 is the corresponding saturation vapor pressure over a flat surface, σ_w is the droplet surface tension, ρ_w is the density of pure water, n_s is the modes of solute, M_w is the molecular weight of water, D_p is the cloud drop diameter, T is the temperature in Kelvin, and R is the gas constant.

The Köhler curve is drawn based on this equation (Figure 1-8). The peak value is defined as the critical supersaturation at the critical diameter. If the supersaturation of the environment exceeds the critical supersaturation, the particle will be activated; it will then grow rapidly and

become a cloud droplet. Particles with larger dry diameters have larger critical diameters and lower critical supersaturation. Hence, larger particles are easier to grow under the same supersaturation in the environment.

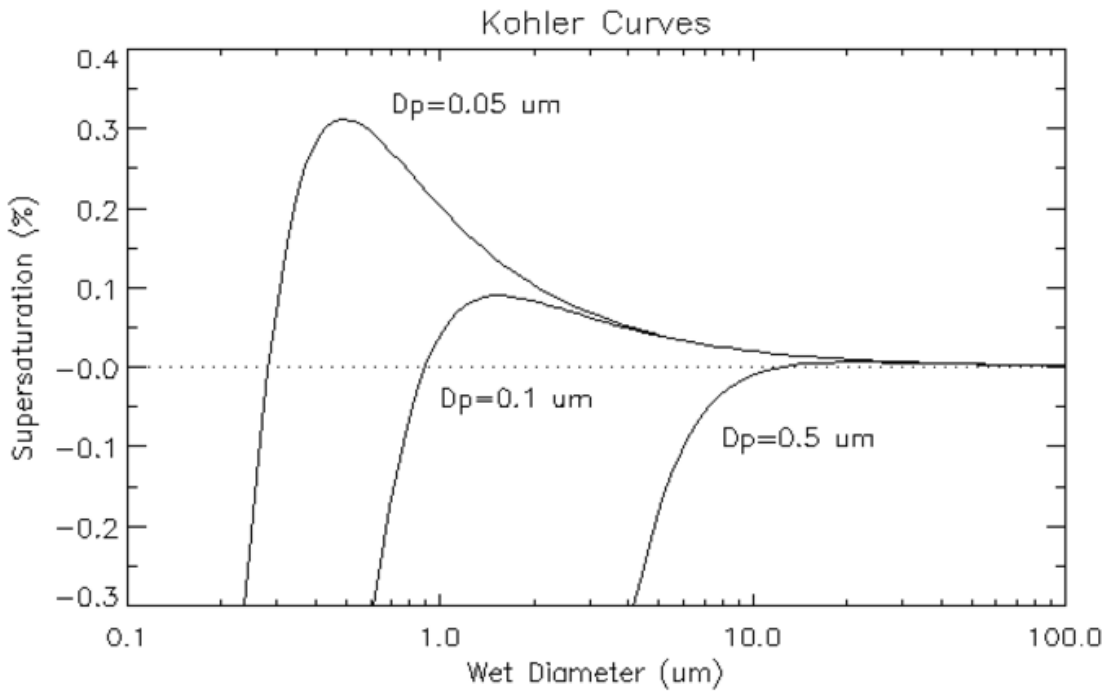

Figure 1-8. Köhler curves for NaCl particles with dry diameters of 0.05, 0.1, and 0.5μm at 293K (Kohler 1936; Seinfeld 2006).

(2) For a mixture of soluble and insoluble aerosols (dust, elemental carbon, etc.), assuming the insoluble portion does not interact with water, a modified Köhler equation is:

$$ln(\frac{p_w(D_p)}{p^0}) = \frac{4M_w\sigma_w}{RT\rho_w D_p} - \frac{6n_s M_w}{\pi\rho_w(D_p^3 - d_u^3)} \quad (1.2)$$

where d_u is the diameter of the insoluble material.

We can see that the effect of insoluble material is to increase the concentration of soluble material for the same overall droplet diameter, which makes the solute effect more significant.

Although dust particles are insoluble, they sometimes contain some hygroscopic materials from the emission source, or they interact with other hygroscopic aerosols. In such case, dust can also be a good source of CCN, especially in regions near the dust source (Figure 1-9) (Karydis et al. 2011; Twohy 2015; Twohy et al. 2009).

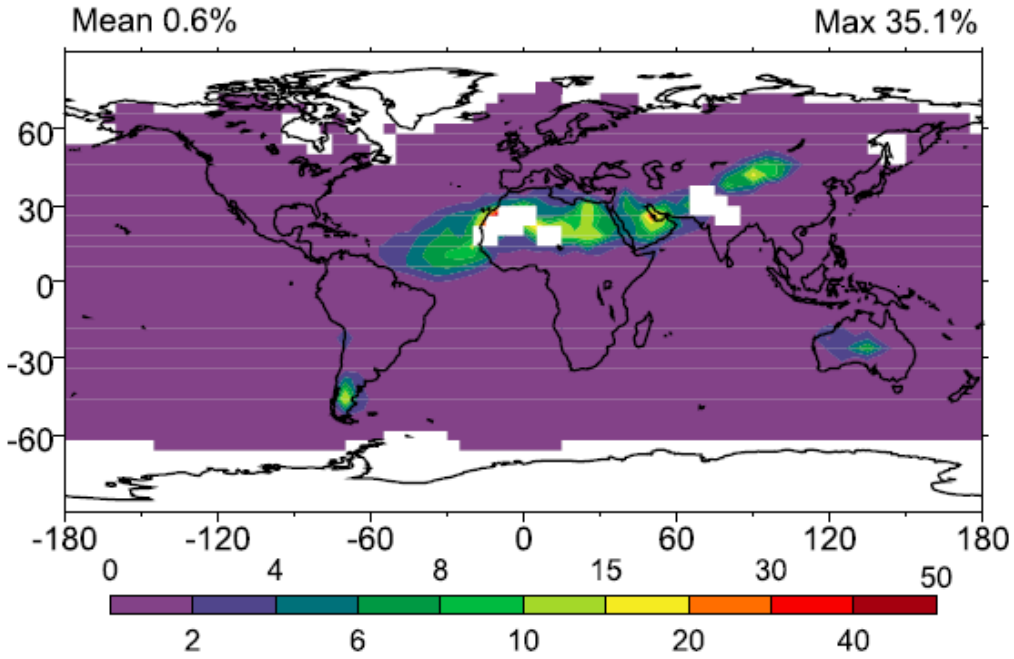

Figure 1-9. Predicted annual mean contribution (%) of mineral dust to total CCN for 0.4% supersaturation for the lowest cloud-forming level (960 hPa). White represents areas that are free of warm clouds throughout the year (Karydis et al. 2011).

In addition to acting as CCN, dust aerosols can become ice nuclei (IN) (Sassen et al. 2003; Twohy et al. 2009; Twohy 2015). Dust enhance the formation of ice crystal and change the precipitation pattern (Smoydzin et al. 2012). Observational studies show that dust particles can be wrapped into the anvil of tropical storms and become the dominant aerosols in that area (Twohy 2015). However, the amount of dust in the TC anvil is much less than that in the SAL. Not all dust

particles are wrapped inside the anvil; even if they do, many of them may have been precipitated before they reach the cloud anvil.

1.3.2 Aerosols decrease precipitation

As more aerosols become CCN, they increase the number of cloud droplets. For the same amount of water content, the droplets compete each other and decrease the average cloud droplet size (Lohmann and Feichter 2001; Haywood 2000; IPCC 2007; Twohy et al. 2009). Large cloud droplets grow faster and rain out earlier if they collect other small cloud droplets. Reducing the size of cloud droplets after adding aerosols leads to the reduction in precipitation. Both observational and modeling studies support this mechanism (Chapman et al. 2008; Mahowald 2003).

Dust particles can be a good source of CCN if they contain soluble component (Karydis et al. 2011; Twohy et al. 2009). There is a positive correlation between dust and low thin cloud in the west coast of North Africa (Mahowald 2003). The precipitation is suppressed in the Saharan dusty region due to little coalescence (Rosenfeld et al. 2001). In addition, more anthropogenic aerosols produce more thin cloud and reduce precipitation (Givati et al. 2004; Chapman et al. 2008).

1.3.3 Aerosols increase precipitation

Although small dust particles and anthropogenic aerosols suppress precipitation, when dust particles are coated with sulfate and other aerosols from evaporation of cloud droplets, they can act as giant cloud condensation nuclei (GCCN) and increase precipitation. With a maximum diameter

of 3.8-6 μm, large dry salt-dust CCN requires less supersaturation to be activated. They grow rapidly at the expense of the smaller droplets by diffusion and by collision-coalescence (Rudich 2002). Thus, the warm rain precipitation process will be faster (Levin et al. 2005; Yin et al. 2002; Levin et al. 1996; Rudich 2002; Karydis et al. 2011). This effect is more significant in the continental clouds, but not significant in the maritime-type clouds (Levin et al. 2005). Smoydzin et al. (2012) showed that the role of GCCN in the enhancement of precipitation is small. They also found that dust aerosols enhance the formation of ice crystals. The total amount of precipitation does not change significantly except in the mountain region where the glaciation of clouds by orographic ascent leads to a local enhancement of rainfall.

Sea salt itself is also a giant aerosol which can grow large enough to collect small droplets. Thus, it accelerates the precipitation at the beginning of the warm rain process (Johnson and Johnson 1982).

1.4 Aerosol Radiative Effect

Dust inside the SAL can alter radiative forcing, which in turn may impact tropical convection. Starting with aerosols radiative effect as general, we discuss the dust radiative effect.

In the earth-atmosphere system, radiative forcing is defined as “measure of the influence a factor has in altering the balance of incoming and outgoing energy in the Earth-atmosphere system and is an index of the importance of the factor as a potential climate change mechanism.” (Bernstein et al. 2007). Radiative forcing comes from changes in the incoming solar radiation, volcanic eruption, active gas, aerosols, etc. (Seinfeld 2006). The radiative forcing is calculated using the change of the radiation flux at different levels in the earth-atmosphere system.

Aerosols can scatter and absorb the radiation. The ratio of scattering efficiency to the extinction efficiency is called single-scattering albedo (w). The ratio can determine the relative importance of scattering and absorbing of aerosols. Different chemical components of aerosols have different abilities to scatter and absorb radiation. A complex refractive index $N=n+ik$ can be used to measure those effects. The real part n represents the scattering effect while the imaginary part k represents the absorption effect. Negative imaginary part means the aerosol absorbs the radiation. Refractive index is also a function of the wavelength of the radiation. The extinction coefficient also depends on the radius of the particles and the wavelength of the radiation.

Aerosol positive forcing indicates that the earth-atmosphere system receives more energy when the aerosol is present while the negative forcing is the opposite. The aerosol radiative forcing can be categorized into aerosol direct effect, semi-direct effect, and indirect effect.

The aerosol radiative effects have been investigated by many studies. Although observations cannot evaluate these radiative effects directly, they do reveal that cloud and precipitation patterns in areas with different aerosol concentrations are different. This can indirectly reveal the mechanism of radiative effects. Many numerical simulations were conducted to study these effects using global climate models (GCM) and high-resolution models with fully interactive aerosol-cloud feedback mechanism (e.g. Gustafson et al. 2007).

1.4.1 Aerosol direct radiative effect

"The direct effect is the mechanism by which aerosols scatter and absorb shortwave and longwave radiation, thereby altering the radiative balance of the earth-atmosphere system," according to IPCC report (IPCC 2007). The direct radiative effect of aerosols is evaluated at

different altitudes: at the top of the atmosphere (TOA), in the atmosphere and at the surface. Radiative forcing at TOA is the sum of radiative forcing within the atmosphere and at the surface. Within each category, we can further classify the direct effect into shortwave direct effect and longwave direct effect.

A. At the top of the atmosphere (TOA)

(a) For shortwave radiation, there is a scattering-absorbing model of an aerosol layer described by Seinfeld (2006). According to this model, the change of outgoing radiative flux can be calculated by the following formula

$$\Delta F = F_0 (1 - A_c) T_a^2 \left[\left(r + \frac{t^2 R_s}{1 - R_s r} \right) - R_s \right] \qquad (1.3)$$

where $t = e^{-\tau} + \omega(1 - \beta)(1 - e^{-\tau})$

$r = (1 - e^{-\tau})\omega\beta$

$\Delta F =$ change in outgoing radiative flux, Wm^{-2}

$F_0 =$ incident solar flux, Wm^{-2}

$A_c =$ fraction of the surface covered by clouds

$T_a =$ fractional transmittance of the atmosphere

$R_s =$ albedo of the underlying Earth surface

$\omega =$ single scattering albedo of the aerosol

$\beta =$ upscatter fraction of the aerosol

$\tau =$ aerosol optical depth

$If\ \left(r+\frac{t^2R_s}{1-R_sr}\right)>R_s, then\ \ \Delta F$>0. There is more outgoing flux from the earth-atmosphere to the space after adding aerosols, which leads to negative forcing.

$If\ \left(r+\frac{t^2R_s}{1-R_sr}\right)<R_s, then\ \ \Delta F$<0. There is less outgoing flux from the earth-atmosphere to the space after adding aerosols, which leads to positive forcing.

$If\ \left(r+\frac{t^2R_s}{1-R_sr}\right)=R_s, then\ \ \Delta F$=0. This is the boundary between aerosols cooling and warming. Based on this formula, we can get the critical single-scattering albedo of the aerosol that defines the boundary between cooling and heating.

$If\ \left(\mathrm{r}+\frac{\mathrm{t}^2\mathrm{R_s}}{1-\mathrm{R_s r}}\right)=\mathrm{R_s}$, by assuming common values to the variables, Figure 1-10 shows the critical single scattering albedo.

The single-scattering albedo corresponds to the albedo value of the underlying earth surface R_s and up-scatter fraction β. If the aerosol has higher single-scattering albedo value than the value on the curve, it scatters more radiation back to space, which leads to the cooling of the earth system. Thus, the cooling region (negative forcing) is above the curve while warming region (positive forcing) is below the curve. The positive slope of the curve means higher albedo of the underlying earth surface corresponds to higher single-scattering albedo of the aerosol.

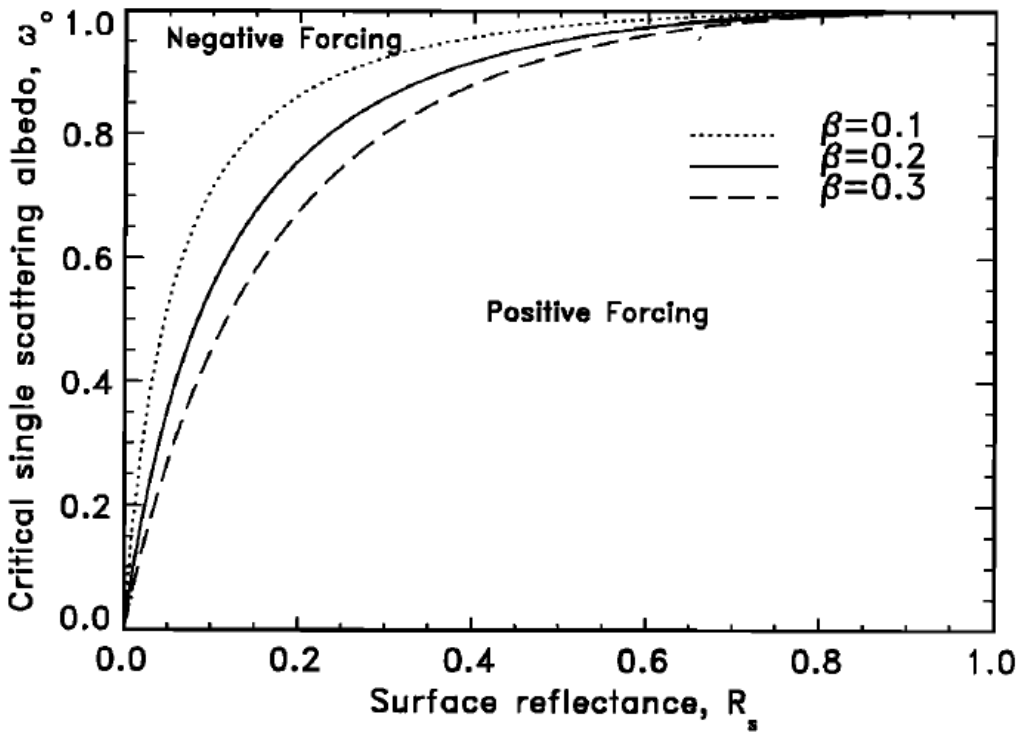

Figure 1-10. The critical single scattering albedo ω_o, at which the clear-sky radiative forcing changes sign as a function of surface reflectance R_s, for different backscattered fractions β(adapted from Haywood 2000).

Observational studies also support this relationship. From the flight data on Morocco on 19 May 2006, the Saharan mineral dust experiment shows the aerosol shortwave radiative forcing at TOA is linearly and positively correlated with the surface albedo (Bierwirth et al. 2009). At very high surface albedo (>0.25), the solar forcing at the top of the atmosphere is positive (Figure 1-11).

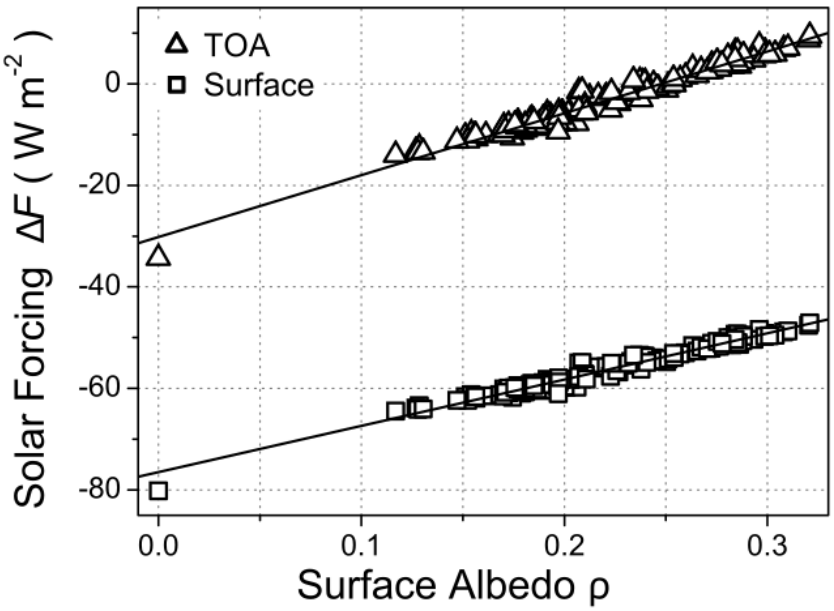

Figure 1-11. Correlation plot of the solar radiative forcing in dependence on the surface albedo for the flight on 19 May 2006 (Bierwirth et al. 2009). The triangle symbols and the rectangular symbols represent solar forcing at the top of the atmosphere and at the surface respectively.

The dark surfaces such as ocean and dark forest have small albedo. According to Figure 1-10, a small amount of scattering by aerosols is enough to produce the cooling effect over the dark surfaces. Figure 1-12 indicates the direct radiative effect of different kinds of aerosols at the tropopause. As aerosols quantities are close to zero above the tropopause, we can use this figure to indicate the aerosol direct radiative effect at TOA. This is verified by comparing figures in two papers: Takemura et al. (2002) and Heald et al. (2014) (figure not shown). Scattering aerosols (for example sulfate, sea salt, and organic carbon) and partially absorbing aerosols (for example dust) enhance scattering of the incoming solar radiation back to the space, and they have negative radiative forcing at the top of the atmosphere (Quaas et al. 2008; Takemura et al. 2002). Black carbon has strong absorption and small scattering characteristics. It exerts positive radiative forcing

(Seinfeld 2006; Takemura et al. 2002). Mineral dust is partially absorbing aerosol, and its radiative forcing at TOA is negative above the dark surface (Lin et al. 2009; Zhu et al. 2007; Conant et al. 2003; Otto et al. 2007; Takemura et al. 2002) (Figure 1-12 and Figure 1-14). Sea salt has negative shortwave radiative forcing by scattering the incoming solar radiation (Ayash et al. 2008; Ma et al. 2008; Takemura et al. 2002) (Figure 1-12d).

On the other hand, when aerosols are above clouds or bright surfaces (desert, snow, and ice), according to the curve, only very strong scattering aerosols can stay in the area above the curve (cooling region); sulfate is an example of this kind of aerosol (Figure 1-12b). For most other aerosols, their radiative forcing is positive because they reduce the albedo of the earth-atmosphere system (Huang et al. 2009; Islam and Almazroui 2012; Otto et al. 2007; Bierwirth et al. 2009; IPCC 2007; Takemura et al. 2002) (Figure 1-12).

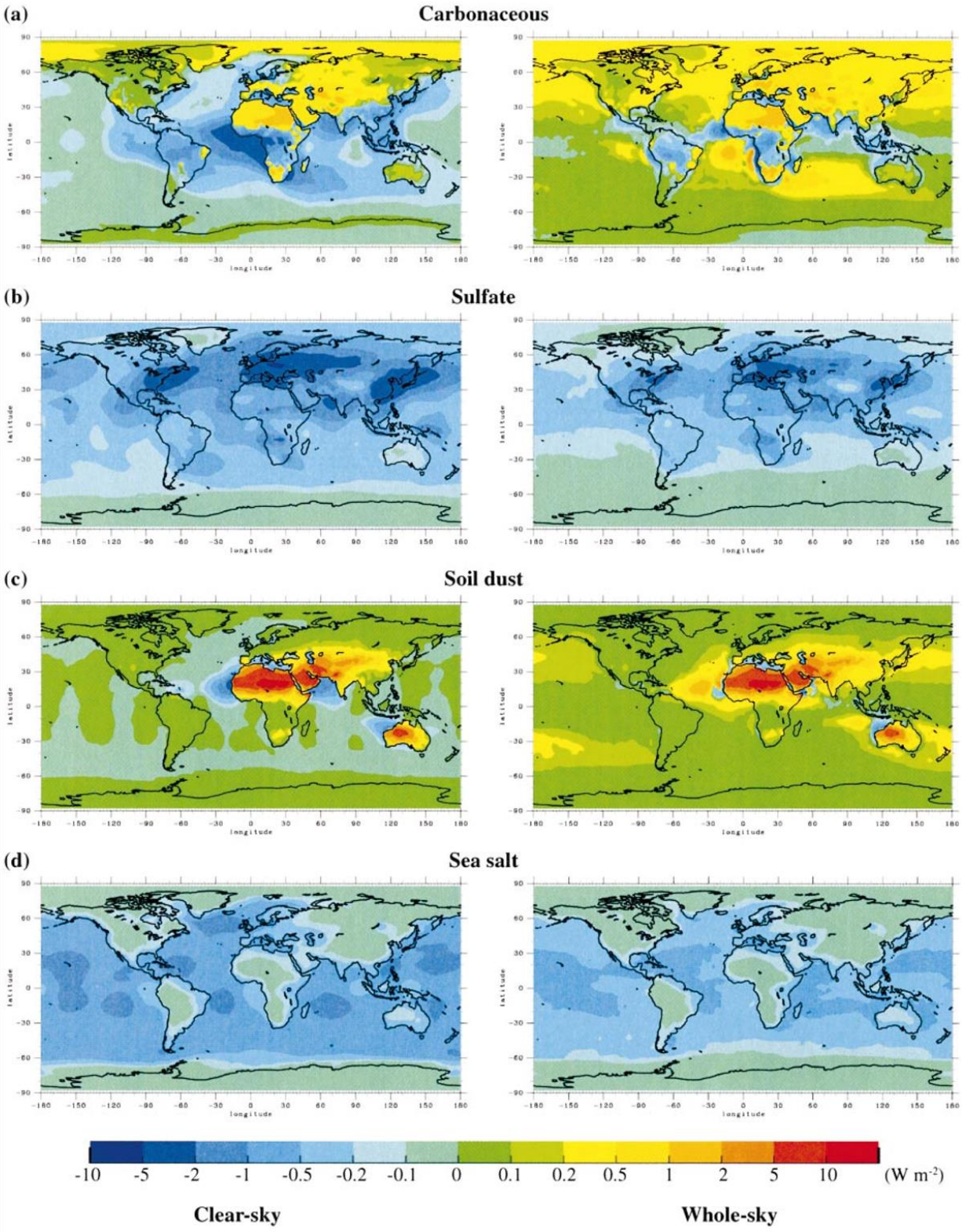

Figure 1-12. Annual mean distributions of the simulated direct radiative forcing at tropopause by each aerosol species of (a) carbonaceous (OC and BC), (b) sulfate, (c) soil dust, and (d) sea salt at the tropopause

under clear-sky (left) and whole-sky (overcast) (right) conditions in W m^{-2} (Adapted from Takemura et al. 2002).

(b) For longwave radiation, the radiative forcing is only substantial if aerosol particles are large and occur in considerable concentrations at higher altitudes (Tegen et al. 1996; IPCC 2007). Large aerosols such as mineral dust have positive longwave radiative forcing above both bright and dark surfaces because there is a reduction of outgoing longwave radiation due to absorption by dust (Figure 1-14) (Deepshikha et al. 2006; Zhu et al. 2007; Huang et al. 2009; Bierwirth et al. 2009). Dust has higher positive longwave radiative forcing when the higher surface temperature is high (Figure 1-13). Because sea salt particles are relatively large, they efficiently absorb the longwave radiation from the surface, which renders positive longwave radiative forcing (Ma et al. 2008; Ayash et al. 2008).

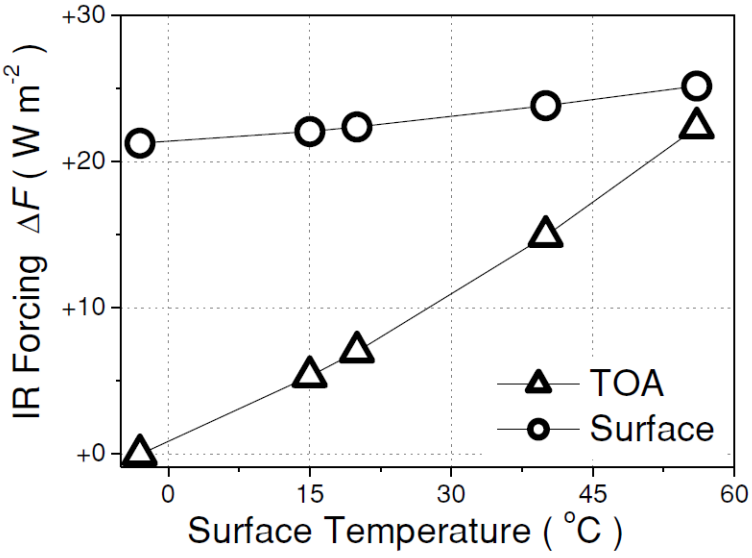

Figure 1-13. Integral thermal infrared radiative forcing for dust conditions of 19 May 2006, and for the surface temperature range during SAMUM: 15°C for the coldest night and 56°C for a hot noon (Bierwirth et al. 2009).

Combining the shortwave and longwave radiation, depending on the surface albedo, the total effect of dust at TOA can be negative or positive (Tegen et al. 1996). Over a dark surface, because dust negative shortwave radiative forcing is stronger than its positive longwave radiative forcing, the total radiative forcing is negative (Zhu et al. 2007). Over a bright surface, since dust shortwave radiative forcing is positive, together with positive longwave radiative forcing, the total effect is still positive (Tegen et al. 1996; Huang et al. 2009).

B. In the atmosphere

Depending on the chemical composition of aerosols, they will either induce positive forcing or negative forcing in the atmosphere. Black carbon is the most efficient aerosol to absorb radiation due to its small single-scattering albedo value, and it heats up the atmosphere (Liu et al. 2014; Seinfeld 2006). Mineral dust is another aerosol which absorbs the incoming solar radiation and heats up the atmosphere, with maximum heating in the dust layer (Figure 1-14; Figure 1-15) (Zhao et al. 2010; Mohalfi et al. 1998; Huang et al. 2009; Zhu et al. 2007; Satheesh and Moorthy 2005; Davidi et al. 2012). Dust can double the shortwave radiation absorption under clear-sky conditions (Satheesh and Moorthy 2005). There is almost no absorption of shortwave radiation by sea salt and sulfate (Takemura et al. 2002; Seinfeld 2006).

Depending on the single-scattering albedo, the warming effect due to absorption of solar radiation can be different. The average dust aerosol single-scattering albedo is high in Sahara (an average ω of 0.95 at 0.67 μm) and Asia (an average ω of 0.93 at 0.67 μm), which produces a small warming effect in the atmosphere (Forster et al. 2007). While in some areas such as Taklimakan, the single-scattering albedo of dust aerosols is 8% less than that in Sahara (an average ω of 0.87 at

0.67 μm), and it produces stronger warming effect (Huang et al. 2009). The net heating rate due to dust aerosols is about 0.5–1.0 K/day below and above the dust layers. The maximum warming occurs near the surface, which is about 0.5 K/day (Huang et al. 2009). The uncertainty of the absorption factors can have an impact on the heating rate in the lower atmosphere (1–3 km). Zhao et al. (2010) found a maximum heating rate of 0.8±0.5 K/day and an average rate of 0.5±0.2 K/day. In addition, dust aerosols can increase absorption when they are mixed with pollutants (Sohn et al. 2007).

There is a cooling effect within and at the top of the dust layer for longwave radiation (Figure 1-14 and Figure 1-15). However, since the shortwave radiative heating during the daytime is dominant, the total effect is warming within and above the dust layer (Figure 1-14 and Figure 1-15) (Zhu et al. 2007; Otto et al. 2007; Huang et al. 2009). Below the dust layer in the boundary layer over the desert, the longwave radiative forcing due to dust is positive because dust absorbs the outgoing longwave radiation (Figure 1-15) (Huang et al. 2009; Zhu et al. 2007). Some other scattering aerosols such as sulfate have negative forcing in the atmosphere. Dust aerosols have a ‘‘warming’’ effect over the Saharan desert which counteracts the shortwave ‘‘cooling effect’’ of other scattering aerosols.

C. At the surface

The aerosol shortwave radiative forcing is negative because the aerosols above the surface scatter and absorb the solar shortwave radiation and reduce the incoming radiation reaching the earth surface (Figure 1-14) (Evan and Mukhopadhyay 2010; Tegen and Fung 1994; Jim Haywood et al. 2003; Zhao et al. 2010; Seinfeld 2006). Such radiative effects are found to be most

pronounced over the desert regions (Mohalfi et al. 1998). Zhao et al. (2010) found that dust can reduce the downwelling shortwave radiation at the surface by 22 Wm^{-2}.

On the other hand, having mean particle sizes of the order of several micrometers, dust aerosols can effectively reduce the earth's outgoing longwave radiation and thereby warm the surface (Figure 1-14) (Sokolik et al. 1998; Zhang 2003; Tegen and Lacis 1996). However, it is not enough to compensate for the loss of the solar radiation reaching the surface (Huang et al. 2009; Zhu et al. 2007). From the climate point of view, dust longwave warming offsets 58% of dust shortwave cooling, and the overall dust radiative effect is to cool the Earth system (Xia and Zong 2009).

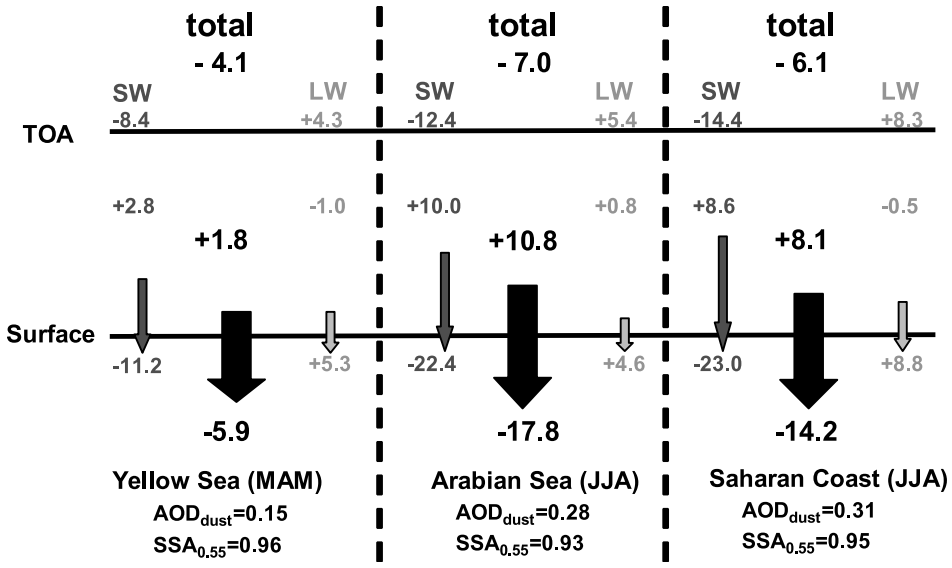

Figure 1-14. Clear-sky regional and seasonal mean SW, LW, and total (SW + LW) radiative forcing (W m^{-2}) by dust plumes (Zhu et al. 2007).

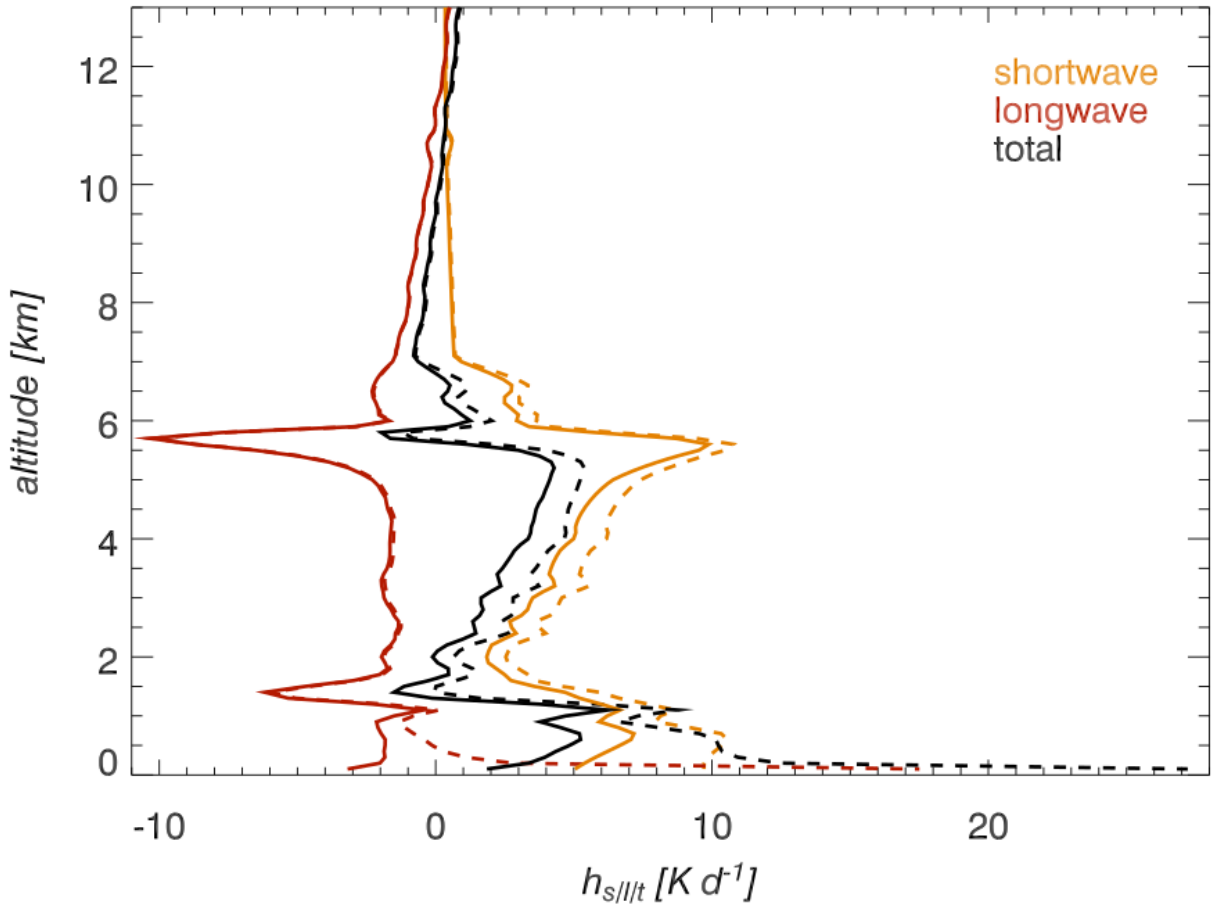

Figure 1-15. Profiles of the shortwave, longwave as well as total radiative heating rates for the reference case: measured ACE-2 dust over the ocean (solid) and desert (dashed) (Otto et al. 2007).

The radiative direct forcing mentioned earlier has some uncertainties. The factors contribute to the uncertainties in calculating the radiative forcing of aerosols include: the size distribution of aerosols, the vertical profile of the aerosol concentration, aerosol loading, surface reflectance, incoming solar zenith angle, refractive indices, single-scattering albedo, stratospheric adjustment, clouds, surface temperature, relative humidity, diurnal averaging, etc.(Osborne et al. 2011; Haywood and Boucher 2000; Seinfeld, John H. 2006). Clouds modify the aerosol radiative forcing. If the aerosol is below the clouds, since the clouds already scatter some part of the solar radiation

upward, the aerosol radiative forcing effect is reduced. Thus, aerosols above the clouds contribute to most of the aerosol radiative forcing in the cloudy region (Seinfeld 2006).

1.4.2 Aerosol semi-direct radiative effect

The semi-direct effect is "Absorption of shortwave radiation by tropospheric aerosols leads to heating of the troposphere that in turn changes the relative humidity and the stability of the troposphere and thereby influences cloud formation and lifetime. "(IPCC 2007). Absorption by aerosols such as black carbon and mineral dust contributes to the warming of the atmosphere and increases the evaporation of the cloud. Thus, the cloud will be reduced (Miller and Tegen 1999; Hansen et al. 1997; Johnson et al. 2004; Miller and Tegen 1998; Huang et al. 2009).

1.4.3 Aerosol indirect radiative effect

The aerosol indirect effect can be mainly classified as the first indirect effect, the second indirect effect, and the glaciation indirect effect.

(1) First indirect effect. Aerosols such as anthropogenic sulfate, carbonaceous aerosols, and dust act as CCNs. Higher concentration of these particles increases the number of cloud droplets. For the same amount of water content, as they compete with each other for CCNs, the average cloud droplet size is reduced (Jones et al. 1994; Haywood 2000; IPCC 2007; Lohmann and Feichter 2001; Jin et al. 2016). As more smaller cloud droplets scatter more shortwave radiation back to space, the shortwave radiative forcing at TOA is negative (Figure 1-16) (Jones et al. 1994; Jiang

et al. 2001; Penner et al. 2006; Boers et al. 2006; Saide et al. 2012). This also means that cloud albedo is increased.

(a) (b)

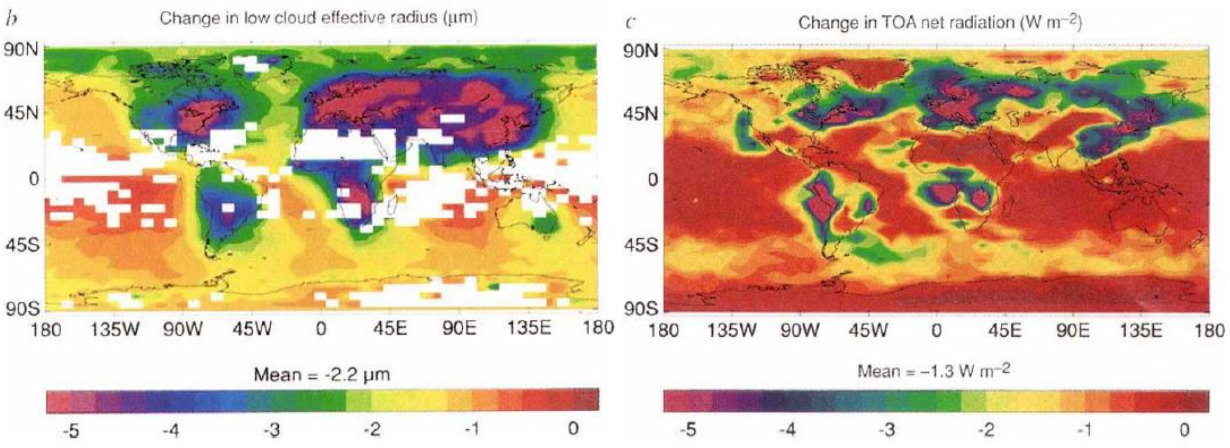

Figure 1-16. Hadley center GCM simulation. (a) Annual-mean composite of the instantaneous change in low cloud droplet effective radius due to changing from natural-only to total aerosol (sulfate) concentration. (b) distribution of the indirect radiative forcing due to the change in aerosol concentration, in terms of the change in the top of the atmosphere(TOA) net radiation (Jones et al. 1994).

(2) Second indirect effect. Because the formation of more cloud droplets due to aerosols such as sulfate and dust decreases the average size of cloud droplets, the precipitation efficiency is decreased, and the cloud lifetime is increased. The radiative forcing of cloud lifetime effect alone is negative at the top of the atmosphere (Haywood 2000; Rotstayn and Liu 2005; IPCC 2007).

For sulfate aerosols, the combination of the first and second indirect effects is negative at the top of the atmosphere (Haywood and Boucher 2000). Uncertainties related to the aerosol indirect effects are the parameterization of the auto-conversion, size distribution of the aerosols, chemical composition, etc.

(3) Glaciation indirect effect. Aerosols such as ice nuclei (IN) increase the precipitation and decrease cloud cover and cloud lifetime. Their effect on the radiation is positive (Yu et al. 2014)

1.5 Aerosol Microphysical Effect on Tropical Convection

In section 1.3, we discuss how dust and other types of aerosols modify atmospheric microphysics processes. They may change the development of a convective system as well. Aerosols can have positive or negative or small impacts on the development of TC.

(1) Negative impact

The mechanism can be explained by invigoration in the peripheral clouds of TC (Figure 1-17) (Rosenfeld et al. 2012; Wang et al. 2014; Zhang et al. 2009; Khain et al. 2010; Jenkins et al. 2008). In the peripheral rain band, as more CCNs from aerosols decrease the average size of cloud droplets and increase the number of cloud droplets, the warm rain process is suppressed. Thus, more cloud droplets are transported upward and form the ice crystals. The formation of ice crystal releases latent heat which invigorates (enhance) the convection. Thus, the enhancement of the vertical motion at the periphery of the storm reduces the flow towards eyewall at the low levels. This means that the convergence at the low levels is weakened, and the pressure at the storm center becomes higher. As the invigoration process continues in the periphery of TC, precipitation in a deep convection induces downdraft. The subsequent melting and evaporation bring colder and dryer

temperature to the lower atmosphere and create a cold pool. The cold pool suppresses the eyewall development by blocking low-level inflow and bringing colder air into the eyewall. The TC finally becomes weaker and larger in size.

In addition, absorbing aerosols such as black carbon will further enhance the invigoration in the periphery of the storm because the absorption of shortwave radiation by aerosols increases the instability (Wang et al. 2014).

Invigoration process mainly occurs in the periphery of the hurricane because, in the eyewall and inner spiral cloud bands, giant CCN produced by strong wind-induced sea spray will prevent invigoration and increase warm rain. The warm rain washes out the aerosols that remain in the eyewall (Rosenfeld et al. 2012; Khain et al. 2010),

This mechanism is summarized after many model studies. Idealized models show that dust from SAL acts as CCNs to decrease hurricane intensity and to increase the convection in the outer rainband (Carrio and Cotton 2011; Zhang et al. 2007, 2009). Climate model simulations reveal that, in the long term, the frequency of tropical storms is negatively correlated with anthropogenic aerosol concentration (Dunstone et al. 2013). High-resolution studies show that anthropogenic aerosols reduce cyclone intensity by the invigoration mechanism (Xinyong et al. 2017; Wang et al. 2014).

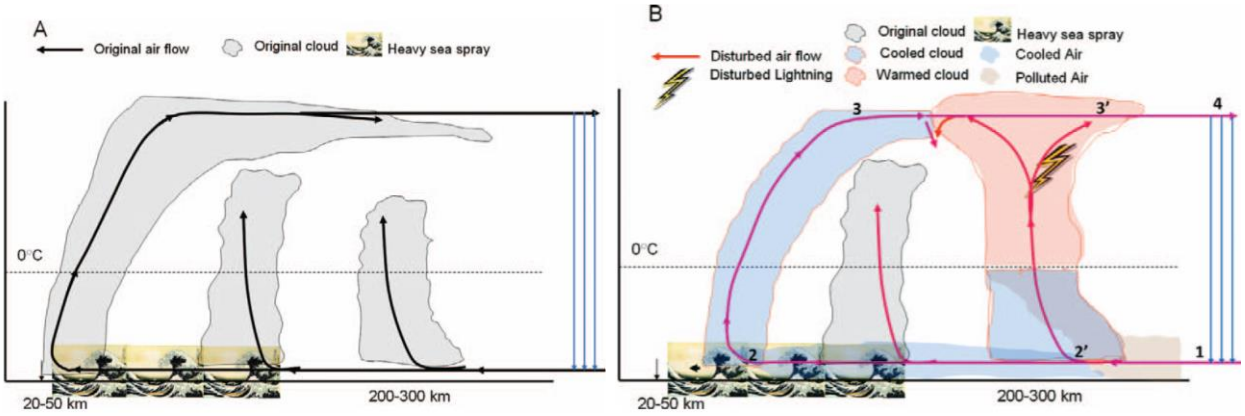

Figure 1-17. A conceptual model of aerosol impacts on tropical cyclones. The (a) undisturbed and (b) disturbed states are shown. (b) Pollution or dust aerosols slow the formation of warm rain in the peripheral clouds, causing invigoration and electrification of the clouds and warming aloft, coupled with stronger downdrafts and intensified low-level cold pools. Strong nucleation and precipitation scavenging and sea spray from the rough sea promote warm rain in the inner cloud bands and eyewall clouds, which reduces the suppression effect resulting from any remaining pollution aerosols that were not washed down, so that little aerosol-induced invigoration can occur there. The convection in the outer cloud bands decreases the inflow toward the eyewall. The cold pools also partially block the inflow, causing cooling, weakening and widening the eyewall, leading to weaker winds. The closure of the circulation system with subsiding air far away from the TC is denoted (blue lines). Adapted from Rosenfeld et al. (2012)

(2) Positive impact

Contrary to the results we discussed earlier, some studies such as Herbener et al. (2014) showed that aerosols may increase the hurricane intensity and decrease its size. By using idealized models, they claimed that the sign (positive or negative) of the impact depends on whether aerosols penetrate the eyewall or not. If aerosols only concentrate in the peripheral rainband, their influence on the TC is negative as we discussed earlier. However, if aerosols penetrate the eyewall (Figure 1-18a), the invigoration increases the convection in the eyewall and stretches the vortex vertically (Figure 1-18b). The surface wind will increase. The vertically stretch of the vortex in the eyewall draws lower equivalent potential temperature (θ_e) from the surroundings towards the eyewall and cool the column temperature of the rainband. As a result, the low-level pressure in the rainband region will be higher, and the pressure gradient between the TC core and the rainband will increase, which enhances the TC intensity.

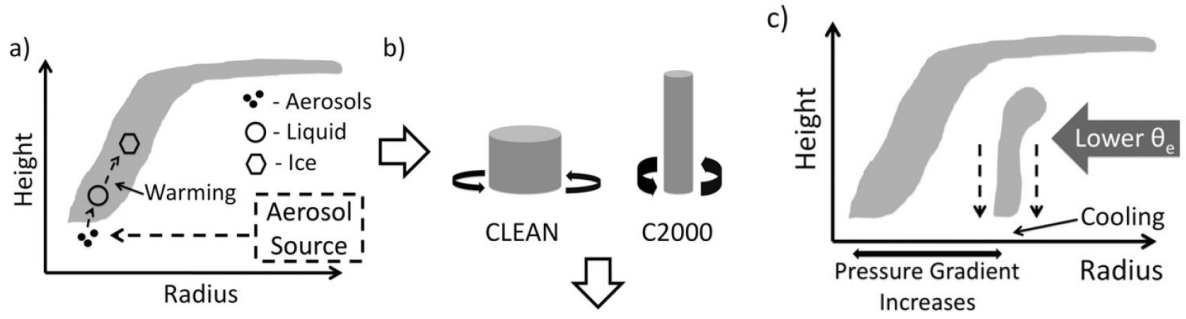

Figure 1-18. Schematic showing aerosol–cloud dynamics interactions taking place in the sensitivity simulations. The sequence of actions: (a) convective invigoration within the eyewall, then (b) vortex stretching in the storm core region, then (c) advection of lower θ_e air followed by column cooling in the rainband region, and finally, the increase of the horizontal pressure gradient between the rainband and storm core regions (Herbener et al. 2014).

(3) Small impact

Anthropogenic pollution may not have a noticeable impact on the intensity and track of typhoon in some cases, but it changes the precipitation, distribution of water hydrometeors, and microphysical processes (Huang et al. 2016). The precipitation rate in the rainband decreases after more aerosols are added into the model.

1.6 Thesis objectives

The above summary shows that there are still many debates about the interaction between tropical weather systems and the SAL/aerosols. In our study, we only focus on the dust effect given

the presence of the SAL. We try to quantify the sole impact from the dust on the convective system using carefully designed experiments.

We notice that researchers who find the large differences in TC/AEW intensity between clean air and polluted air (including dust) often use models with simplified settings to study the subject. Their methods have two main issues:

(1) A prescribed average aerosol profile is often used as the initial and boundary conditions in the simulations (Zhang et al. 2007b; Wang et al. 2014b). Given the non-linear nature of AEWs and TCs, inaccurate aerosols in the initial and boundary conditions may produce a large error as the system evolves. In addition, sensitivity tests in those studies usually give the uniform change of aerosols in their domain. However, in reality, the change of aerosols can be different at different levels and in different regions due to the physical processes.

(2) Some important physical processes are ignored in the simulations in some studies. For instance, a fixed aerosol layer is used in an idealized model in which transport and removal process are ignored (Ma et al. 2012). In reality, aerosols can be transported horizontally or vertically, which results in a change of aerosol distribution with time. Some studies focus on the radiative effect of dust but ignore the effect of dust in the microphysics processes (Grogan et al. 2016). Some researchers ignore longwave radiation in the model (Wang et al. 2014; Zhao et al. 2010). In some studies, the model background is not accurately described. For example, the distribution of dust is prescribed, an average sounding is assigned, but the SAL is ignored (Zhang et al. 2007). However, when TC is heavily surrounded by the SAL, the condensation will be prohibited due to its dryness no matter dust is present or not. It is not clear whether dust still significantly weakens TC if the SAL is considered.

In summary, the non-linear interactions between aerosols, cloud, and tropical systems are complicated. Assigning idealized aerosol profiles or ignoring some processes in idealized or simplified models may influence the results dramatically. Because of the limitations of the experiment designs in some of the previous studies, they reached different conclusions.

We here propose some methods to overcome those limitations. The first issue mentioned above can be addressed by using realistic initial and boundary conditions of the atmosphere, which can be obtained from existing global model data or from a data assimilation system. The second issue can be resolved by using a more "complete" model which considers as many important processes as possible. Particularly, a meteorological model coupled with an online chemistry/aerosol module can describe the interactions between aerosols and other meteorological variables in a complete manner. More recent works have already taken this approach to study how anthropogenic aerosols can affect TC developments in their mature stage (Jiang et al. 2016; Shen 2017). However, relatively few studies have applied these coupled models to study the relationship between SAL/dust and tropical weather systems. In this thesis, we will fill this gap.

The early development stage of Hurricane Earl (2010) is chosen in our study. Given the storm is weak and in the vicinity of the direct downstream of the Sahara Desert, we anticipate the dust may play a bigger role in determining the fate of the storm. The early development stage of the hurricane Earl (2010) consists of a weak disturbance stage, a tropical low stage, and a tropical depression stage. For simplicity, we use 'Earl' throughout this thesis without distinguishing its strength and stages. A coupled atmosphere and chemistry/aerosol model is used to investigate this impact qualitatively and quantitatively. The initial and boundary conditions for the aerosols in our simulation are taken from the global aerosol models. Thus, we can compare our results to previous studies given that our experiment designs can overcome their limitations mentioned above.

1.7 Thesis overview

The thesis is organized into the following chapters. Chapter 2 describes the numerical model and the observation. Chapter 3 describes a case study of hurricane Earl (2010) in numerical simulations. We first validate the meteorological forecast by the model using observations and reanalysis data. Then we validate the aerosol forecast using aerosol observations. Finally, we analyze the model result. We discuss the following topics: (1) dust aerosols direct radiative effect; (2) dust aerosols impact the zonal mean of AEJ and AEW; (3) dust aerosols affect the tropical low and the tropical depression. Chapter 4 illustrates how data assimilation technique can improve the forecast of the TC and aerosols. Chapter 5 gives conclusions and future works.

2. Data and model description

2.1 MODEL

To accurately evaluate the effect of SAL and dust aerosols in modeling hurricanes, we use the Weather Research and Forecasting model coupled with Chemistry (WRF-Chem) in our study. The model contains meteorological component and chemistry component. The chemistry component of the model is consistent with the meteorological component. Both components use the same transport scheme, the same grid, and the same physics schemes for subgrid-scale transport (Grell et al. 2005).

WRF-Chem has been widely used in the scientific community for different research purposes including studying aerosol direct and indirect effects (Zhao et al. 2010; Saide et al. 2012; Chapman et al. 2008; Jose et al. 2015; Baro et al. 2015). Generally speaking, models can simulate a variety of variables spatially and temporally more accurately when aerosol direct and indirect effects are included in the model. For instance, the model used by Saide et al. (2012) can well represent the liquid water path, cloud optical depth, top and base height, rain rate, and droplet concentration when the aerosol-cloud interaction process is included in the model.

The model domain in our study is shown in Figure 2-1. The horizontal resolution is 36 km. There are 376 x 163 horizontal grid points and 57 vertical levels up to 10 hPa.

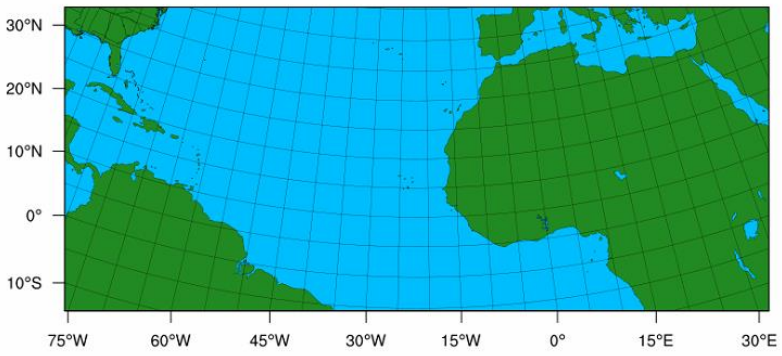

Figure 2-1. Model domain for the case study.

2.1.1 Meteorological Initial and Boundary Conditions

Regional atmospheric models require initial and boundary conditions. NCEP (National Center for Environmental) FNL Operational Global Analysis data can provide the regional model with the meteorological initial and boundary conditions (http://rda.ucar.edu/datasets/ds083.2). FNL has 1-degree by 1-degree grid spacing prepared operationally every six hours using the Global Data Assimilation System (GDAS). It continuously collects and assimilates various observational data for analyses. The analyses are available on the surface and at 26 mandatory (and other pressure) levels from 1000 hPa to 10 hPa. The boundary conditions of our simulation derived from FNL data are also updated every 6 hours.

2.1.2 Model Physics Schemes

WRF offers multiple physical options, enabling users to optimize its performance for specific scales, geographical locations, and applications. Based on earlier sensitivity test results, the physics

schemes that are chosen for all the experiments in this thesis are summarized in Table 2-1. The interactions among the physics schemes are shown in Figure 2-2.

Table 2-1. WRF physics schemes chosen in this study.

Options in WRF	**Name of the physics scheme**
Radiation	RRTMG scheme
Cumulus	New Grell scheme
Microphysics	Morrison double moment scheme
Surface layer	Revised MM5 Monin-Obukhov scheme
land-surface	Unified Noah land-surface model
Planetary Boundary Layer	Yonsei University scheme

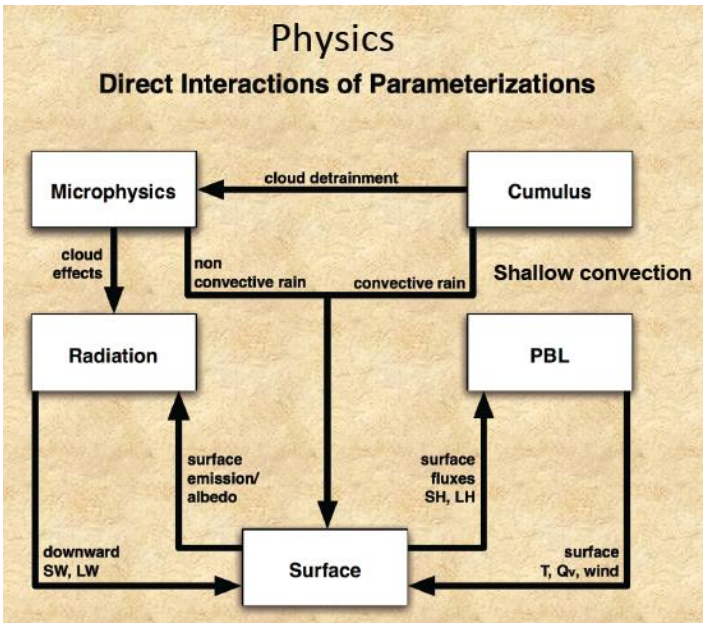

Figure 2-2. Direct interactions of parameterizations in WRF (Dudhia and Wang 2014).

We particularly describe Morrison double-moment microphysics scheme here since it is important in our study. The two-moment scheme (or double moment scheme) is better than the one-moment scheme. One-moment microphysics scheme only predicts the mass concentration of different particles. For example, the equation for the mass concentration of each hydrometeor species (cloud droplets, cloud ice, snow, and rain) can be written as (Morrison et al. 2005):

$$\frac{\partial q}{\partial t} = -\nabla \cdot (\boldsymbol{v} q) + \frac{\partial}{\partial z}(V_{qx}) + \nabla_D q + \left(\frac{\partial q}{\partial t}\right)_{PRO} + \left(\frac{\partial q}{\partial t}\right)_{COND/DEP} + \left(\frac{\partial q}{\partial t}\right)_{AUTO} + \left(\frac{\partial q}{\partial t}\right)_{COAG} + \left(\frac{\partial q}{\partial t}\right)_{MLT/FRZ} + \left(\frac{\partial q}{\partial t}\right)_{MULT} \quad (2.1)$$

where the q is the mass mixing ratio of each hydrometeor species, $\boldsymbol{v}$ is the 3D wind vector, V_{qx} denote the mass-weighted terminal particle fall speed for each species. $\nabla_D$is a turbulent diffusion operator for models that parameterize turbulent mixing.

The first three terms of the righthand side of the equation involve spatial derivatives: advection, sedimentation, and turbulent diffusion. The remainder of the terms on the right-hand side are the microphysical processes. The last six terms are primary production (ice nucleation or droplet activation), condensation/deposition (evaporation/sublimation), autoconversion (parameterized transfer of mass and number concentration from the cloud ice and droplet classes to snow and rain due to coalescence and diffusional growth), collection between hydrometeor species, melting/freezing, and ice multiplication (transfer of mass from the snow class to ice).

However, in reality, the number concentration of particles can be independent of their mass concentrations. For instance, during the accretion or breakup of particles, the mass concentration

and number concentration change independently. An additional equation is needed to predict the evolution of the number concentration:

$$\frac{\partial N}{\partial t} = -\nabla \cdot (\boldsymbol{v}N) + \frac{\partial}{\partial z}(V_{Nx}) + \nabla_D N + \left(\frac{\partial N}{\partial t}\right)_{PRO} + \left(\frac{\partial N}{\partial t}\right)_{EVAP/SUB} + \left(\frac{\partial N}{\partial t}\right)_{AUTO} + \left(\frac{\partial N}{\partial t}\right)_{SELF} + \left(\frac{\partial N}{\partial t}\right)_{COAG} + \left(\frac{\partial N}{\partial t}\right)_{MLT/FRZ} + \left(\frac{\partial N}{\partial t}\right)_{MULT} \quad (2.2)$$

where N is the number concentration of each hydrometeor species in the model: cloud droplets, cloud ice, snow, and rain. The last seven terms on the right side are primary production, evaporation/sublimation, autoconversion, self-collection, collection between hydrometeor species, melting/freezing, and ice multiplication.

Because the radiative transfer is impacted by the absorption and scattering of the cloud droplets, predicting cloud droplets number concentration and their size distributions more accurately will improve the accuracy of the radiative transfer process (Chapman et al. 2009). Moreover, cloud droplet activation depends on the aerosol distribution, chemical components, and supersaturation of the environment. Thus, the two-moment microphysics scheme can be coupled with an aerosol scheme to study the aerosol-cloud interaction, i.e. the indirect effect.

In the WRF-Chem model, if the chemistry process is turned on, the number of cloud droplets are activated by aerosols. The aerosols are predicted by the chemistry aerosol module. If the chemistry process is turned off, we choose to use the two-moment microphysics scheme with prescribed aerosols for cloud droplet activation.

2.1.3 Chemistry and Aerosol schemes

a. Gas-phase chemistry

CBM-Z chemical mechanism (Zaveri and Peters 1999) is used for gas-phase chemistry in our study. The scheme has 67 species and 164 reactions in a lumped structure approach which classifies organic compounds according to their internal bond types. Rates for photolytic reactions within CBM-Z are derived using the Fast-J scheme (Wild et al. 2000).

b. Aerosol chemistry

The aerosol module used in our study is Model for Simulating Aerosol Interactions and Chemistry (MOSAIC). MOSAIC is implemented into WRF-Chem (Fast et al. 2006; Zaveri et al. 2008). The scheme treats major aerosol species such as sulfate, nitrate, chloride, carbonate, black carbon, primary organic mass, and other inorganic mass (OIN). Dust is considered as OIN.

The aerosol size distribution in MOSAIC is described in a sectional approach. There are 8 bins, and each bin has its upper and lower diameters defined in Table 2-2. Each bin is assumed to be internally mixed, which means that all particles in each bin have the same chemical components.

One of the limitations of the MOSAIC aerosol scheme is that the diameter of the dust particles in reality can be larger than the maximum bin size (10 μm) in the model. The dust effect in the vicinity of its source region may be underestimated because of this limitation. Those large particles are heavy and tend to sediment before they move off the coast. Hence having 10 μm maximum bin size is expected to not generate large bias over the ocean. In spite of the limitation,

WRF-Chem with MOSAIC 8-bin aerosol scheme has successful simulated many aerosol processes in the scientific community for different research purposes (Zhao et al. 2010; Chapman et al. 2008).

Table 2-2. Particle dry-diameter ranges for MOSAIC 8 bins module.

	Bin 1	Bin 2	Bin 3	Bin 4	Bin 5	Bin 6	Bin 7	Bin 8
Minimum Diameter (μm)	0.039	0.078	0.156	0.312	0.625	1.25	2.5	5.0
Maximum Diameter (μm)	0.078	0.156	0.312	0.625	1.25	2.5	5.0	10.0

The aerosol direct effect is included in the WRF-Chem model. RRTMG radiation scheme has been coupled to MOSAIC aerosol module to include radiation feedback from aerosols (Zhao et al. 2011). Each chemical component has a specific refractive index which depends on the wavelength and the chemical composition. For dust aerosols, the refractive index for shortwave radiation is 1.55+0.003i, which is the default value in WRF and is used in other studies (Zhao et al. 2010). The overall refractive index for a given size bin is calculated by volume averaging all the refractive indices of all the chemical components. By using Mie theory, the aerosol optical properties such as extinction efficiency, scattering efficiency, and intermediate asymmetry factor are then determined and are passed to radiation scheme to calculate direct forcing (Fast et al. 2006).

Aerosol-cloud interaction can be studied by connecting MOSAIC and microphysics scheme such as Morrison double moment scheme. Aerosol size distribution and composition determine CCN. Within double moments schemes, cloud droplet number nucleation and evaporation rates

correspond to the aerosol activation and resuspension rates from the aerosol module (Chapman et al. 2009).

2.1.4 Emission

A large portion of aerosols come from the emission from the ground. Dust in the atmosphere is lifted by wind from the dust source. An "off-line" model named Georgia Tech/Goddard Global Ozone Chemistry Aerosol Radiation and Transport (GOCART) describes the dust emission process (Ginoux et al. 2001; Chin et al. 2000a,b; Chin et al. 2002). WRF-Chem adapts this scheme but changes to "on-line" mode (Zhao et al. 2010).

Dust flux equation is

$$F_p = CSs_p u_{10m}^2 (u_{10m} - u_t) \qquad if\ u_{10m} > u_t$$

$$\text{or } F_p = 0 \qquad \text{otherwise} \qquad (2.3)$$

F_p: dust flux ($\mu g\ m^{-2} s^{-1}$)

C : a dimensional factor ($\mu g\ s^2 m^{-5}$), it is tunable

S: source function. It comprises surface factors and potential dust source regions

s_p : a fraction of each dust size class in the emission

u_{10m} : 10-meter horizontal wind speed (m/s)

u_t : threshold of wind velocity, a function of surface wetness, air density, and particle size (m/s)

It is a common practice that, based on different experiments, the emission is tuned to match the observation. Constant 'C' in the flux equation can be tuned. There is another constant (we name

it constant ‘B’) to adjust the emission inside the model code, which acts the same purpose as the constant ‘C’ in the flux equation. Using a test experiment, we change the constant ‘B’ from 1.0 to 0.5 to fit the MODIS AOD observation while keeping the ‘C’ unchanged.

The emission rate for sea salt is reduced in our study as well. A constant is adjusted from 1.0 to 0.8 to match the MODIS AOD value. Other researchers also suggested that WRF-Chem model tends to overestimate sea salt (Saide et al. 2012).

2.1.5 Chemistry Initial Condition and Boundary Conditions

Usually, when researchers use the aerosol model, they provide a climatological chemistry initial and boundary conditions to the model. Since they are the climatological average of the chemistry quantities, we underestimate the chemistry quantities if we use them to study some weather events. Therefore, taking the initial and boundary conditions from another chemistry model is an effective way to improve the representation of chemistry species (Liu et al. 2011). Especially, time-varying chemical boundary condition from global chemistry models can improve the regional model accuracy (Tang et al. 2009).

In our study, two model outputs are potentially suitable for providing initial and boundary conditions. They are MOZART-4/GEOS-5 (Model for Ozone and Related Chemical Tracers, version 4 and Goddard Earth Observing System Model, Version 5) and MACC-II (Monitoring Atmospheric Composition and Climate, version 2). Both include the MOZART model as their chemical transport model (CTM). MOZART is version 4 in MOZART-4/GEOS-5 and is version 3 in MACC-II.

MOZART is an off-line global chemical transport model built on the framework of the Model of Atmospheric Transport and Chemistry (MATCH) (Rasch et al. 1997; Emmons et al. 2010a). Sea salt and dust are divided into four size bins. Other aerosols such as sulfate, black carbon, organic carbon, secondary organic, and ammonium nitrate are assumed to have lognormal number distributions. As MOZART is an off-line model, it requires meteorological fields from other models to drive it. These models can be climate models, NCEP/NCAR reanalysis (Kalnay et al. 1996), Goddard Earth Observing System Model Version 5 (GEOS-5), European Centre for Medium-Range Weather Forecasts' (ECWMF) Integrated Forecast System (IFS), etc.

Although GEOS-5/MOZART-4 has a newer version of the MOZART model, it tends to overestimate aerosol optical depth (AOD) over North Atlantic Ocean compared to MODIS AOD retrievals (Emmons et al. 2010). We found the same result in our study. Other disadvantages of this model are: (1) The data set is not available before 2007; (2) dust is the time average value which prevents us to generate high-temporal resolution boundary conditions, as we need to update the aerosol boundary conditions every 6 hours. Because of these disadvantages, we use MACC-II data in our study.

MACC-II product has MOZART version 3 as its chemical transport model (CTM) which coupled with ECWMF Integrated Forecast System (IFS). It predicts chemically reactive gases, greenhouse gases, and aerosols. Such coupled system is used by IFS data assimilation system to assimilate satellite observations for both meteorology and chemistry fields. In this coupled system, IFS and CTM run parallelly, and they exchange information every hour. IFS has 80 km horizontal resolution, while CTM has $1.125^{o} \times 1.125^{o}$ resolution to save the model running time. Both models have 60 vertical levels up to 0.1 hPa.

MACC-II includes dust, sea salt, organic carbon, black carbon, and sulfate aerosols. The modeled AOD has been validated against AOD observations from AERONET, MODIS, and CALIPSO (Morcrette et al. 2009). The model generally produces a comparable result to the observations horizontally and temporally. Satellite observations were assimilated into the model to improve the background and produced a better analysis. More detail description of MACC-II can be found in Inness et al. (2013). Many numerical studies have used MACC-II aerosol output as their model initial and boundary conditions (Archer-Nicholls et al. 2014, 2015; Giordano et al. 2015; Wang et al. 2015).

In the reanalysis product from MACC-II, AOD is mainly from dust, sea salt, black carbon, organic carbon, and sulfate. These aerosol species are converted from MOZART 4 bins in MACC-II to MOSAIC 8 bins in WRF-Chem to drive the model. Detailed conversions method is shown in the appendix.

2.2 Observations

2.2.1 Conventional Observations

Conventional observations include radiosonde observations, aircraft observation, marine surface observations, land surface observations (https://rda.ucar.edu/datasets/ds337.0/#!access). The radiosonde measurement is used to verify the simulations in our study. Other observations are used in the data assimilation. Their descriptions can be found in chapter 4.

2.2.2 Satellite Retrievals

(1) CIMSS Satellite wind data (http://tropic.ssec.wisc.edu/#): They are assimilated into the model. Detail will be discussed in chapter 4.

(2) Cloud-Aerosol Lidar and Infrared Pathfinder Satellite Observation (CALIPSO) (https://www.nasa.gov/mission_pages/calipso/main/index.html): It includes extinction coefficient, attenuated backscattering, depolarization ratio, and backscattering color ratio data. This dataset is used to verify the vertical distribution of the aerosol in our model forecast.

(3) Atmospheric Infrared Sounder (AIRS) (https://airs.jpl.nasa.gov/): It provides a daily global view of the three-dimensional physical state of the atmosphere (air temperature, water vapor, and clouds). Temperature profiles from the data achieve an accuracy of 1K for every 1 km layer in the troposphere and an accuracy of 1 k for every 4 km layer in the stratosphere. Humidity profiles from the data achieve an accuracy of 15% in 2 km layers in the lower troposphere and an accuracy of around 50% in the upper troposphere.

The AIRS Level 3 products contain gridded statistical summaries of the AIRS Level 2 geophysical quantities. It has daily, eight-day, and monthly Grid products. We use Level 3 data to analyze the temperature and humidity fields in the Atlantic Ocean and Sahara regions.

There are three processing streams of each Level 2 and Level 3 data type in the latest version (version6) data product: AIRS+AMSU, AIRS+AMSU+HSB, and AIRS-only. They differ in the combination of instrument radiances used in the retrieval process. AIRS+AMSU is the main version 6 product based on the combined AIRS and AMSU observations (Texeira 2013). Since this product is commonly used in the science community, we also use it.

(4) The Moderate Resolution Imaging Spectroradiometer (MODIS) (https://modis.gsfc.nasa.gov/): It monitors the ambient aerosol optical thickness over the oceans globally and over a portion of the continents. Satellite products used in this research include (a) Level 2 aerosol data which are based on narrow-swath subsets along CloudSat field of view track. Within each day, there are many files which represent different observation time. Data assimilation experiments in our study assimilate this product; (b) Level 3 daily joint aerosol/water vapor/cloud product, which is a combination of Level 2 product. It is used to verify the forecast of AOD from the model. Both are from the newest collection 6.1 version. A detailed description of Level 2 data will be provided later in the data assimilation chapter.

2.2.3 Aeronet

The Aerosol Robotic Network (AERONET) established by NASA and PHOTONS provides globally distributed observations of spectral AOD (https://aeronet.gsfc.nasa.gov/). This data is used in our study to verify the forecast of AOD from the model.

2.2.4 Hurricane observation

The "best track" data from National Hurricane Center (NHC) contain tropical cyclone center locations, the minimum sea level pressure, and the maximum surface wind speed (https://www.nhc.noaa.gov/data/#hurdat). We use them to verify our simulations.

3. Case study: Hurricane Earl (2010)

3.1 Overview

Earl developed from a tropical wave over the west coast of Africa on August 24, 2010. It became a hurricane on August 29, 2010 (Figure 3-1). Earl continued to intensify to a Category 4 hurricane, and it started to weaken when it later turned north-eastward. During the weakening stage, it made landfall on Nova Scotia on September 4, 2010 as a Category 1 hurricane. It brought damages to areas where it passed. It claimed five lives, caused a storm surge which destroyed many houses. The NHC official track forecasts starting from August 26 to 30, 2010 for hurricane Earl are shown in Figure 3-2. While its genesis was predicted, the forecasted tracks in the early stage were biased toward the east.

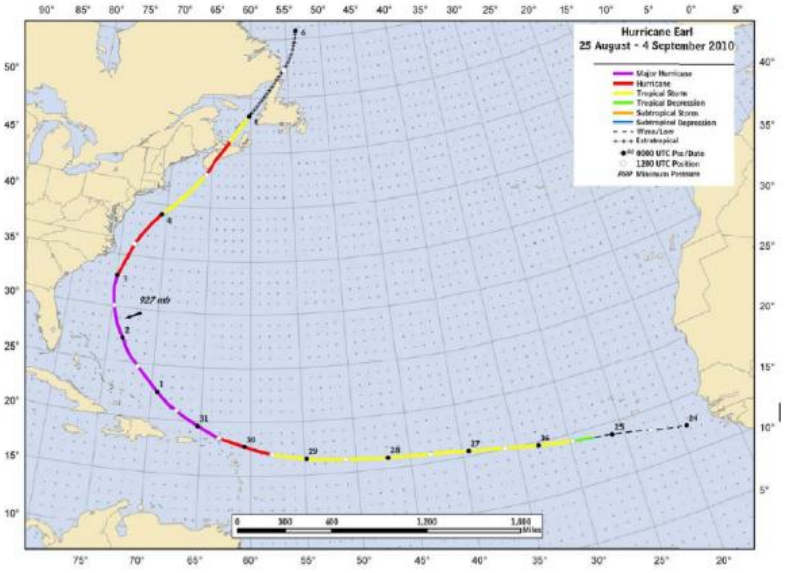

Figure 3-1. Hurricane Earl best track from 24 August to 4 September 2010 (Cangialosi 2011).

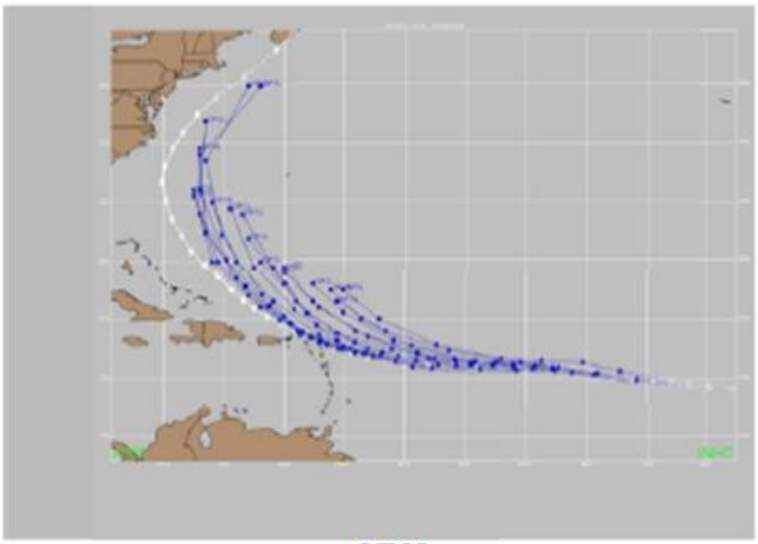

a. OFCL

Figure 3-2. Official track forecast from 26 August to 30 August (Cangialosi 2011).

3.2 Observational analysis of SAL

Hurricane Earl (2010) was under the influence of SAL when it was located in the central and eastern Atlantic (Cangialosi 2011). The combined Dry Air/SAL images showed that SAL signal was significant on the west African coast (Figure 3-3). On August 24, 2010, when it was a tropical low, it was located to the west of the African coast (Figure 3-3a). At the same time, SAL was located on its north side. One day later on August 25, SAL extended further to the west, and it began to wrap around Earl as it moved to the west side of Earl (Figure 3-3b). On August 26, the "wrap up" process was intensified as the leading edge of SAL moved to the south-west side of Earl (Figure 3-3c). On August 27, the "wrap up" process was weakened since SAL signal around Earl was weaker, especially on the west and north side (Figure 3-3d). Earl finally escaped and moved

ahead of SAL (Figure 3-3f). Given the above-mentioned process, it is reasonable to expect that SAL might impact the formation and development of Earl.

(a) (b)

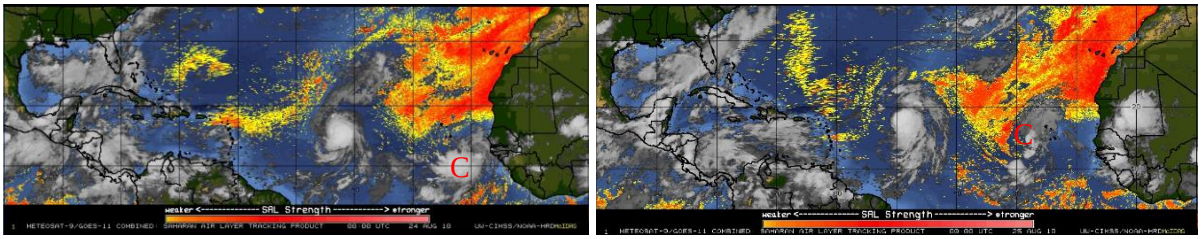

(c) (d)

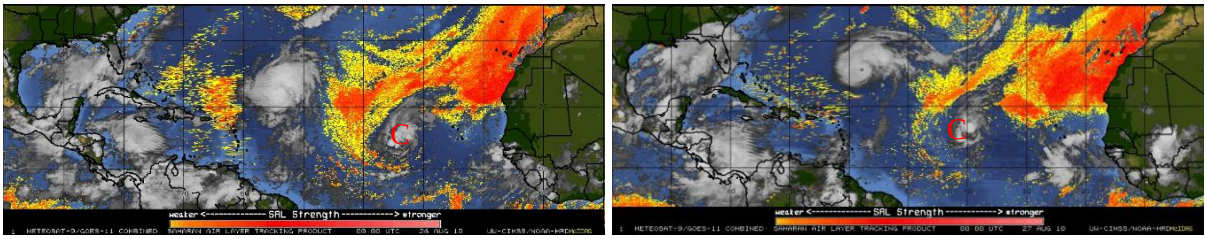

(e) (f)

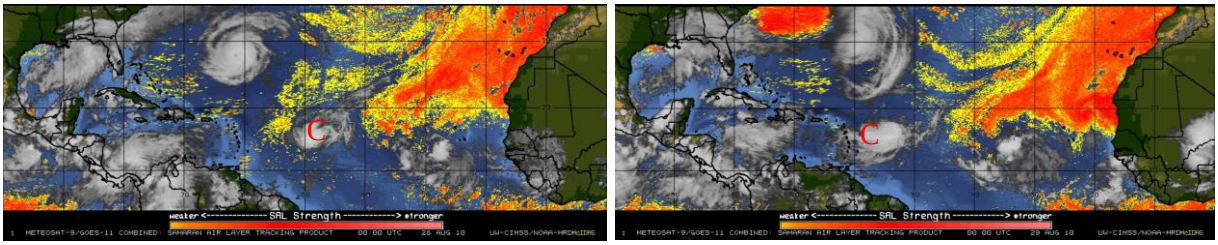

Figure 3-3. +METEOSAT-7/GOES-11 combined Dry Air/SAL Product (CIMSS/ University of Wisconsin-Madison) at (a) 00UTC 24 August, (b) 00UTC 25 August, (c) 00UTC 26 August, (d) 00UTC 27 August, (e) 00UTC 28 August, (f) 00UTC 29 August 2010. Red letter C indicates the position of Earl or its precursor.

SAL is dry, warm and dusty. We can verify these properties by using AIRS and MODIS products. From August 24 to 29, there is a warm region in North Africa and its west coast (Figure 3-4). Comparing the temperature distribution among all the layers (figures not shown), the temperature gradient is highest at around 850 hPa level. Relative humidity has a similar pattern as the temperature (Figure 3-5). At 850 hPa, relative humidity to the northwest coast of Africa can reach under 10%. MODIS AOD L3 product (Figure 3-6) shows that aerosols indicated by high AOD values generally collocate with dry and warm air.

(a) (b)

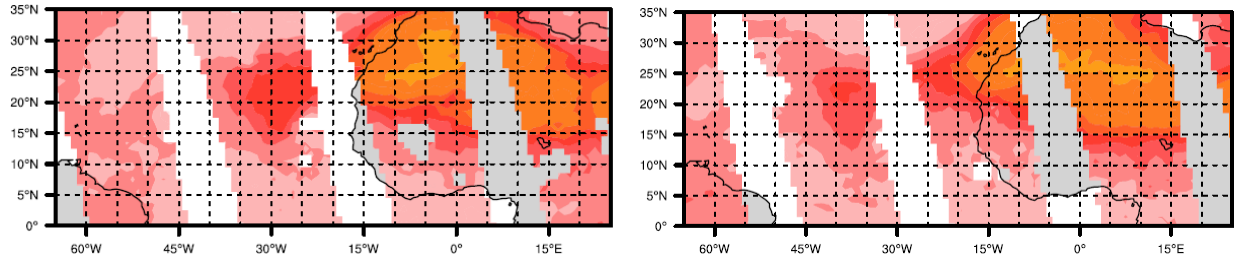

(c) (d)

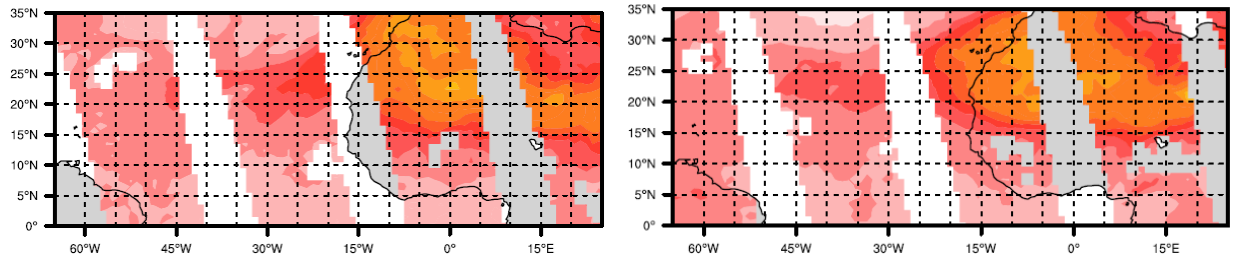

(e) (f)

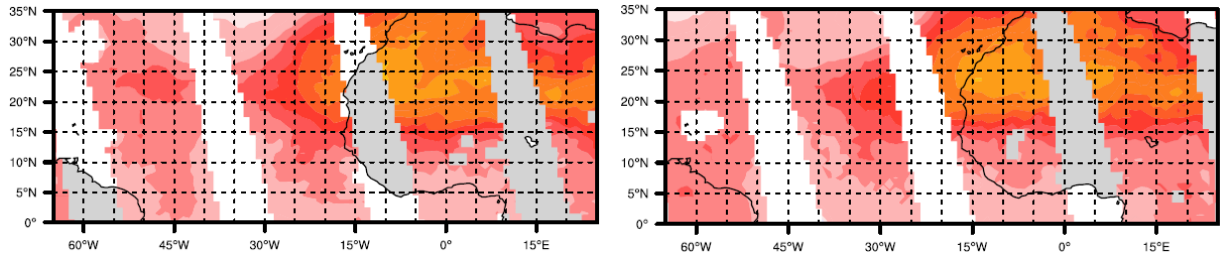

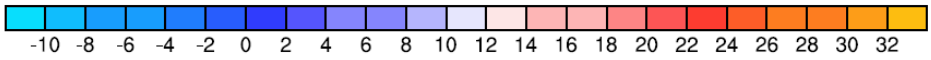

Figure 3-4. Temperature (°C) from AIRS L3 at 850 hPa on (a) 24 August, (b) 25 August, (c) 26 August, (d) 27 August, (e) 28 August, (f) 29 August 2010.

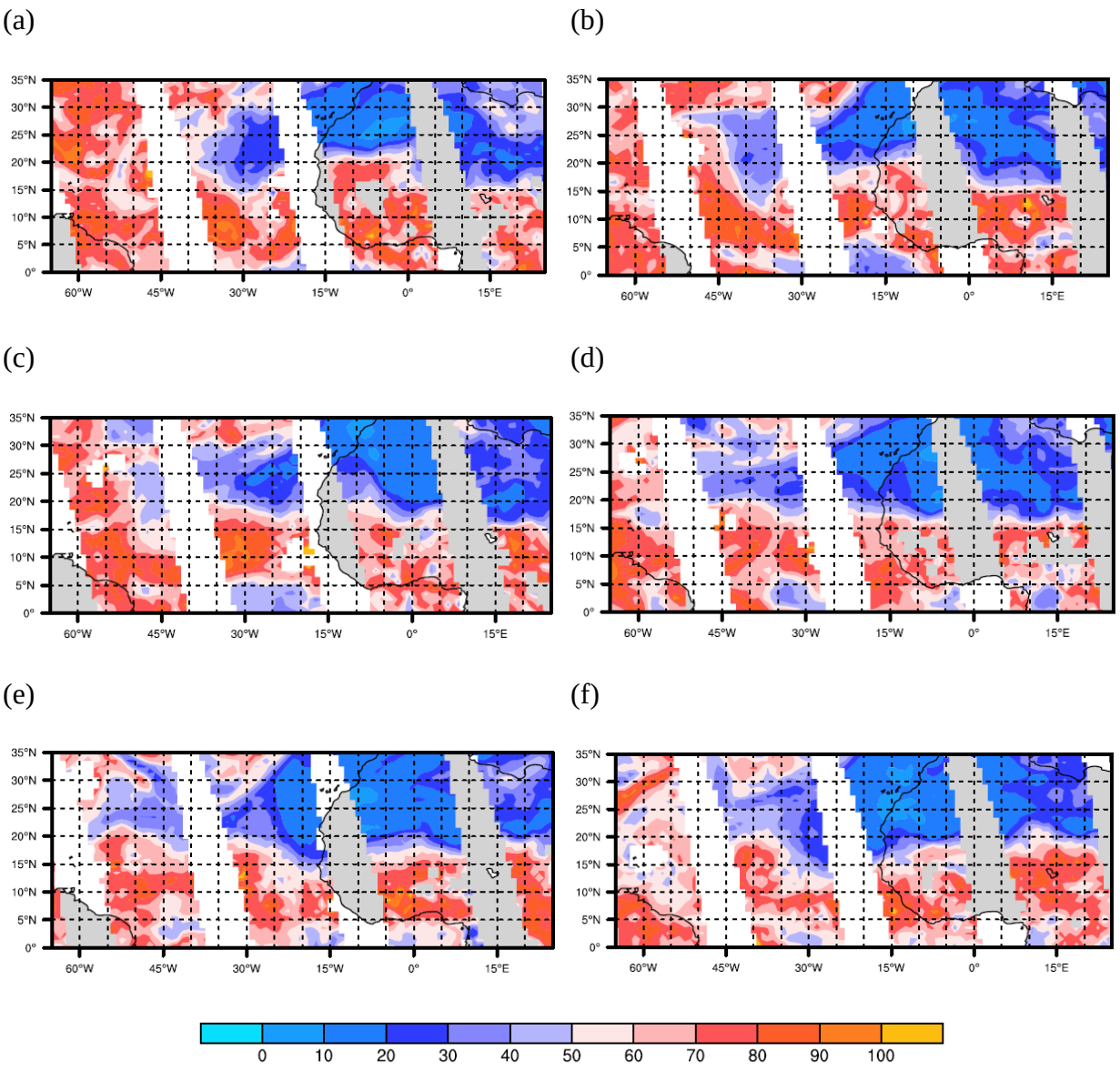

Figure 3-5. Relative humidity from AIRS L3 at 850 hPa on (a) 24 August, (b) 25 August, (c) 26 August, (d) 27 August, (e) 28 August, (f) 29 August 2010.

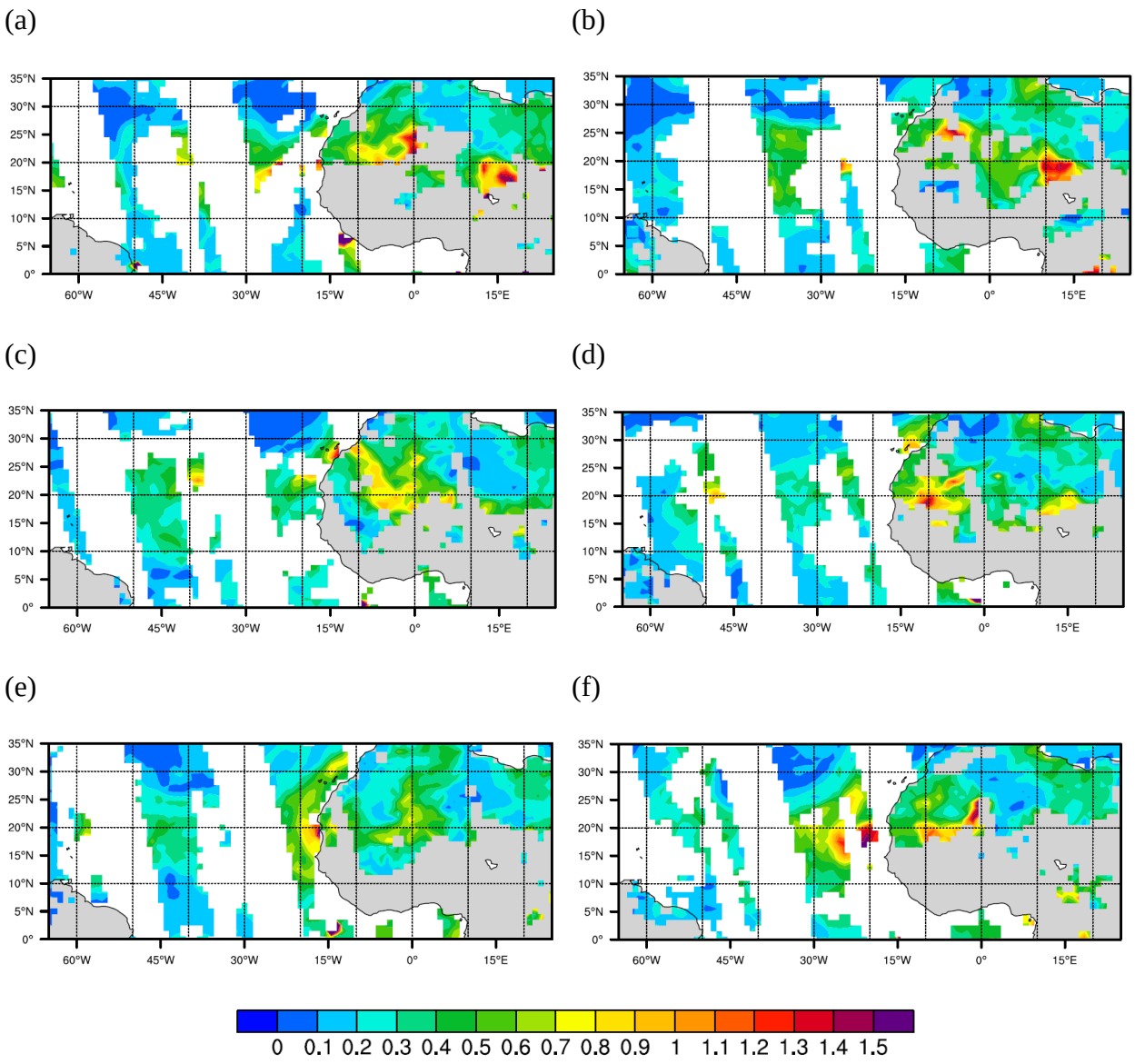

Figure 3-6. Aerosol optical depth at 550nm from MODIS L3 on (a) 24 August, (b) 25 August, (c) 26 August, (d) 27 August, (e) 28 August, (f) 29 August 2010.

3.3 Model simulation

3.3.1 Experiment design

To conduct the sensitivity test of the impact of aerosols on the hurricane, WRF control experiment excluding chemistry process is conducted first. A series of experiments are carried out to choose a suitable initial time for the control experiment. WRF simulations are initialized at different times ranging from 12 UTC August 19 to 00UTC August 23 and run for 5 days. Figure 3-7 shows the simulated tracks and the NHC best track. All tracks are plotted from 00UTC August 24 when a closed-surface circulation developed. Better track forecasts generally are achieved when the models are initialized at a later time. However, we notice that when the model is initialized at 12UTC August 20 and 00UTC August 21, the simulated tracks are less accurately placed compared to the simulation launched at 00UTC on August 20. This means that the initial conditions from FNL at these two times may contain larger errors. Initializing the model at 00UTC on August 20 also does not produce good results because the model produces a spurious hurricane later (figure not shown). Thus, we choose to initialize the model at 12UTC on August 21, which is early enough to include significant impacts from dust and can lead to a reasonable track forecast among all the simulations.

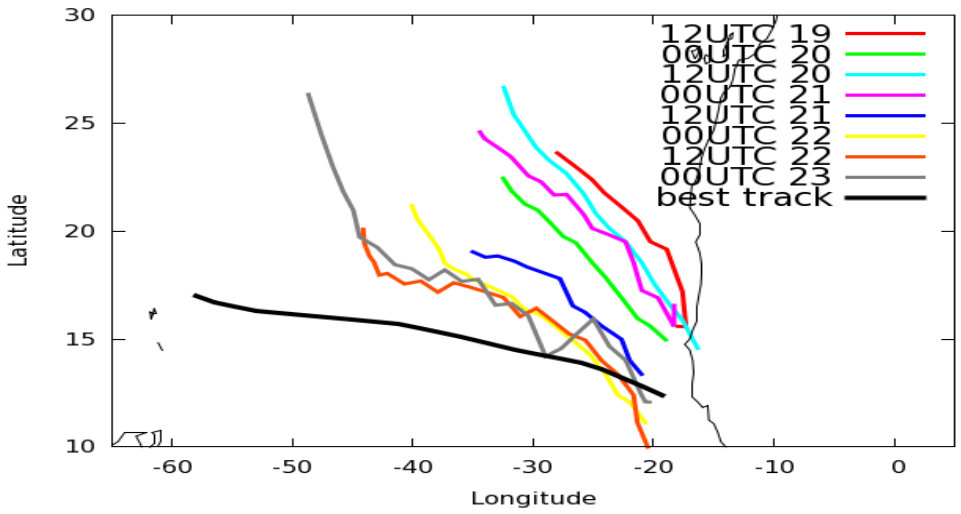

Figure 3-7. Model simulated tracks from different initial times and the best track (Black line). All tracks are plotted from 00UTC 24 August 2010. The legends on the upper right corner indicate different initial times.

We notice that TC forecast errors grow significantly with forecast time. According to NHC tropical cyclone report for hurricane Earl (Cangialosi 2011), the track forecast errors arrange from 377.6 km (203.9 n mi (nautical mile)) to 768.6 km (415 n mi) at 120h from different models. The track forecast error in ExC is 527.8 km (285 n mi) at 120h (12UTC 26), which is still in the reasonable range of the official forecasts. Therefore, we will not attempt to correct the track errors at this time, rather we will focus on how aerosols will affect the forecasts.

Two additional experiments (experiment ExO and ExDO) are based on the control experiment ExC, but the chemistry processes are added to the model (Table 3-1). All experiments are initialized at 12UTC on August 21, 2010 and run for 5.5 days until 00UTC August 27. As mentioned earlier, the control experiment is conducted using the WRF model without any chemistry. The experiment ExO is WRF-Chem simulation with aerosols (black carbon, organic carbon, sea salt, sulfate, but no dust) included into the model initial and boundary conditions. In the experiment ExDO, dust and other aerosols mentioned above are added to the model. By

comparing the experiment ExO and the experiment ExDO, we can investigate the added effect of dust.

Table 3-1. Experiment configurations.

	Chemistry	Dust	Black carbon, Organic carbon, Sea salt, Sulfate
Control experiment ExC	None	None	None
Experiment ExO	Yes	None	Yes
Experiment ExDO	Yes	Yes	Yes

3.3.2 Model evaluation

3.3.2.1 Evaluation of Meteorological variables

The model simulated track is determined by locating the minimum sea level pressure of the system. We can see that three simulations have similar tracks, and they are biased to the north-east (Figure 3-8). As forecasts from other models such as ECWMF show no better results, our track biases are not a result of the deficiency in our experimental design. Possible reasons are errors in the initial and boundary conditions in the models. The track of a tropical cyclone is mainly controlled by its ambient large-scale flows and interactions between the TC and other weather systems. In the case of Earl, hurricane Danielle (2010) developed before Earl may have disturbed the environmental flow in front of Earl (Figure 3-3). Improving the TC forecast requires the improvement of the prediction of multiscale physical processes over disparate regions of the

hemisphere, rather than just locally over the disturbance of interest (Fowler and Galarneau 2017). We will show later in chapter 4 that the data assimilation indeed can improve the track forecast when the large-scale background flow becomes more accurate. Here we focus on one aspect of the model errors, that is whether considering aerosols especially dust will change the TC forecast.

Adding aerosols to the model improves the track slightly before 18UTC on August 25 (east of 29 ^{o}W) since both tracks in ExDO and ExO are closer to the best track. ExDO track forecast outperforms ExC throughout the whole period with track error reduced by 7% on average from 00UTC 24 to 12UTC 26 (60h to 120h). Overall, the track forecast improvement is small but noticeable when the simulations include aerosols.

All simulations produced stronger sea-level low pressure and higher maximum wind compared to the observations. (Figure 3-9 and Figure 3-10). Many factors may have contributed to this overprediction. For example, interactions between the storm and its environment including the ocean, and the cumulus parameterization scheme that may trigger too much convection. After 12UTC on August 25, the minimum pressure in ExDO becomes higher than that in the other simulations, and its maximum wind becomes lower. It shows that dust aerosols reduce the intensity overprediction by 35% in the minimum SLP and 32% in the maximum wind at the 120h forecast.

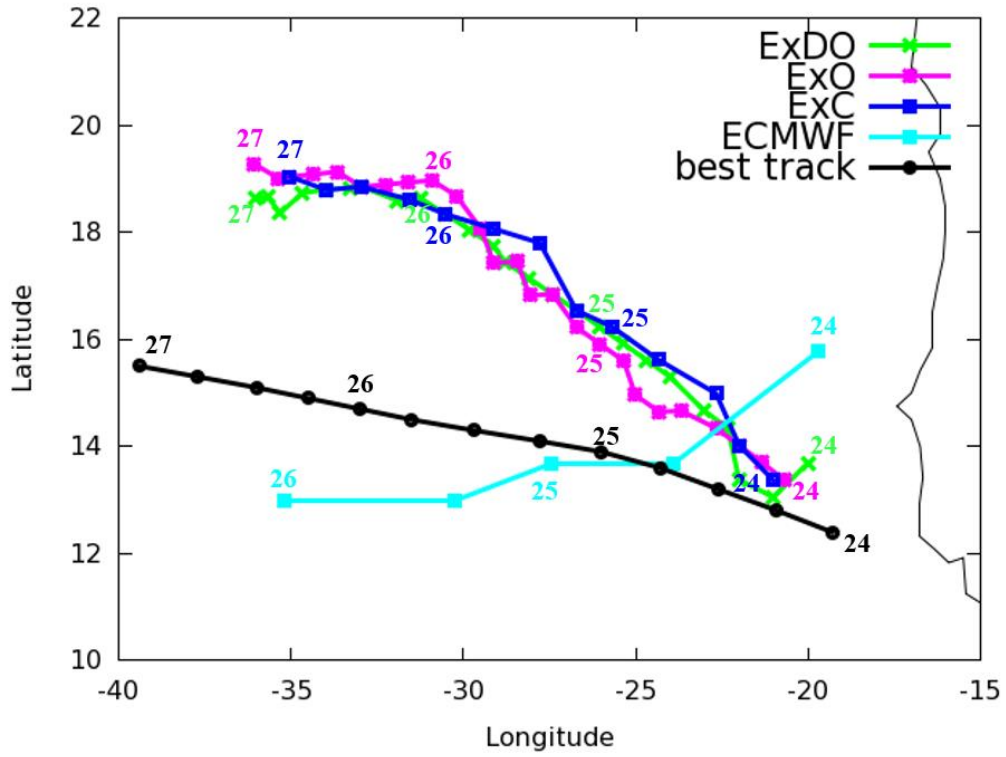

Figure 3-8. The simulated tracks and the best track for Earl. The ECMWF track forecast is from 12UTC 24 to 12UTC 26 at every12 hours. The other tracks are from 00UTC 24 to 00UTC 27 August 2010. The track from ExC and the best track are in 6 hours interval. The tracks from ExDO and ExO are in 3hours intervals. The numbers indicate the days. Detail description of the experiment configurations can be found in Table 3-1.

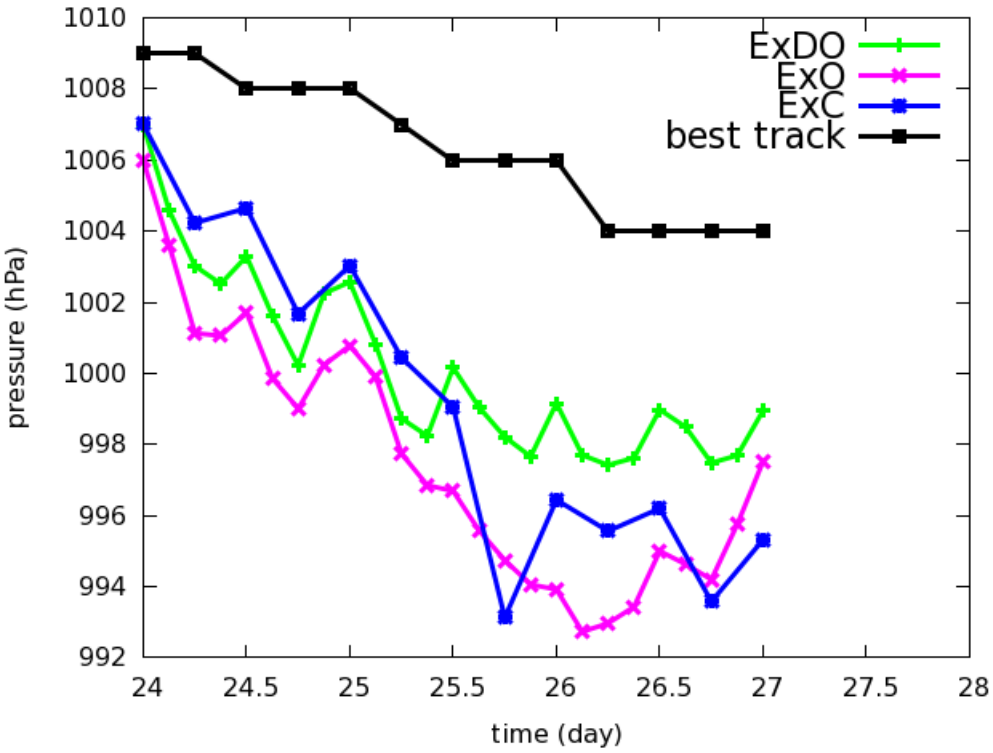

Figure 3-9. Minimum sea level pressure (units: hPa). ExC and best track are in 6 hours interval while ExDO and ExO are in 3hours intervals. Detail description of the experiment configurations can be found in Table 3-1.

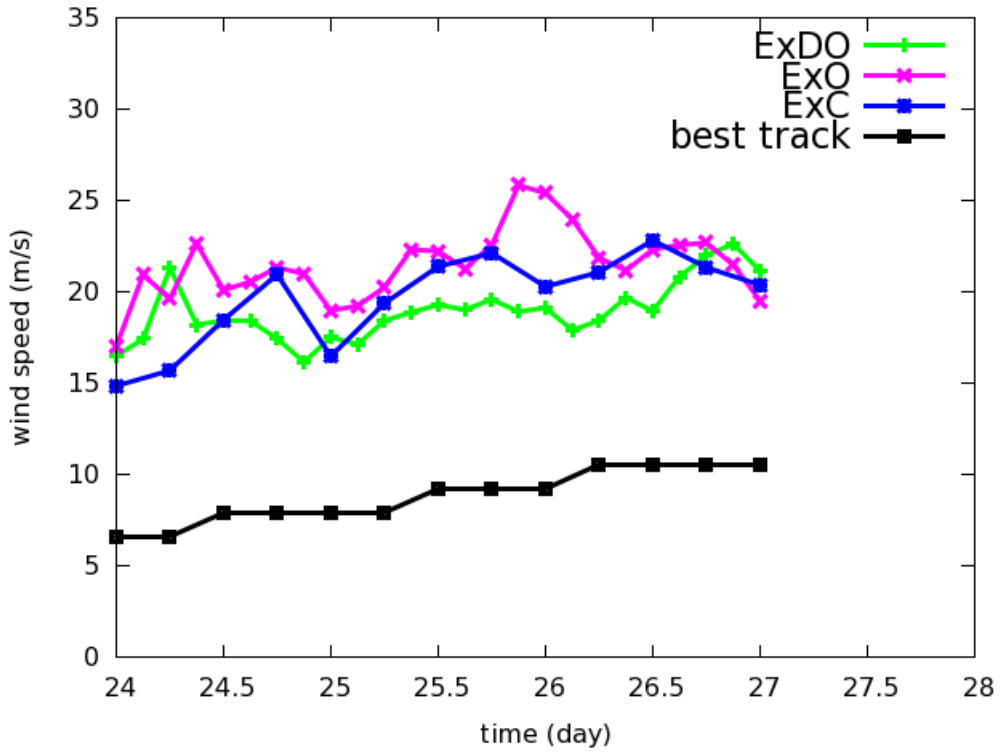

Figure 3-10. Maximum surface wind speed (units: m/s). ExC and best track are in 6 hours intervals while ExDO and ExO are in 3-hour intervals.

Although the simulations produce stronger low-pressure center and biased track compared to the observations, the overall distribution and evolution of the systems are comparable to the FNL reanalysis (Figure 3-11). At 12UTC on August 22, one day after the simulation starts, in the experiment ExDO, a low-pressure system is present in North Africa (Figure 3-11a). The system is stronger and is located to the south in our simulations than that in FNL. We will analyze this system in detail in the following chapters, to show this system is a part of the AEW system that generates hurricane Earl later.

At the beginning of tropical low stage at 00UTC on August 24, a low-pressure center is located on the west coast Africa (Figure 3-11b). The location in our simulation is close to FNL reanalysis, but our simulation still shows a stronger center. One day later at 00UTC on August 25,

the system moves to the west and develops into a tropical depression (Figure 3-11c). The system in our simulation is still stronger than that in FNL, and its location is to the north of its position in FNL. Other experiments (ExC and ExO) have similar patterns in sea-level pressure as the experiment ExDO (figures not shown).

(a)

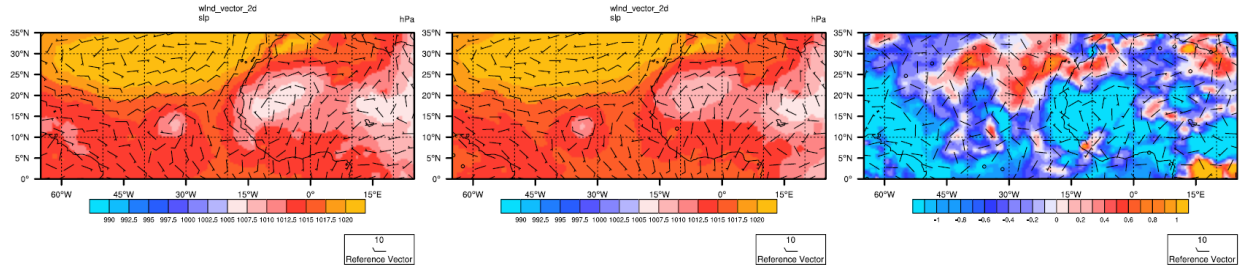

(b)

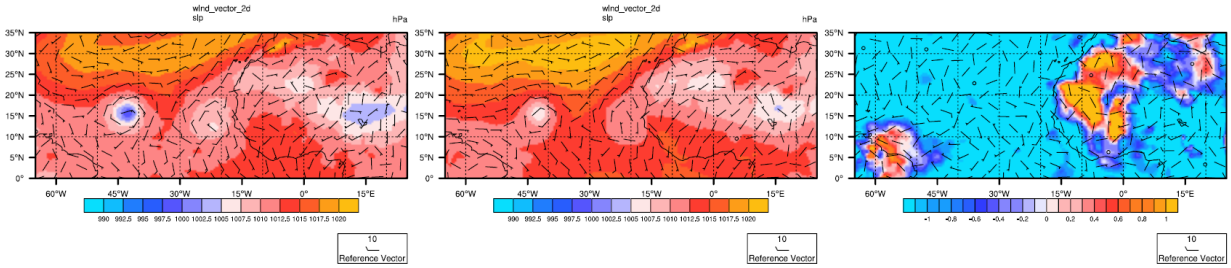

(c)

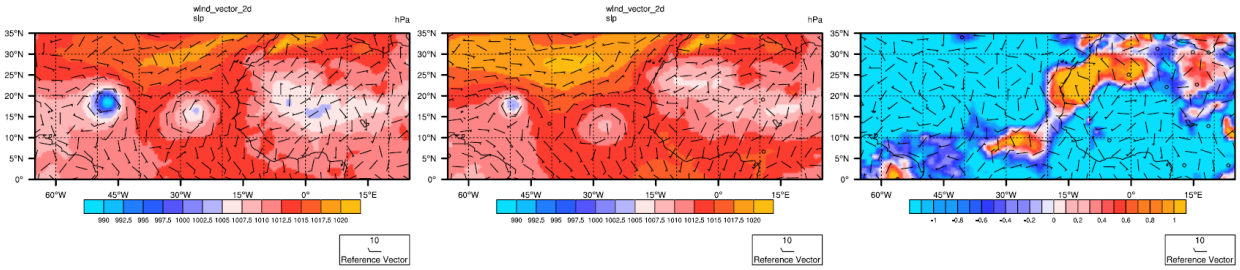

Figure 3-11. Sea level pressure (hPa, shading) and wind vector for (left) the experiment ExDO, (middle) the FNL reanalysis, and (right) the difference (ExDO-FNL) at (a) 12UTC 22; (b) 00UTC 24; (c) 00UTC 25 August 2010.

The low-pressure system at the surface is a part of a complex convective system which has a wave pattern at the upper levels. We named the wave "African Easterly Wave" (AEW) which is significant at 600 hPa level. A local maximum relative vorticity and a curvy streamline can be seen at around 10^{o}N, 0^{o}E at the beginning of the simulation ExDO at 12UTC on August 21, 2010 (Figure 3-12). This indicates the location of the AEW trough. The dense streamline represents African Easterly Jet (AEJ) which is an axis of maximum easterly wind. AEW and AEJ continue to move to the west. AEW is located at 10^{o}W one day later at 12UTC 22 August (Figure 3-13). The denser streamline and higher relative vorticity in ExDO simulation compared to FNL indicate that the wave is stronger in the simulation. The stronger wave corresponds to a stronger low-pressure system at the surface. One day later at 12UTC 23 August (Figure 3-14), AEW in the simulation is still stronger than that in FNL, and its trough position is to the north of AEW in FNL. At the tropical low stage at 00UTC 24 August (Figure 3-15), the stronger AEW corresponds to the stronger surface pressure in the simulation. Its trough is still biased to the north compared to FNL. Such bias remains in the whole life of this system in the simulation (Figure 3-8). AEWs in other simulations (ExO and ExC) have similar patterns as the experiment ExDO (figures not shown).

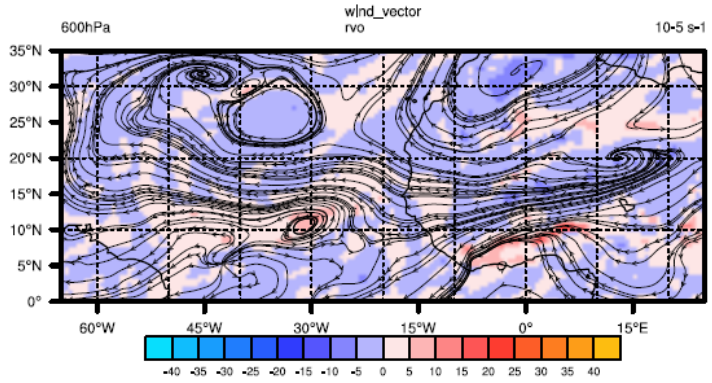

Figure 3-12. The 600 hPa streamline and the relative vorticity (shading) at the beginning of the simulation ExDO at 12UTC 21 August 2010.

(a) (b)

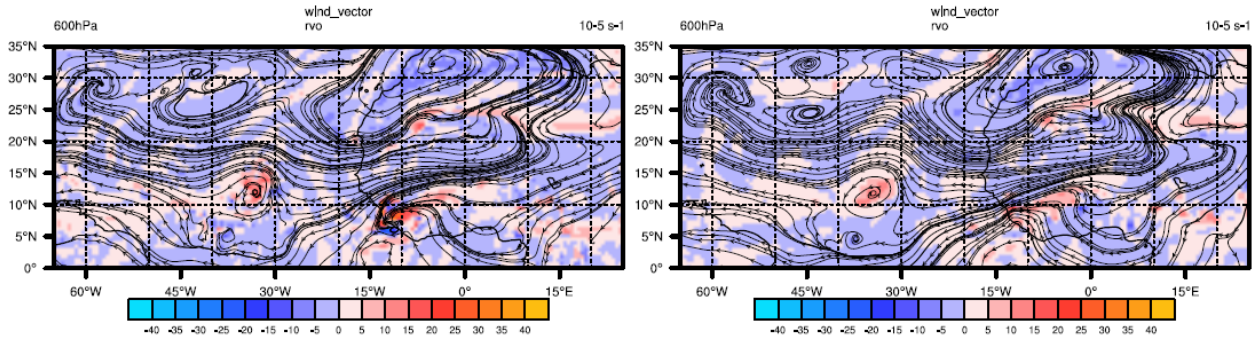

Figure 3-13. The 600 hPa streamline and the relative vorticity (shading) at 12UTC 22 August 2010 for (a) ExDO, (b) FNL.

(a) (b)

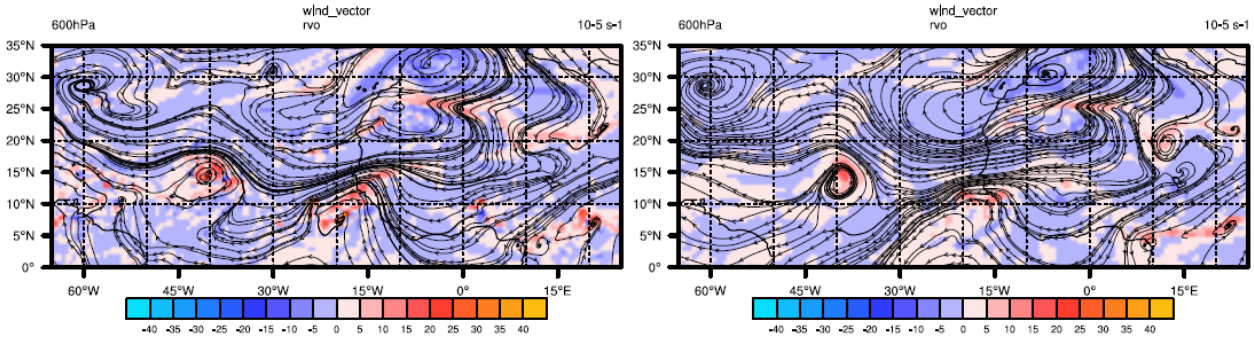

Figure 3-14. Same as Figure 3-13 but at 12UTC 23 August 2010.

(a) (b)

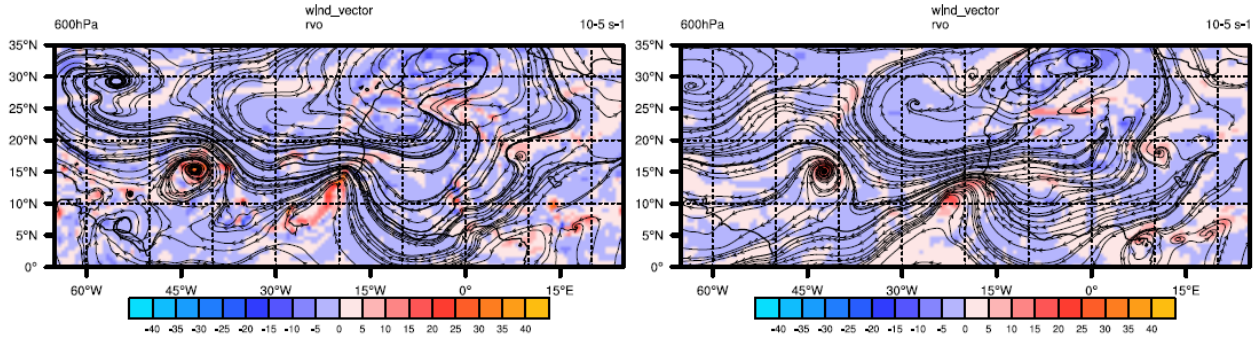

Figure 3-15. Same as Figure 3-13 but at 00UTC 24 August 2010.

AEJ is important to provide energy to the growth of AEW which can trigger convective systems over the ocean. We compare the time and zonal average of the zonal wind between our simulation ExDO and FNL (Figure 3-16). A maximum of easterly wind is located at around 600-700 hPa level indicates AEJ is present in the region. AEJ and associated low-pressure system at the surface are stronger in our simulation. The westerly wind under AEJ is a part of the monsoon flow that supplies air to the low-pressure system. It is stronger in our simulation as well. The meridional cross section of the averaged zonal wind shows that the position of AEJ in our simulation is comparable to FNL, the location of its trough related to the precursor of Earl generally is biased to the north against FNL as shown in Figure 3-12 to Figure 3-15. AEJ in other simulations (ExO and ExC) also have similar patterns to the experiment ExDO (figures are shown).

(a) (b) (c)

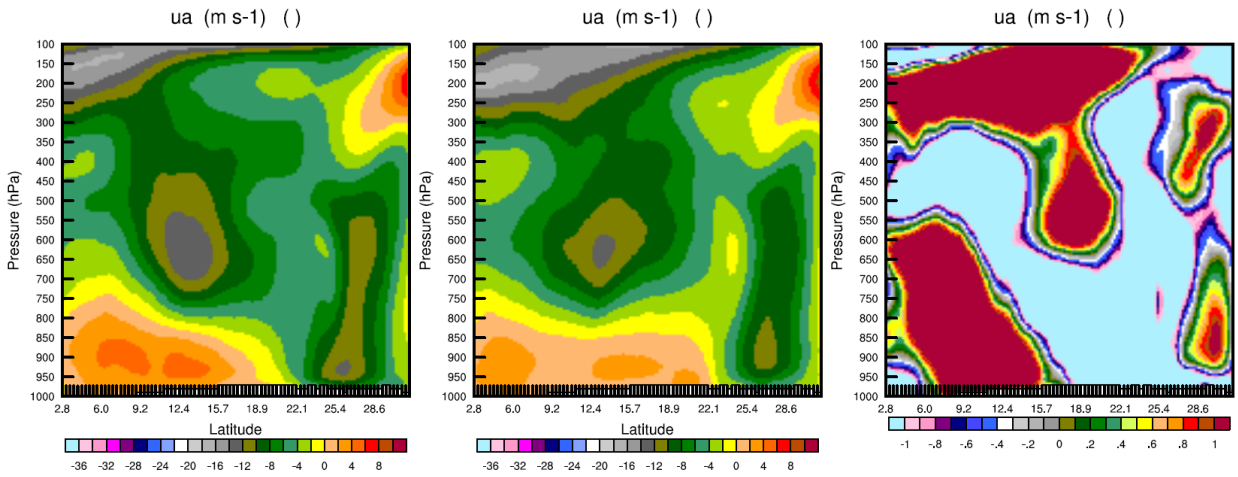

Figure 3-16. The vertical meridional cross sections of 5-day-averaged (from 12UTC 21 to 12UTC 26) zonal wind, averaged between 10W and 10E for (a) experiment ExDO, (b) FNL reanalysis, (c) and their difference (ExDO-FNL).

Radiosonde observations from three stations are selected to validate the simulation results (

Figure 3-17). In-Salah station is located in the Sahara region where the atmosphere is dry. Niamey-Aero station is located near Sahel region (around 15^{o}N) where it shares the boundary between dry and wet regions. Guimar-Tenerife station is located on the west coast of North Africa.

At In-Salah station, 24 hours after the model was initialized, at 12UTC 22, the Skew-T plot of the radiosonde data shows that the layer is very dry since the difference between the dewpoint and the temperature is large (Figure 3-18a). The environmental temperature has a dry adiabatic lapse rate up to 600 hPa, which indicates that the boundary layer is well mixed and thick. This is a result of strong heating over the desert region. Such sounding profile is typical in the Sahara region (e.g. Messager et al. 2010). The Skew-T plot from the simulation has the similar sounding profile (Figure 3-18b). 12 hours later at 12UTC 23, while the radiosonde observation changes little, the

profile from the simulation becomes wetter as indicated by smaller dewpoint depression (Figure 3-19).

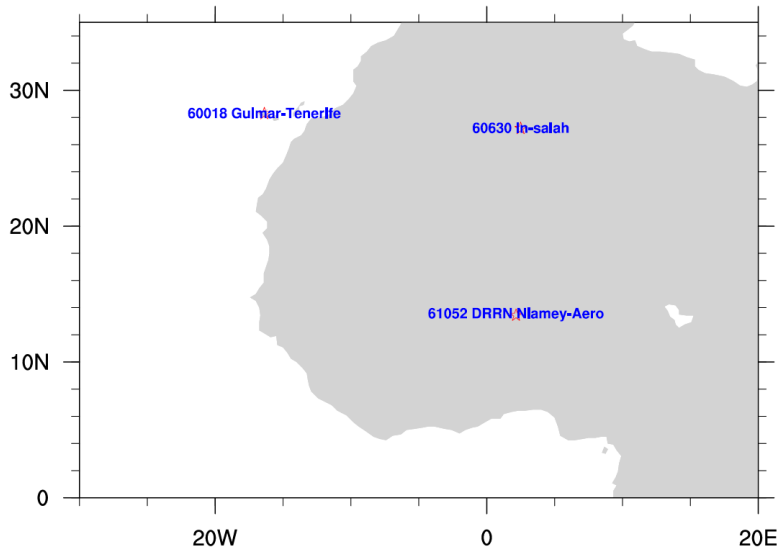

Figure 3-17. Locations of the radiosonde stations

(a) (b)

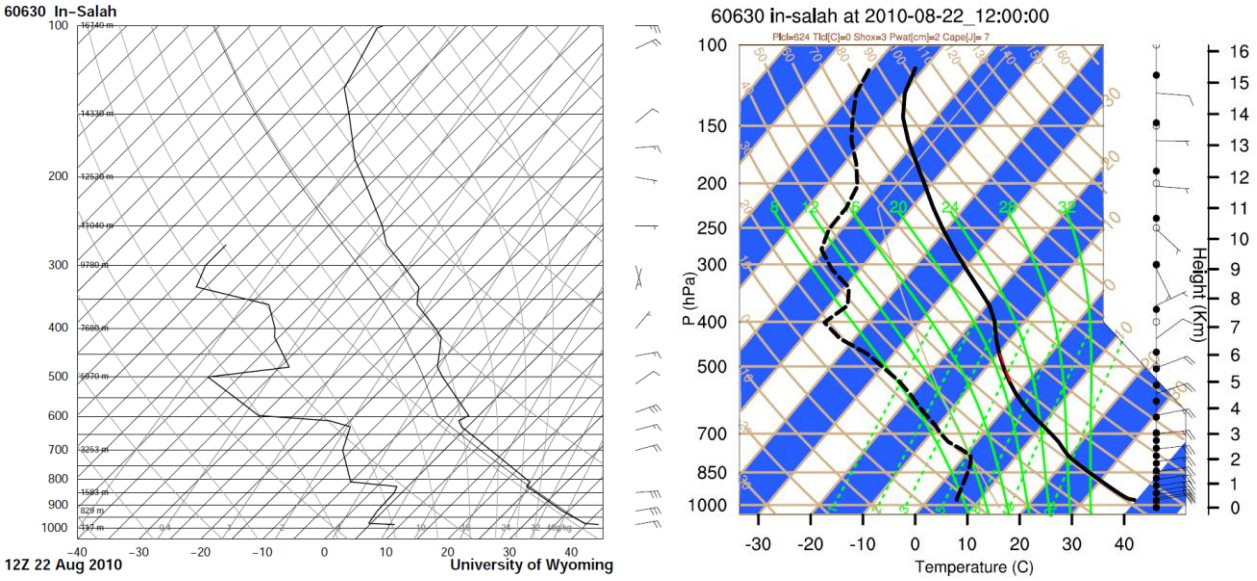

Figure 3-18. The Skew-T plot at In-Salah station at 12UTC 22 August 2010 for (a) radiosonde from the station, and (b) the simulated sounding profile in ExDO. The radiosonde observation is obtained from the University of Wyoming.

(a) (b)

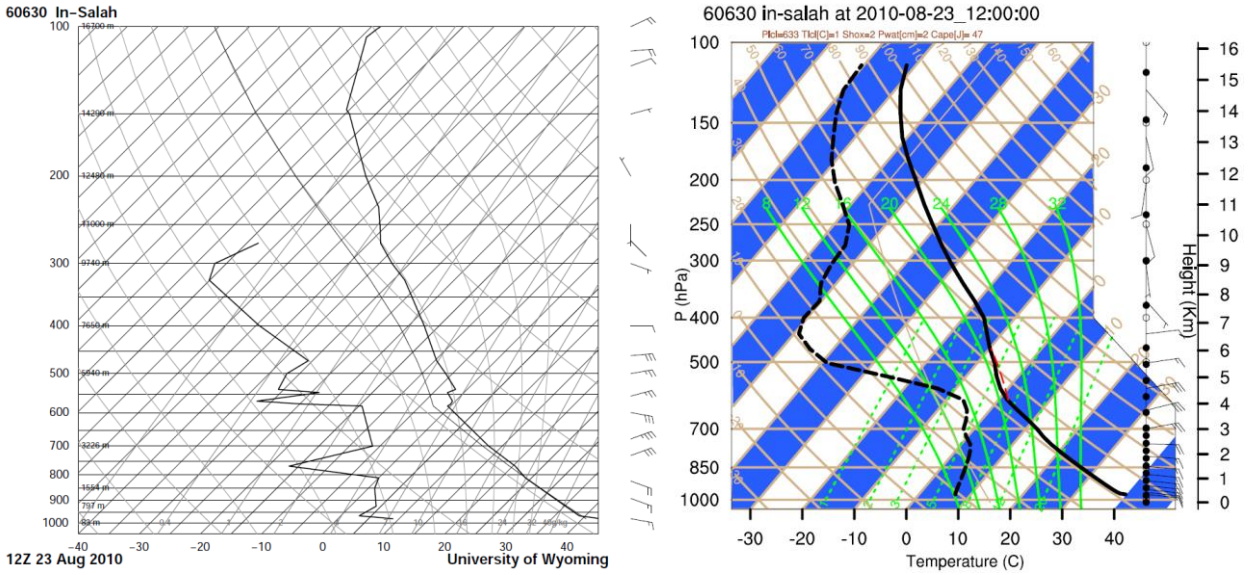

Figure 3-19. Same as Figure 3-18 but at 12UTC 23 August 2010.

At around 15^{o}N where Niamey-Aero station is located, the sounding profile is significantly different from the sounding profile in the dry region in the north (Figure 3-20). The dewpoint depression is much smaller, and the air is relatively wet. This is the boundary region between the dry air in the north and the tropical wet air in the south. Because the AEJ is located in this region, the AEW usually forms here and increases the moisture in this region by convection. The model simulations produce similar sounding profiles to the observations, although the simulation is wetter (Figure 3-20, Figure 3-21, Figure 3-22).

(a) (b)

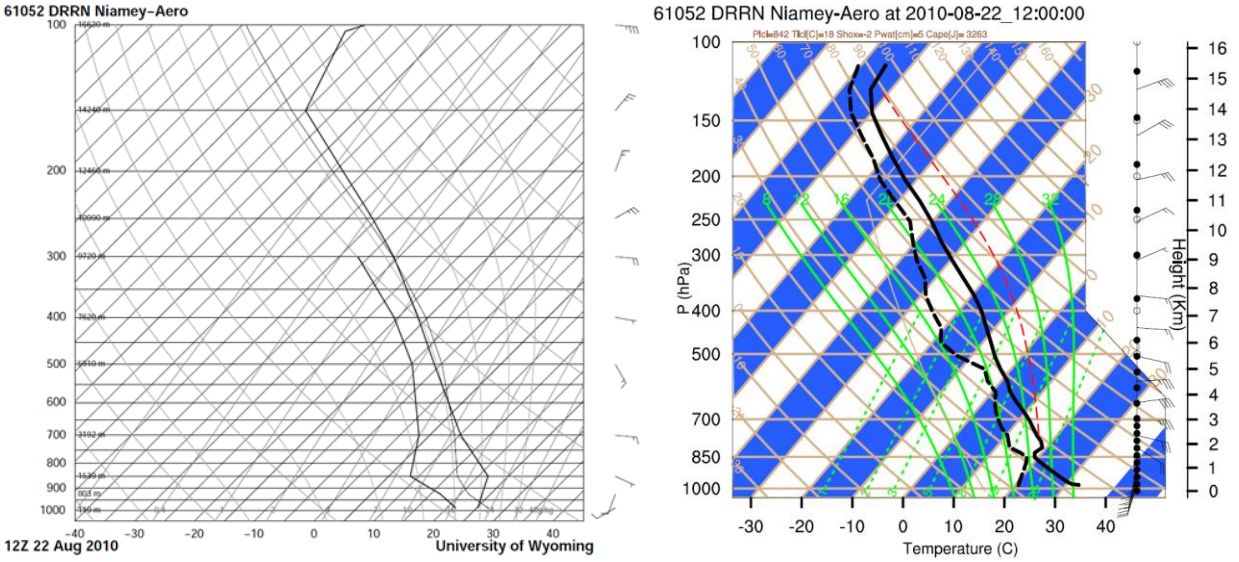

Figure 3-20. Same as Figure 3-18 but for Niamey-Aero station at 12UTC 22 August 2010.

(a) (b)

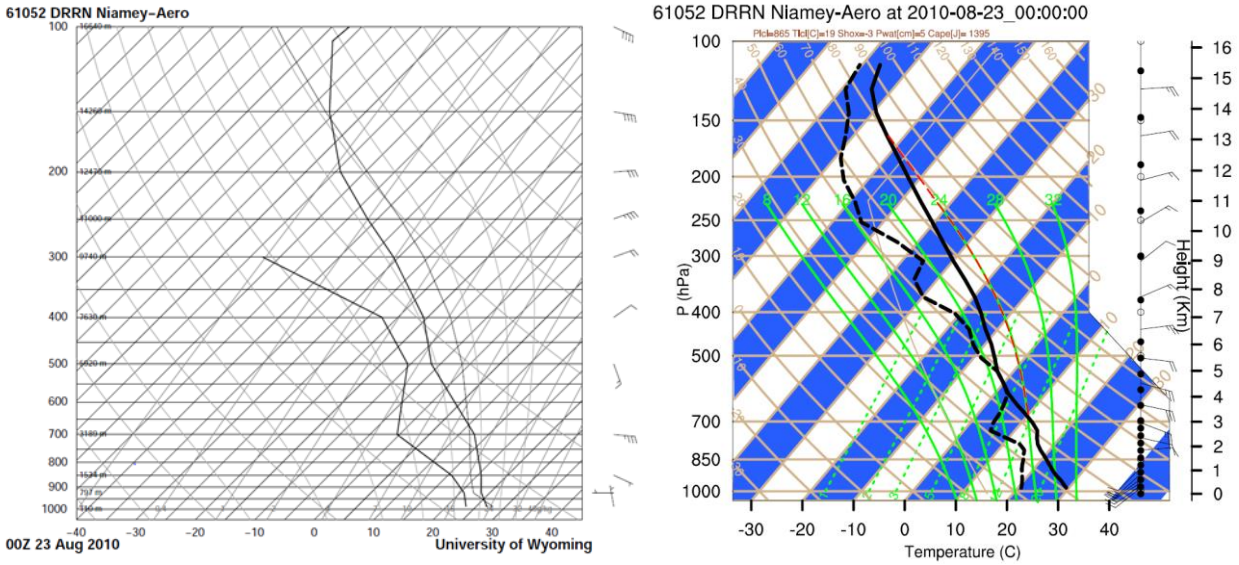

Figure 3-21. Same as Figure 3-18 but for Niamey-Aero station at 00UTC 23 August 2010.

(a) (b)

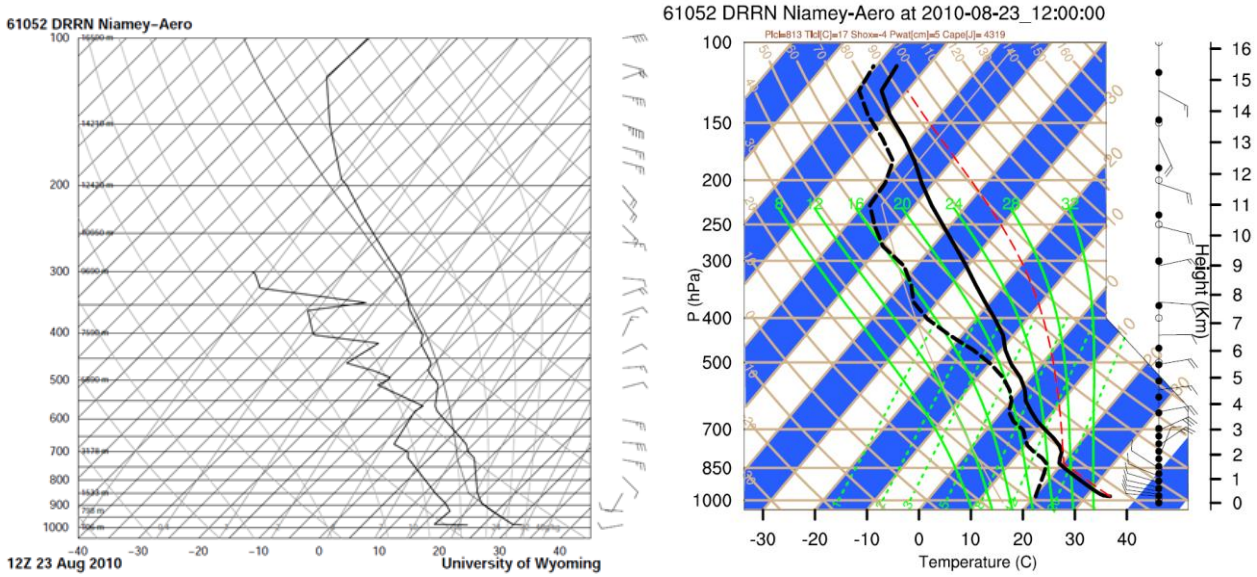

Figure 3-22. Same as Figure 3-18 but for Niamey-Aero station at 12UTC 23 August 2010.

The Guimar-Tenerife station located off the west coast of North Africa and over the Atlantic Ocean has a significantly different sounding profile compared to the stations on land (Figure 3-23, Figure 3-24, Figure 3-25). In both observations and the simulation, a clear temperature inversion layer can be seen between 850 hPa and 950 hPa levels. The dewpoint has its minimum in this layer. The warmness and dryness of this layer is a part of the Sahara Air Layer which dominates over North Africa in the summer and fall. The layer is undercut by the moist atmosphere near the ocean surface below 950 hPa. The sounding profiles from the simulation also show the dry inversion layer. It indicates that the model can represent the SAL features over the ocean.

Overall, the simulation produces similar sounding profiles as the radiosonde observations on dry land, wetland and over the ocean near the coast. Although we only show the sounding profiles

of the experiment ExDO, other experiments (ExO and ExC) have similar profiles (figures not shown). Thus, the model can represent the meteorological characteristics of the atmosphere in our simulated region.

(a) (b)

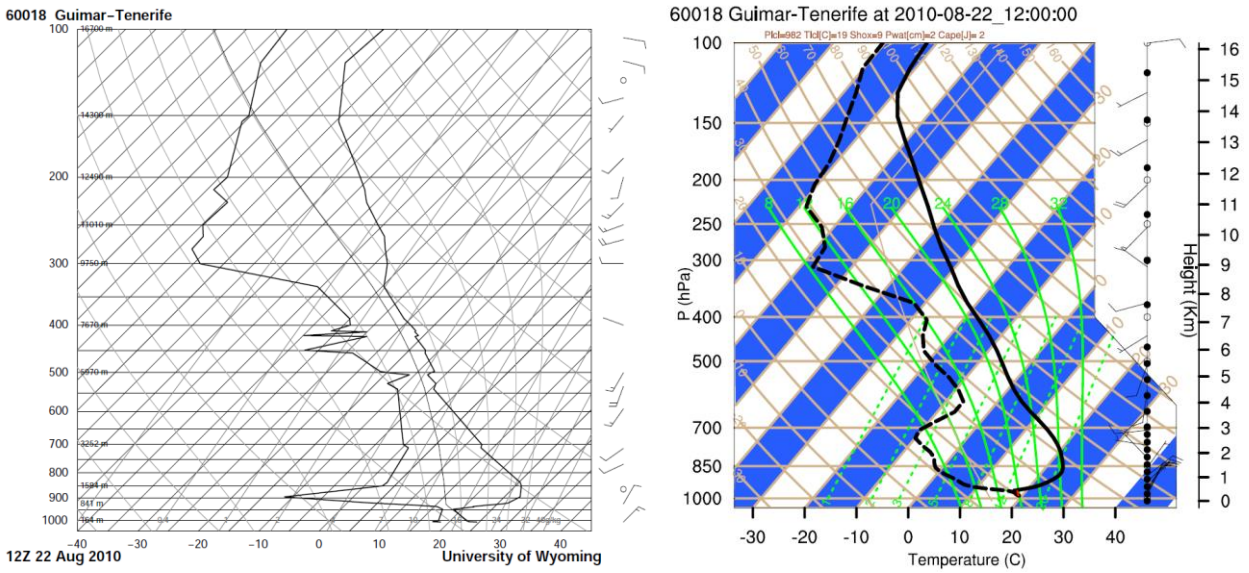

Figure 3-23. The Skew-T plot at Guimar-Tenerife station at 12UTC 22 August 2010 for (a) radiosonde from the station, and (b) the simulated sounding profile in ExDO.

(a) (b)

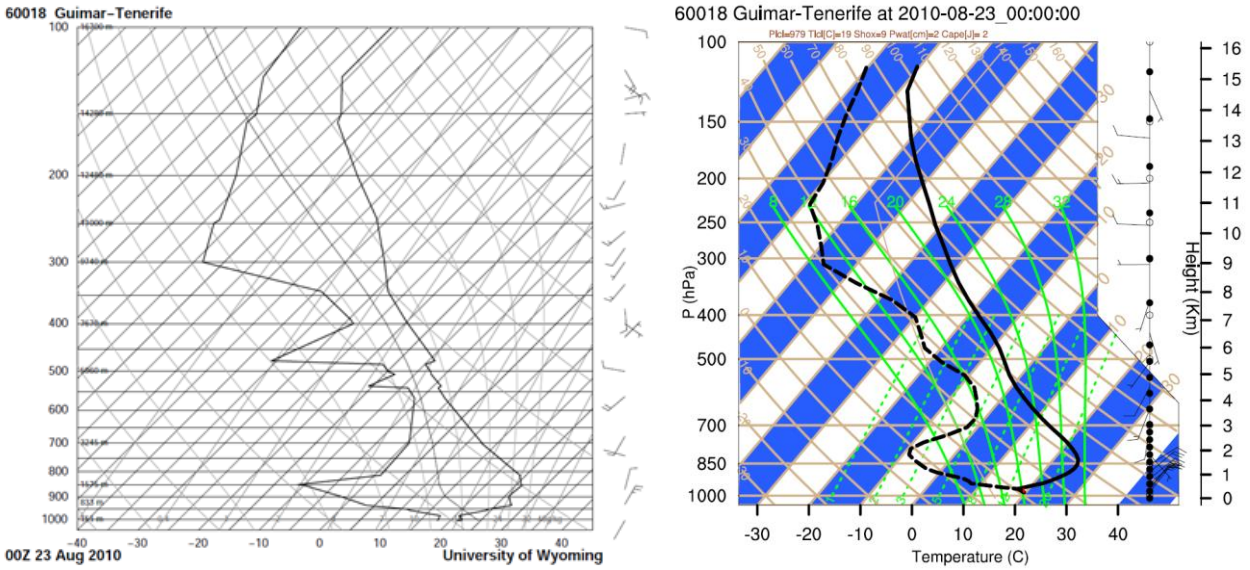

Figure 3-24. Same as Figure 3-23 but at 00UTC 23 August 2010.

(a) (b)

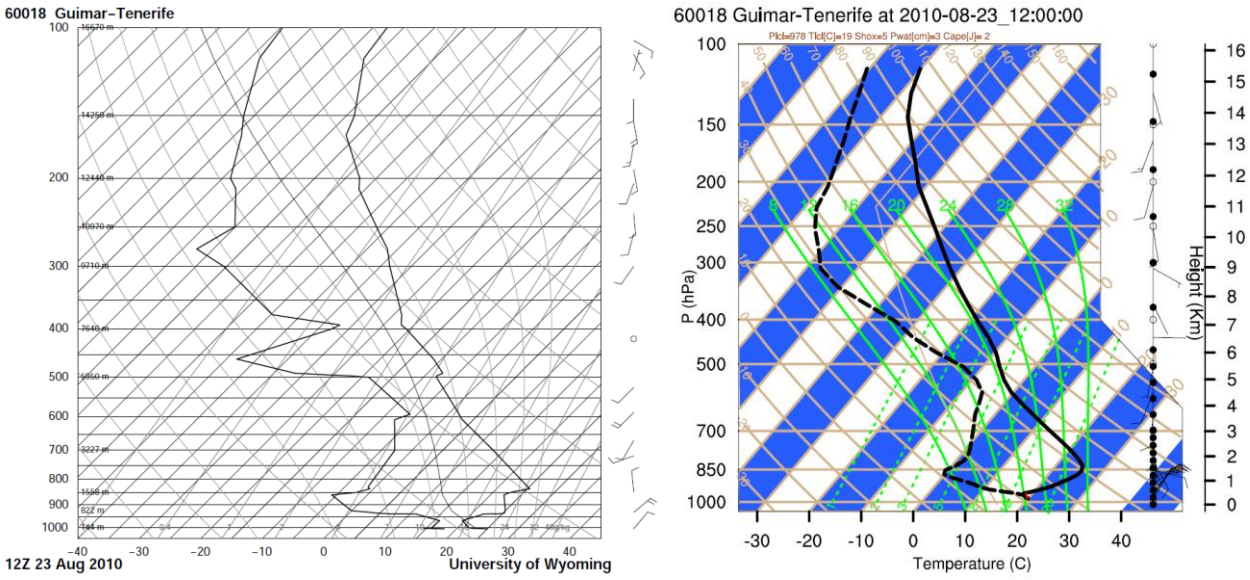

Figure 3-25. Same as Figure 3-23 but at 12UTC 23 August 2010.

3.3.2.2 Evaluation of Aerosols

Modeling the evolution of aerosols including dust is crucial for quantifying the dust effects reasonably. The AOD measurement from AERONET is a standard aerosol dataset for validation. Here AERONET level 2.0 data are used to validate the model performance because these data have been pre-field and post-field calibrated, cloud-screened, and quality-assured. AERONET provides AOD measurements at different wavelengths. As the model outputs simulated AOD at 550 nm, AERONET AODs at 440 nm and 675 nm are utilized to obtain the AERONET AOD at 550 nm using the following equation:

$$\frac{\tau_\lambda}{\tau_{\lambda_0}} = (\frac{\lambda}{\lambda_0})^{-\alpha} \quad (3.1)$$

where τ_λ is the AOD at wavelength λ, and τ_{λ_0} is the AOD at the reference wavelength λ_0 . α is Angstrom exponent which is calculated by

$$\alpha = -\frac{log\frac{\tau_{\lambda_1}}{\tau_{\lambda_2}}}{log\frac{\lambda_1}{\lambda_2}} \quad (3.2)$$

where τ_{λ_1} and τ_{λ_2} are measurements of AOD taken at two different wavelengths λ_1 and λ_2 respectively. (Tan et al. 2015)

Angstrom exponent α covering the wavelength range 440-675 nm is already provided by AERONET data. Thus, following the first formula above, AOD (at 550nm) =AOD (at 440nm) * $(550/440)^{-\alpha}$.

The AERONET AOD is the total AOD from all aerosols. Simulated AOD from ExDO, which also contains all aerosols, is compared with AERONET AOD in every three hours. Because the observation time of AERONET measurement is not exactly at the 3-hour time (00UTC, 03UTC, etc.), we define a time window (±1hour) every three hours. An observation within the time window and closest to the 3-hours time is treated as the observation at that 3-hour time.

Five AERONET sites are selected (Figure 3-26). The Capo Verde and Darkar stations are located in the western coastal region, while the other three stations are located around the Sahel region. The comparisons of these stations show that although model AOD is not exactly matching the AERONET AOD on some occasions, the model can predict the time evolution of AOD reasonably well. It can represent the general trend and the timing of the peak and the trough (Figure 3-27). For example, the model AOD at Zinder airport shows the upward trend from 06 UTC 22 to 06 UTC 25 similar to AERONET AOD observations. The AERONET AOD and model AOD both reach peak at 06 UTC 25 and valley at 15 UTC 22.

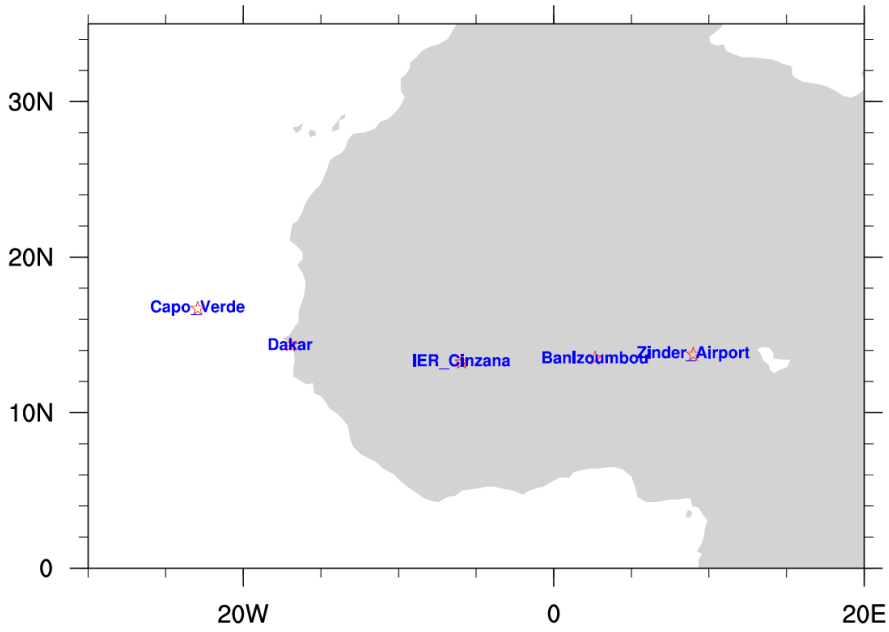

Figure 3-26. The locations of AERONET stations.

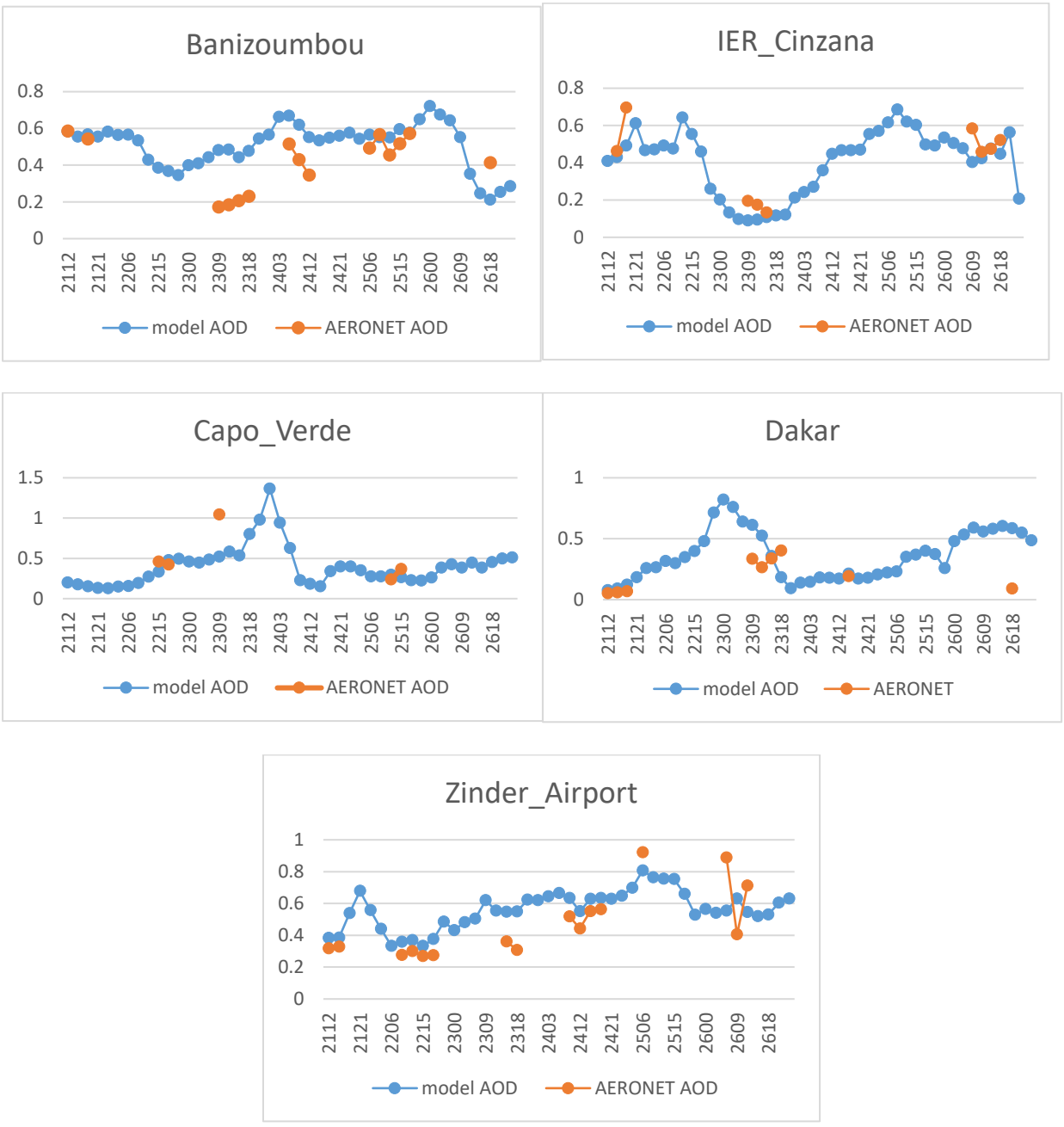

Figure 3-27. AOD at 550 nm from five AERONET sites and the corresponding simulated AOD from the experiment ExDO from 21UTC 21 to 00UTC 27 August 2010.

MODIS AOD Level 3 product provides daily horizontal distribution of aerosols. AOD from the experiment ExDO and MODIS AOD are compared to verify whether the model can represent the aerosol horizontal distribution and time evolution (Figure 3-28). Both model and observational AOD include contributions from all aerosol species. The left column shows the result from the simulation ExDO at 12UTC from day 21 to day 26. The right column shows MODIS AOD from day 21 to 26. There is no hour information in MODIS Level 3 product, only one figure each day. We use AOD from the model at 12UTC each day to compare with the MODIS AOD daily product. This comparison is not ideal since MODIS level 3 product is a daily product containing many granules throughout the whole day. However, since only Level 3 product provides a whole picture of AOD, and the model AOD does not very quickly within a day, this comparison is reasonable.

Figure 3-28 shows that high AODs are mainly located over the Sahara Desert and its downstream region in both simulation and MODIS observations. Dust contributes to the most part of AOD, verified by MACC-II model AOD (figures not shown).

At the beginning of the simulation, the AOD value in the model is lower than the observation (Figure 3-28a, b). On 22 August, AOD from the model is under 0.7 while AOD can reach 1.3 in MODIS. The distribution is similar in the north and west coast of Africa between the model and the observation. The low bias in the modeled AOD is improved as more dust being emitted into the atmosphere in the simulation. Overall, AOD on the west coast of Africa is underestimated in the simulation while AOD in north Africa gradually matches with the AOD from the observation.

(a)

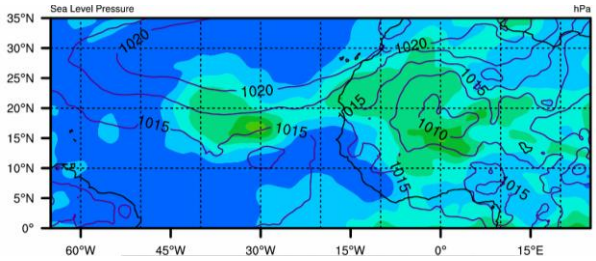
Sea Level Pressure
hPa
35°N
30°N
25°N
20°N
15°N
10°N
5°N
0°
60°W
45°W
30°W
15°W
0°
15°E
1020
1015
1010

(b)

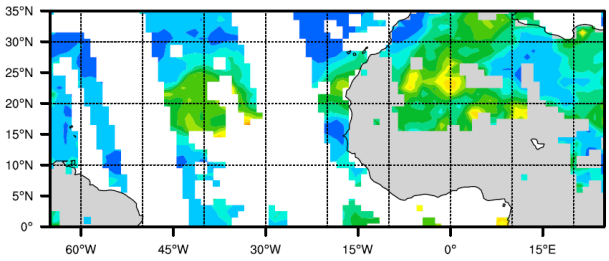
35°N
30°N
25°N
20°N
15°N
10°N
5°N
0°
60°W
45°W
30°W
15°W
0°
15°E

(c)

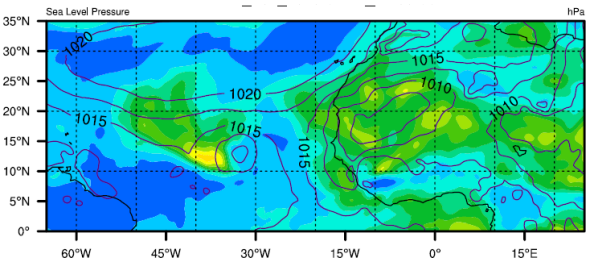
Sea Level Pressure
hPa
35°N
30°N
25°N
20°N
15°N
10°N
5°N
0°
60°W
45°W
30°W
15°W
0°
15°E
1020
1015
1010

(d)

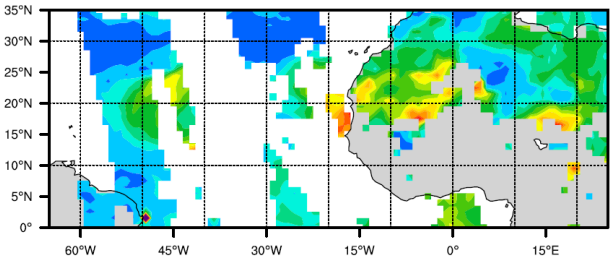
35°N
30°N
25°N
20°N
15°N
10°N
5°N
0°
60°W
45°W
30°W
15°W
0°
15°E

(e)

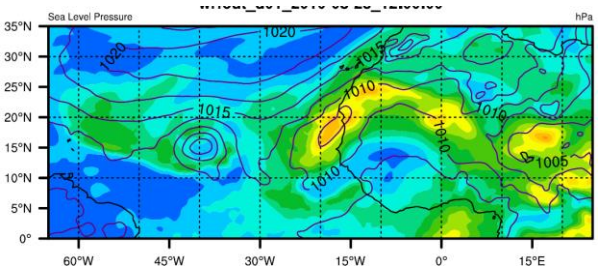
Sea Level Pressure
hPa
35°N
30°N
25°N
20°N
15°N
10°N
5°N
0°
60°W
45°W
30°W
15°W
0°
15°E
1020
1015
1010
1005

(f)

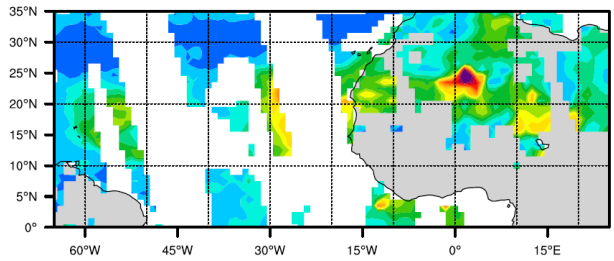
35°N
30°N
25°N
20°N
15°N
10°N
5°N
0°
60°W
45°W
30°W
15°W
0°
15°E

(g)

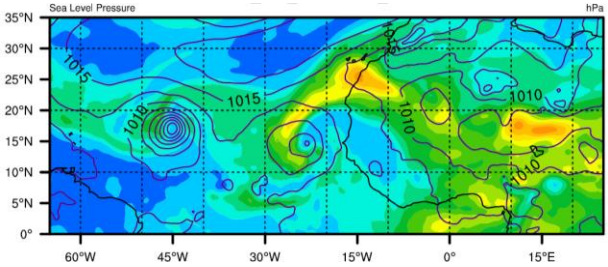
Sea Level Pressure
hPa
35°N
30°N
25°N
20°N
15°N
10°N
5°N
0°
60°W
45°W
30°W
15°W
0°
15°E
1015
1010

(h)

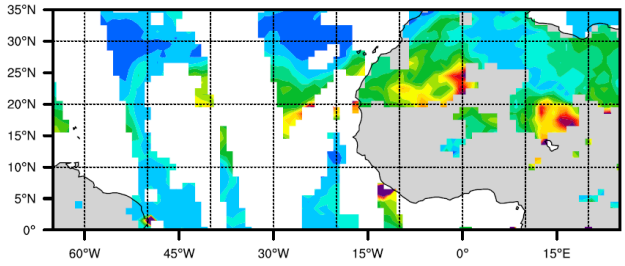
35°N
30°N
25°N
20°N
15°N
10°N
5°N
0°
60°W
45°W
30°W
15°W
0°
15°E

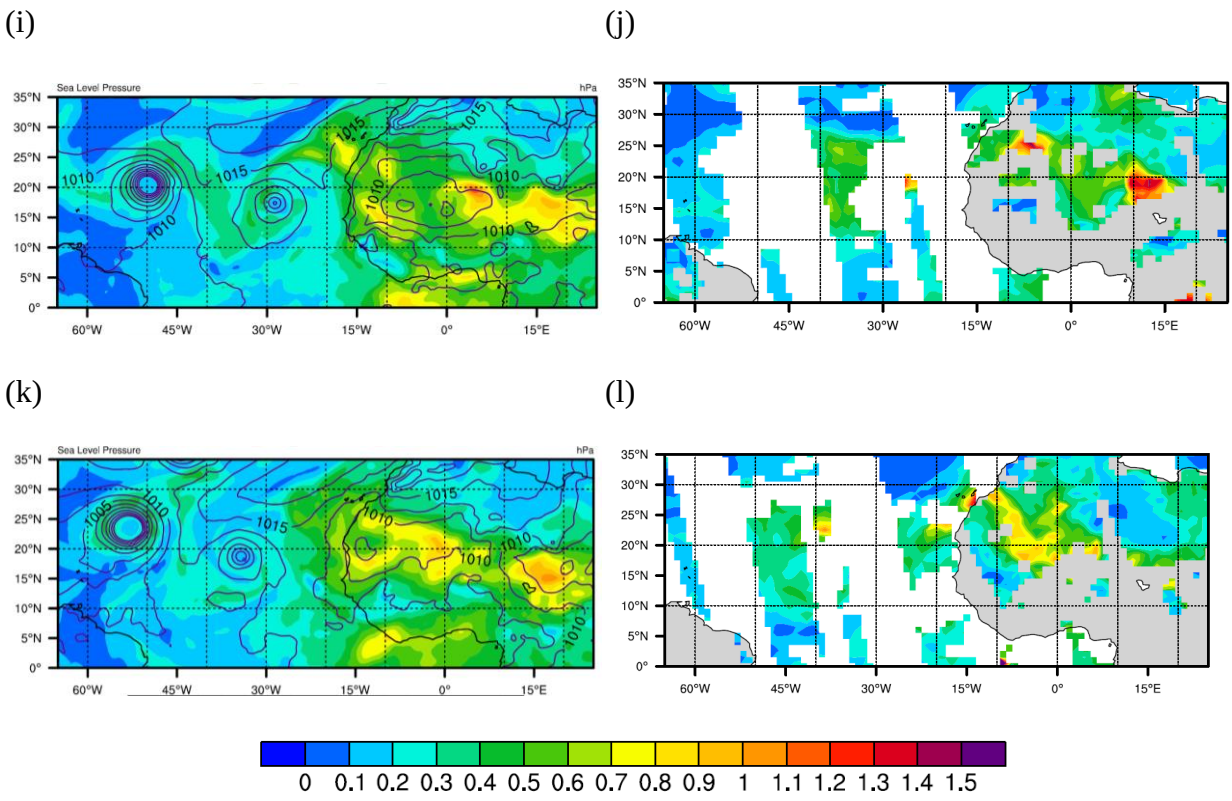

Figure 3-28. Aerosol optical depth from the simulation ExDO (left column) and MODIS L3 product (right column). In August 2010 at (a)12UTC 21th, (b) 21th, (c)12UTC 22th, (d)22th, (e)12UTC, 23th, (f) 23th, (g)12UTC, 24th, (h) 24th, (i) 12UTC, 25th, (j) 25th, (k)12UTC, 26th, (l) 26th.

The vertical distribution of dust and other aerosols from the model can be verified by the CALIPSO aerosol subtypes data. The dust aerosols extinction coefficient in the model is approximated by the difference between the total extinction coefficient in ExDO and ExO (Figure 3-29 to Figure 3-32). At 14UTC 22, dust aerosol extinction coefficient from the simulation reaches 4 km (Figure 3-29d) while the CALIPSO data shows the dust aerosols can reach 5 km height (Figure 3-29c). At 14UTC 23, CALIPSO data shows the dust lays above the other aerosols (Figure 3-30c). The simulated extinction coefficient also indicates dust is the main aerosol type reach upper atmosphere above 1 km (Figure 3-30d), and other aerosols are concentrated in the lowest 1 km

beneath the dust(Figure 3-30e). At 14 UTC 25 (Figure 3-31), dust extinction coefficient region coincides with CALIPSO data. At 15 UTC 26 (Figure 3-32), although the modeled dust extinction coefficient only appears in a layer between 3 km and 4 km, the simulation picked up a contribution from other aerosols observed by CLLIPSO. Overall, the horizontal and vertical distribution of dust and other aerosols match the CALIPSO observation.

(a) (b)

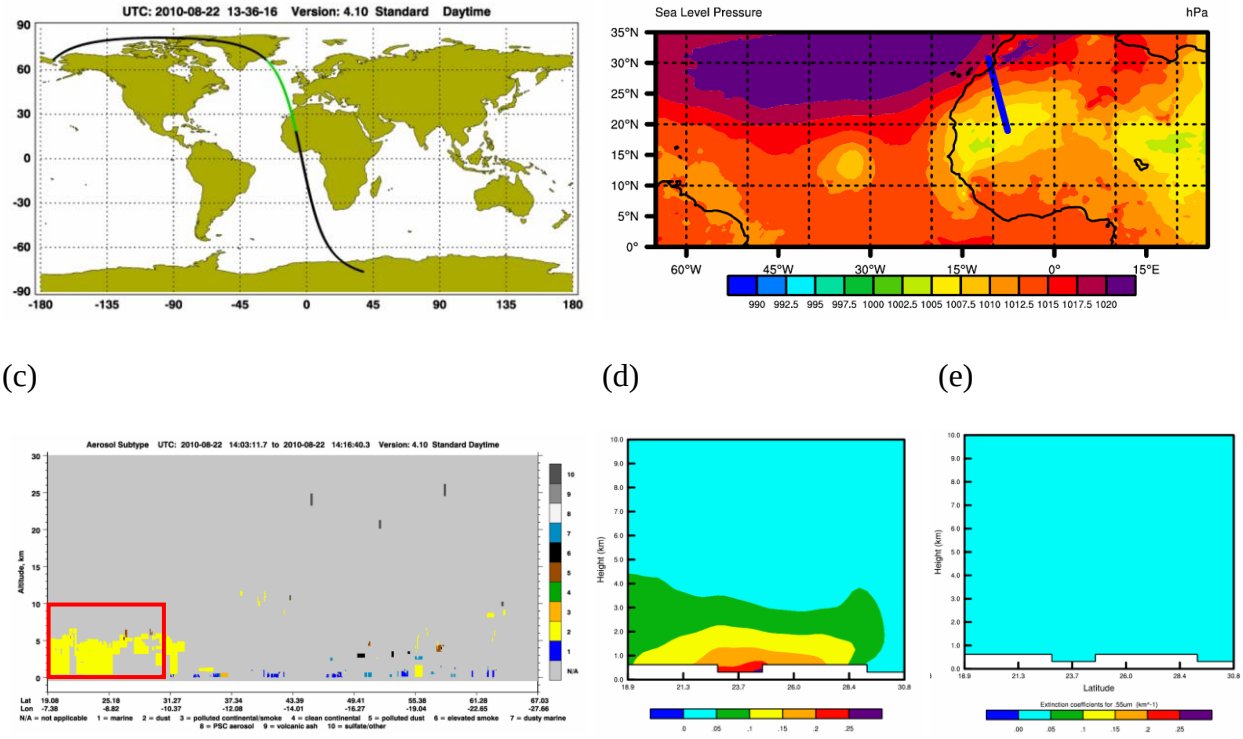

(c) (d) (e)

Figure 3-29. Comparison of the aerosol subtypes in CALIPSO and the aerosol extinction coefficient in the model at 14 UTC 22 August 2010. (a) CALIPSO track. (b) Position of the cross section in the model (blue line). (c) CALIPSO aerosol subtype. Yellow color indicates dust; deep blue indicates dusty marine aerosol; light blue indicates marine aerosol. (d) The difference (ExDO-ExO) of aerosols extinction coefficient at 550 nm represents dust contribution. (e) extinction coefficient at 550 nm due to other aerosols (without dust) in ExO. Red frame in (c) is the area that compare to (d) and (e).

(a) (b)

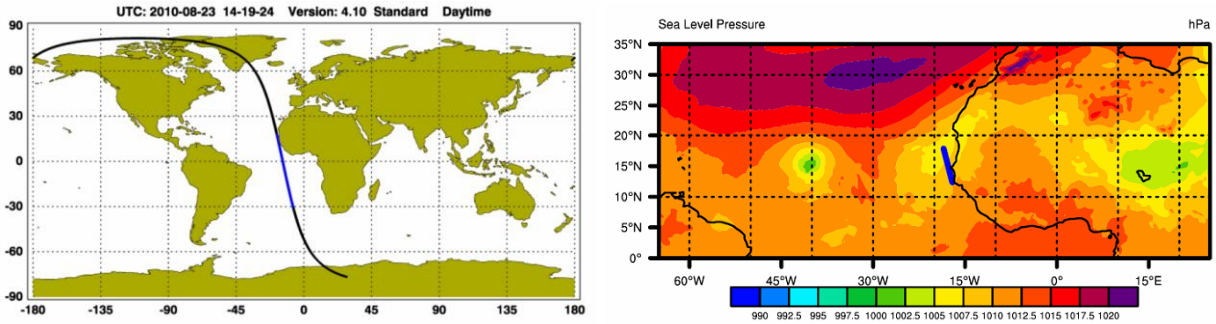

(c) (d) (e)

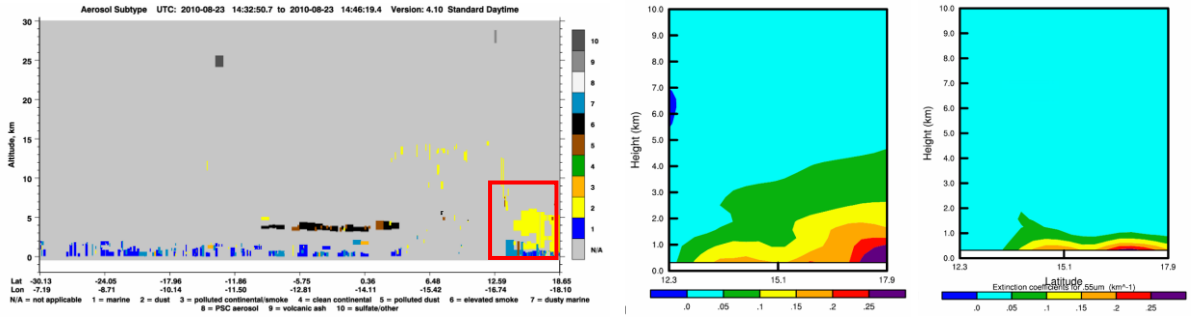

Figure 3-30. Same as Figure 3-29 but at 14UTC 23 August 2010.

(a) (b)

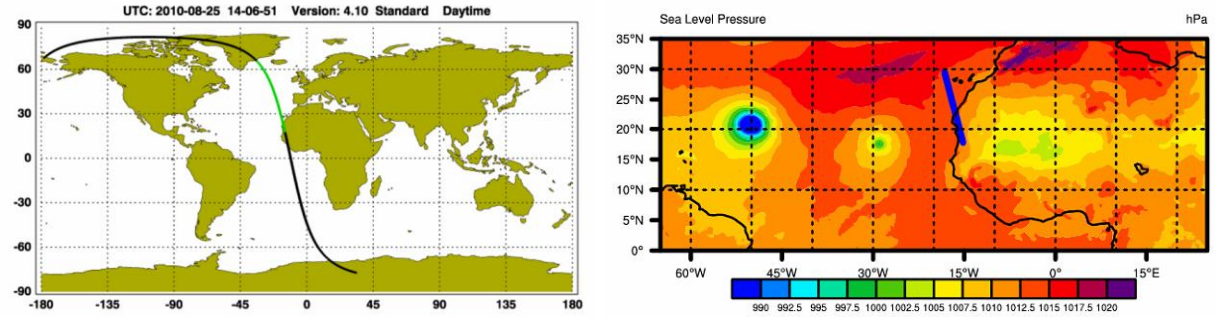

(c) (d) (e)

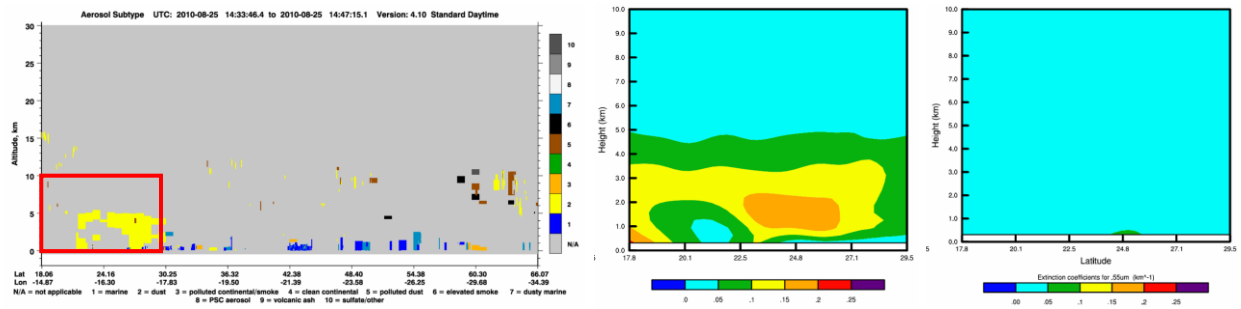

Figure 3-31. Same as Figure 3-29 but at 14UTC 25 August 2010.

(a) (b)

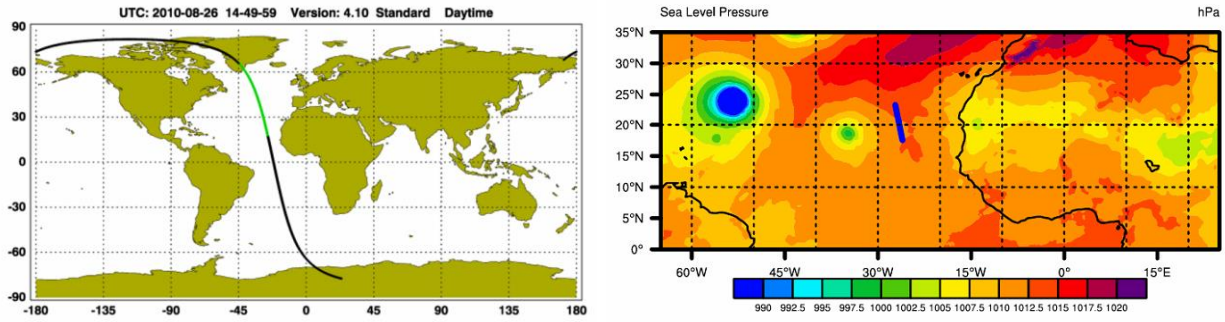

(c) (d) (e)

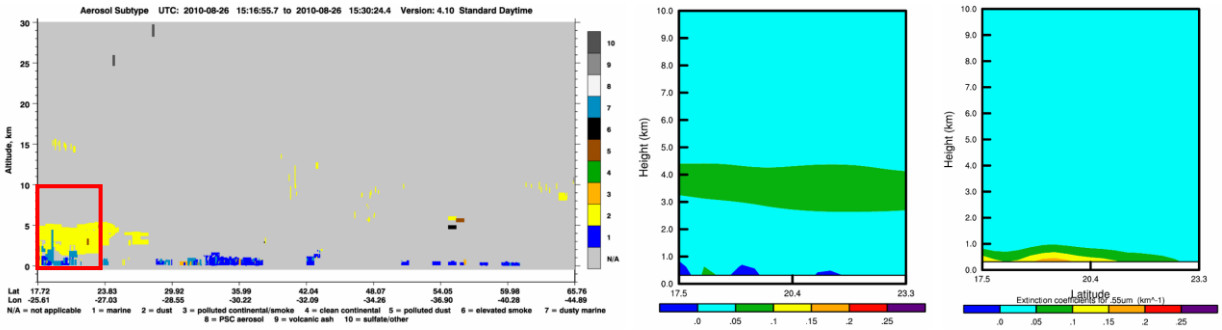

Figure 3-32. Same as Figure 3-29 but at 15UTC 26 August 2010.

In summary, compared to best track and reanalysis data, the simulations produce stronger AEW, AEJ, and surface low-pressure system. Their tracks are biased to the north-east but similar

to all other operational forecasts. The evolution of the low-pressure system generally agrees with the reanalysis data. The model depicts SAL vertical structure over land and ocean reasonably well when we compare the model sounding profiles to the radiosonde data. The model also predicts reasonable horizontal and vertical distributions of the aerosols, and it can forecast their evolution.

The model verification gives us confidence that the simulation results can be used to study the impact of dust aerosols on Earl.

3.3.3 Model result analysis

3.3.3.1 Dust direct effect

To understand how the dust affects the convective system, we begin to analyze the system when it is located in North Africa. Prior to its westward movement towards the Atlantic Ocean, the low-pressure system is free of clouds due to the absence of abundant moisture. Thus, dust directly affects the radiation budget of the earth-atmosphere system.

Dust begins to influence the atmosphere when the model is initialized at 12UTC 21 August 2010. One hour after the simulation starts, at 13UTC, we take a horizontal area average (indicated by the red box in Figure 3-33) to obtain the vertical heating profiles for both ExDO and ExO. Their differences show the dust effect.

Shortwave radiation warms up the atmosphere in both experiments (Figure 3-34a). This is a result of the absorption of the solar shortwave radiation by the atmosphere. However, when dust is considered in the model (experiment ExDO), the heating rate is larger than that in the experiment excluding dust effect (experiment ExO) (Figure 3-34b). Dust aerosols absorb extra shortwave

radiation from the sun. Because the dust aerosol concentration decreases with height, dust-induced heating also decreases with height. The maximum dust heating rate, which is around 0.01K/hour, is located at the lowest level, and it drops to close to zero above 10 km (Figure 3-34b).

We further conduct the cross-section analysis of the heating rate. The cross-section is obtained by zonally averaging between 10^{o}E and 10^{o}W. The shortwave radiative heating rate is positive in the cross-section in the experiment ExO (without dust) (Figure 3-35a). If the model includes dust, the heating rate is increased in the dusty region, with maximum heating rate located below 3 km to the north of 17.2 ^{o}N (Figure 3-35b). The magnitude of the maximum heating can be around 0.03 K/hour, larger than the maximum area-averaged heating rate (0.01 K/hour).

While the atmosphere absorbs shortwave radiation, it also emits longwave radiation upward and downward at the same time. The outgoing longwave radiation decreases the temperature of the atmosphere above 800 meters (Figure 3-36a and Figure 3-37a). At this layer, although the atmosphere is also absorbing longwave radiation from the surface, the warming effect is smaller than the cooling effect from the outgoing longwave radiation in the atmosphere. However, in a thin layer near the surface (below 800 meters), the absorption of longwave radiation from the surface need to be considered, which is larger than the outgoing longwave radiation in this layer. Thus, the heating rate is positive in this thin layer (below 800 meters) (Figure 3-36a and Figure 3-37a).

When dust is added to the model, the following changes are noticed: above 800 meters, the cooling effect due to longwave radiation becomes stronger while below 800 meters, the positive heating effect becomes weaker (Figure 3-36b and Figure 3-37b). We discuss these changes separately. **(1)** Above 800 meters, dust enhances the longwave cooling (Figure 3-36b and Figure 3-37b). Dust absorbs shortwave radiation from the sun and heats up the atmosphere, and higher temperature emits more longwave radiation at the same time. **(2)** Below 800 meter, although the

longwave radiative heating rate is still positive even when the dust is present, the addition of dust reduces the positive heating rate (Figure 3-36b and Figure 3-37b). The heating rate considered here is a combination of upward and downward longwave radiation in the atmosphere and the absorption of longwave radiation from the surface. Two reasons can explain this dust effect: firstly, upward and downward longwave radiation becomes stronger, which is a result of enhancing radiation cooling in the dust layer as we mentioned earlier; secondly, the presence of dust reduces the longwave radiation from the ground (Figure 3-45b) because the temperature is reduced at the surface (Figure 3-44b) due to absorption of shortwave radiation by dust (Figure 3-34b). As the longwave radiation from the ground is reduced, the warming below 800 meters is reduced as well. Because of these two reasons, the total effect near the surface layers is negative after dust is considered in the model (Figure 3-36b). The negative effect due to dust in the whole column is greatest at the lowest level, around -0.02 K/hour on the domain average.

Considering both shortwave and longwave radiations of the atmosphere, the heating rate is positive because the shortwave radiation dominates over the longwave radiation except at the near surface levels (Figure 3-38a and Figure 3-39a). At the near surface levels (below 800 meters), the longwave radiative heating is larger than the shortwave radiative heating, and the total effect is still warming. The maximum heating rate is around 0.6K/hour in the domain average, and it exceeds 1 K/hour in the zonal averaged vertical cross-section (Figure 3-38a and Figure 3-39a).

When dust effect is considered in the model, the combined shortwave and longwave radiative heating rate is stronger above 800 meters because dust shortwave radiation warming effect is stronger than dust longwave radiation cooling effect (Figure 3-38b and Figure 3-39b). At the near surface level in some areas, however, the reduction of the longwave radiative heating from the

surface is stronger than the enhancement of the shortwave radiative heating. Therefore, the total heating rate becomes smaller.

We compare our findings to a typical observational study by Huang et al. (2009) who investigated dust effect using satellite observations in Taklimakan Desert (Figure 3-40). There are several differences between our results and theirs:

(1) Dust vertical distribution in their case is different from ours. Since there is a single elevated dust layer at about 5 km above the ground in their case, the maximum shortwave radiative heating and longwave radiation cooling are concentrated at around 5 km height. In our experiment, however, the maximum warming rate and cooling rate are near the surface where the most dust aerosols are located.

(2) In their case, dust longwave radiation heats up the atmosphere below the dust layer because of the enhancement of downward longwave radiation from the dust layer, which acts like "greenhouse effect". While in our case, dust longwave radiation effect is negative above 800 meters because the emission of longwave radiation is enhanced due to dust. While below 800 meters, the effect is still negative in our case as discussed earlier.

(3) In their case, the net radiative heating is positive within and below the dust layer. On the other hand, our experiment shows the net heating effect is positive within the dust layer except at the surface. The averaged net heating rate by dust in our case is around 0.12 K/day (0.01K/hour * 12 hours), which is much less than 6 K/day in their case. This could be because the dust concentration in our case is less than theirs, and the dust single-scattering albedo over Sahara in our case is higher than that over Taklimakan desert in their case. Thus, dust aerosols over Sahara absorb less shortwave radiation, and dust heating rate in our case is smaller.

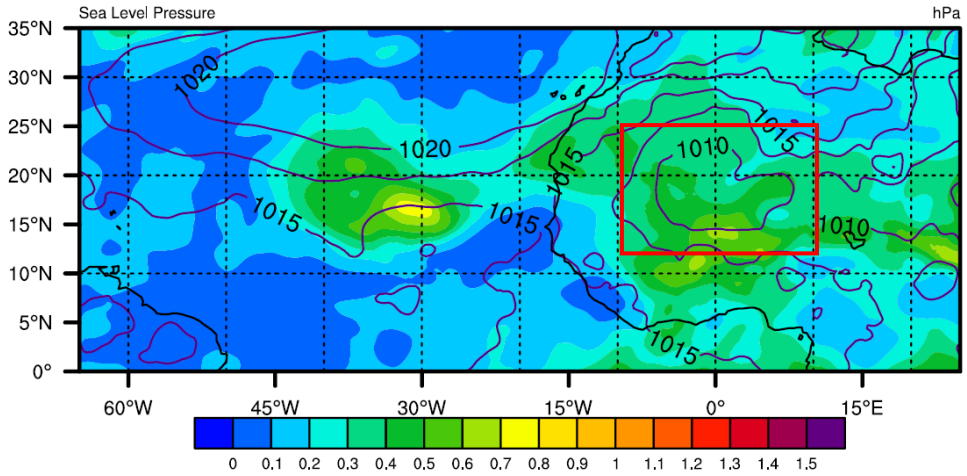

Figure 3-33. The aerosol optical depth(shading) and the sea level pressure (contour, units: hPa) in ExDO at 13UTC 21 August 2010. Red rectangular frame indicates the area where the horizontal averages are taken.

(a) (b)

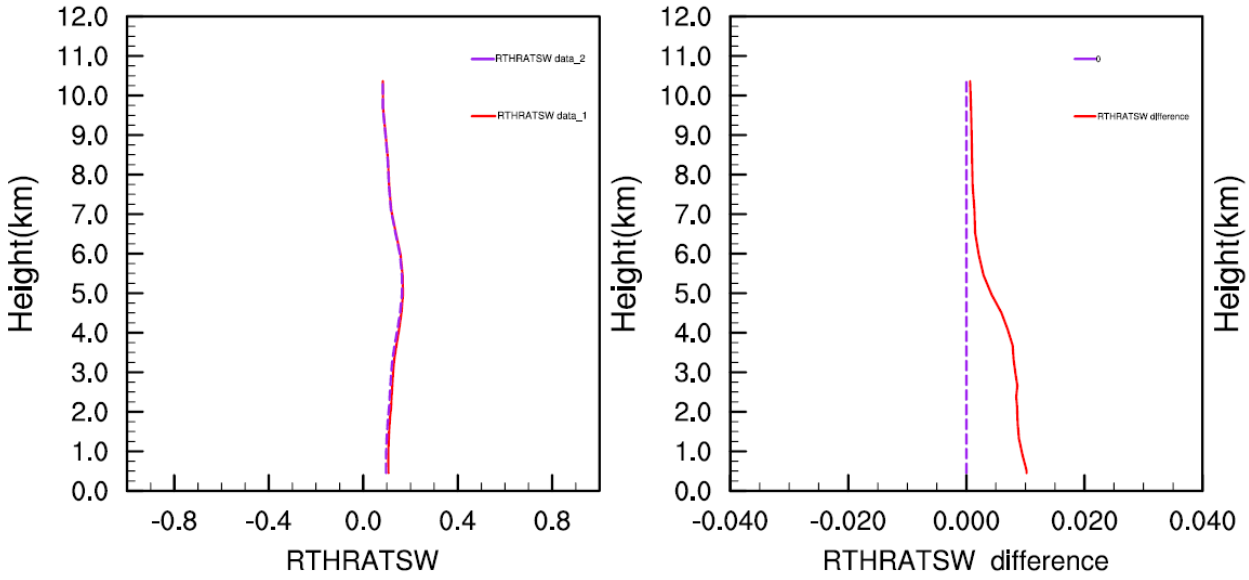

Figure 3-34. The averaged potential temperature tendency (K/hour) due to the shortwave radiation at 13UTC 21 August 2010 in (a) the experiment ExDO (with dust) (Red line) and the experiment ExO (only other aerosols, no dust) (purple line); (b) their difference (ExDO-ExO) (red line), zero value line (purple line).

(a) (b)

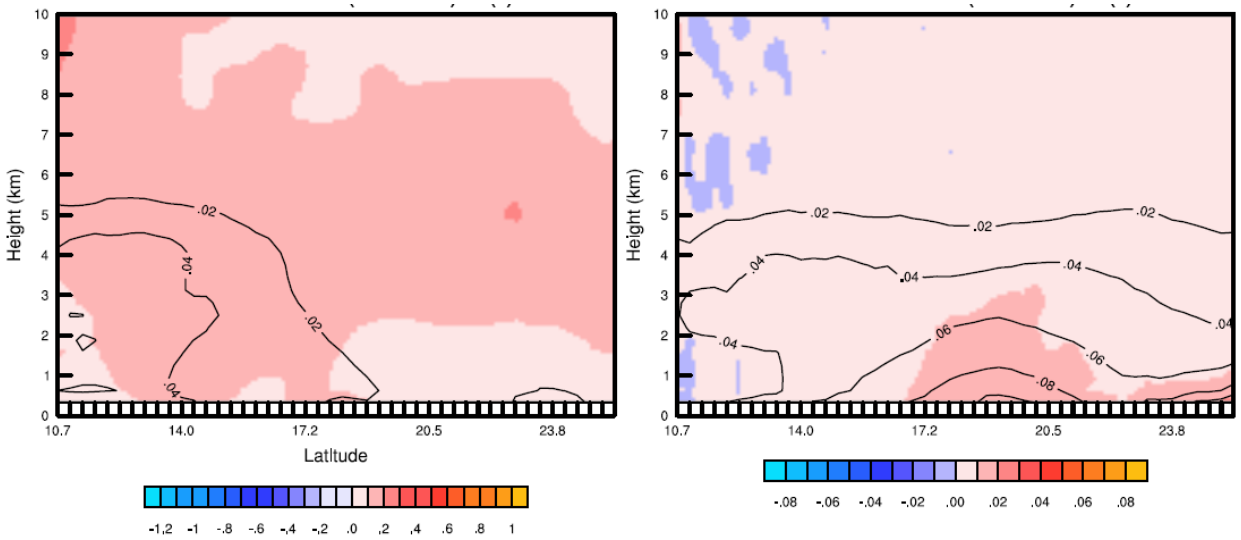

Figure 3-35. Vertical cross sections (height vs latitude) of zonal mean (10°W to 10°E) of potential temperature tendency due to shortwave radiation (shading, K/hour), and extinction coefficient at 550nm (contour) at 13UTC 21 August 2010 for (a) the experiment ExO, and (b) the difference due to dust (ExDO-ExO).

(a) (b)

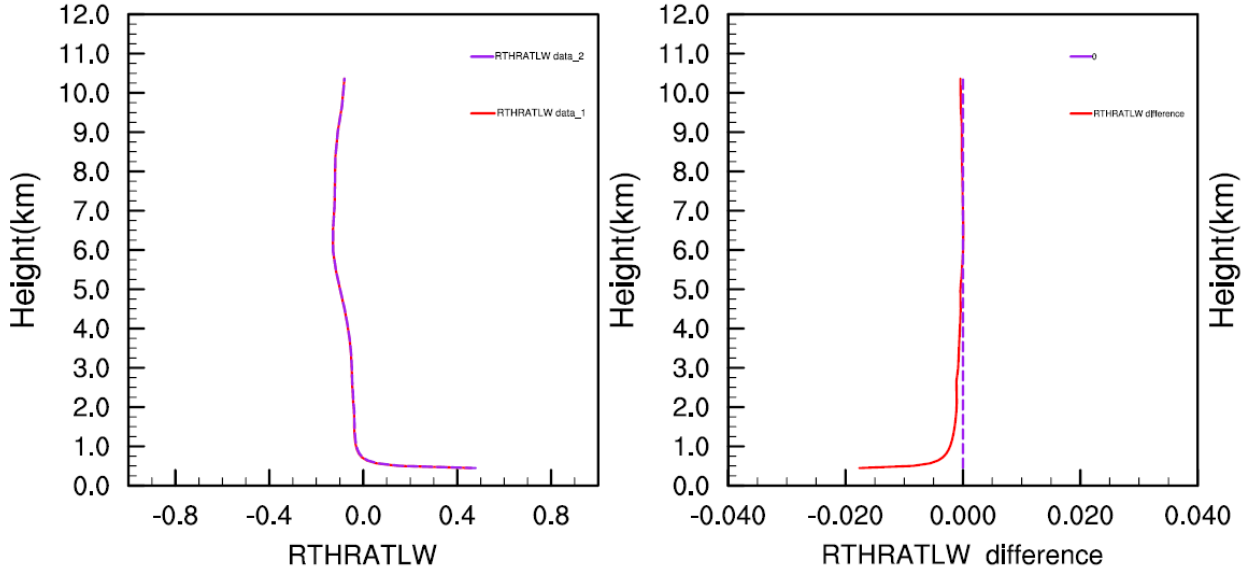

Figure 3-36. Same as Figure 3-34 but for longwave radiation.

(a) (b)

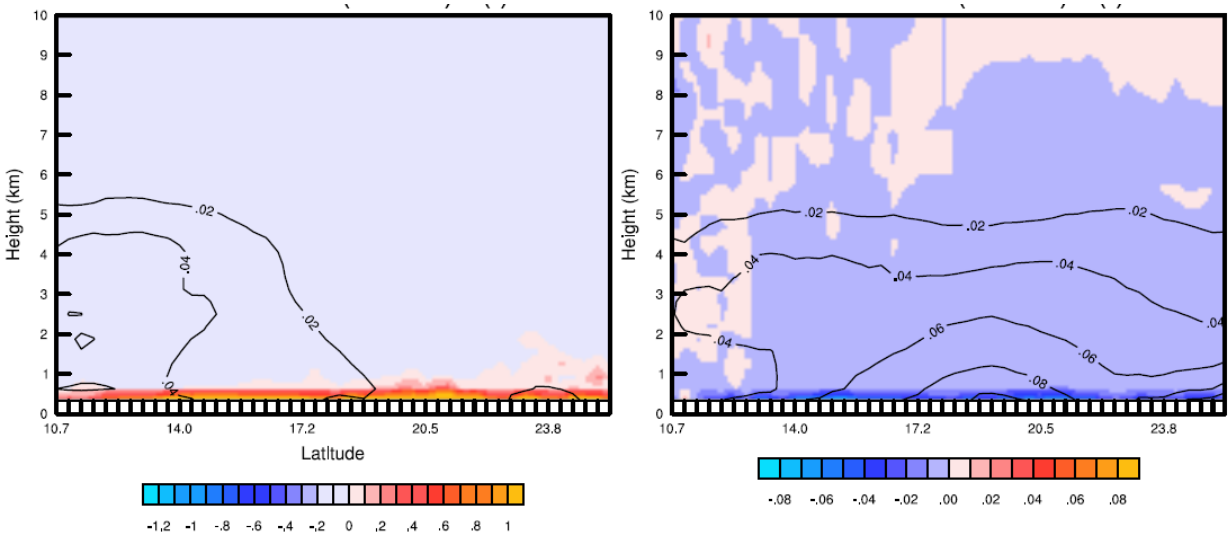

Figure 3-37. Same as Figure 3-35 but for longwave radiation

(a) (b)

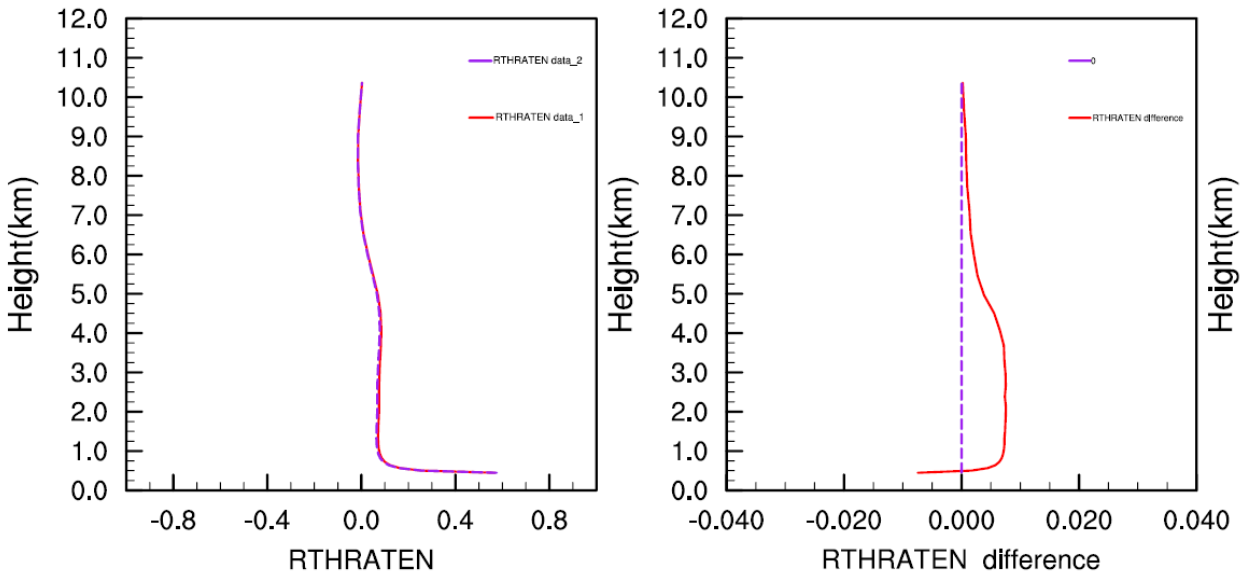

Figure 3-38. Same as Figure 3-34 but for shortwave + longwave radiation.

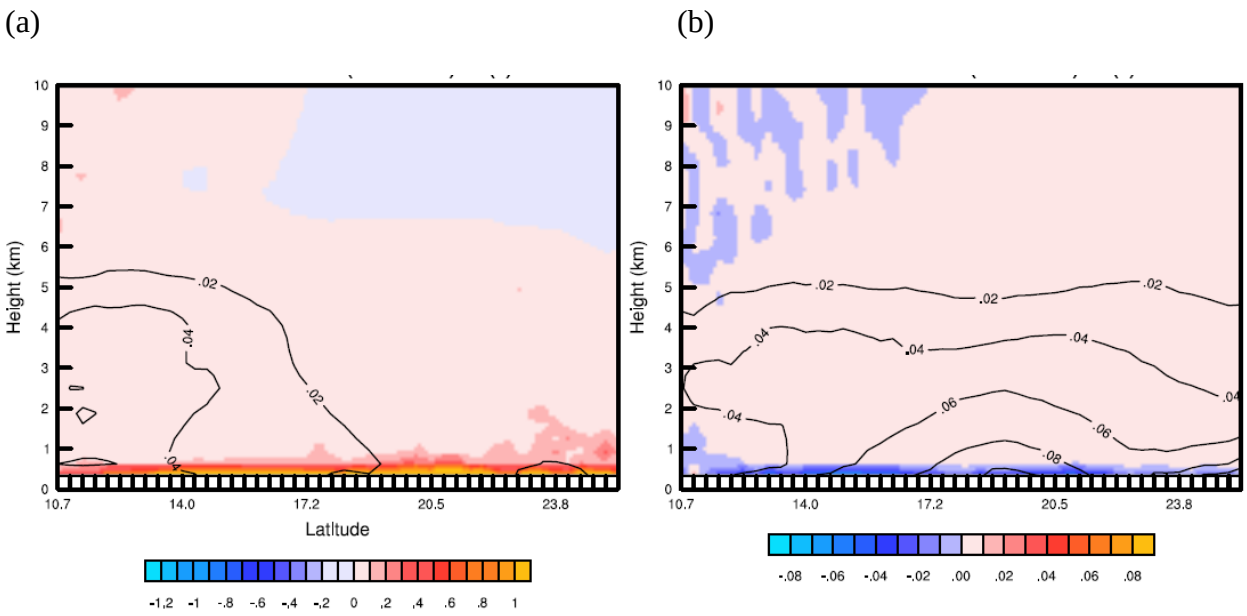

Figure 3-39. Same as Figure 3-35 but for shortwave+longwave radiation.

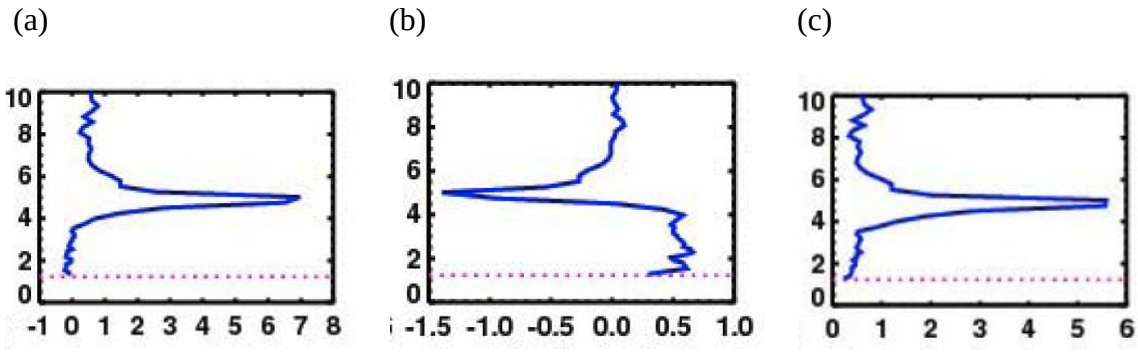

Figure 3-40. Daily averaged heating rates due to dust aerosols. Orbit-averaged vertical profile for 29 July. Unit: K day^{-1}. (a) Short wave radiative heating; (b) Long wave radiative heating; (c) Net radiative heating. Adapted from Huang et al.(2009).

The modeled potential temperature tendency in the boundary layer is closely related to the land-surface scheme and the planetary boundary layer (PBL) scheme. The land-surface models (LSMs) use the information of the surface layer, radiative forcing, precipitation forcing, and land-surface properties to provide heat and moisture fluxes over land and sea ice. These fluxes then give

a lower boundary condition for the vertical transport in PBL schemes (Skamarock 2008). PBL scheme computes the vertical transport of heat, water vapor, and momentum due to turbulent mixing (Kalverla et al. 2016).

We analyze the potential temperature tendency due to the boundary layer process. We also calculate the surface energy budget. As shown in Figure 3-41a and Figure 3-42a, positive heating produced by the PBL scheme has a depth of around 3~4 km. In the daytime, the heat fluxes, which includes sensible heat flux (Figure 3-49a) and latent heat flux (figure not shown) from the surface to the boundary layer. Because the region is desert where the air is very dry, the latent heat flux is negligible, and sensible heat flux is responsible for the heating in this layer.

In North Africa where dust and high surface temperature are located (Figure 3-44a), the net shortwave radiation flux to the surface in the experiment ExDO is smaller than that in the experiment ExO (Figure 3-43b). This means the shortwave radiation received at the surface is reduced when dust is added to the model.

The reduction of shortwave radiation received at the surface makes the surface temperature lower by 0~1^{o}C in the experiment with dust (Figure 3-44b). The cooler surface in the experiment ExDO emits less longwave radiation upward (Figure 3-45b). This explains why the longwave radiative heating effect below 800 meters in the atmosphere is reduced as we mentioned earlier. Downward longwave radiation from the atmosphere heats up the surface (Figure 3-46a). In the dust experiment, such downward flux is enhanced (Figure 3-46b). This is because, as mentioned earlier, the longwave radiation cooling in the atmosphere is enhanced by dust radiative effect, and this enhanced longwave radiation will increase the downward longwave radiation to the surface. Thus, the surface receives more longwave radiation because of the presence of dust. This effect is similar to the “greenhouse effect”.

The combination of upward longwave radiation from the surface and the downward longwave radiation fluxes received by the surface is shown in Figure 3-47a. The value of the net longwave radiation (downward-upward) is negative, which indicates that the upward longwave radiation dominates over the downward longwave radiation. The surface transfer energy to the atmosphere. The difference in the net longwave radiation between these two experiments is positive indicating that the net longwave radiation flux from the surface is reduced when dust is considered in the process (Figure 3-47b). This results from dust reducing the upward longwave radiation from the surface and dust enhancing the downward longwave radiation to the surface.

Net shortwave radiation dominates net longwave radiation (Figure 3-48a). During the daytime, surface receives shortwave radiation flux from the sun. Surface transfers energy to the atmosphere by emitting longwave radiation flux, which is less than the downward shortwave radiation flux. The difference between the experiment ExDO and ExO is negative, which indicates that the surface gets less solar energy because of the dust radiative effect (Figure 3-48b).

During the daytime, the temperature at the surface is higher than the temperature in the lower atmosphere. Sensible heat transfers from the surface to the lower atmosphere (Figure 3-49a). When dust is added into the model, because surface receives less energy and becomes cooler, the sensible heat flux from the surface to the lower atmosphere becomes less (Figure 3-49b). As a result, the heating at the boundary layer is reduced, which can explain the reduction of the heating rate in the lower atmosphere when dust is included in the simulation (Figure 3-41b and Figure 3-42b).

(a) (b)

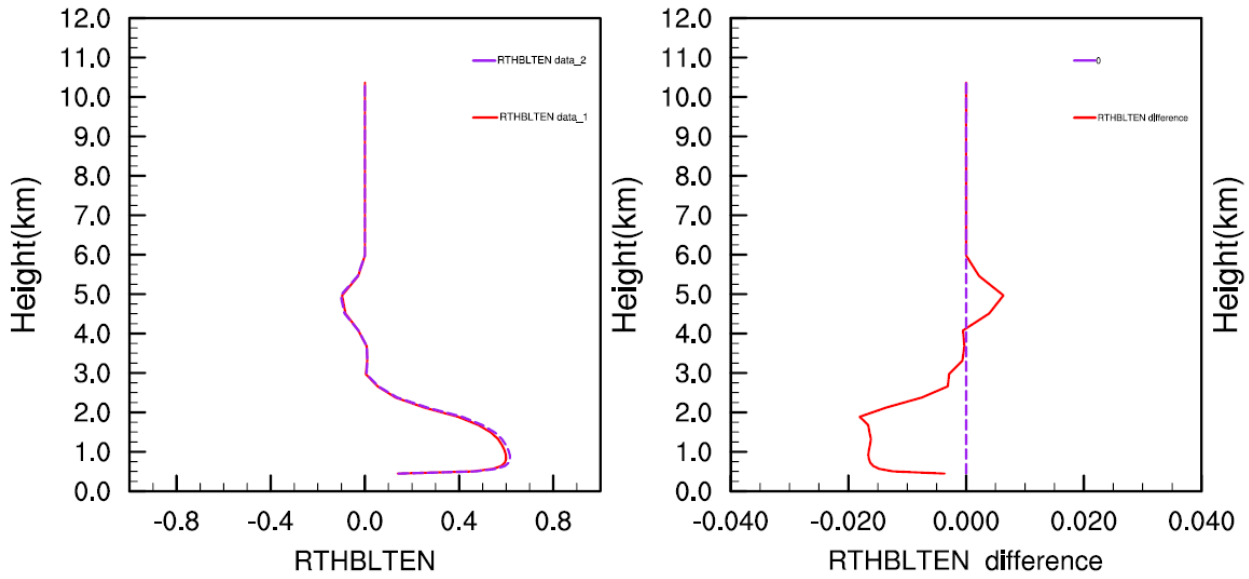

Figure 3-41. The averaged potential temperature tendency (K/hour) due to the boundary layer heating at 13UTC 21 August 2010. (a) the experiment ExDO (with dust) (Redline), the experiment ExO (only other aerosols, no dust) (purple line). (b) the difference due to dust (ExDO-ExO) (red line), zero value line (purple line).

(a) (b)

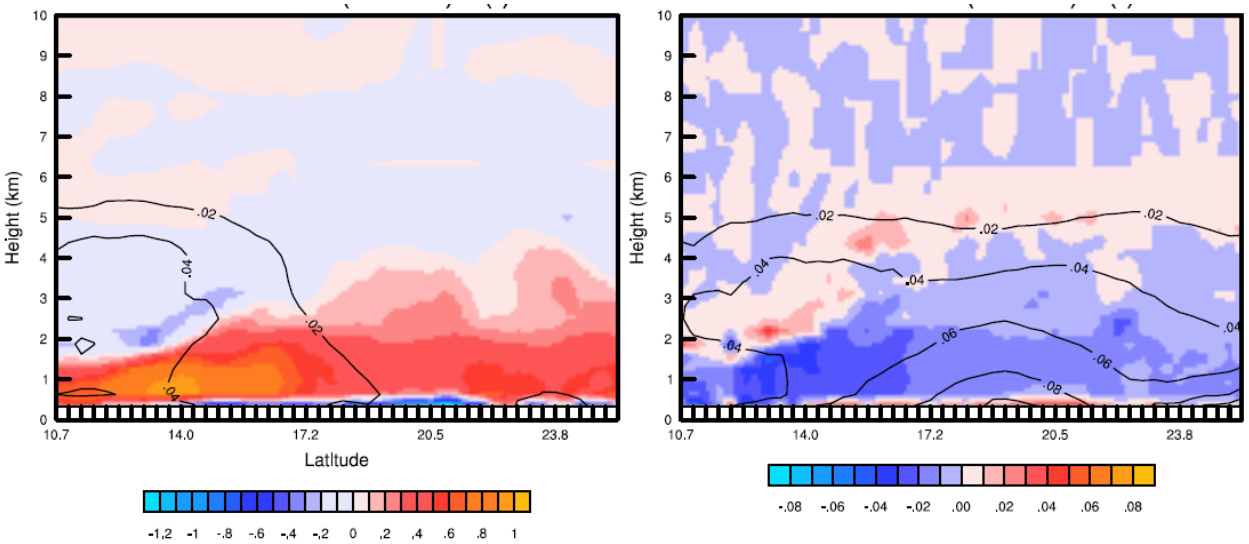

Figure 3-42. The vertical cross sections (height vs latitude) of the zonal mean (10°W to 10°E) of the potential temperature tendency due to the boundary layer heating (shading, K/hour), and the extinction coefficient at 550 nm (contour) at 13UTC 21 August 2010 for (a) the experiment ExO, and (b) the difference due to dust (ExDO-ExO).

(a) (b)

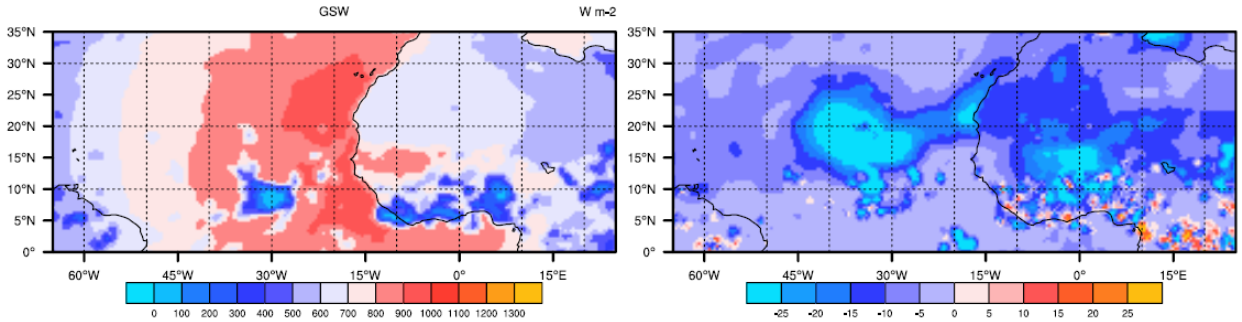

Figure 3-43. The net shortwave radiation flux (W/m^2) received at the surface at 13UTC 21 August 2010 from (a) the experiment ExO, and (b) difference due to dust (ExDO-ExO). The positive number in (b) means downward flux is increased.

(a) (b)

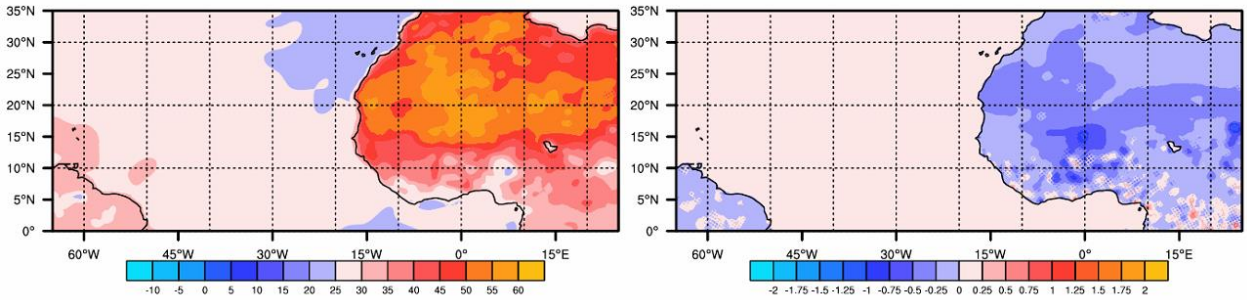

Figure 3-44. The surface skin temperature (°C) at 13UTC 21 August 2010 from (a) the experiment ExO, and (b) the difference due to dust (ExDO-ExO).

(a) (b)

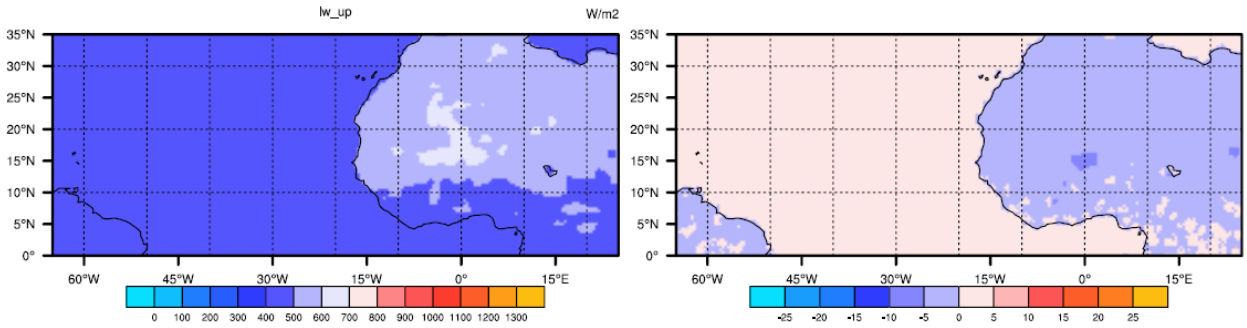

Figure 3-45. The upward longwave radiation flux (W/m^2) from the surface at 13UTC 21 August 2010 from (a) experiment ExO, and (b) the difference due to dust (ExDO-ExO). The positive number in (b) means upward flux is increased.

(a) (b)

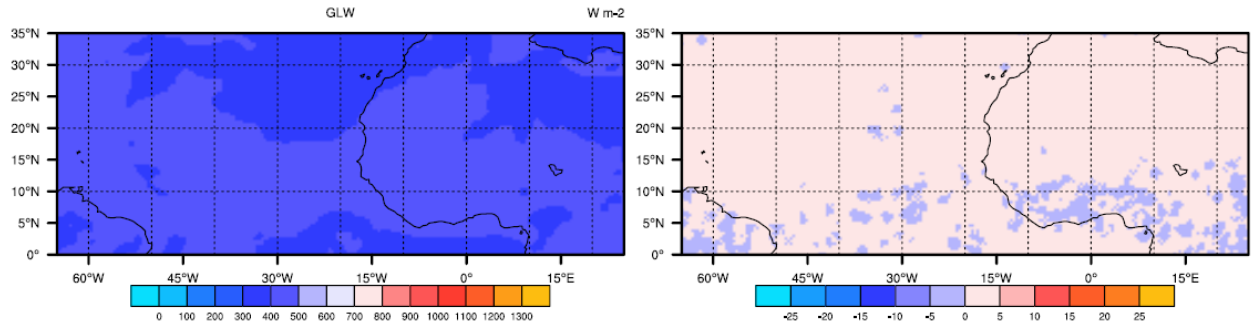

Figure 3-46. The downward longwave radiation flux (W/m^2) to the surface at 13UTC 21 August 2010 from (a) the experiment ExO, and (b) the difference due to dust (ExDO-ExO). The positive number in (b) means downward flux is increased.

(a) (b)

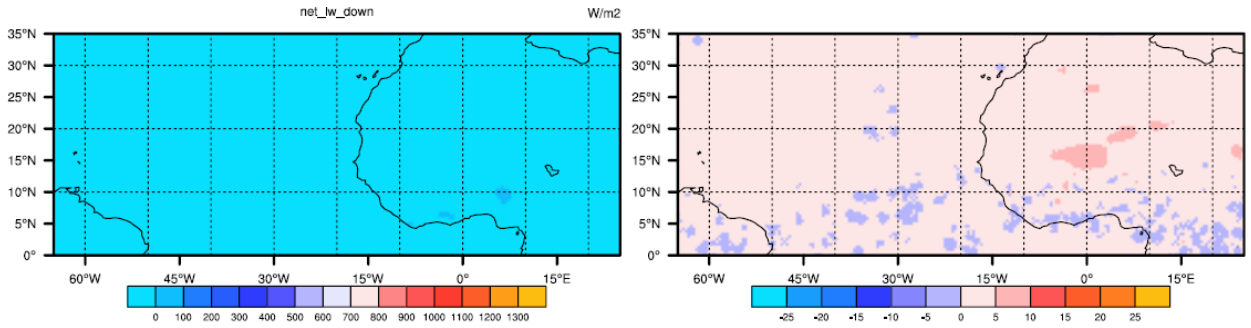

Figure 3-47. The net longwave radiation flux (W/m^2) (downward-upward) at 13UTC 21 August 2010 from (a) the experiment ExO, and (b) the difference due to dust (ExDO-ExO). Positive number means downward direction.

(a) (b)

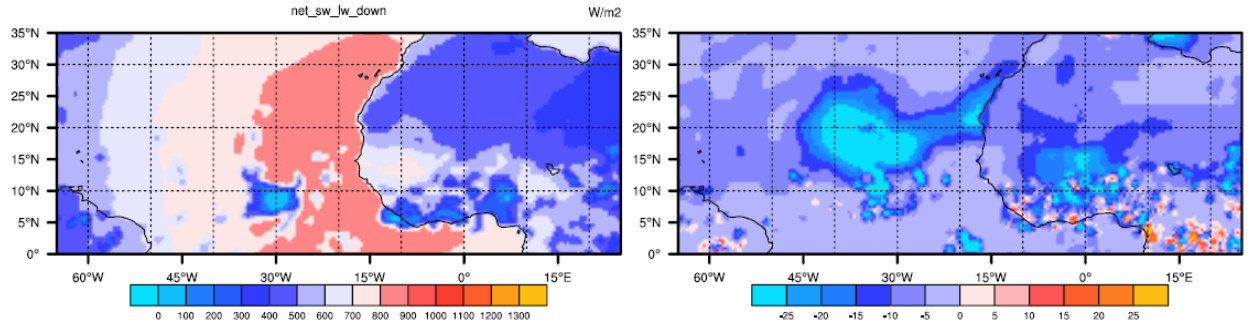

Figure 3-48. The net shortwave radiation + net longwave radiation flux (W/m^2) at the surface at 13UTC 21 August 2010 from (a) the experiment ExO, and (b) the Difference due to dust (ExDO-ExO). Positive number means downward direction.

(a) (b)

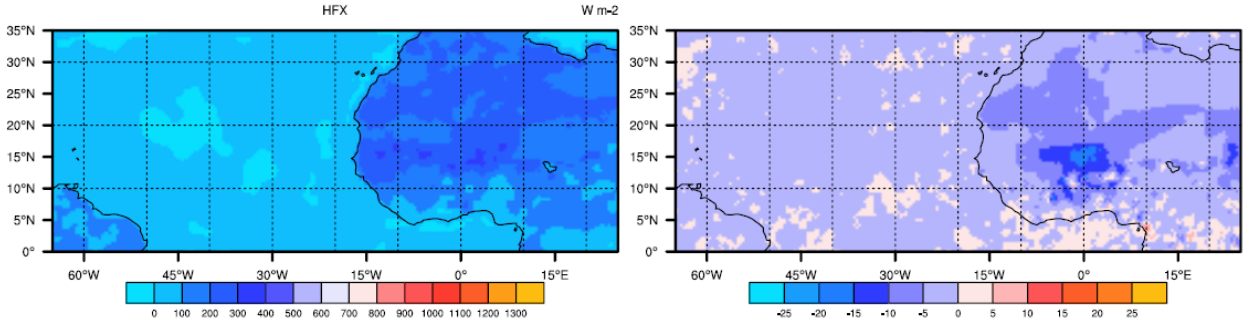

Figure 3-49. The sensible heat flux (W/m^2) from the surface at 13UTC 21 August 2010 from (a) the experiment ExO, and (b) the difference due to dust (ExDO-ExO). Positive number means upward direction.

Total potential temperature tendency includes the heating contributed from radiation, PBL parameterization, cumulus scheme, potential temperature advection, and microphysical latent heat release. The heating from the radiation and boundary layer processes is the major contributing factors; other heating terms are negligible (which is the case for this selected region and time, figures not shown). The combination of these two terms leads to a positive heating from the surface up to 4~5 km in the atmosphere. There is a maximum heating rate at the surface due to the strong sensible heat flux (Figure 3-50a and Figure 3-51a).

When dust is added to the simulation, the heating rate becomes smaller below 2.5 km (Figure 3-50b and Figure 3-51b). Although dust radiative effect warms up the atmosphere in this layer, it cannot compensate the dust cooling effect in the boundary layer. Above 2.5 km height, dust heats the atmosphere due to its radiative effect.

The difference in the potential temperature vertical profile between these two experiments is similar to the difference in the total heating rate vertical profile, with cooling under 2.5 km and

warming above it (Figure 3-52b and Figure 3-53b). Thus, the temperature difference between these two experiments is a result of total heating difference due to dust.

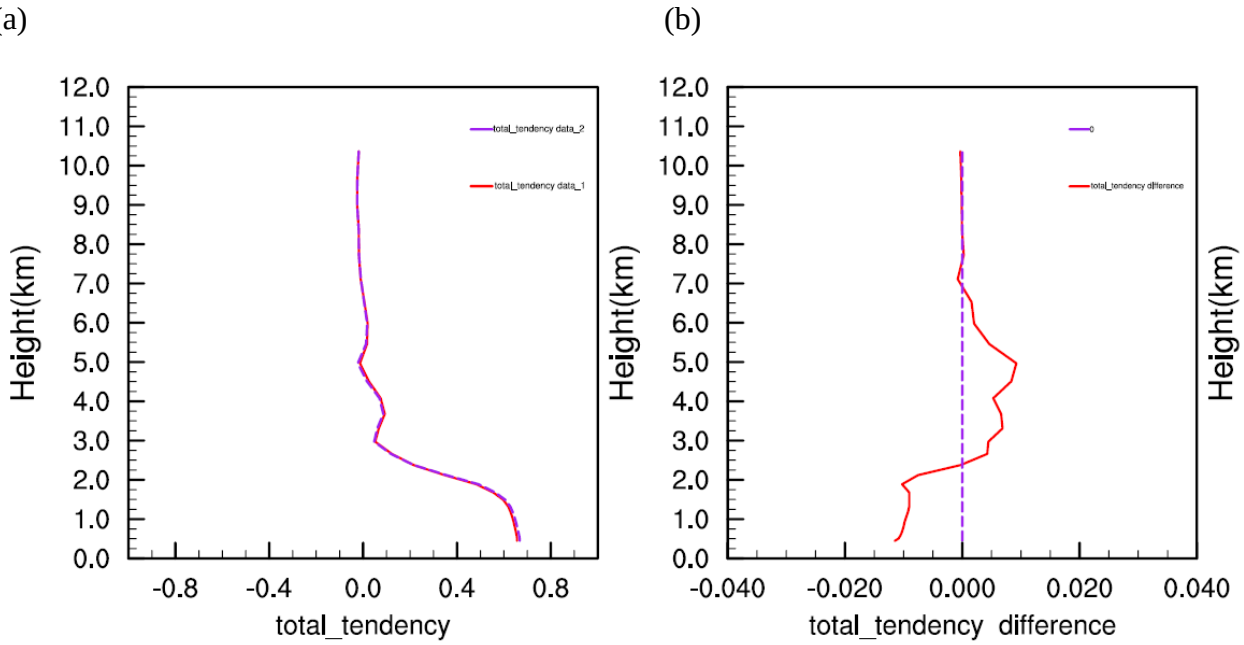

Figure 3-50. The averaged potential temperature tendency (K/hour) due to the total tendency (radiation + PBL parameterization + cumulus scheme + microphysics latent heat+ advection) at 13UTC 21 August 2010. (a) experiment ExDO (with dust) (Red line), experiment ExO (only other aerosols, no dust) (purple line). (b) Difference due to dust (ExDO-ExO) (red line), zero value line (purple line).

(a) (b)

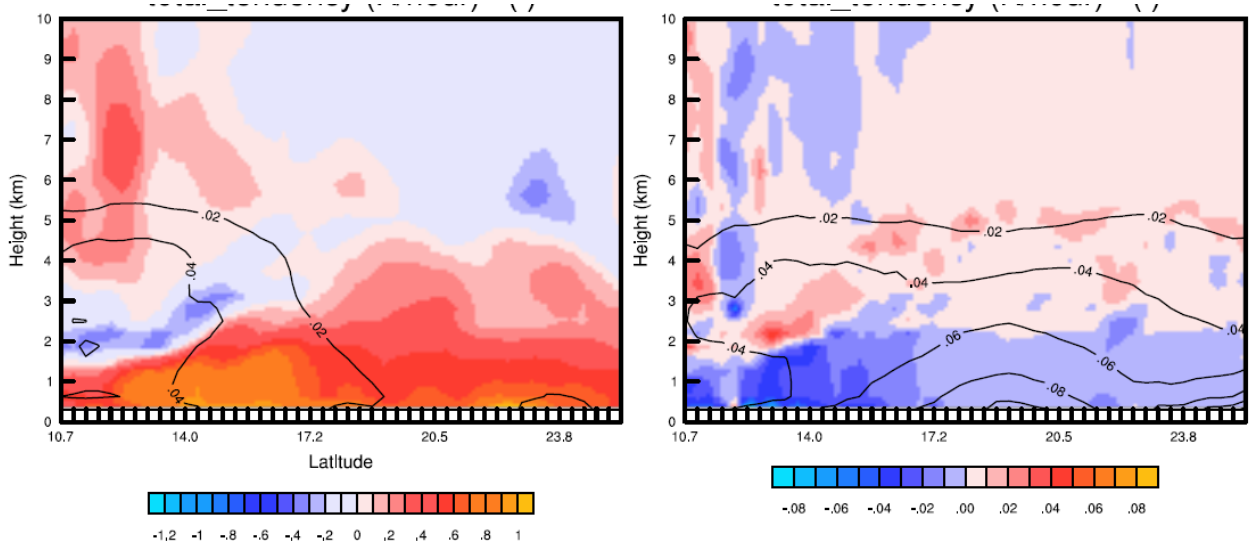

Figure 3-51. The vertical cross sections (height vs latitude) of the zonal mean (10°W to 10°E) of the potential temperature tendency due to the total tendency (radiation + PBL parameterization + cumulus scheme + microphysics latent heat+ advection) (shading, K/hour), and the extinction coefficient at 550nm (contour) at 13UTC 21 August 2010 for (a) the experiment ExO, and (b) the difference due to dust (ExDO-ExO).

(a) (b)

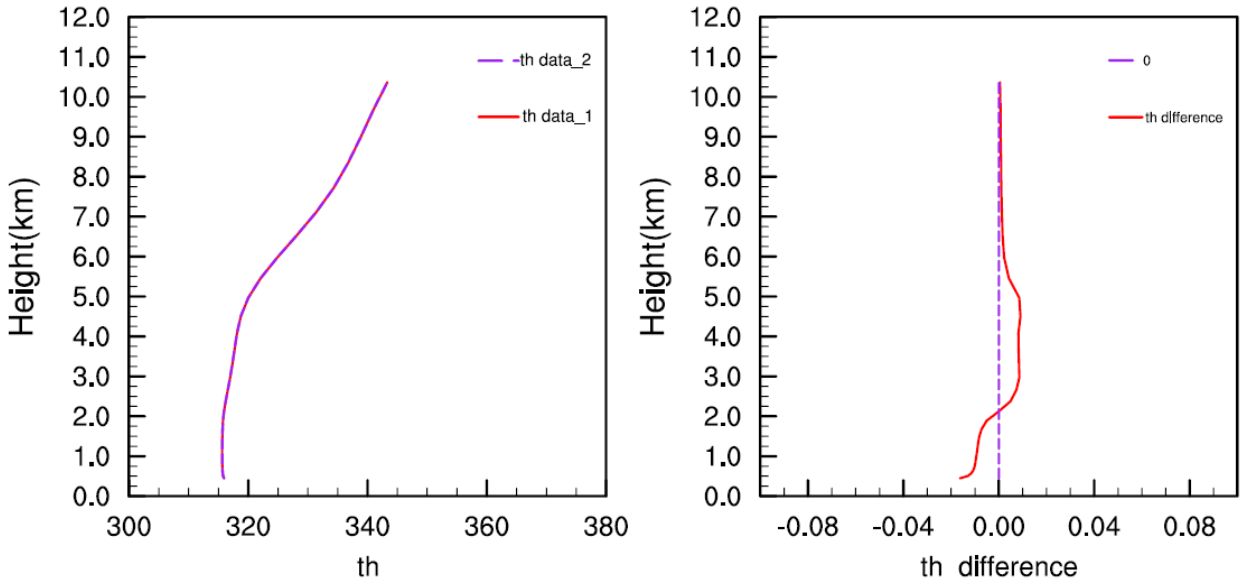

Figure 3-52. The average potential temperature (K) at 13UTC 21 August 2010. (a) experiment ExDO (with dust) (Red line), experiment ExO (only other aerosols, no dust) (purple line). (b) Difference due to dust (ExDO-ExO) (red line), zero value line (purple line).

(a) (b)

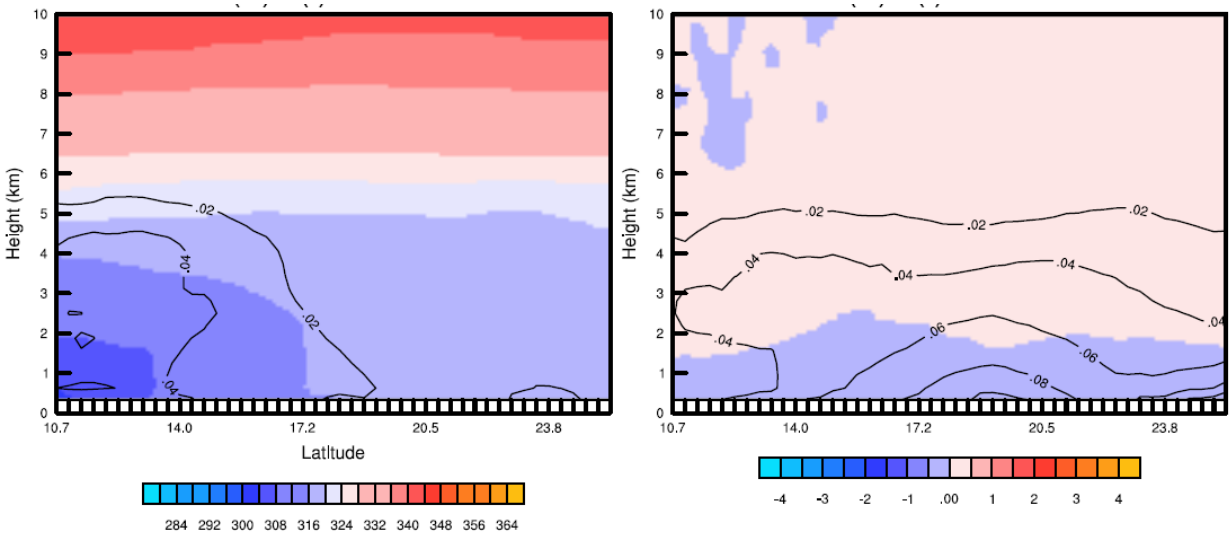

Figure 3-53. The vertical cross sections (height vs latitude) of the zonal mean (10°W to 10°E) of the potential temperature (shading, K) and the extinction coefficient at 550 nm (contour) at 13UTC 21 August 2010 for (a) the experiment ExO, and (b) the difference due to dust (ExDO-ExO).

At 00UTC 22, we use the same cross-section and area previously used at 13UTC 21 to analyze the heating rate and the impacts of dust (Figure 3-54). There is no shortwave radiation at nighttime, the longwave radiation cools the atmosphere (Figure 3-55a and Figure 3-56a). The cooling rate decreases with height below 3 km because the temperature decreases with height, and layers with lower temperature emit less longwave radiation. Although the atmosphere receives longwave radiation from the surface at the lower levels, it emits much more than it receives. Thus, the maximum cooling rate is around -0.3K/hour at the lowest level (Figure 3-55a). When the

simulation includes dust, the cooling effect is stronger (Figure 3-55b and Figure 3-56b). The downward longwave radiation to the surface is stronger between 15~30°N and 10°E~10°W (Figure 3-57b). The maximum of downward longwave radiation difference corresponds to the maximum surface temperature difference (Figure 3-58b), which indicates that dust has a "greenhouse effect" at the surface. The maximum temperature difference in Figure 3-58b is also matching the maximum upward longwave radiation flux in the same region because the surface with higher temperature in the dust experiment emits more longwave radiation to the atmosphere (Figure 3-59).

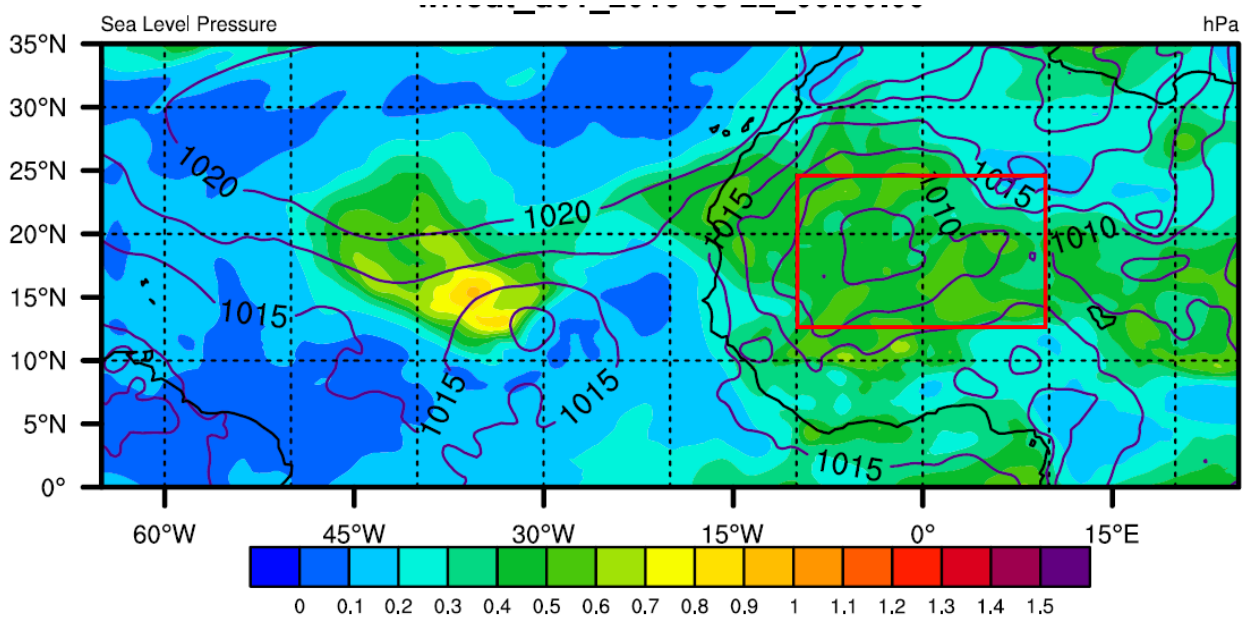

Figure 3-54. The aerosol optical depth (shading) and the sea level pressure (contour, units: hPa) at 00UTC 22 August 2010. Red rectangular frame indicates the area where the horizontal domain average is taken.

(a) (b)

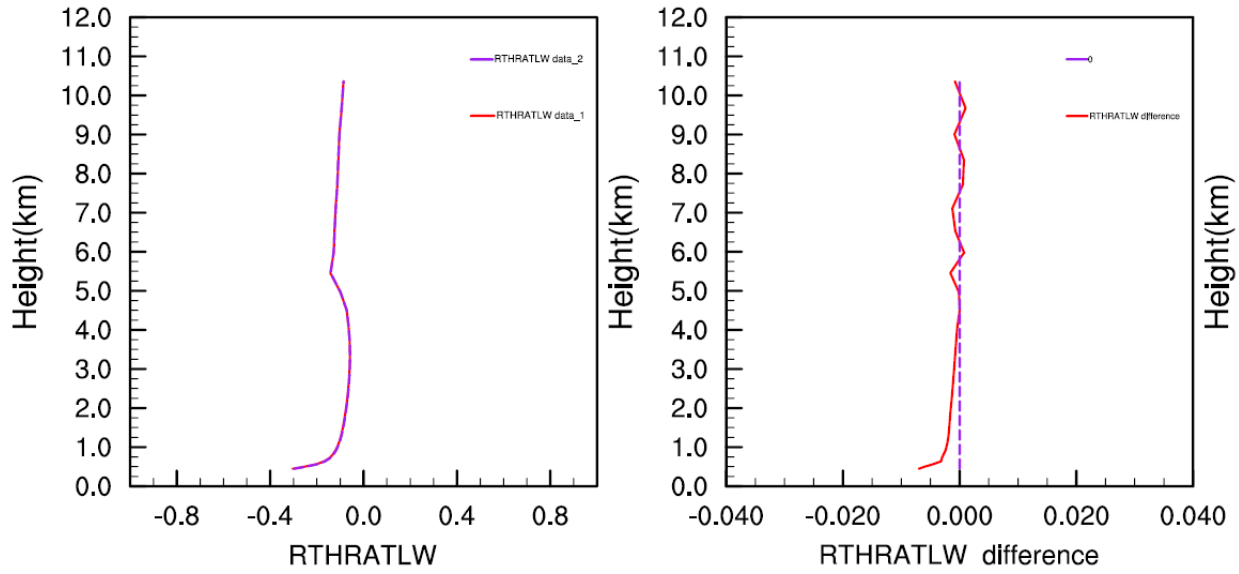

Figure 3-55. The averaged potential temperature tendency (K/hour) due to longwave radiation at 00UTC 22 August 2010. (a) experiment ExDO (with dust) (Redline), experiment ExO (only other aerosols, no dust) (purple line). (b) Difference due to dust (ExDO-ExO) (red line), zero value line (purple line).

(a) (b)

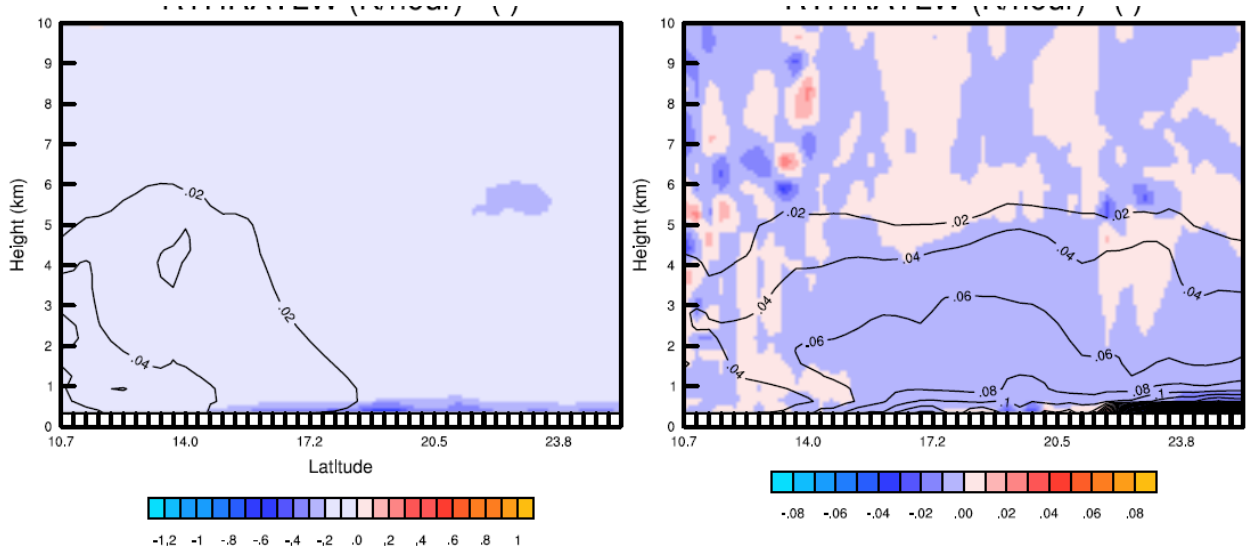

Figure 3-56. The vertical cross sections (height vs latitude) of the zonal mean (10°W to 10°E) of the potential temperature tendency due to the longwave radiation (shading, K/hour), and extinction coefficient at 550nm (contour) at 00UTC 22 August 2010 for (a) the experiment ExO, and (b) the difference due to dust (ExDO-ExO).

(a) (b)

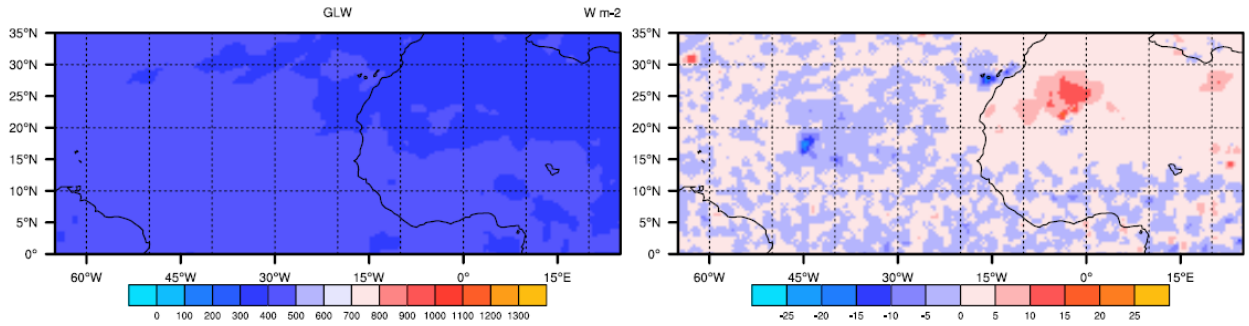

Figure 3-57. (a) The downward longwave radiation flux (W/m^2) to the surface at 00UTC 22 August 2010 from (a) the experiment ExO, and (b) the difference due to dust (ExDO-ExO). Thee positive number in (b) means downward flux is increased.

(a) (b)

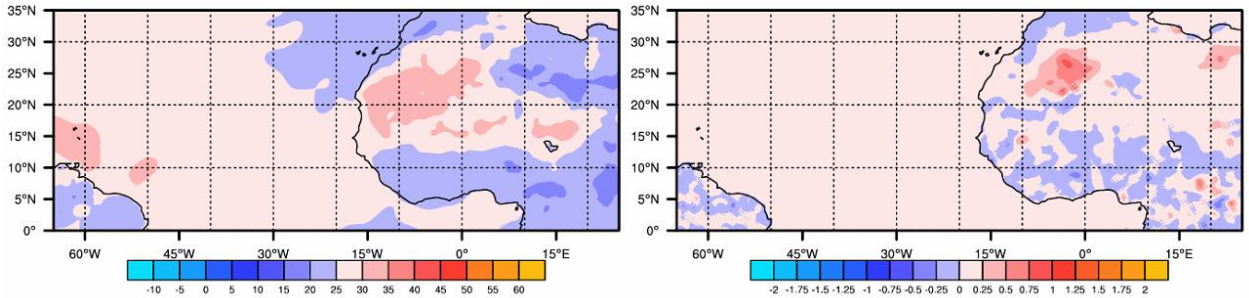

Figure 3-58. The surface skin temperature (°C) at 00UTC 22 August 2010 from (a) experiment ExO, and (b) difference due to dust (ExDO-ExO).

(a) (b)

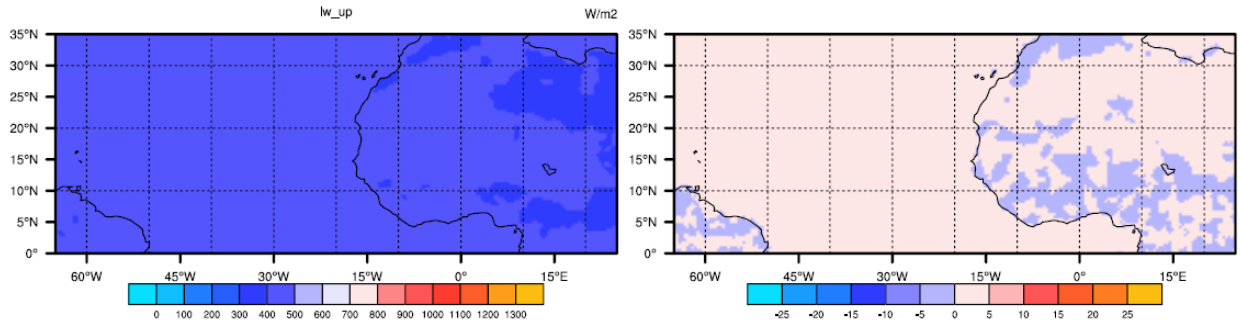

Figure 3-59. The upward longwave radiation flux (W/m^2) from the surface at 00UTC 22 August 2010 from (a) experiment ExO, and (b) the difference due to dust (ExDO-ExO). Positive number in (b) means upward flux is increased.

At night, the surface temperature is lowered faster than the atmosphere near the surface. This results in a downward sensible heat flux near the surface (Figure 3-60a). The potential temperature tendency due to boundary layer parameterization is negative in the boundary layer (below 500 m in Figure 3-61a and below 1 km in Figure 3-62a), which indicates that the boundary layer is cooled down because of the downward sensible heat flux.

Dust enhances the downward longwave radiation flux from the dust layer, the surface temperature drops less than the experiment without dust. The temperature difference between the surface and the boundary layer is smaller. With the reduction of downward sensible heat flux, the cooling rate in the boundary layer is reduced below 1 km (Figure 3-61b and Figure 3-62b). The domain averaged potential temperature tendency due to boundary heating in the boundary layer changes very little between 1 km and 4 km height when dust is added. Overall, these nighttime changes are small comparing to the daytime changes.

The horizontal domain averaged total heating rate due to all physical processes (including radiation, PBL parameterization, cumulus scheme, microphysics latent heat, and advection) is negative. It means the atmosphere over this region is losing energy in the whole column (Figure

3-63a). The cooling above 1 km is contributed from the longwave radiation cooling. While below 1 km, it results from a combination of longwave radiation cooling and the turbulence mixing. Several warming patches in the cross-sections are due to the advection (Figure 3-64a).

In the presence of dust, the atmosphere overall loses more energy because of stronger longwave radiation cooling (Figure 3-63b and Figure 3-64b). There is a slight warming (less cooling) due to dust at the lowest level (Figure 3-63b). The reason has been mentioned earlier. The change of potential temperature due to dust is corresponding to the change of total heating rate, and the atmosphere has lower potential temperature after adding dust (Figure 3-65b and Figure 3-66b).

(a) (b)

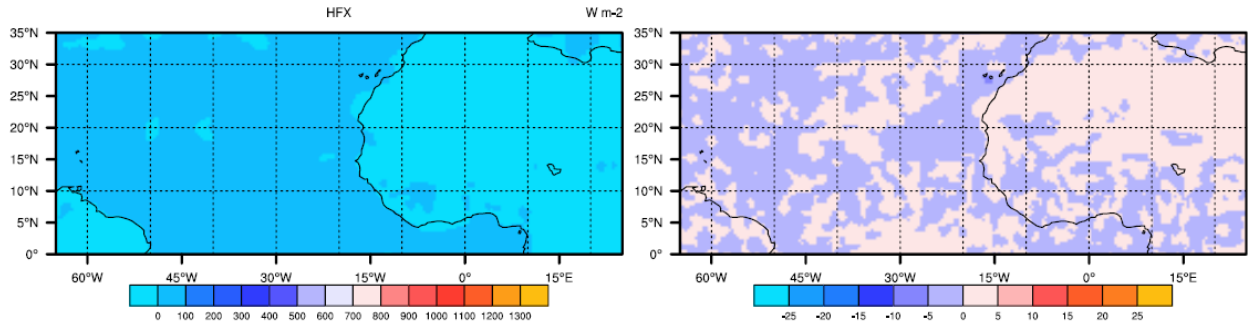

Figure 3-60. The sensible heat flux (W/m^2) from the surface at 00UTC 22 August 2010 from (a) the experiment ExO, and (b) the difference due to dust (ExDO-ExO). Positive number means upward direction.

(a) (b)

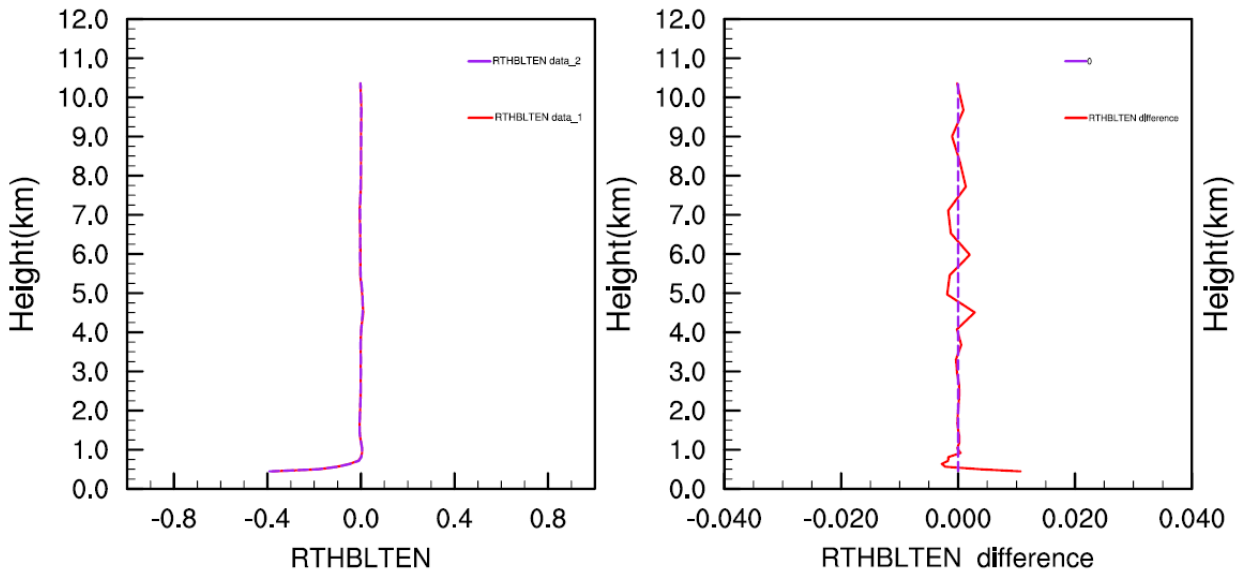

Figure 3-61. The averaged potential temperature tendency (K/hour) due to boundary layer heating at 00UTC 22 August 2010. (a) experiment ExDO (with dust) (Red line), experiment ExO (only other aerosols, no dust) (purple line). (b) Difference due to dust (ExDO-ExO) (red line), zero value line (purple line).

(a) (b)

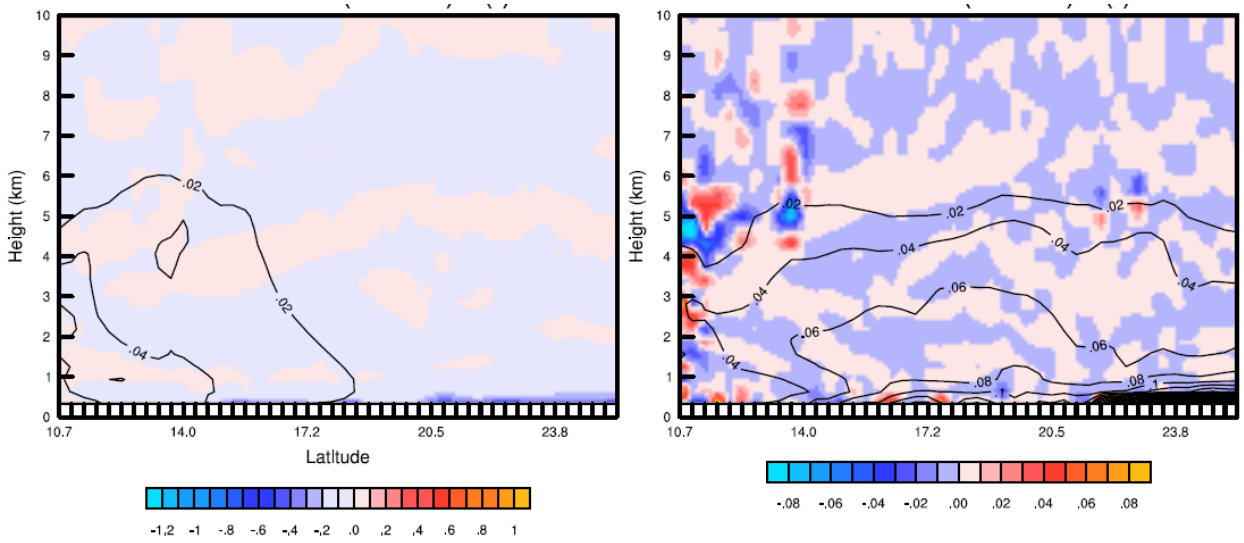

Figure 3-62. The vertical cross sections (height vs latitude) of the zonal mean (10°W to 10°E) of the potential temperature tendency due to the boundary layer heating (shading, K/hour) and extinction coefficient at 550

nm (contour) at 00UTC 22 August 2010 for (a) the experiment ExO, and (b) the difference due to dust (ExDO-ExO).

(a) (b)

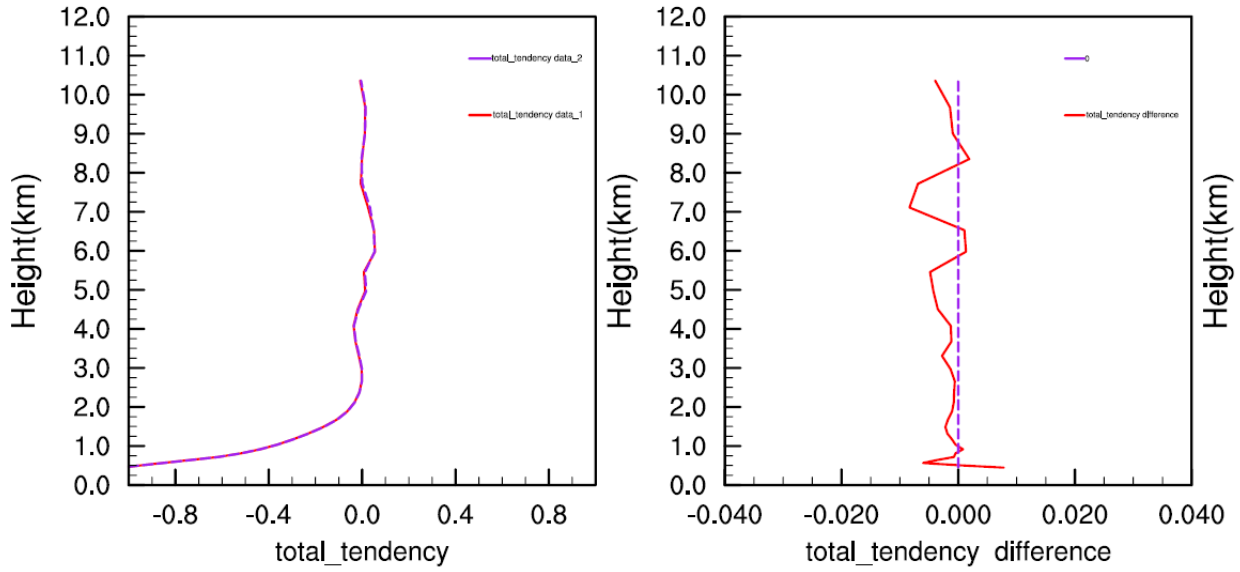

Figure 3-63. The averaged potential temperature tendency (K/hour) due to all physical processes at 00UTC 22 August 2010. (a) experiment ExDO (with dust) (Red line), experiment ExO (only other aerosols, no dust) (purple line). (b) Difference due to dust (ExDO-ExO) (red line), zero value line (purple line).

(a) (b)

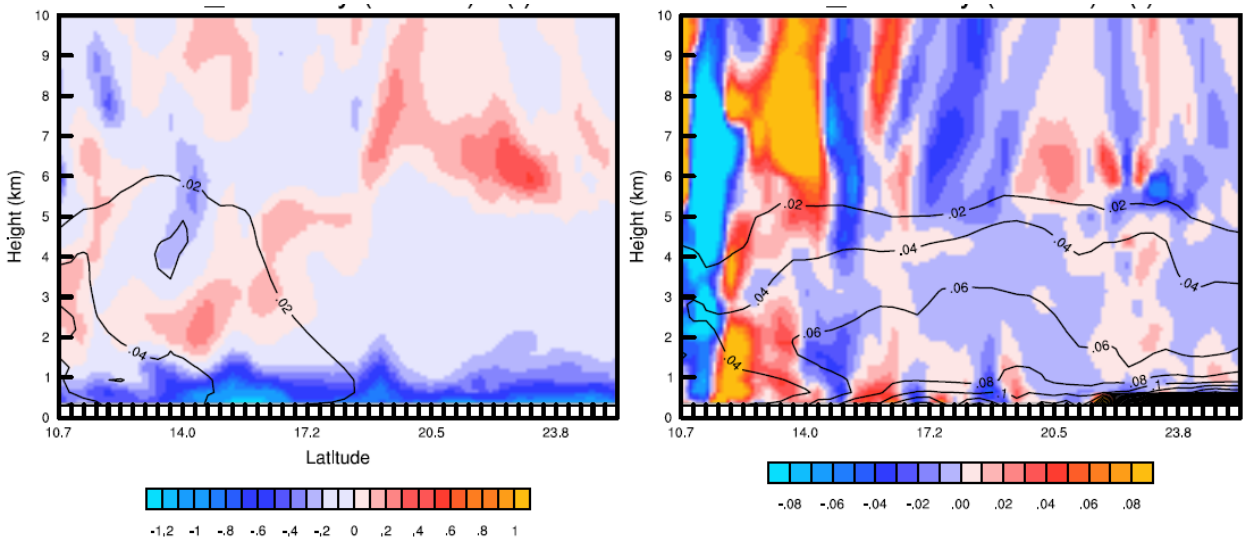

Figure 3-64. The vertical cross sections (height vs latitude) of the zonal mean (10°W to 10°E) of the potential temperature tendency due to all physical processes (shading, K/hour), and extinction coefficient at 550nm (contour) at 00UTC 22 August 2010 for (a) the experiment ExO, and (b) the difference due to dust (ExDO-ExO).

(a) (b)

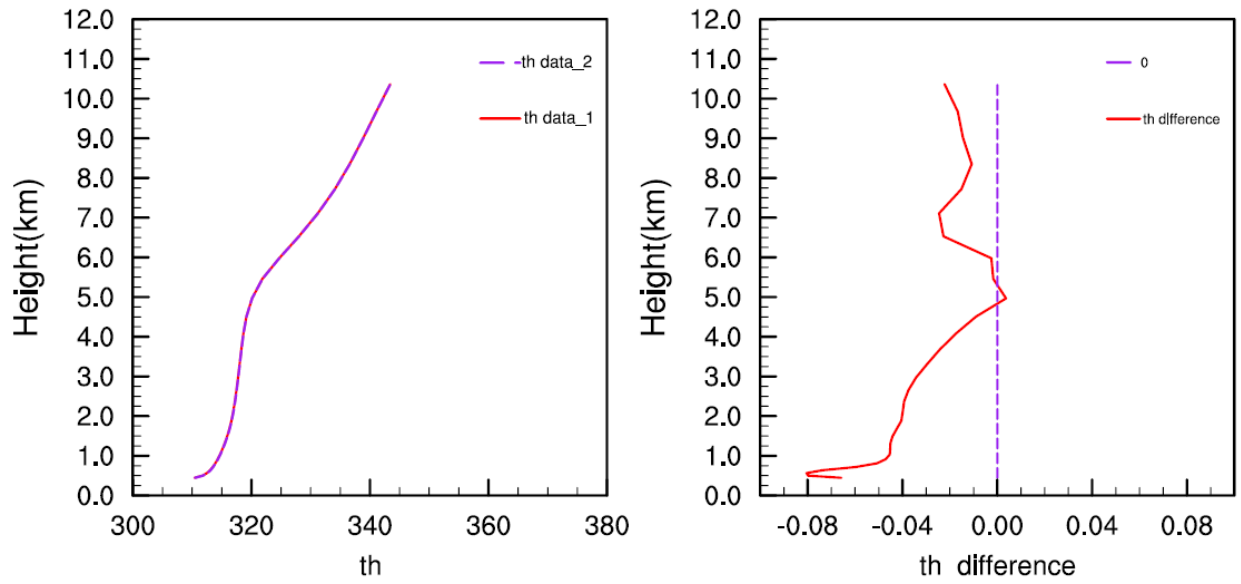

Figure 3-65. The average potential temperature (K) at 00UTC 22 August 2010. (a) experiment ExDO (with dust) (Red line), experiment ExO (only other aerosols, no dust) (purple line). (b) Difference due to dust (ExDO-ExO) (red line), zero value line (purple line).

(a) (b)

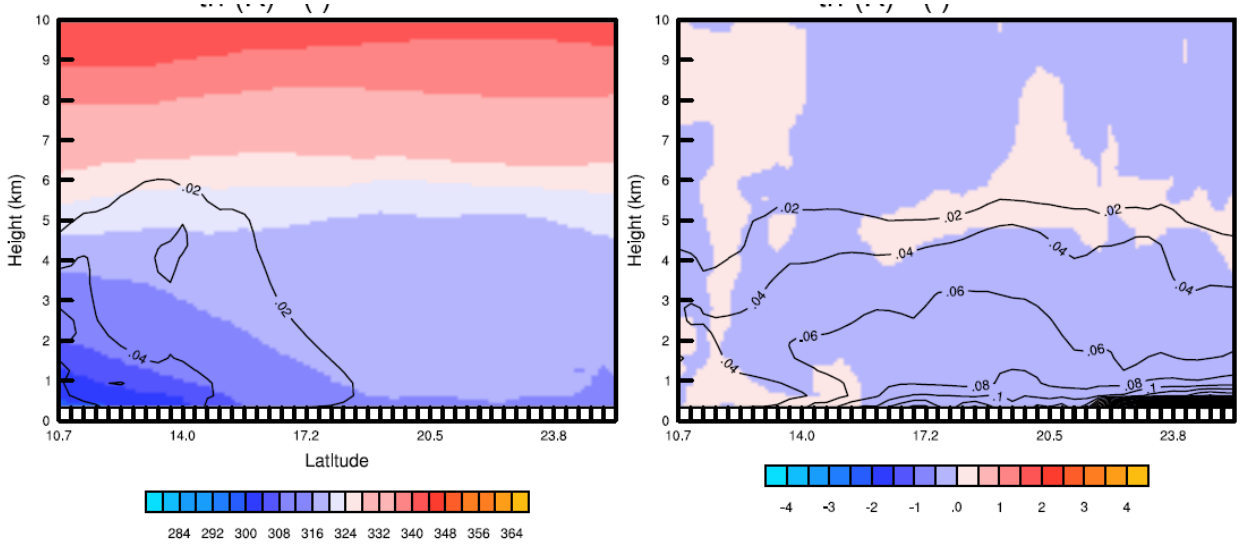

Figure 3-66. The vertical cross sections (height vs latitude) of the zonal mean (10°W to 10°E) of the potential temperature (shading, K) and extinction coefficient at 550 nm (contour) at 00UTC 22 August 2010 for (a) the experiment ExO, and (b) the difference due to dust (ExDO-ExO).

The radiation flux, sensible heat flux and surface skin temperature at the surface at the times we analyzed above in the two experiments are shown in Figure 3-67~Figure 3-70 and Table 3-2~ Table 3-5. We summarize the findings as follows.

(1) During the daytime, at 13UTC 21 August 2010 (Figure 3-67 and Table 3-2), dust reduces net shortwave radiation to the surface by 2.23% by scattering and absorbing shortwave radiation above the surface. Shortwave radiation dominates longwave radiation, the combination of

shortwave and longwave radiation is reduced by 2.22% considering dust. The net reduction of radiation leads to the reduction of surface skin temperature by 0.64% and the reduction of upward longwave radiation from the surface by 0.41%. Less energy received at the surface leads to the reduction of sensible heat flux from the surface to the atmosphere by 3.03%. Downward longwave radiation is enhanced by 0.31%. Net longwave radiation at the surface is upward, which is reduced by 2.26% in ExDO because the reduction of upward longwave radiation by the surface is larger than the enhancement of downward longwave radiation emitting to the surface.

One day later, at 12UTC 22 August 2010 (

Figure 3-69 and Table 3-4), the changes of fluxes and surface skin temperature are similar except the magnitudes are larger because the dust concentration is higher. Especially, the reduction of total shortwave and longwave radiation is 17.33 W/m^2. The value is close to the values obtained by Zhu et al. (2007a) and Miller and Tegen (1998), but it is less than half of the value found by Huang et al. (2009).

(2) During the nighttime, at 00UTC 22 August 2010 (Figure 3-68 and Table 3-3), downward longwave radiation is increased by 0.68% if dust is present because dust absorbs longwave radiation from the ground and reemits it back to the surface. This reduces the loss of energy at the surface, and the surface skin temperature is up by 0.24%. Higher surface skin temperature emits more longwave radiation upward by 0.09%. As the surface loses more longwave radiation than it receives, the net longwave radiation is upward, and it is decreased by 6.47% due to dust "greenhouse effect". Since the ground loses more energy than the lower atmosphere does, the surface sensible heat flux is downward towards the surface from the atmosphere. Dust reduces such flux by 2.25%. The similar situations occur one day later at 00UTC 23 August except at larger magnitudes (Figure 3-70 and Table 3-5).

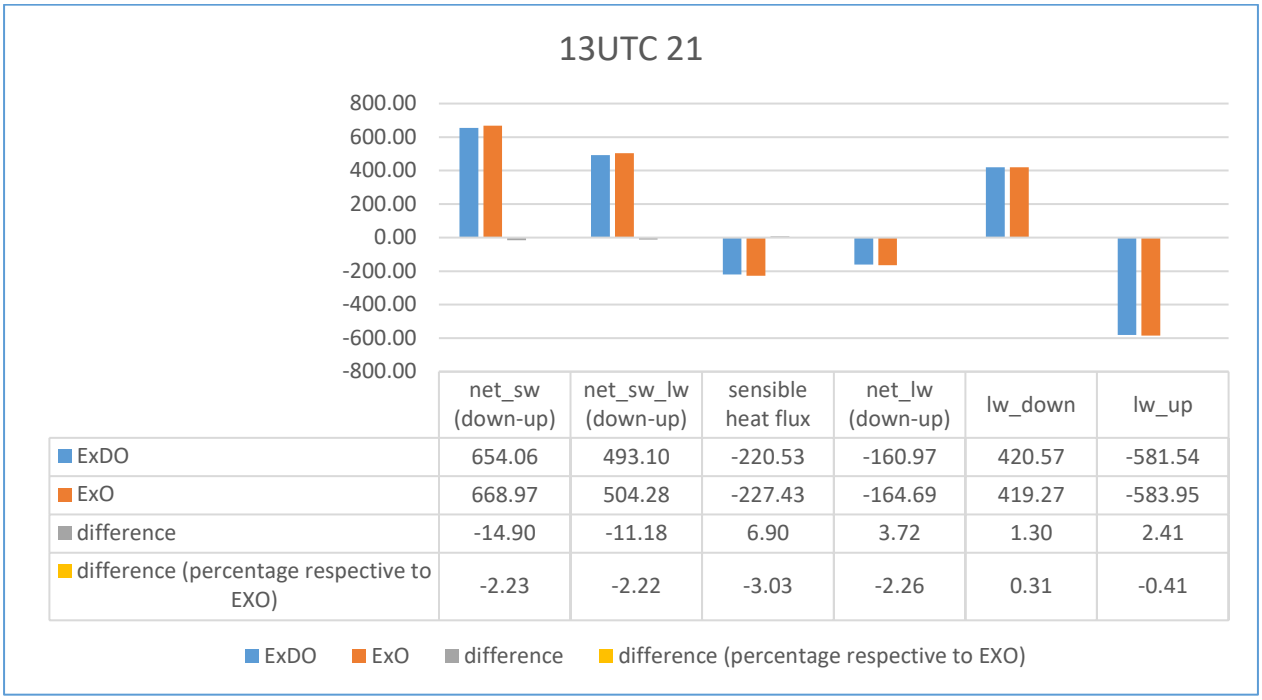

Figure 3-67. Compare different fluxes (W/m^2) at the surface at 13UTC 21 August 2010. The positive values indicate the fluxes are downward.

Table 3-2. Surface skin temperature (^oC) at 13UTC 21 August 2010.

ExDO(dust) (^oC)	ExO(No dust) (^oC)	Differnece(ExDO-ExO) (^oC)	Percentage change (%)
52.373	52.53	-0.33	-0.64

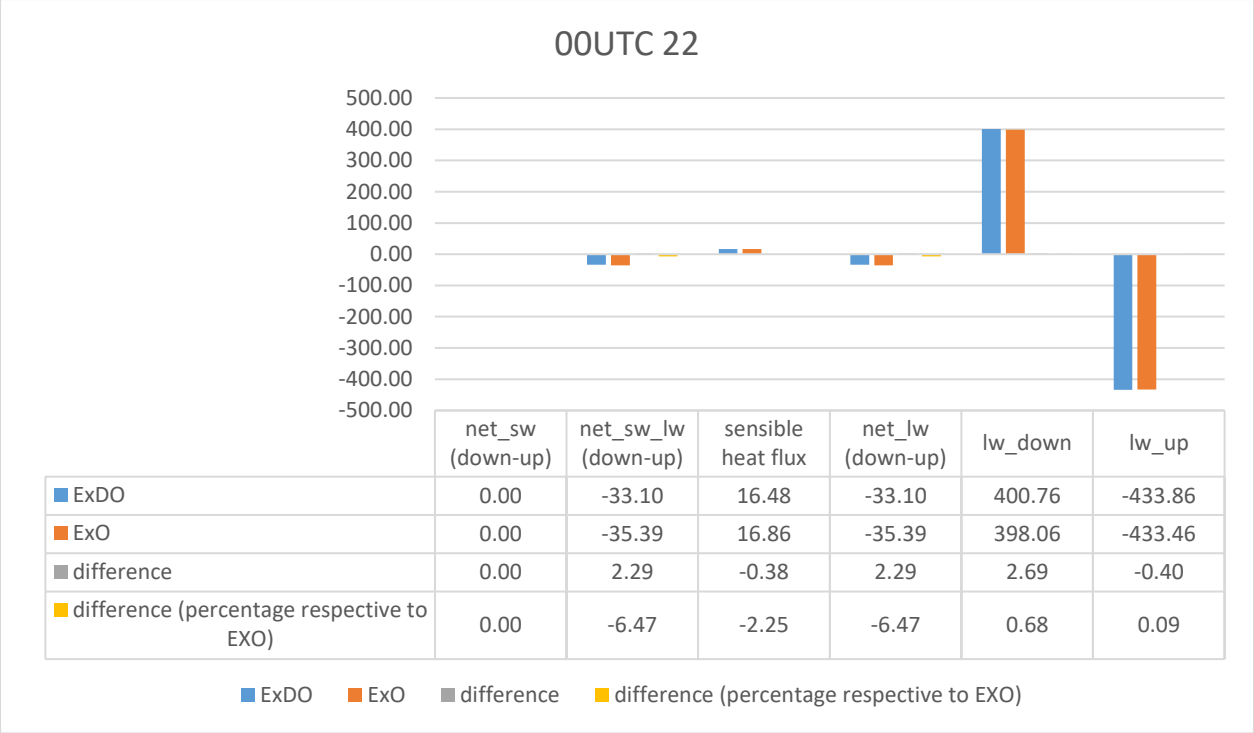

	net_sw (down-up)	net_sw_lw (down-up)	sensible heat flux	net_lw (down-up)	lw_down	lw_up
ExDO	0.00	-33.10	16.48	-33.10	400.76	-433.86
ExO	0.00	-35.39	16.86	-35.39	398.06	-433.46
difference	0.00	2.29	-0.38	2.29	2.69	-0.40
difference (percentage respective to EXO)	0.00	-6.47	-2.25	-6.47	0.68	0.09

Figure 3-68. Compare different fluxes (W/m^2) at the surface at 00UTC 22 August 2010. The positive values indicate the fluxes are downward.

Table 3-3. Surface skin temperature (^oC) at 00UTC 22 August 2010.

ExDO(dust) (^oC)	ExO(No dust) (^oC)	Differnece(ExDO-ExO) (^oC)	Percentage change(%)
29.23	29.16	0.07	0.24

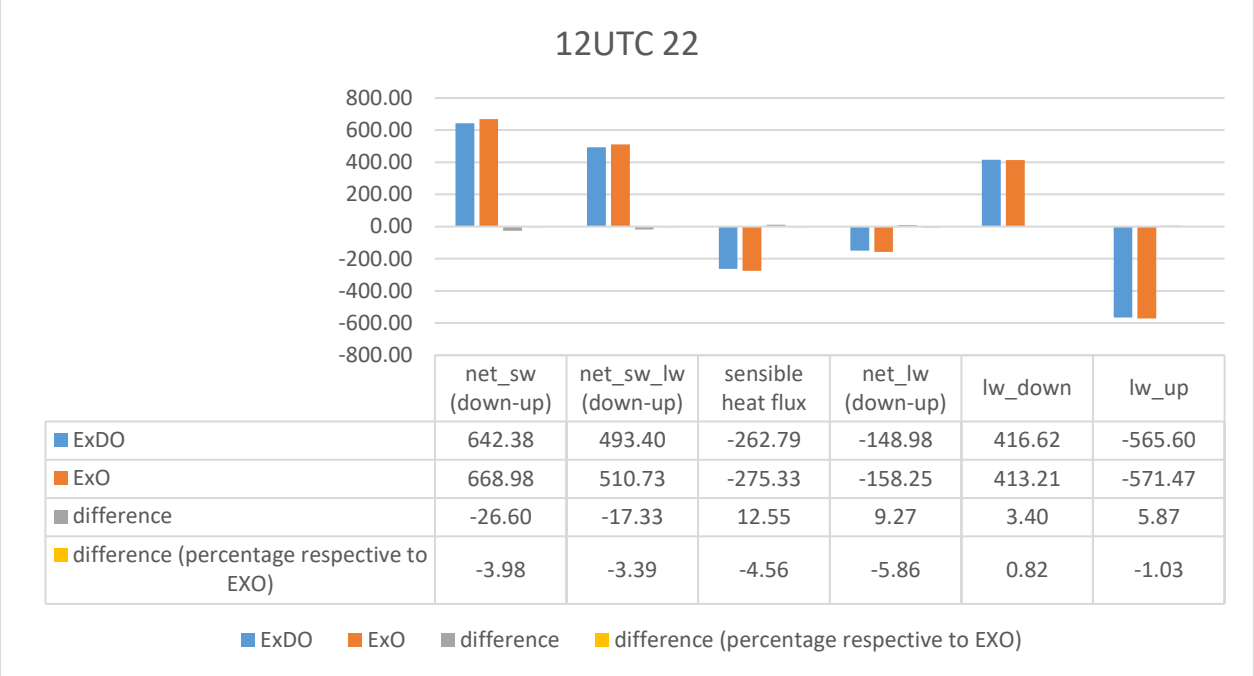

	net_sw (down-up)	net_sw_lw (down-up)	sensible heat flux	net_lw (down-up)	lw_down	lw_up
ExDO	642.38	493.40	-262.79	-148.98	416.62	-565.60
ExO	668.98	510.73	-275.33	-158.25	413.21	-571.47
difference	-26.60	-17.33	12.55	9.27	3.40	5.87
difference (percentage respective to EXO)	-3.98	-3.39	-4.56	-5.86	0.82	-1.03

Figure 3-69. Compare different fluxes (W/m^2) at the surface at 12UTC 22 August 2010. The positive values indicate the fluxes are downward.

Table 3-4. Surface skin temperature (^oC) at 12UTC 22 August 2010.

ExDO(dust) (^oC)	ExO(No dust) (^oC)	Differnece(ExDO-ExO) (^oC)	Percentage change (%)
49.94	50.78	-0.84	-1.65

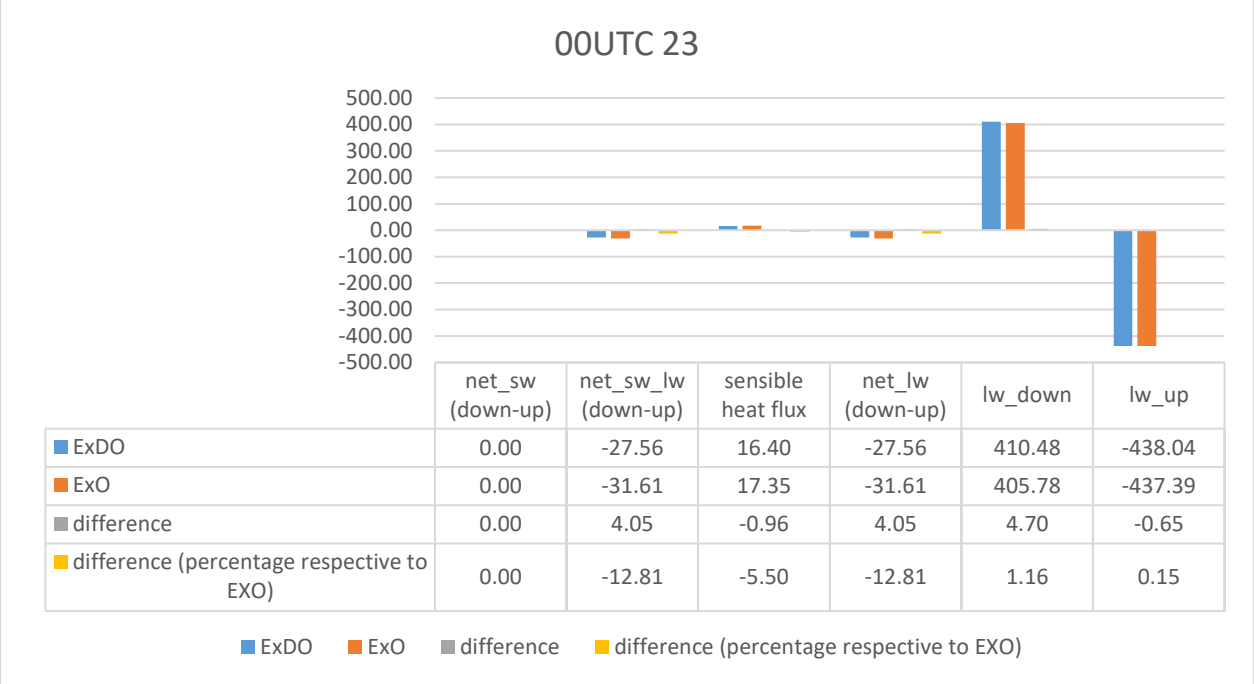

	net_sw (down-up)	net_sw_lw (down-up)	sensible heat flux	net_lw (down-up)	lw_down	lw_up
ExDO	0.00	-27.56	16.40	-27.56	410.48	-438.04
ExO	0.00	-31.61	17.35	-31.61	405.78	-437.39
difference	0.00	4.05	-0.96	4.05	4.70	-0.65
difference (percentage respective to EXO)	0.00	-12.81	-5.50	-12.81	1.16	0.15

Figure 3-70. Compare different fluxes (W/m^2) at the surface at 00UTC 23 August 2010. The positive values indicate the fluxes are downward.

Table 3-5. Surface skin temperature (^oC) at 00UTC 23 August 2010.

ExDO(dust) (^oC)	ExO(No dust) (^oC)	Differnece(ExDO-ExO) (^oC)	Percentage change (%)
29.96	29.84	0.12	0.39

Temperature over the whole atmosphere column in ExDO is colder than that in ExO because of the above-mentioned changes of heating rates and fluxes due to dust (Table 3-6). The cooling effect of dust has an increasing trend (Figure 3-71). The major processes involved in the dust direct effect in this dry region can be illustrated in Figure 3-72. Adding dust contributes to the cooling of the atmosphere column by a chain of related processes. Because the low-pressure system

is a warm core system in this case, the lowered temperature will raise the surface pressure and weaken the low-pressure system.

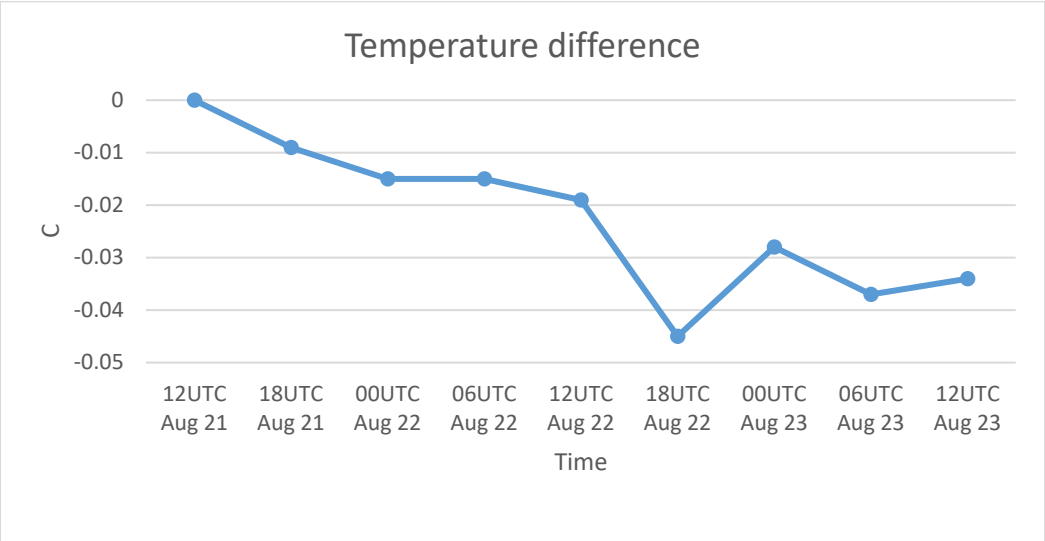

Figure 3-71. Column temperature (°C) difference (ExDO-ExO) from 12UTC 21 to 12UTC 23 August 2010. The column temperature is a mass-weighted average of the whole atmosphere column.

Table 3-6. Averaged column temperature (°C) from 12UTC 21 to 12UTC 23 August 2010.

ExDO(dust) (°C)	ExO(No dust) (°C)	Differnece(ExDO-ExO) (°C)	Percentage change (%)
-18.539	-18.504	-0.0347	-0.19

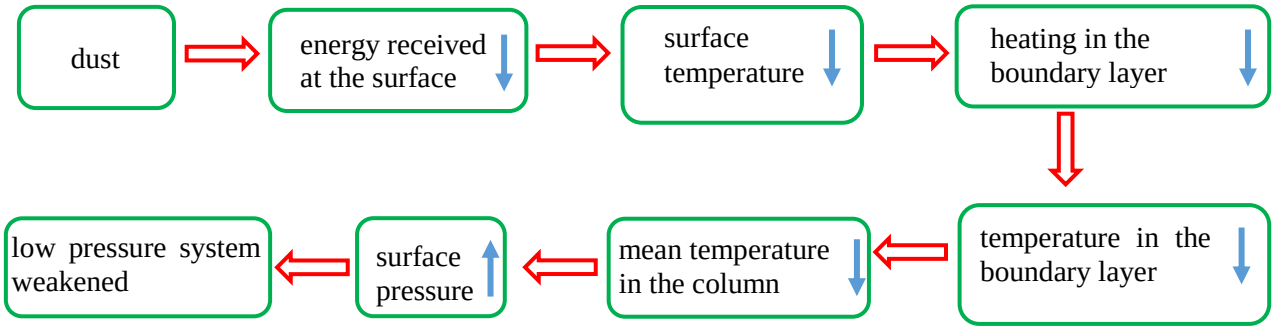

Figure 3-72. The changes of variables due to dust.

3.3.3.2 Dust impacts on AEJ

Hurricane Earl (2010) developed from an AEW disturbance. The origins of the AEW disturbances are believed to be generated by the instability of the AEJ over North Africa (Burpee 1972). AEJ provides energy for the growth of AEW when AEW. Therefore, any changes in AEJ caused by dust may be considered as the first stage of dust effect on tropical cyclones. We decompose the fields into basic states (zonal mean) and perturbations superimposed on them. We first analyze the effect of dust on the basic states of AEJ.

When the zonal wind is averaged between 10^{o}W and 10^{o}E over a period of 5 days (12UTC 21 to 12UTC 26), the AEJ can be identified in the 550-700 hPa layer and between 12.4N-15.7N. Its maximum intensity is about 16m/s (Figure 3-73 a, b). The westerly wind below AEJ is part of the monsoon system. The easterly wind is also present between 22.1^{o}N and 28.6^{o}N where the atmosphere is dry and hot over the Sahara Desert. The mean changes in the troposphere are generally barotropic with a magnitude less than 1 m/s (Figure 3-73c). AEJ is intensified in the south and weakened in the north when the simulation includes dust. It implies a slight southward shift of AEJ. We also notice that the bottom part of AEJ located at around 13 ^{o}N is intensified. The maximum intensification is around 1 m/s at about 750 hPa. The monsoon westerly beneath it is also enhanced by as much as 1 m/s. This increased shear indicates a stronger temperature gradient in the low level.

(a) (b) (c)

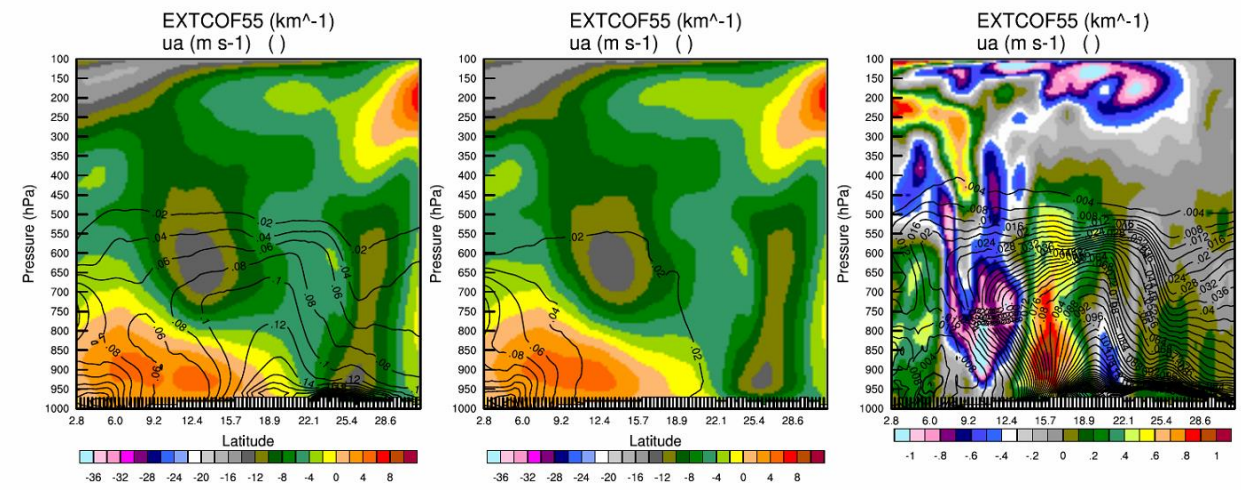

Figure 3-73. The vertical meridional cross sections of 5-day-averaged (from 12UTC 21 to 12UTC 26) zonal mean wind (10W to 10E, shading, m/s) and aerosol extinction coefficient at 550 nm (contour) in (a) Experiment ExDO, (b) Experiment ExO, and (c) their difference (ExDO-ExO).

Figure 3-74 shows the meridional cross-section of the zonal mean potential temperature. The horizontal potential temperature gradient is strongly positive below 600 hPa and slightly negative above it near 13^{o}N (Figure 3-74a, b). It is where the strongest vertical wind shear occurs due to thermal wind balance. The AEJ core is located at around 600 hPa. Looking at the difference in potential temperature (Figure 3-74c), north of 22^{o}N, dust cools the atmosphere up to 600 hPa. Such cooling effect supports our previous analysis that adding dust cools the atmosphere. However, at the same time, dust warms the atmosphere between 600-850 hPa layer south of 22^{o}N.

The analysis in the previous subsections has revealed that on average dust cools the atmosphere in the lower part of the troposphere. The cooling effect appears in the dusty region north of 22^{o}N and south of 17^{o}N. With slight warming in between (Figure 3-74c). The enhanced temperature gradient in the southern branch of the maximum cooling leads to the formation of the

increased vertical wind shear below the AEJ core and the slight southward shift of the AEJ shown in Figure 3-73. However, the weakening of the westerly at around 10°N and the decreased temperature gradient do not match. We have yet to find the exact reason.

(a) (b) (c)

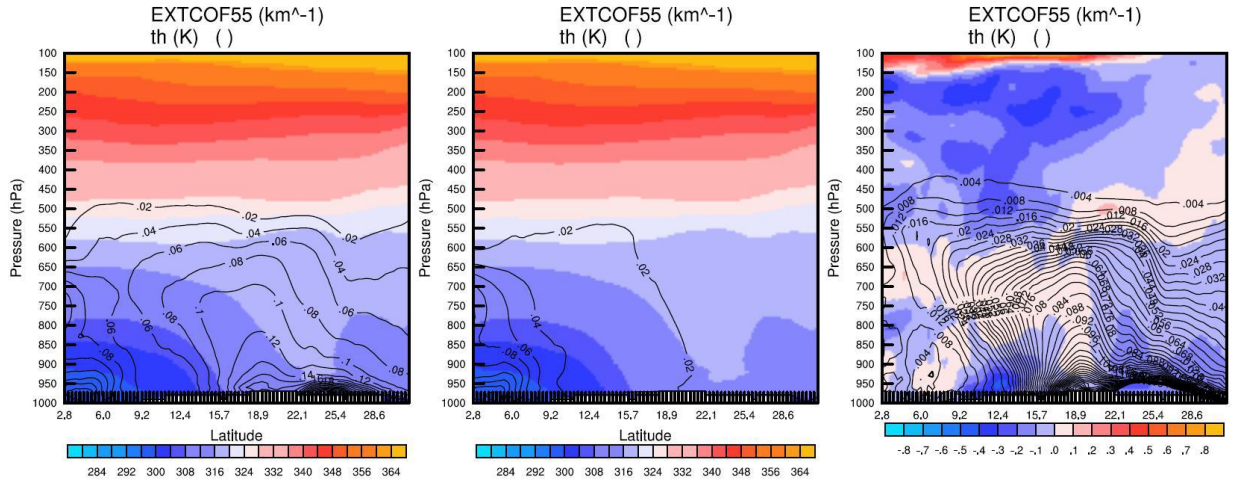

Figure 3-74. Same as Figure 3-73, but shading is for potential temperature(K).

One possible reason is that the impact of dust on the system does not maintain a consistent pattern. For example, the 84-hour forecast shows that adding dust cools most of the area (Figure 3-75c). Similar patterns can be seen before that time (figures not shown). Such cooling effect was discussed in previous sections. After this time, a positive temperature difference primarily due to moist convection grows at 9.2°N and then propagates to 22.1°N. It gradually replaces the negative difference caused by dust cooling effect in the north.

(a) (b) (c)

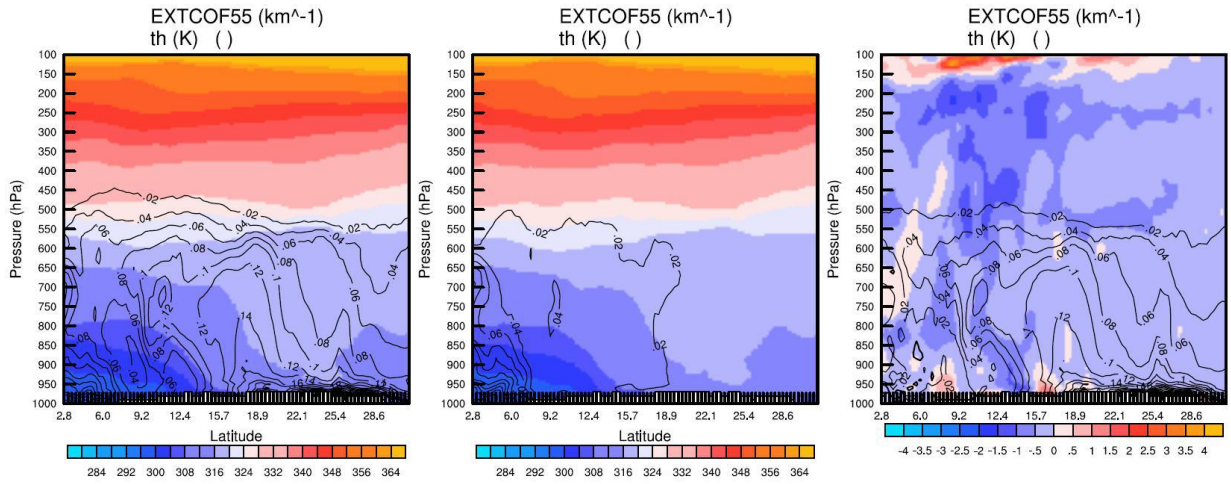

Figure 3-75. The vertical meridional cross sections of the potential temperature (shading, K) and the aerosol extinction coefficient at 550 nm (contour) at 00UTC 25, average between 10W and 10E. (a) Experiment ExDO, (b) Experiment ExO, (c) Difference (ExDO-ExO).

Reale et. al. (2011b) used the NASA GEOS-5 global model to study the impact of aerosols on AEJ. They observed a systematic shift of AEJ to the north and to the higher altitude when the simulation includes aerosols (mainly mineral dust in North Africa) (Figure 3-76 left panel). The 5-day averaged temperature is warmer north of 22^{o}N after adding dust. It increases the temperature gradient and leads to the northward and upward shift of AEJ. The magnitudes of the temperature and the wind changes are less than 1 K and 1 m/s respectively, similar to our findings. However, the changes in their simulations are opposite to that in our case, and the change of temperature in their results is more organized than ours, which might explain an organized change of AEJ.

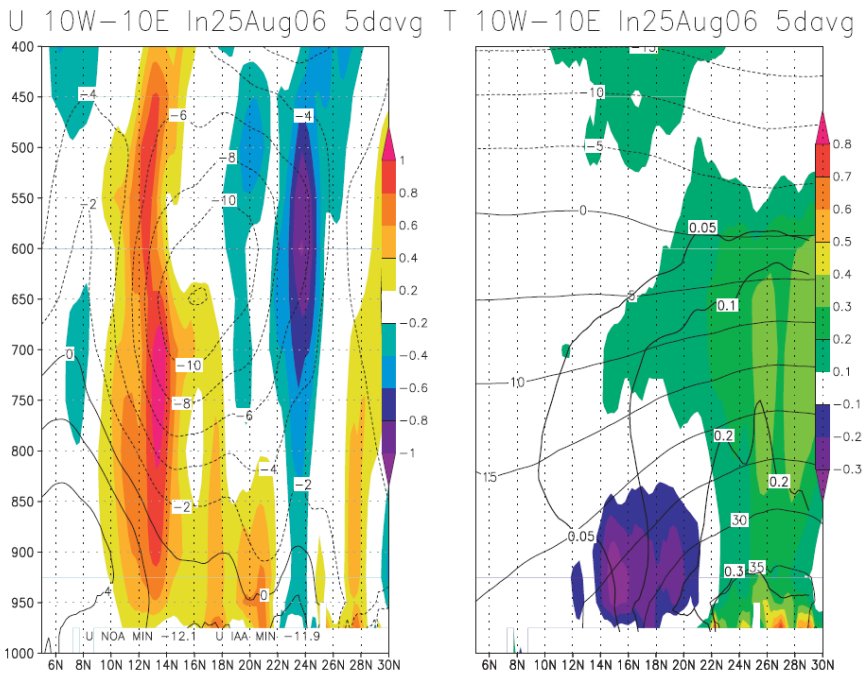

Figure 3-76. Vertical meridional cross sections of (left) 5-day-averaged zonal wind (m/s) and (right) temperature (°C), averaged between 10W and 10E in the GEOS-5NOA$_{25}$ simulation initialized at 0000 UTC 25 Aug 2006. In both panels, solid lines with whole numbers represent NOA $_{25}$ (no aerosols) and the IAA $_{25}$ (with aerosols)-NOA25 differences are color shaded. In the right panel, the solid line with decimal numbers shows the corresponding dust mixing ratio (10^{-6} kg kg^{-1}). Adapted from Oreste Reale, Lau, & da Silva (2011b)

3.3.3.3 Dust impacts AEJ and AEW

Past studies have shown that, under suitable conditions, the AEW can grow by drawing energy from the AEJ (e.g. Burpee 1972; Thorncroft et al. 1994). The zonal and 5-day average of the potential vorticity is positive everywhere except in the south border of the domain (Figure 3-77). In the south, the maximum potential vorticity is between 750 to 300 hPa levels over 9.2°N to 12.4°N.

To its north, the meridional potential vorticity gradient is negative while it is positive to the south. Such pattern satisfies the "Charney-Stern instability criteria" in which the potential vorticity gradient on a constant pressure surface changes sign in the fluid interior while the temperature gradient is close to zero at the lower boundary (Pytharoulis and Thorncroft 1999) (Figure 1-4). AEW can potentially grow at around 600 hPa level.

Over the Sahara region, the strong heating produces strong potential vorticity below 950 hPa. The potential vorticity gradient above 950 hPa is small and helps to maintain the strong negative meridional potential vorticity gradient at around 12.4^{o}N. At the surface, the meridional potential temperature south of 12.4^{o}N is positive (Figure 3-74). As a result, meridional potential vorticity gradient at 600 hPa and meridional potential temperature gradient at the surface have opposite sign and therefore again satisfies the "Charney-Stern instability criteria". Under these conditions, low-level waves may grow by drawing kinetic energy from AEJ. The meridional potential vorticity gradient at AEJ region seems to have not changed after adding dust (Figure 3-77c).

(a) (b) (c)

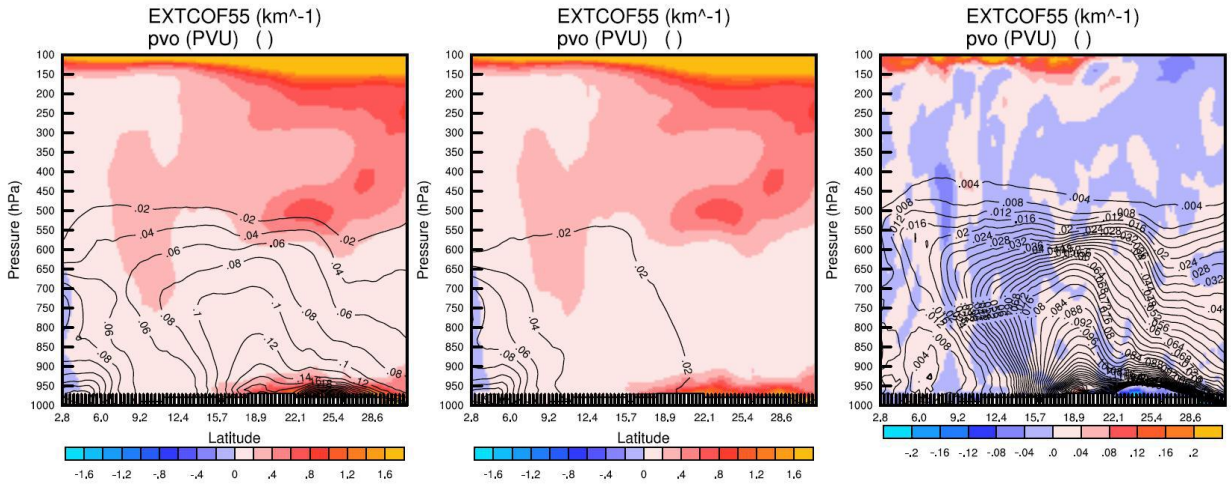

Figure 3-77. Vertical meridional cross sections of 5-day-averaged (from 12UTC 21 to 12UTC 26) potential vorticity (shading) and aerosol extinction coefficient at 550 nm (contour), average between 10W and 10E. (a) Experiment ExDO, (b) Experiment ExO, (c) Difference (ExDO-ExO).

The evolution of the AEW disturbance, the precursor of Earl, at 600 hPa and 850 hPa levels are shown in Figure 3-78. The AEW disturbance at 600 hPa is tracked by following the trough, which can be identified as the local maximum in relative vorticity field at 600hPa (Green and blue lines in the figure). At 850 hPa, AEW has a closed circulation pattern, so its track is found by following the local minimum wind at 850 hPa level from 12UTC 21 to 21UTC 24 and by following the local maximum 850 hPa relative vorticity after 21UTC 24 (magenta and light blue lines in the figure).

When AEW is over land, the trough position at 600 hPa level (9^oN, 2^oE) is to the south of 850 hPa circulation center at (15^oN, 2^oE) (The circulation at 7^oN, 1^oE is not related to our study). This is a typical pattern observed in this region (Ross and Krishnamurti 2007; Thorncroft and Hodges 2001; Pytharoulis and Thorncroft 1999). However, in those studies, AEW at 850 hPa level is located in the north of the average position of AEJ (15^oN). Although AEW can grow as a consequence of both barotropic and baroclinic instability (Thorncroft et al. 1994), the further it is positioned to the north, the more it may show its baroclinic nature because the strong meridional temperature gradient over Sahara interacts with positive meridional potential vorticity above (Pytharoulis and Thorncroft 1999). Since the AEW at 850 hPa level in our case is not positioned far to the north, it may be more barotropic in nature. Finally, we observe that once AEW moves over the ocean, the vertical alignment of the trough at 600 hPa and the center at 850 hPa occurs

(Figure 3-78), similar to what other studies have observed. At 00UTC 24, the disturbance becomes a tropical low, and its circulation extends vertically. At 00UTC 25, it becomes a tropical depression.

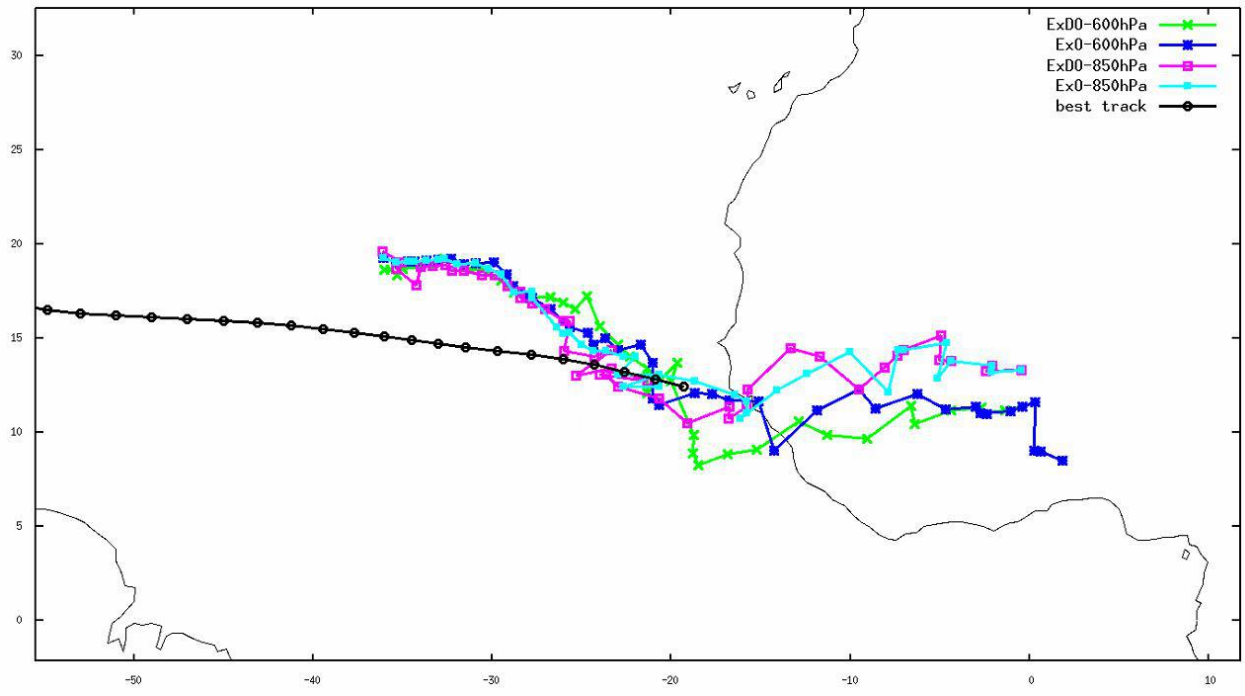

Figure 3-78. Tracks of the convective systems. The Green line is the positions of the maximum relative vorticity at 600 hPa in ExDO; The Blue line is the positions of the maximum relative vorticity at 600 hPa in ExO; The Magenta line is the positions of the minimum wind speed (from 12UTC 21 to 21UTC 24) and the maximum relative vorticity (after 21UTC24) at 850 hPa in ExDO; The cyan line is the positions of the minimum wind speed (from 12UTC 21 to 21UTC 24) and the maximum relative vorticity (after 21UTC24) at 850 hPa in ExO; all begin from 12UTC 21. The black line is the best track from 00UTC 24. The position symbols are plotted every 6 hours.

The intensity of the maximum relative vorticity can be used to indicate the strength of AEW. Hurricane Earl can be traced back to a disturbance at 600 hPa level located at (2^{o}E,9^{o}N) at 12UTC 21 August (

Figure 3-79a, black dot). AEJ can be represented by the dense streamline at 600 hPa, which extends from (20°E, 20°N) in the east to (0°W, 10°N) in the west at 12UTC 21 (

Figure 3-79a). The position of the maximum wind (indicating the intensity of AEJ) around the trough is marked by the green dot.

AEW at 850 hPa has a circulation center at (2°E, 15°N) just beneath the AEJ (

Figure 3-79b). Other studies have shown that AEW at 850 hPa usually forms to the north of AEJ when the baroclinic instability plays a bigger role than barotropic instability. AEW in our case seems to have more barotropic characteristics. The 600 hPa trough is located to the south of the circulation center at 850 hPa, and they move together to the west.

(a) (b)

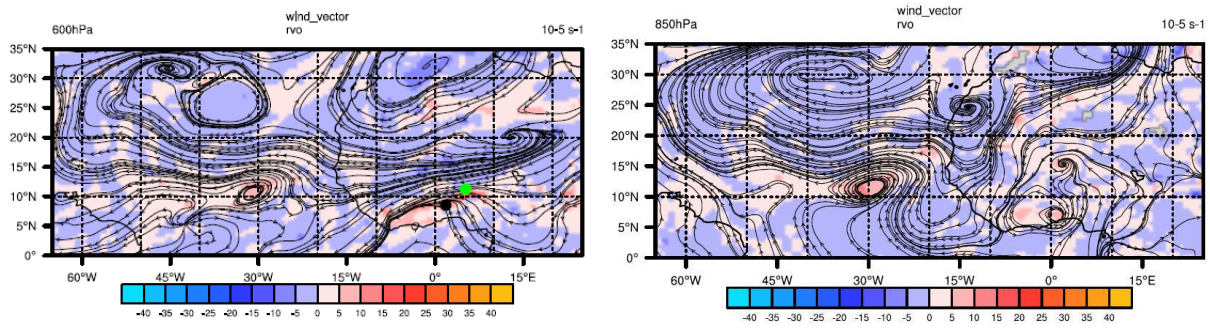

Figure 3-79. Streamline and relative vorticity (shading) at 12UTC 21 (a) at 600 hPa and (b) at 850 hPa. Black dot indicates the local maximum relative vorticity at the trough, green dot indicates position of the maximum wind around the trough.

Figure 3-85 shows that the maximum relative vorticity and the maximum wind at 600 hPa have an upward trend and then a downward trend before 21UTC 22. After the trough moves over the ocean at 06UTC 23, the system begins to intensify because of the increased moisture and latent

heat release (figure not shown). The intensification can be also seen at the 850 hPa level (Figure 3-87).

Dust seems to have no effect to the system during the first 18 hours before 06UTC 22, as the maximum relative vorticity values and maximum wind at 600 hPa are very close in both the experiments ExDO and ExO (Figure 3-80a, b and Figure 3-85). The positions of the circulation center and the maximum wind at 850hPa are also similar between the two experiments (Figure 3-80c, d and Figure 3-87).

However, starting from 09UTC 22, the wave amplitudes and their positions in two experiments begin to show more differences (Figure 3-81 to Figure 3-85). From 12UTC 22 to 12UTC 23, the position of maximum relative vorticity at 600 hPa in ExDO is always on the west or south-west of the position in ExO (Figure 3-81 to Figure 3-83). This indicates that wave grows on the equatorial side of the AEW trough after adding dust. In addition, the position discrepancy gets larger when the system moves closer to the west coast of Africa. This could be due to moisture processes amplify the difference (Figure 3-83).

When AEW moves over the ocean at 00UTC 23, the cyclogenesis occurs (e.g. Thorncroft and Hodges 2001). Dust can sometimes strengthen and sometimes weaken AEW at 850 hPa before 09UTC 23 (Figure 3-87).

(a) (b)

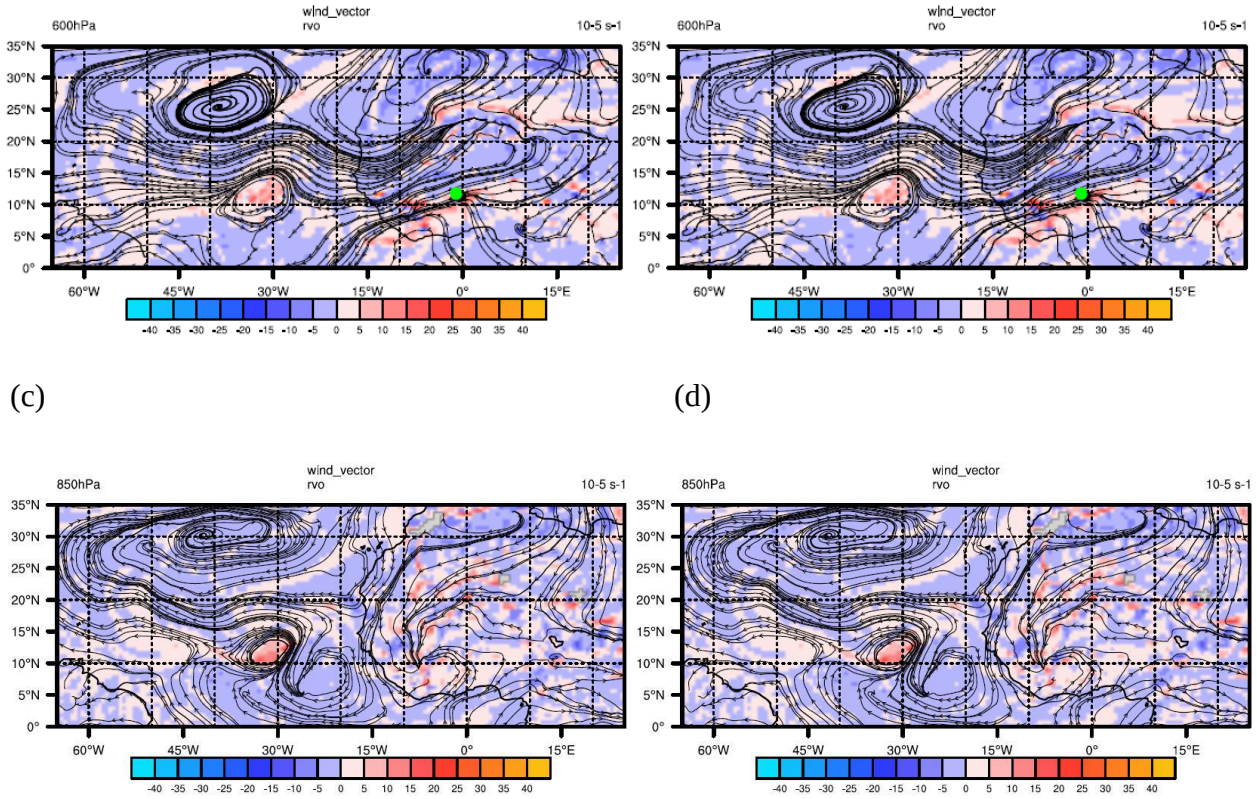

(c) (d)

Figure 3-80. Streamline and relative vorticity (shading) at 00UTC 22. (a) at 600 hPa from ExDO; (b) at 600 hPa from ExO. Black dot indicates the local maximum relative vorticity at the trough, green dot indicates the maximum wind around the trough; (c) at 850 hPa from ExDO; (d) at 850 hPa from ExO.

(a) (b)

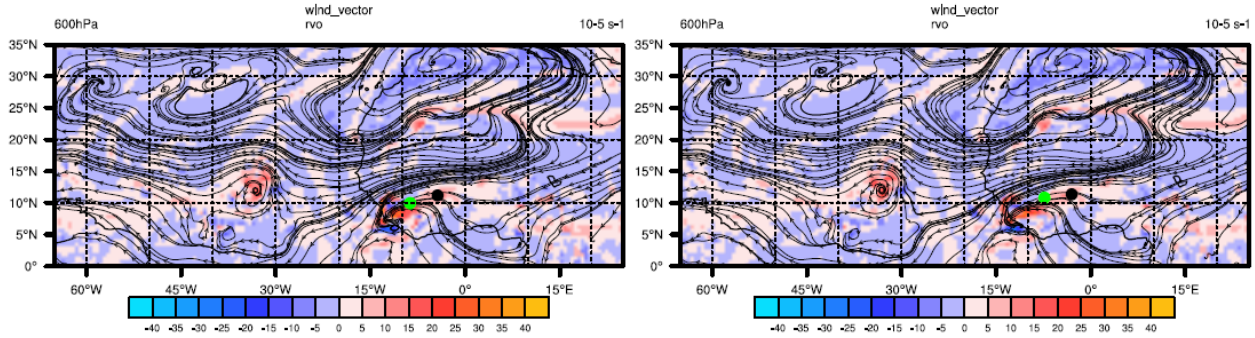

(c)

(d)

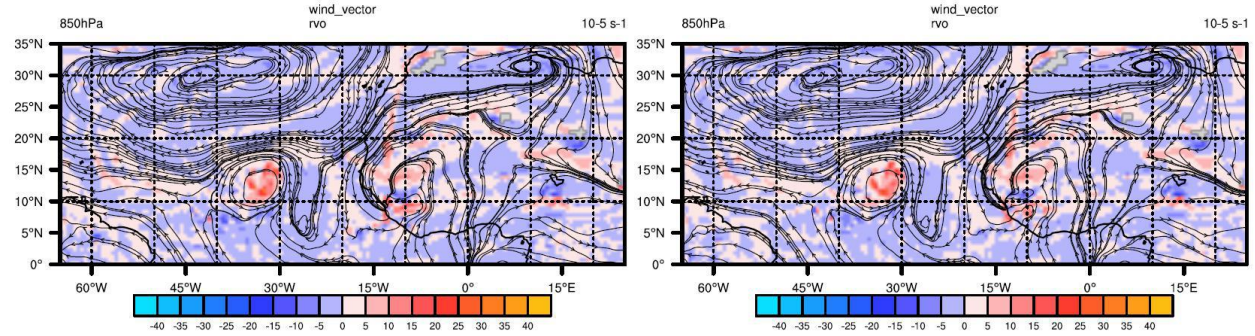

Figure 3-81. Same as Figure 3-80, but at 12UTC 22.

(a)

(b)

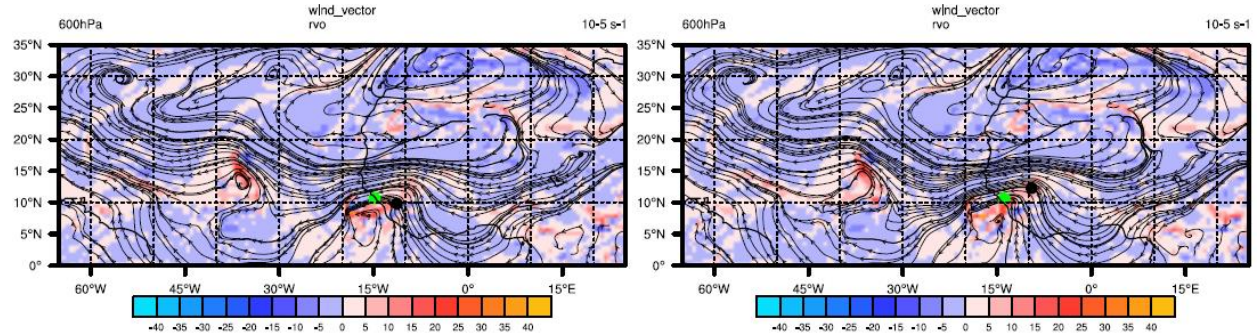

(c)

(d)

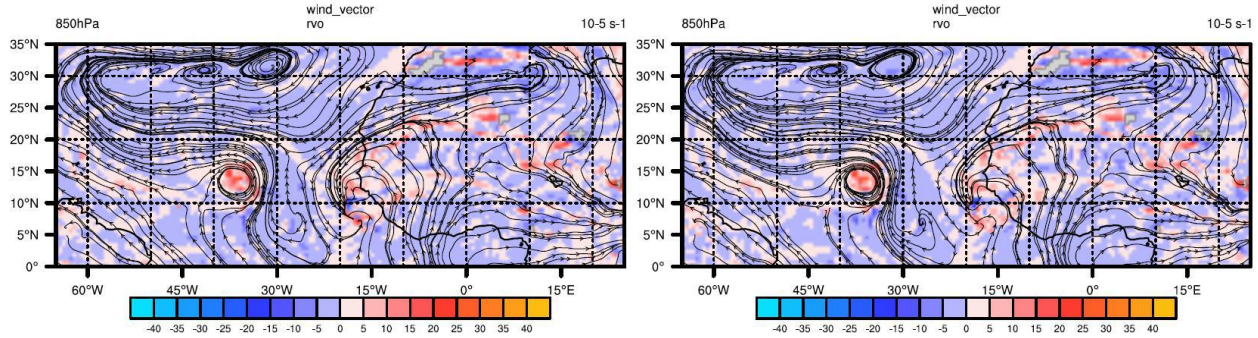

Figure 3-82. Same as Figure 3-80 but at 00UTC 23.

(a) (b)

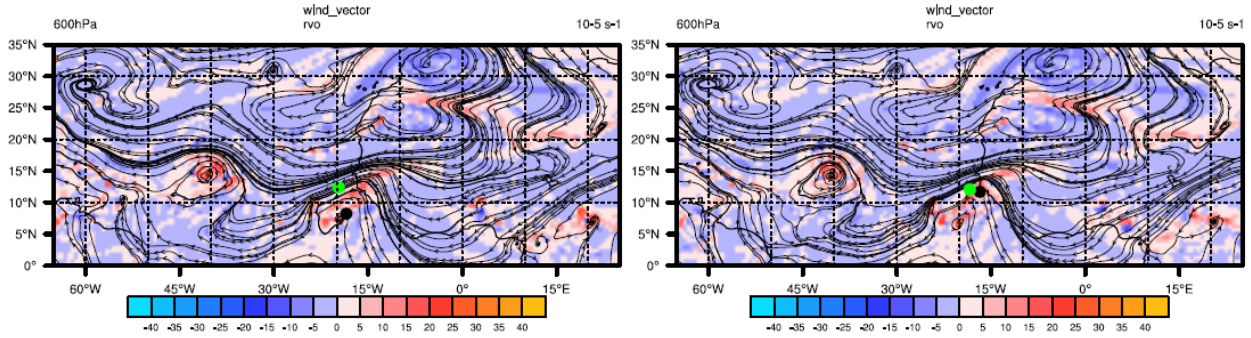

(c) (d)

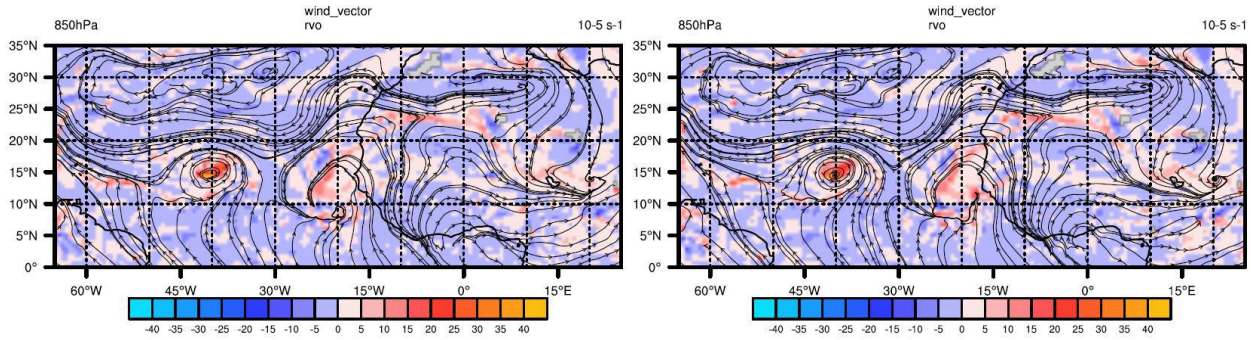

Figure 3-83. Same as Figure 3-80 but at 12UTC 23.

After 09UTC 23, the maximum wind speed at 600 hPa takes the upward trend, which indicates that the system is growing by gaining significant energy from release latent heat (Figure 3-85). The maximum relative vorticity and the maximum wind speed near the 600 hPa trough in ExDO are smaller than that in ExO (

Figure 3-84a, b, Figure 3-85 and Figure 3-86).

The intensity of AEW at 850 hPa is weaker in ExDO as well after 09UTC 23, indicated by the reduction of the maximum wind speed if dust is added into the simulation (Figure 3-87). Thus,

dust reduces the intensity of the convective system just before the tropical low forms, and the system continues to weaken during its remaining lifetime.

(a) (b)

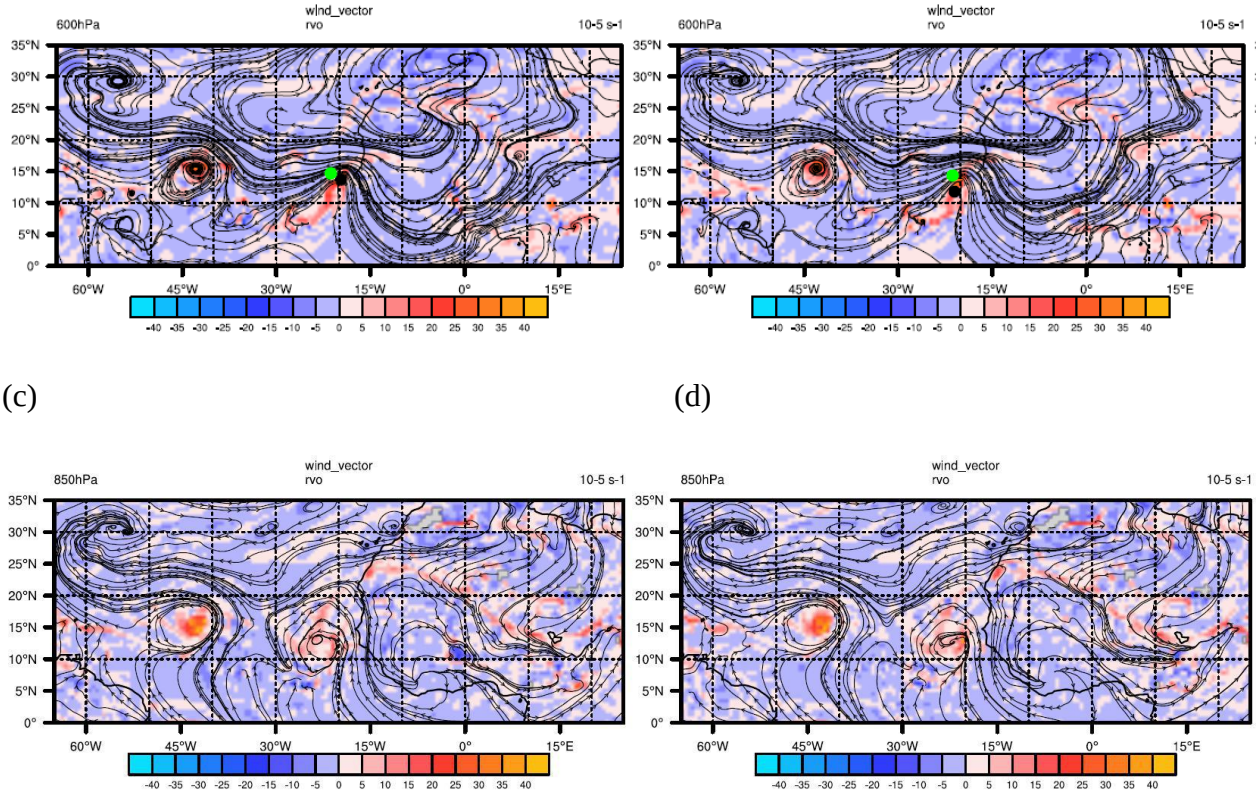

(c) (d)

Figure 3-84. Same as Figure 3-80, but at 00UTC 24.

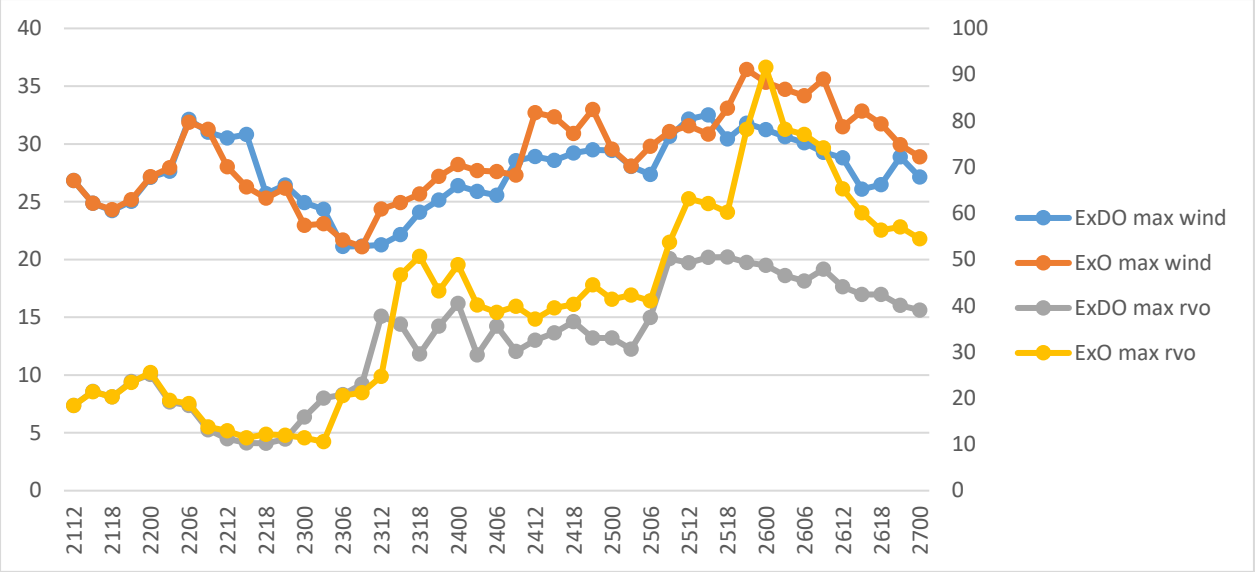

Figure 3-85. Time series of the maximum wind speed and the maximum relative vorticity at 600 hPa in ExDO and ExO.

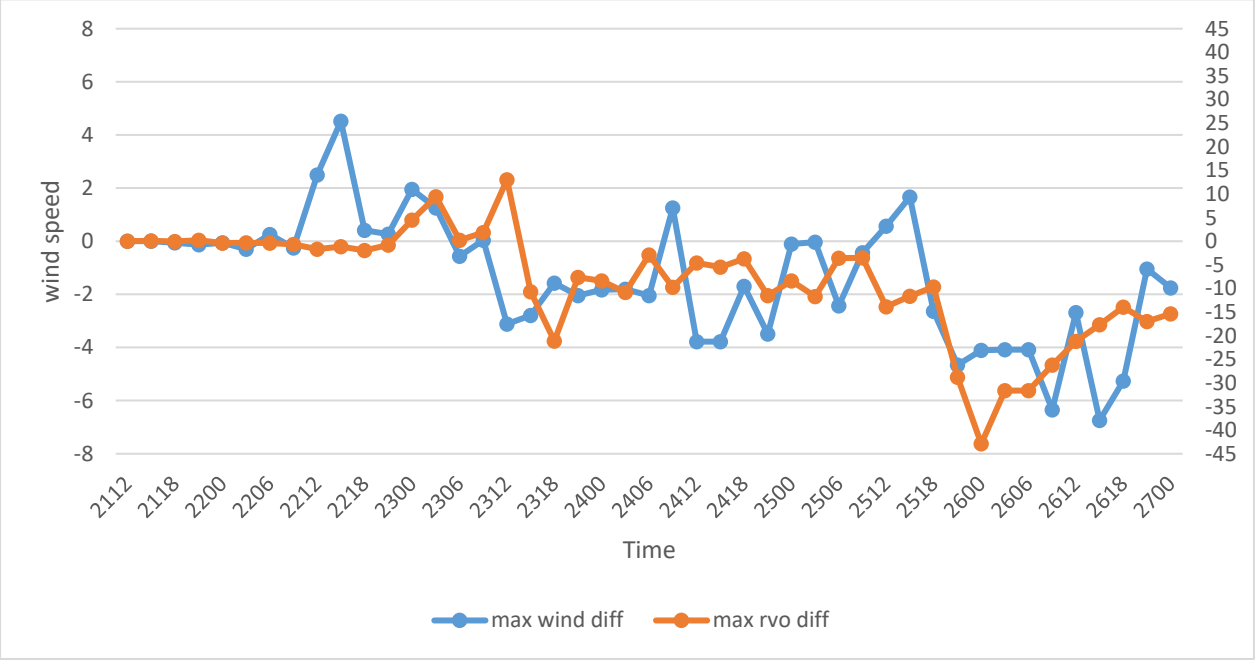

Figure 3-86. Time series of the maximum wind speed and the maximum relative vorticity differences at 600 hPa between ExDO and ExO (ExDO-ExO). Y-axis on the left is the value for wind speed difference, and Y-axis on the right is for relative vorticity difference.

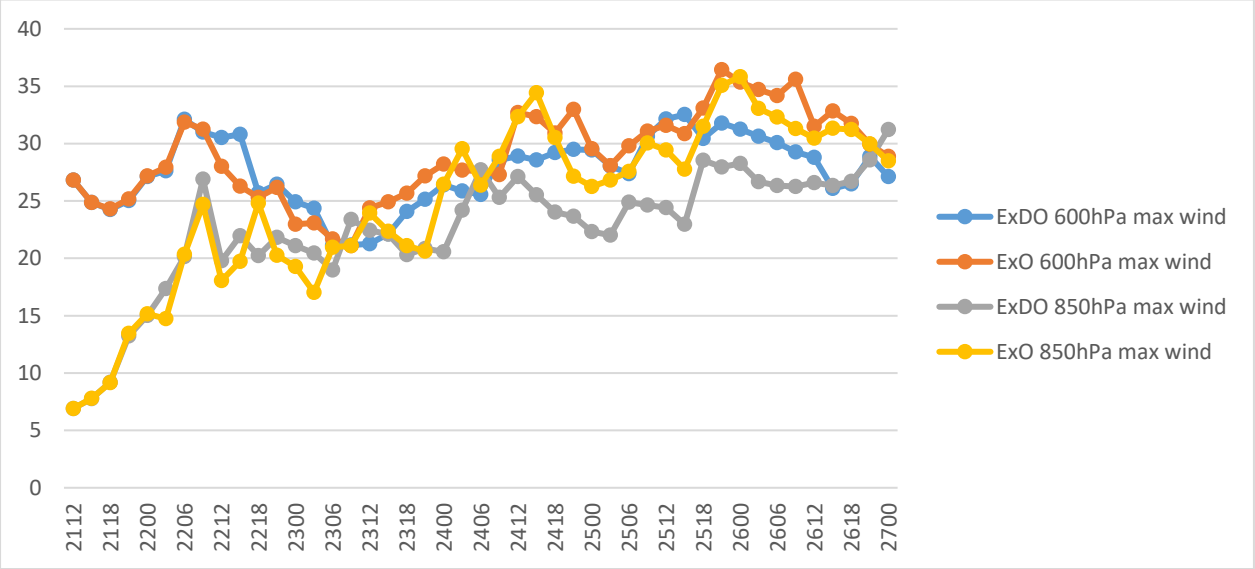

Figure 3-87. Time series of the maximum wind speed at 600 hPa and 850 hPa in ExDO and ExO.

In summary of this section, hurricane Earl can be traced back to the AEW originated in Africa. AEW at 600 hPa level is located to the south of AEJ while AEW at 850 hPa is just below AEJ. The waves are found to be more susceptible to barotropic instability.

AEW at 600 hPa decays gradually before it moves to the ocean where it benefits from the abundant moisture. AEW at 600 hPa southward slightly after adding dust. Figure 3-86 shows that, compared to the no dust experiment, the intensity of AEW (maximum relative vorticity) changes little at the beginning, then increases, and finally decreases. At the same time, adding dust increases AEJ intensity at the beginning, and decreases it later as indicated by the change of the maximum wind at 600 hPa.

AEW at 850 hPa generally increases as it moves to the west due to the availability of more moisture. Adding dust strengthens AEW at first, then weakens it later, shown by the maximum 850 hPa wind (Figure 3-87).

Overall, the convective system becomes weaker when dust is added in the model.

3.3.3.4 Dust impacts the tropical low and the tropical depression

The AEW we analyzed above continues to move over the ocean and develops into a tropical low and then into a tropical depression. When the system moves over the ocean, moisture processes become more important. The previous simulations (ExDO and ExO) have used both cumulus and microphysics schemes. With a horizontal resolution of 36 km, convective moist processes represented by the cumulus parameterization scheme. The microphysics scheme contributes less. However, once the system moves over the ocean, accurate representation of the microphysics processes becomes essential, particularly when the dust aerosols indirect effect need to be considered. It is therefore necessary to increase the model horizontal resolution and to resolve the clouds explicitly.

3.3.3.4.1 High resolution model configuration

Four nested higher resolution simulations are launched at 00UTC 23 August before the low-pressure system reaches the ocean (Table 3-7). Figure 3-88 shows the nested domain with a horizontal resolution of 4 km. One-way nest strategy is used. A WRF utility program called "ndown" is applied to generate high resolution initial and boundary conditions from the coarse resolution simulation output.

The experiment ExC-H is a high-resolution counterpart of ExC. It uses the interpolated output of ExC from 00UTC 23 to 00UTC 27 as the initial and boundary conditions. The cumulus scheme is turned off. In addition, the chemistry scheme is turned off.

Similarly, the experiment ExDO-H is a high-resolution counterpart of ExDO, its initial and boundary conditions are from ExDO. It considers all the aerosols including dust.

The experiment ExO-H is a high-resolution counterpart of ExO. It includes all aerosols except dust.

In previous sections, we compared the results from ExDO and ExO to investigate the radiative effect of dust and its impact on AEW and AEJ when the convective system was over land. When the system moves over the ocean, we now compare higher resolution simulations (ExDO-H and ExO-H) to investigate the radiative effect and microphysical effect of dust on the tropical low and the tropical depression.

Finally, we conduct high-resolution simulation ExDO-H-TurnoffDust and compare it to ExDO-H. As indicated in the previous section, ExDO-H-TurnoffDust has the same configuration as ExDO-H, except that it does not have dust in its initial and boundary conditions. We are interested in studying whether removing dust can have impacts on the development of the system given the identical initial conditions except for dust. We want to emphasize that ExDO-H-TurnoffDust is different from ExO-H. Although both do not contain dust, they obtain their initial and boundary conditions from different "parent" simulations.

In the following sections, we first analyze ExC-H, ExDO-H, and ExO-H, and then we compare them to ExDO and ExO presented previously. Then we compare ExDO-H and ExDO-H-TurnoffDust.

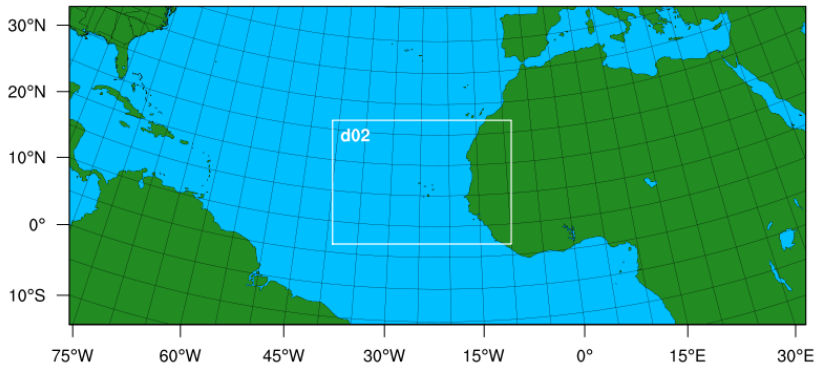

Figure 3-88. Model domain, rectangular frame d02 indicates the nested domain.

Table 3-7. Experiment set up for the higher resolution simulations.

Experiment	Chemistry scheme	Start time	Initial and boundary condition	Dust	Other aerosols	Cumulus scheme	Microphysics scheme
ExC-H	No	00UTC 23	From ExC	No	No	No	Yes
ExDO-H	Yes	00UTC 23	From ExDO	Yes	Yes	No	Yes
ExDO-H-TurnoffDust	Yes	00UTC 23	From ExDO	No	Yes	No	Yes
ExO-H	Yes	00UTC 23	From ExO	No	Yes	No	Yes

3.3.3.4.2 Model evaluation

The hurricane tracks in the high resolution simulations are obtained by following the position of the minimum surface wind from 00UTC 24 to 18UTC 24 because the system is weak at the

beginning, and the position of the minimum pressure is not necessarily the center of the system. After 18UTC 24, the position of minimum sea level pressure is used as the tracking criteria.

Before 03UTC 25, when the system is located around 17ºN, 27ºW, the tracks from all higher resolution simulations are located to the south of their 'parent' 36-km resolution simulations (ExDO and ExO) (Figure 3-89). Then their tracks move closer to ExDO and ExO. Overall, the 4-km resolution simulations produce tracks that are not worse than the tracks in the 36-km resolution simulations.

However, the central sea level pressure values in 4-km simulations are all higher than those in the 36-km resolution simulations, and they are closer to the observation (Figure 3-90). For experiments ExC and ExC-H, the error of the central pressure is reduced by 58% in the higher resolution. Similarly, 4-km resolution simulations have better forecasts of the maximum surface wind speed than 36-km resolution simulations. The error is reduced by 46%. Thus, the intensity prediction has been improved by increasing the model resolution.

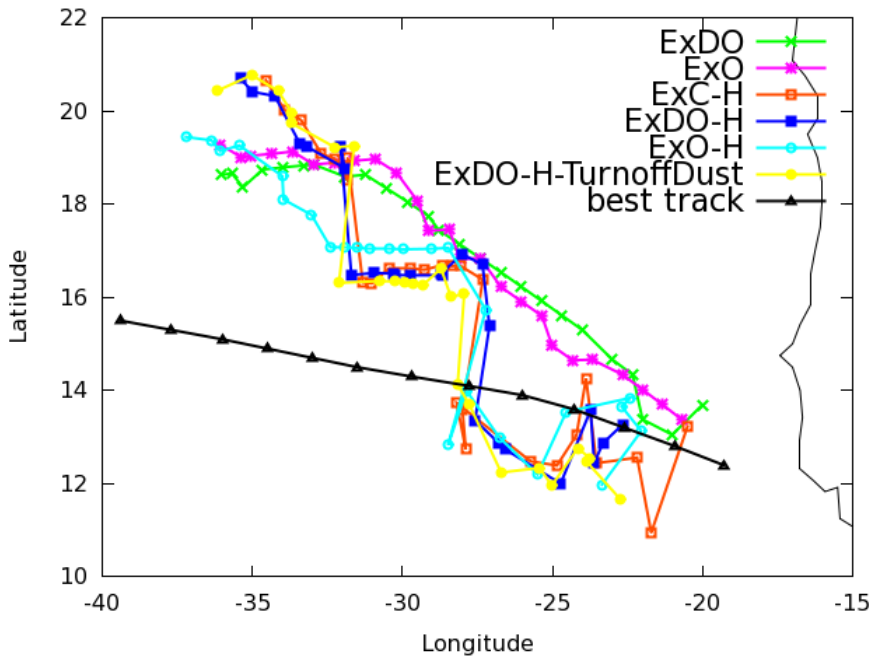

Figure 3-89. Tropical convective system tracks. The best track positions are in 6 hours intervals. Other tracks are in 3hour intervals.

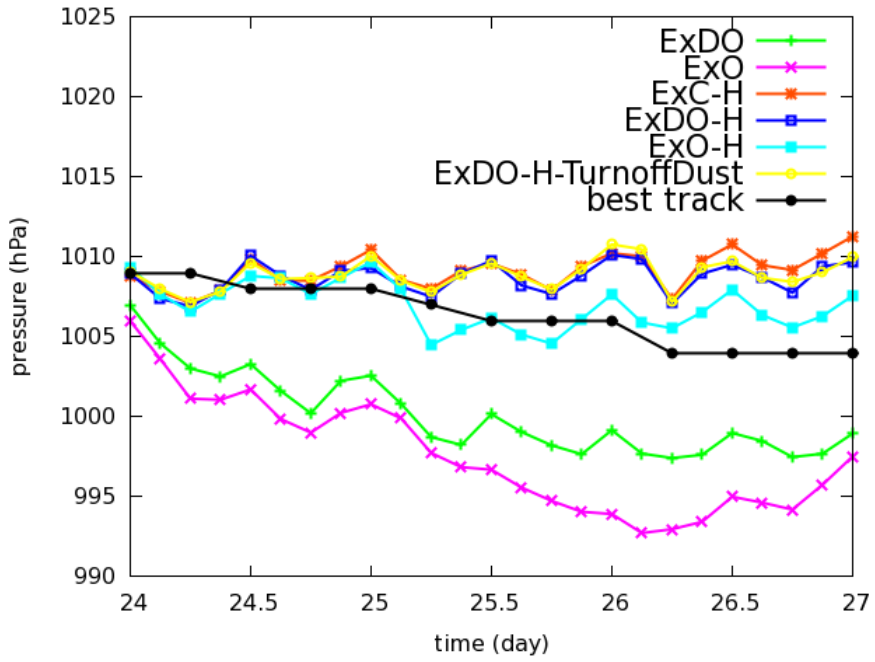

Figure 3-90. Minimum sea level pressure (hPa). The x-axis represents days. The best track data are in 6 hours intervals. Other data are in 3 hours intervals.

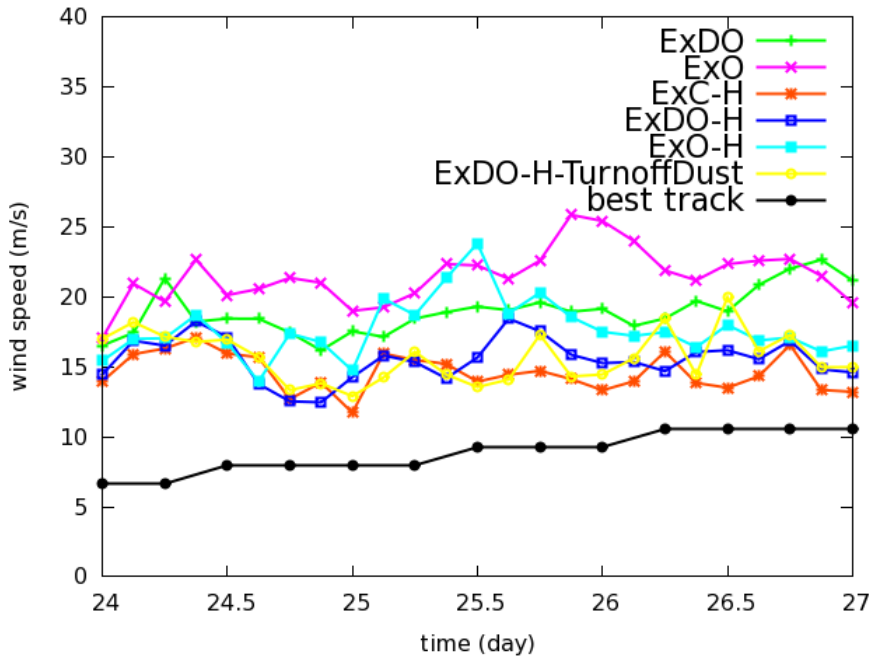

Figure 3-91. Maximum surface wind speed (m/s). The x-axis represents days. The best track data are in 6 -hour intervals. Other data are in 3-hour intervals.

3.3.3.4.3 Development of the tropical low and the tropical depression

Tropical low begins to form at 00UTC 24 as indicated by NHC forecast (Figure 3-92). The difference in the sea level pressure from the two experiments shows that the system in ExDO-H is weaker than that in ExO-H (Figure 3-92c). It is consistent with our analysis of the AEW

development in the coarse resolution simulations ExDO and ExO. The weaker system is a result of adding dust into the model at the beginning when the system is in the form of AEW over Africa. From 12UTC 21 to 00UTC 24, the system gets weaker because of dust.

The system remains stable between 00UTC 24 and 00UTC 25 in both experiments ExDO-H and ExO-H. But the center positions and the locations of the maximum 10-wind fluctuate (Figure 3-90 to Figure 3-93).

(a) (b) (c)

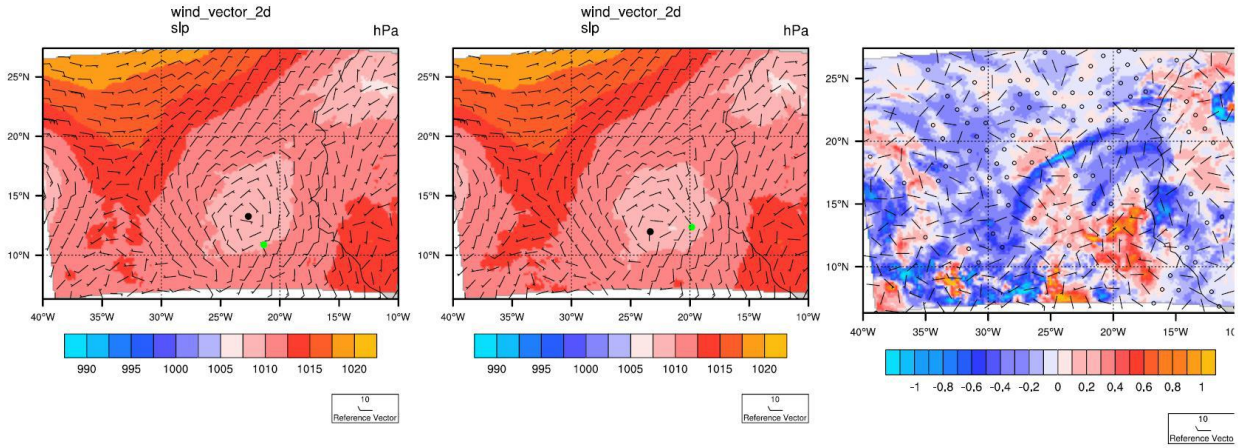

Figure 3-92. Sea level pressure (shading) and wind bars at 00UTC 24 from the simulation. (a) ExDO-H, (b) ExO-H, and (c) ExDO-H minus ExO-H. Black dot indicates center position and green dot indicates maximum 10-meter wind.

(a) (b) (c)

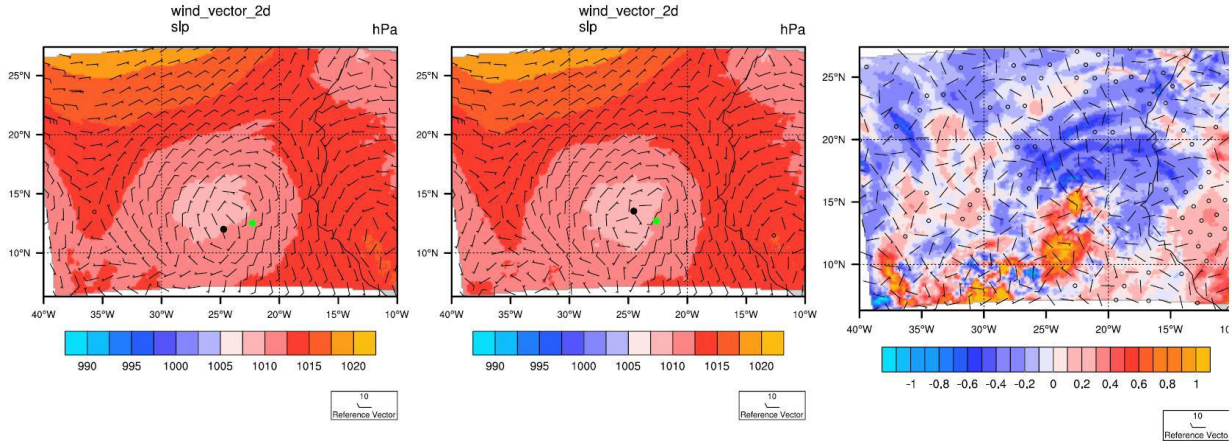

Figure 3-93. Same as Figure 3-92 but at 12UTC 24.

At 00UTC 25, the system starts to deepen quickly. Its pressure drops and wind speed increases (Figure 3-90 and Figure 3-91). The area of low pressure at the center shrinks in ExDO-H (Figure 3-94a). This rapid development corresponds to the tropical depression stage. The system in the simulation reaches this stage 12 hours earlier than the observed time-12UTC 25 reported by NHC forecast.

The intensity fluctuates after becoming the tropical depression (Figure 3-90and Figure 3-91). The system in ExDO-H is always weaker than that in ExO-H (Figure 3-95 and Figure 3-96).

(a) (b) (c)

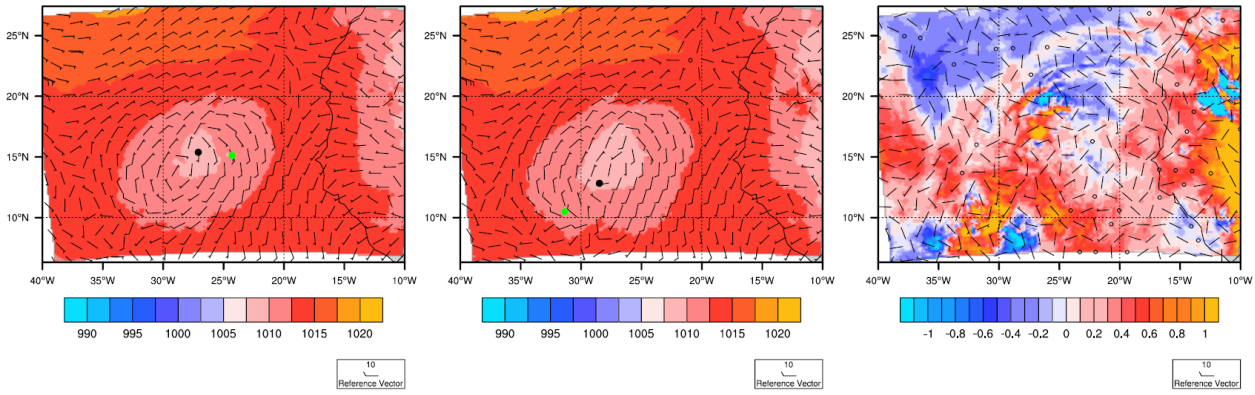

Figure 3-94. Same as Figure 3-92 but at 00UTC 25.

(a) (b) (c)

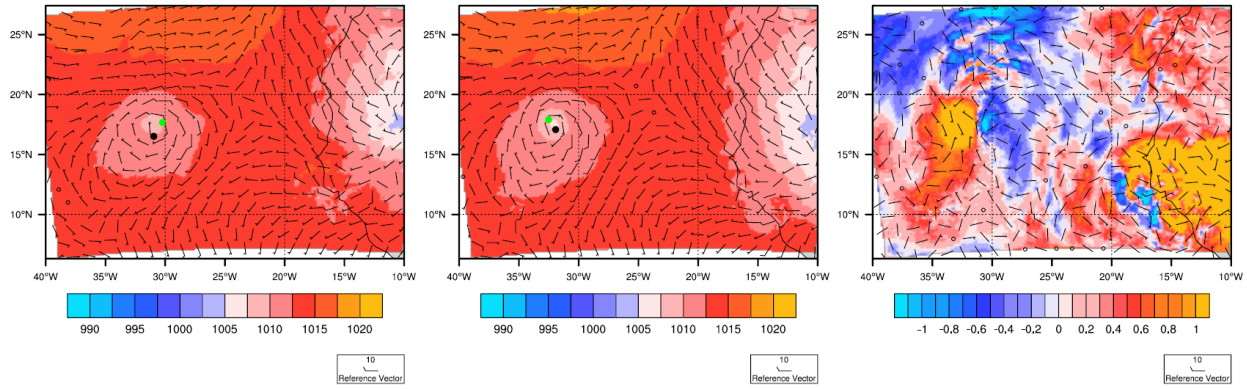

Figure 3-95. same as Figure 3-92 but at 00UTC 26.

(a) (b) (c)

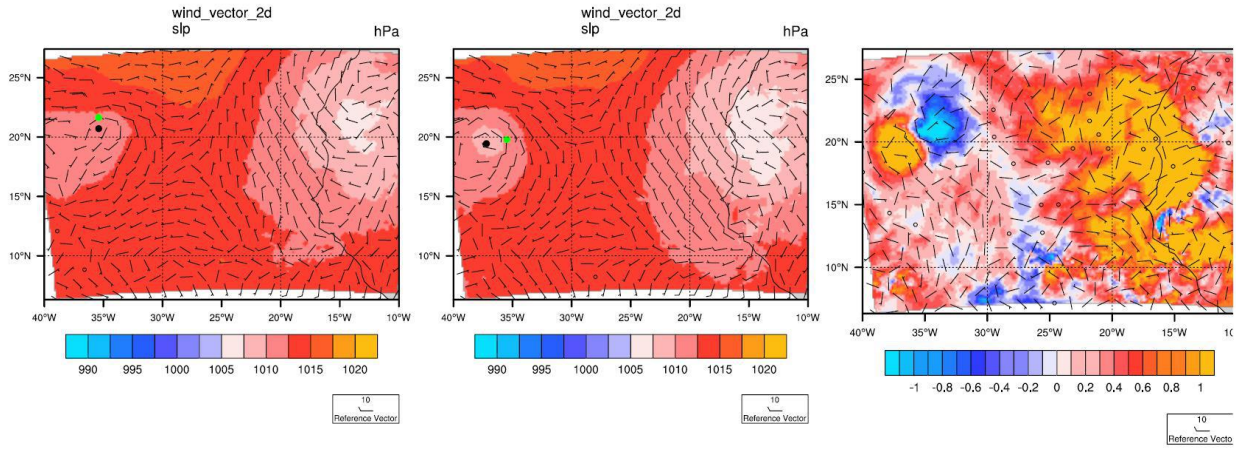

Figure 3-96. Same as Figure 3-92 but at 00UTC 27.

3.3.3.4.4 Dust impacts microphysics and dynamics

The 4-km high-resolution simulations we compared above (ExDO-H and ExO-H) are based on their 'parent' 36-km resolution simulations (ExDO and ExO). Since the 36-km resolution simulations started at 12UTC 21, 60-hour simulations have been performed when the 4-km nested run starts. The differences between these two high resolution simulations arise not only from the differences in aerosols but also from meteorological fields. To isolate the effect of dust on the dynamic and microphysical processes of the convective system, we launch another high resolution simulation as mentioned in Table 3-7. The experiment ExDO-H-TurnoffDust uses the same initial and boundary conditions as ExDO-H except that the dust aerosols are removed.

The AOD and sea level pressure for these experiments are shown in Figure 3-97 to Figure 3-100. At the beginning of the simulation at 00UTC 23, dust indicated by large AOD is present in the center of the low-pressure system (Figure 3-97a). One day later in the tropical low stage, at

00UTC 24, both dust and other aerosols increase in the atmosphere, and they still occupy the center of the system (Figure 3-98a). At 00UTC 25, when the system becomes a tropical depression, some dust aerosols are carried by the circulation and wrapped around the center (Figure 3-99a). At 00UTC 26, the system continues to move to the west. Some dust remains inside the system, while the transport of dust from the north-east direction is cut-off. Thus, the system is less influenced by dust (Figure 3-100a).

Although dust stays inside and around the system for several days, its impact on the system is limited. Dust barely changes the dynamical behavior of the system. Removing dust aerosols produces almost identical tracks (Figure 3-89). The central pressure of the system becomes higher in the tropical depression stage when dust is removed, but the difference is small (less than 1 hPa) (Figure 3-90). The maximum wind speed fluctuates, and the differences between the two experiments can reach 5 m/s after two days. But considering it is a single grid point value, the difference may be overemphasized. Overall, dust has little effect on the dynamics of this tropical system. In typhoon aerosol simulation papers (Jiang et al. 2016; Shen 2017), they also found that increasing pollutant concentration does not affect the typhoon circulation in its mature stage.

(a) (b)

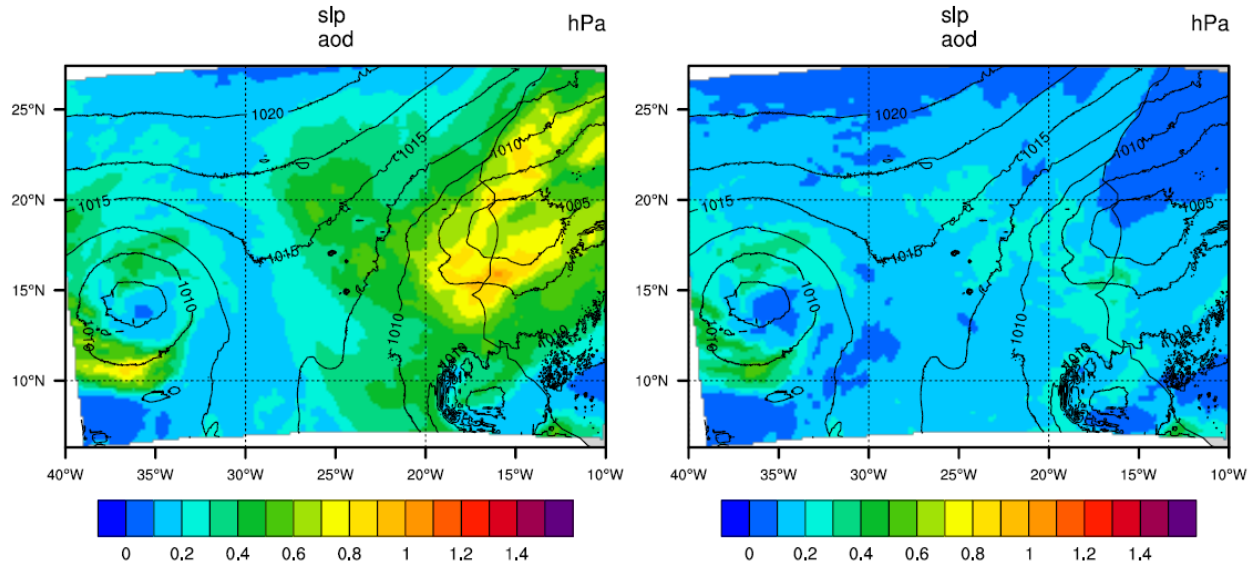

Figure 3-97. Aerosol optical depth (Shading) and sea level pressure (contour, hPa) from the model at 00UTC 23 for (a) ExDO-H and (b) ExDO-H-TurnoffDust

(a) (b)

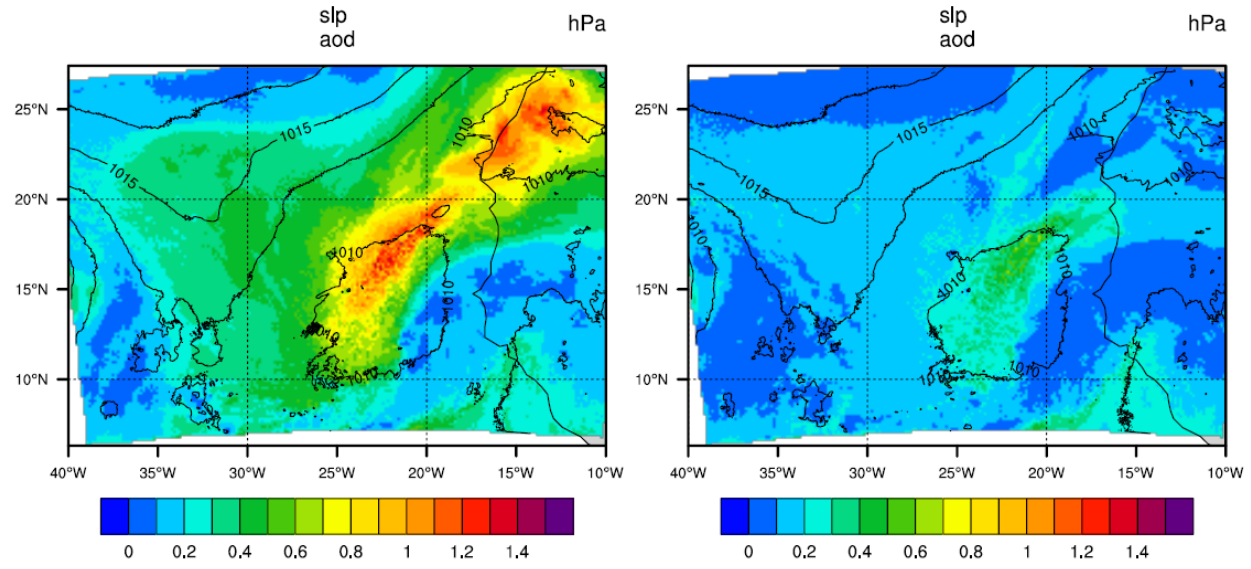

Figure 3-98. Same as Figure 3-97 but at 00UTC 24.

(a) (b)

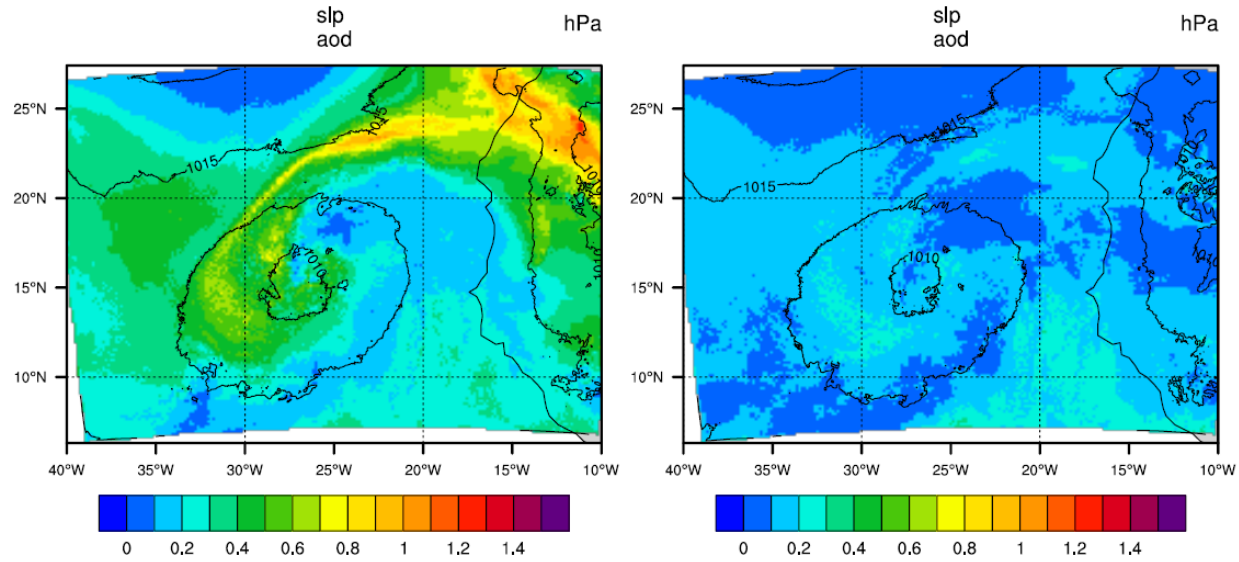

Figure 3-99. Same as Figure 3-97 but at 00UTC 25.

(a) (b)

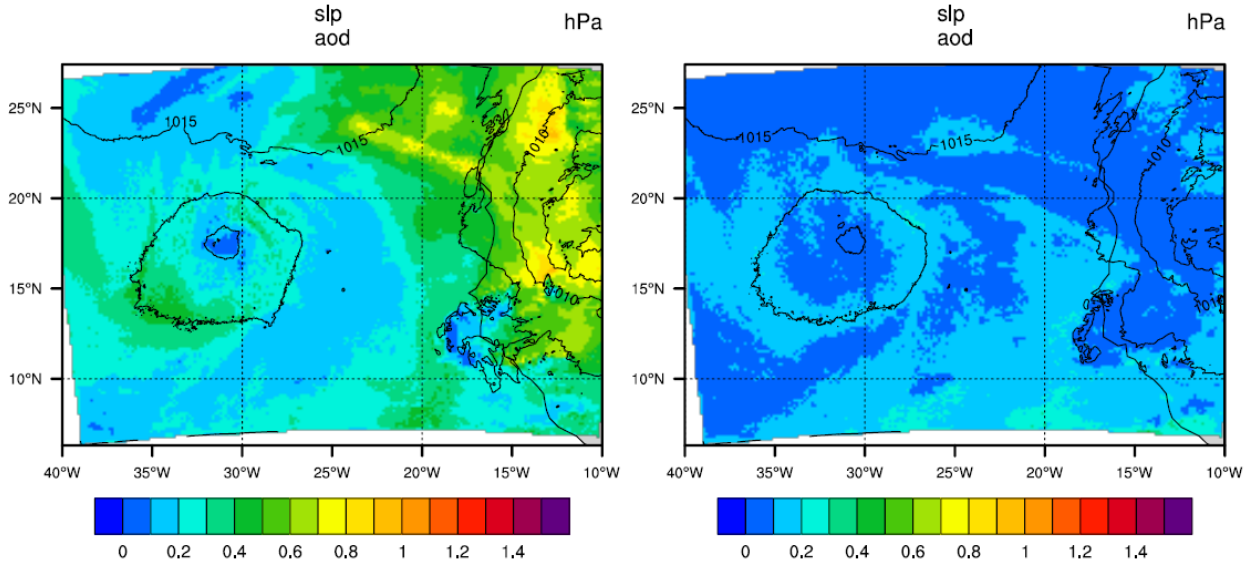

Figure 3-100. Same as Figure 3-97 but at 00UTC 26.

Although dust seems to have little impact on the intensity and track of the system, it is still important to understand its effects on the dynamics and microphysical processes in detail.

At the beginning of the higher resolution simulations at 00UTC 23, the low-pressure center with a minimum sea-level pressure of 1002.6 hPa is located over the land (Figure 3-101a). When it moves westward, it is weakened (Figure 3-101b). At 12 UTC 23, the minimum sea-level pressure rises to 1006.3 hPa. At 18UTC 23, the circulation at the surface appears to the south of 15N (Figure 3-101c). The minimum sea-level pressure associated with it is 1008 hPa. The southwest-ward jump of the surface low-pressure center is caused by the decay of the low-pressure system in the north and the new development of a surface low in the south. We will discuss this in detail.

As shown in Figure 3-78 to Figure 3-82, AEW at 850 hPa has a circulation pattern, and it moves continuously from the east to the west. The AEW trough at 600 hPa and the 850 hPa circulation aligned vertically when they moved over to the ocean. AEW at low levels leads to the surface cyclogenesis (e.g. Thorncroft and Hodges 2001). Therefore, we can use the maximum wind at 850 hPa to track the tropical cyclone at this later stage.

(a) (b) (c)

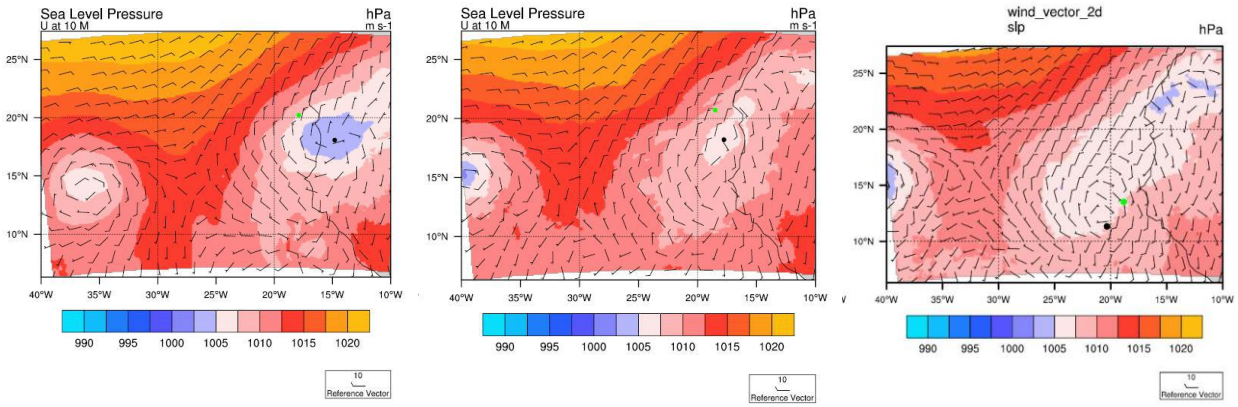

Figure 3-101. Sea level pressure (shading) and wind barbs in ExDO-H-TurnoffDust. (a) 00UTC 23, (b) 12UTC 23, (c) 18UTC 23. Black dot is the center of the circulation. Green dot is the position of the maximum wind around the center.

Figure 3-102 shows that the maximum wind speed at 850 hPa is larger than that at the surface. It is usually true before a tropical cyclone becomes a mature hurricane. When the system is over the ocean after 18UTC23, the maximum wind speeds at the 850 hPa and at the surface follow each other. Their correlation is 0.6. The maximum wind speed changes at 850 hPa and at the surface due to dust are also similar. As a result, it further confirms that the maximum wind speed at 850 hPa can be an indicator of the storm intensity.

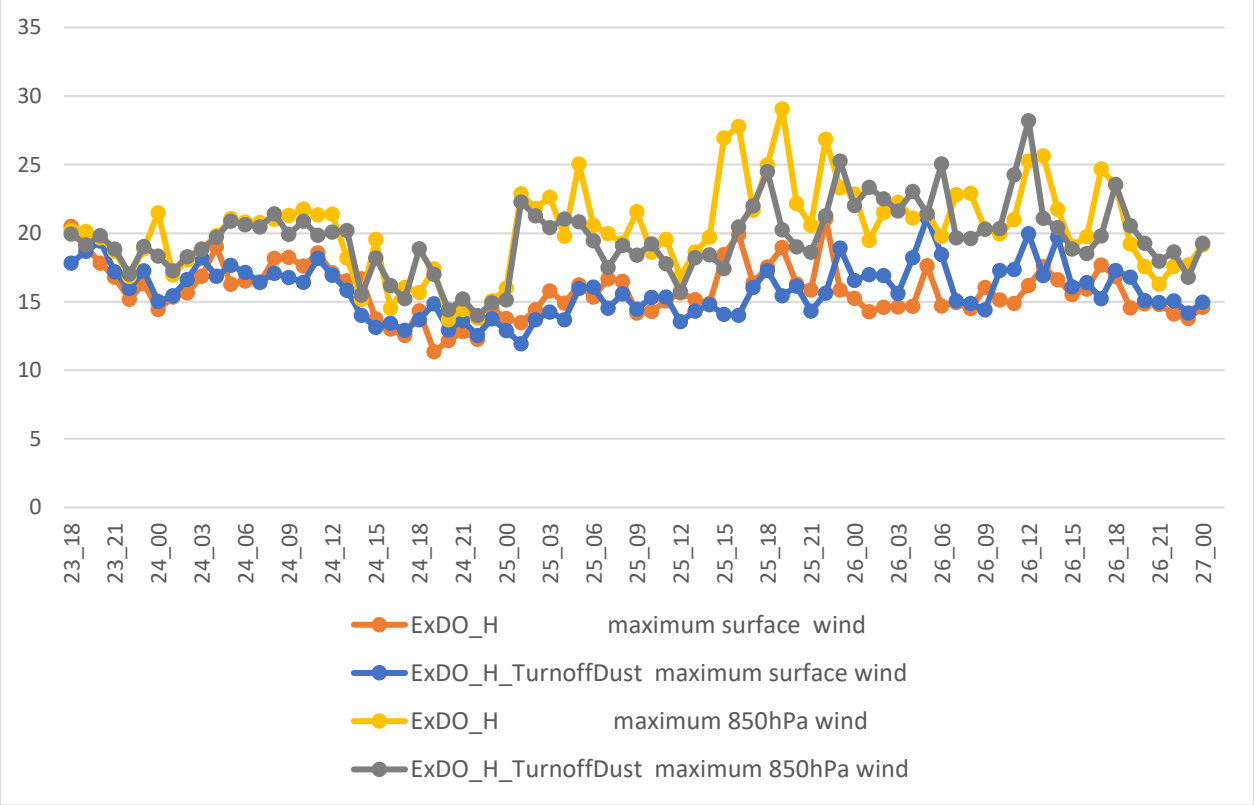

Figure 3-102. The maximum wind speed at the surface and 850 hPa in different experiments.

The NHC reported that the system became tropical low at 00UTC 24 and tropical depression at 12UTC 25. However, our simulation shows that the storm experiences stronger development at 00UTC 25. Therefore, we divided the evolution of the system into three stages: (1) prior to the tropical low stage from 00UTC 23 to 00UTC 24, (2) tropical low stage from 00UTC 24 to 00UTC 25, and (3) tropical depression stage after 00UTC 25. We will analyze the storm structure and how dust changes it in different stages.

A. Prior to tropical low stage

The high-resolution simulation is initialized at 00UTC 23. Within the first 24 hours, the simulated system undergoes the spin-up process in which the dynamic and thermodynamic fields are adjusted toward a new balance.

Figure 3-103 shows the maximum wind speed at 850 hPa. The maximum wind speed at 850 hPa is reduced in the first 12 hours at the higher resolution simulations, suggesting the spin-up process takes about 12 hours. Turning off the dust process from the beginning of the simulation may only add insignificant influence that has been overwhelmed by the spin-up process. Thus, we leave the analysis of dust impact at the later stages.

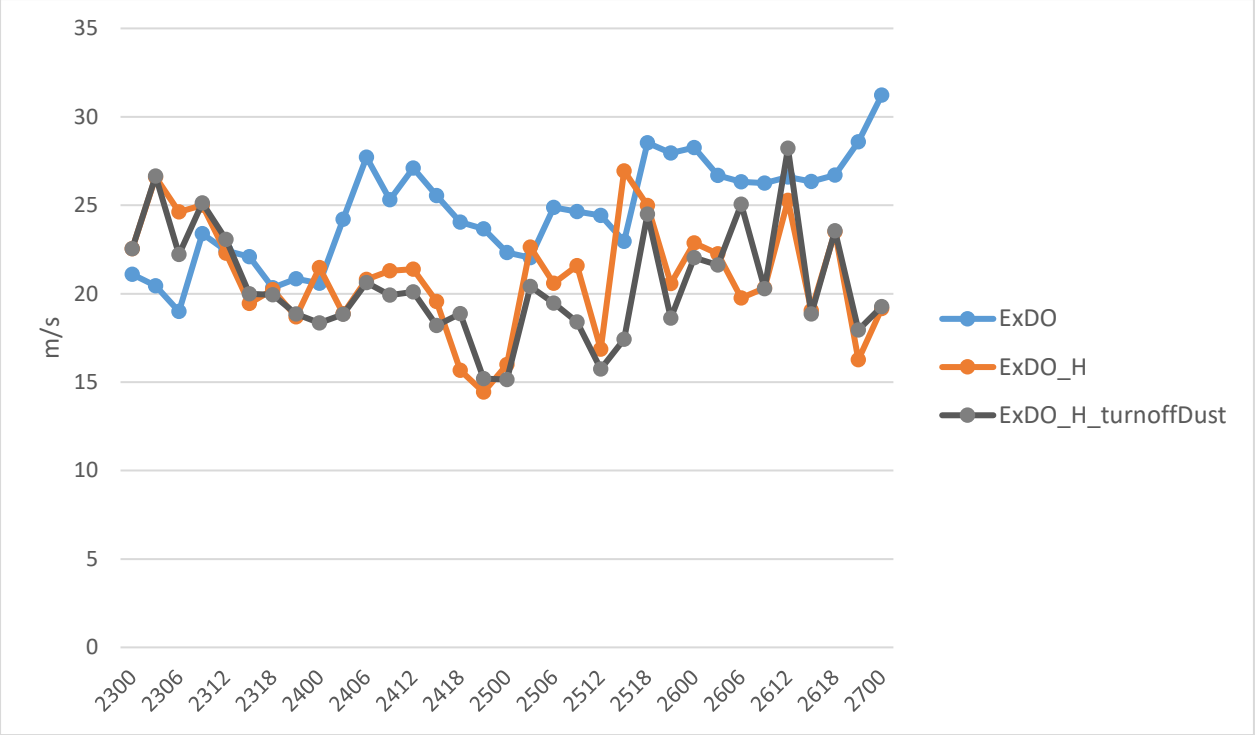

Figure 3-103. The maximum wind speed at 850 hPa in different experiments.

B. Tropical low stage

Following the storm center, we compute the azimuthal and time-averaged fields including vertical velocity, tangential wind, radial wind, CCN, extinction coefficient, number of cloud droplets, cloud mass mixing ratio, ice mass mixing ratio, rain mass mixing ratio, snow and graupel mass mixing ratio, latent heating rate, relative humidity, water vapor mass mixing ratio, and total heating tendency (Figure 3-105 to Figure 3-122).

In the tropical low stage, both experiments have broad upward motions within 500 km radius except in the mid-level between 4-10 km and within 200km (Figure 3-105a). Vertical motions can be enhanced by latent heat release or dynamical forcings. As we analyzed in previous sections, the

convergence associated with the low-level AEW trough triggers upward motions. In the presence of water vapor and CCN, condensation may occur. If the updraft is strong enough, freezing may happen above the melting level. Latent heat release from condensation or freezing will, in turn, enhance upward motion. As shown in Figure 3-106a, the pattern of microphysical latent heat release is similar to the vertical velocity. Negative latent heat release caused by the evaporation or melting is associated with the downward motion.

Several cross-sections are taken to analyze the storm structure. The positions of the cross-sections relative to the storm center are shown in Figure 3-104. Figure 3-105 b ~e show that upward motions are stronger on the southern side of the system. The maximum positive vertical velocity is located more than one hundred kilometers away from the center. The air is also wetter there, as shown by the higher relative humidity in Figure 3-107. There are two dry layers: one is in the Sahara Air Layer (SAL) (2-4 km), and the other dry layer above 6 km comes from the large-scale descending air in the mid to upper-levels over the subtropical and eastern Atlantic region (Braun 2010). The downward motion in the center at about 7 km height is from the large-scale descent motion in the mid and upper atmosphere.

In the high relative humidity region, with the presence of CCN, the cloud droplets form below 6 km (Figure 3-108). Inside SAL from 2 km to 3 km, there are fewer cloud droplets. The number of cloud droplets reaches maximum below 1km where the relative humidity is high (Figure 3-107 and Figure 3-108). The number of cloud droplets is fewer in the downdraft region because downward motion suppresses condensation and increases evaporation. The cloud mass mixing ratio has a similar distribution as the number of the cloud droplets (Figure 3-109). Water cloud forms below 7 km height, while ice cloud forms above 8 km height in regions with a strong updraft. Strong updraft transports cloud droplets to higher altitudes, and the cloud droplets change into ice

particles. The latent heat released by the freezing will reinforce the upward motion. Some ice particles are transported toward the center by the radial inflow (Figure 3-111).

In the experiment ExDO-H, more cloud droplets are formed due to increased CCN from dust (Figure 3-108 and Figure 3-109). Specifically, the increment is largest below 2 km where the relative humidity is high, which makes the condensation more efficient (Figure 3-107).

Rain and snow+graupel distributions are similar to the above-mentioned cloud droplet distribution (Figure 3-110). Inside 108 km radius, there are relatively few clouds, and the rain is also less. However, outside the 108-km radius, the rain is heavier. Snow and graupel form above 5 km. The rain is generated by the mixed-phase rain process in which cloud droplets grow into rain droplets, and ice particles grow into the snow. The process is much efficient than warm rain process which does not have ice particles formed. The region of snow and rain coincides with the area of positive vertical motion because stronger updraft increases the formation of snow and rain, and vice versa. There are more rain, snow, and graupel on the southern periphery of the system where convection is more active (Figure 3-110c, d, e).

The rain is suppressed in some region after adding dust, as shown by azimuthally averaged and cross-section plots (Figure 3-110). Outside the 216-km radius in the azimuthally averaged plot, the rain is reduced after adding dust (Figure 3-110a, right column). “Invigoration theory” is typically used to explain this phenomenon (Rosenfeld, et al. 2012). The theory states that as more cloud droplets compete with each other to obtain water vapor to grow, the average cloud droplet size will decrease. It reduces the efficiency of the formation of precipitation and increases the cloud lifetime. More cloud droplets will be transported upward and turned into ice. As more ice particles are formed, the diabatic heating increases the upward motion. Such theory might not explain the phenomenon in our study. We notice that the upward motion is reduced (Figure 3-105a, right

column). Cloud water and ice mixing ratios are decreased in the region, particularly between 250-350 km radius where the main convective region is located in the azimuthally averaged sense (Figure 3-109a). The rain and snow+graupel mixing ratios are also decreased in this region. The diabatic heating is reduced correspondingly (Figure 3-106). However, the cross-sections show that upward motion increases slightly inside the main convective region at around 200 km radius in the dust experiments (Figure 3-105). More rain, ice, and snow are found in the same region. The strengthened and weakened upward motions and latent heat release after adding dust happen along the edge of the dust region, mainly on the south side of the system (Figure 3-105 and Figure 3-106). Convections occur only in the moist region or along the edge of SAL where there is strong moisture gradient. Dust is inside the SAL. Only at the edge of the SAL, dust starts to interact with strong convections. The invigoration process may be active in the inner edge of dusty SAL to enhance vertical motion. But dust reduces the convection in the outer edge of SAL. The dynamic consequence is the contraction of updraft and acceleration of tangential wind inside of the convective region (Figure 3-105).

Latent heat release dominates over other heating processes, as can be seen by comparing the latent heating rate with the total heating rate which includes shortwave radiative heating, longwave radiative heating, boundary layer heating, latent heat rate, and temperature advection (Figure 3-113). The latent heating rate pattern resembles the total heating rate pattern.

We summarize the process in the tropical low stage. Convection is more active on the southern periphery of the system where more moisture is available. Convection promotes the cloud, rain, snow, and graupel formed in the convection. Latent heat release increases the convection. Downward motion around the center in the mid-level is not a result of SAL; it is the large-scale

descent motion from the mid and upper atmosphere. Latent heating dominates over other heating processes; while earlier when the system is on land, boundary heating is the largest heating source.

Dust increases the low-level cloud at 1-2 km height. It reduces the rain in the outer edge of the SAL region between 250 km to 350 km radii. While increase rain in the inner edge at around 200 km. The associated latent heat release shifts the updraft radially inward. The dynamical consequence is the acceleration of tangential wind and the mid-level cyclogenesis.

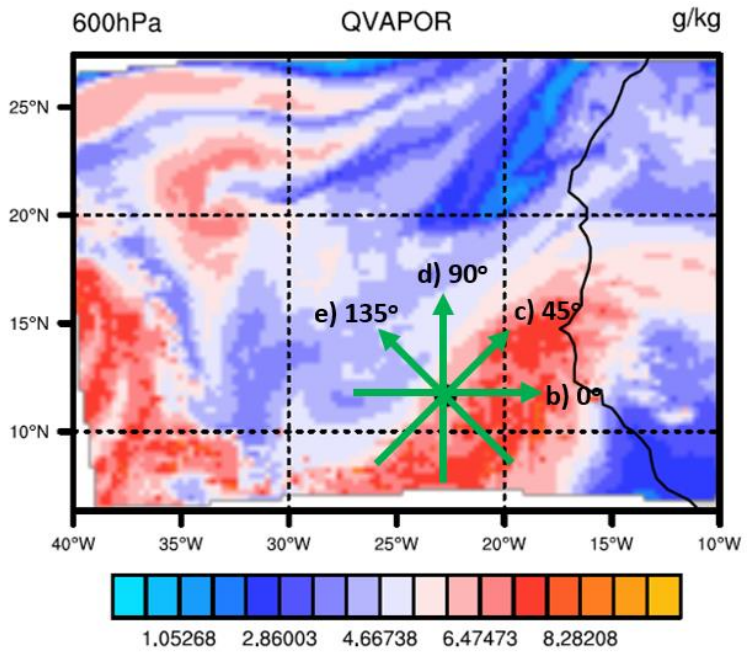

Figure 3-104. The water vapor mass mixing ratio (shading, units: g/kg) at 600hPa and cross-section positions relative to the tropical system at 00UTC 24 August 2010. (b) –(e) indicate the IDs of the following cross-sections. The value is the angle started from the east direction. Arrows indicate the positive direction in the cross-sections.

(a)

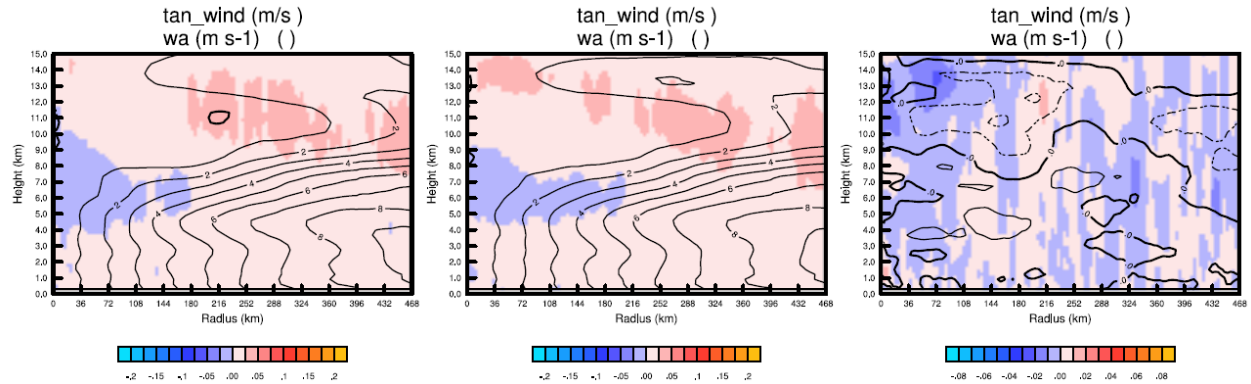
tan_wind (m/s)
wa (m s-1) ( )
Height (km)
Radius (km)
tan_wind (m/s)
wa (m s-1) ( )
Height (km)
Radius (km)
tan_wind (m/s)
wa (m s-1) ( )
Height (km)
Radius (km)

(b)

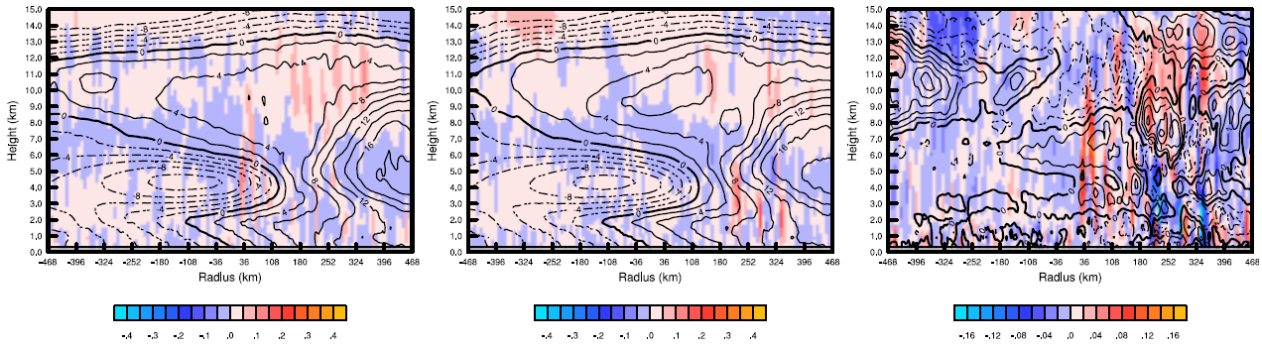
Height (km)
Radius (km)
Height (km)
Radius (km)
Height (km)
Radius (km)

(c)

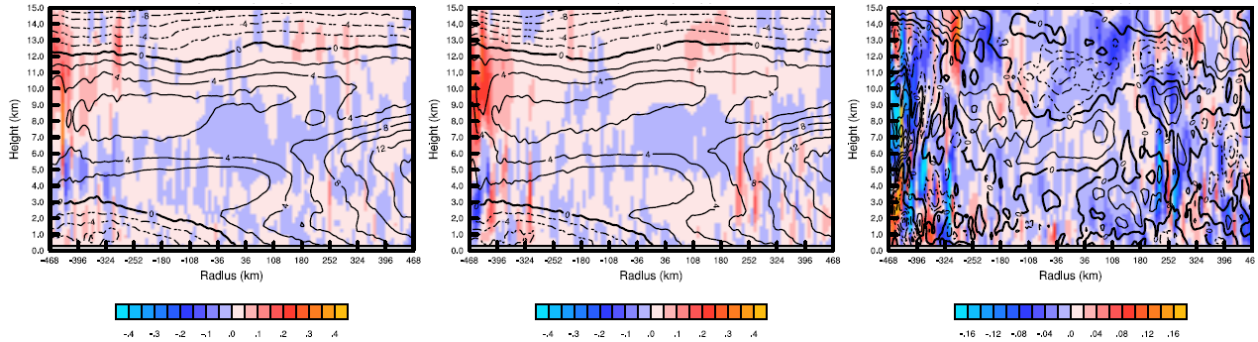
Height (km)
Radius (km)
Height (km)
Radius (km)
Height (km)
Radius (km)

(d)

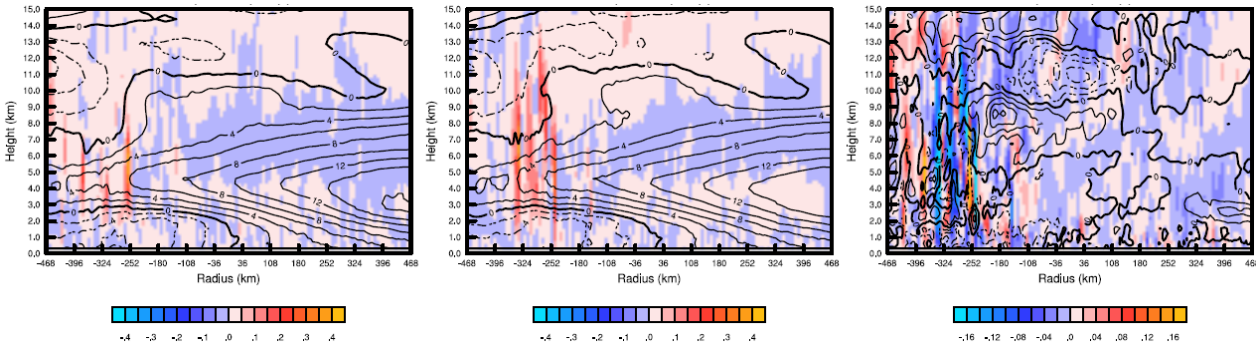

(e)

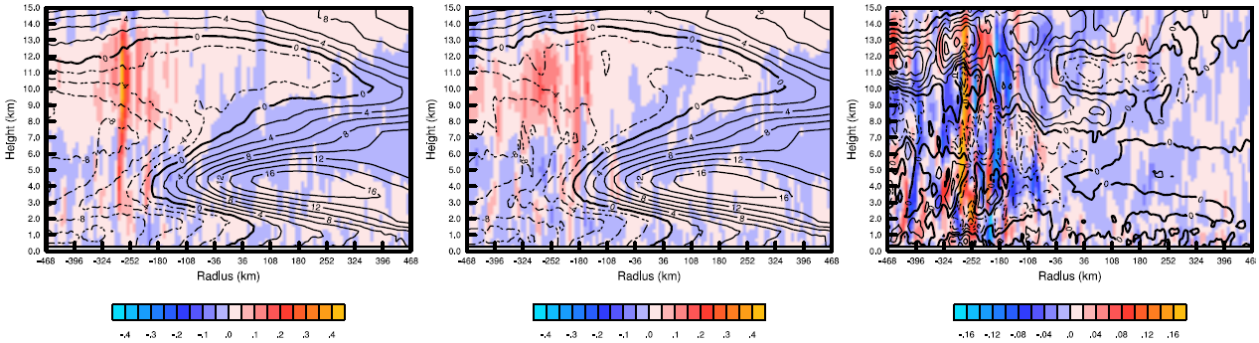

Figure 3-105. (a) The azimuthally averaged and time-averaged vertical velocity (shading, units: m/s) and tangential wind (contour, units: m/s). Solid contour lines indicate positive values and dashed contour lines indicate negative values. The time average is taken from 00UTC 24 August to 00UTC 25 August 2010. (b)-(e) are cross-sections in time average for the same variables. (b) Cross-section at 0°; (c) Cross-section at 45°; (d) Cross-section at 90°; (e) Cross-section at 135°. Their positions are indicated in Figure 3-104. (left) ExDO-H; (middle) ExDO-H-TurnoffDust; (right) ExDO-H minus ExDO-H-TurnoffDust.

(a)

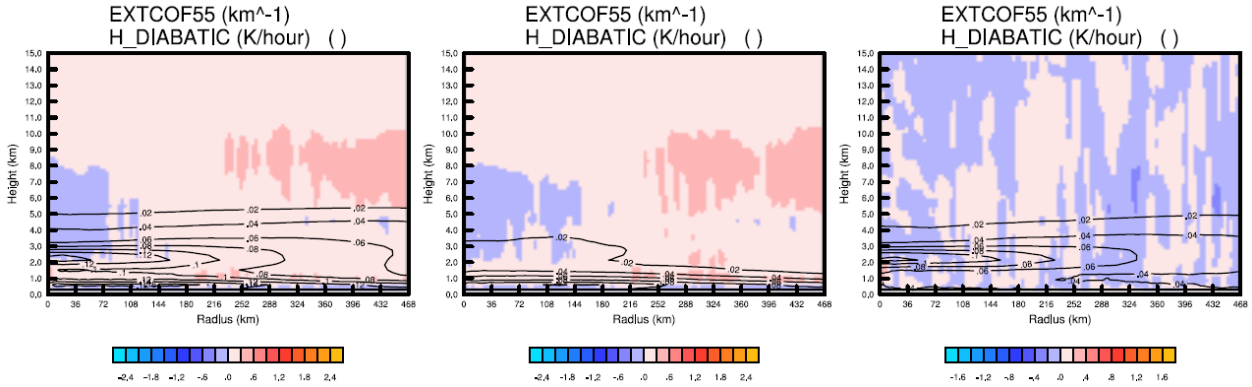
EXTCOF55 (km^-1)
H_DIABATIC (K/hour) ( )
EXTCOF55 (km^-1)
H_DIABATIC (K/hour) ( )
EXTCOF55 (km^-1)
H_DIABATIC (K/hour) ( )
Height (km)
Radius (km)

(b)

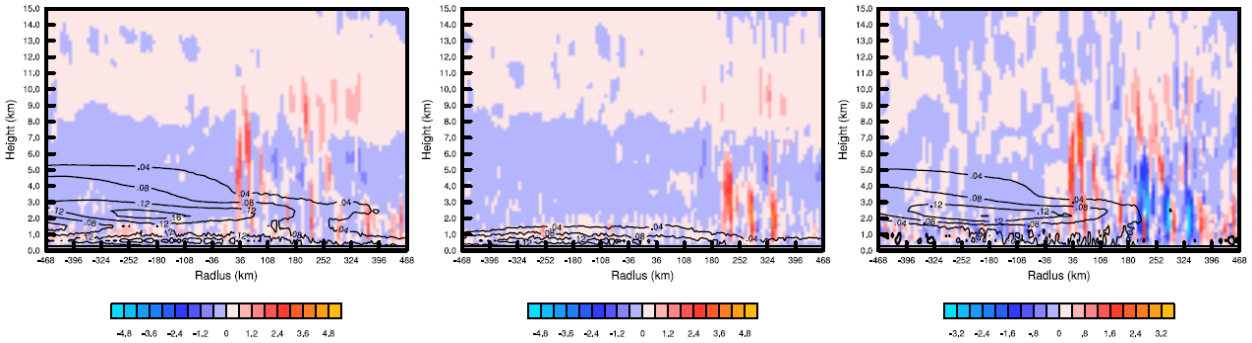
Height (km)
Radius (km)

(c)

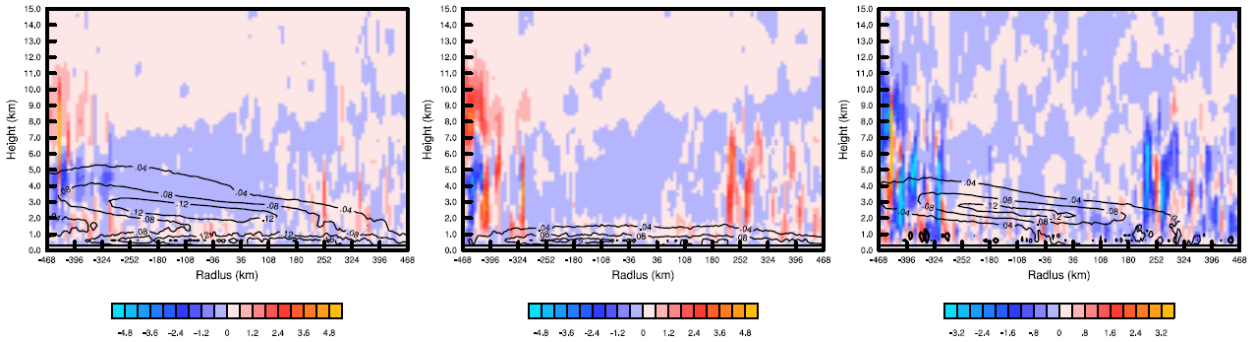
Height (km)
Radius (km)

(d)

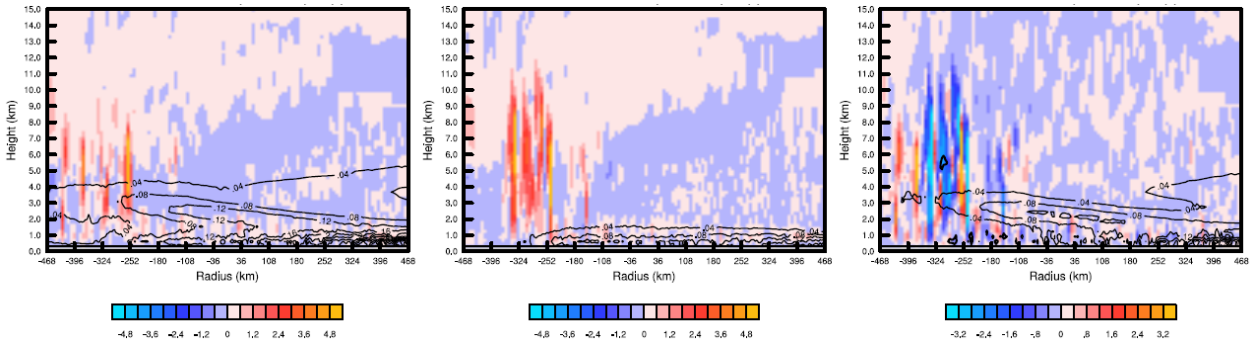

(e)

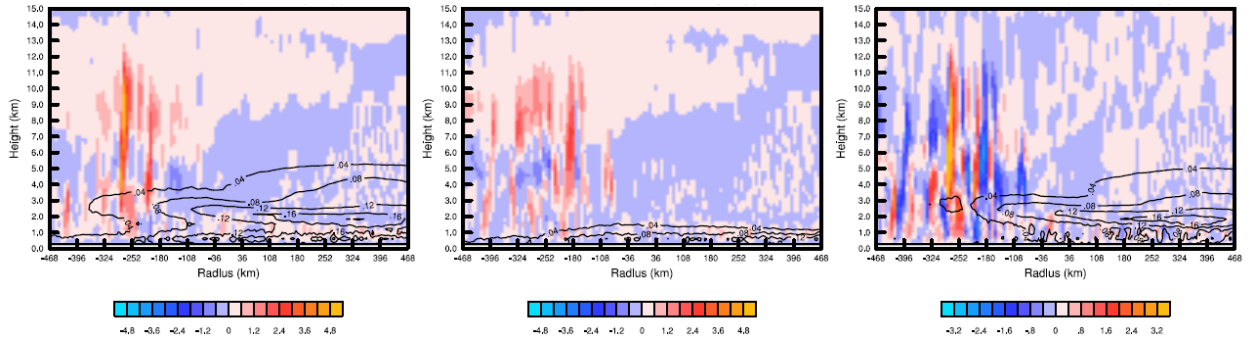

Figure 3-106. (a) The azimuthally averaged and time-averaged vertical latent heating rate (shading, units: K/hour) and extinction coefficient at 550nm (contour, units: km^{-1}). The time average is taken from 00UTC 24 August to 00UTC 25 August 2010. (b)-(e) are cross-sections in time average for the same variable. (b) Cross-section at 0º; (c) Cross-section at 45º; (d) Cross-section at 90º; (e) Cross-section at 135º. Their positions are indicated in Figure 3-104. (left) ExDO-H; (middle) ExDO-H-TurnoffDust; (right) ExDO-H minus ExDO-H-TurnoffDust (Solid contour lines indicate positive values and dashed contour lines indicate negative values).

(a)

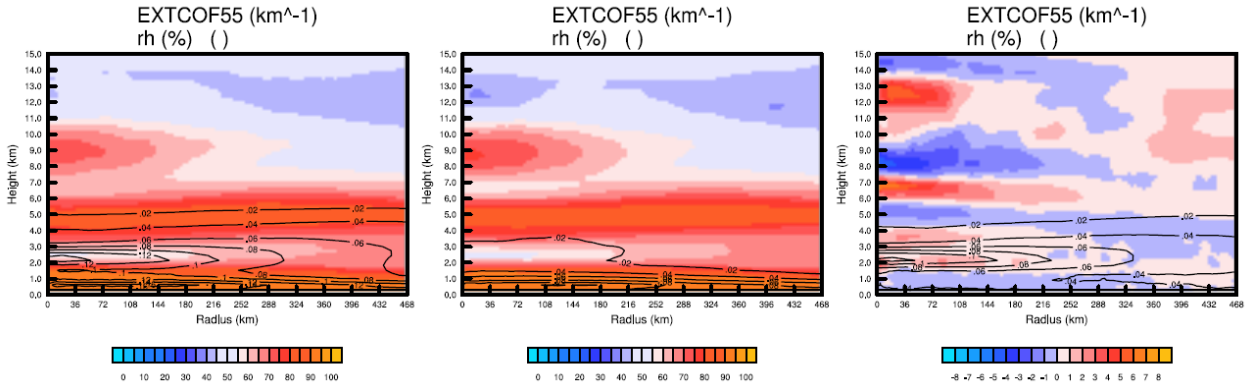
EXTCOF55 (km^-1)
rh (%) ( )
EXTCOF55 (km^-1)
rh (%) ( )
EXTCOF55 (km^-1)
rh (%) ( )
Height (km)
Radius (km)

(b)

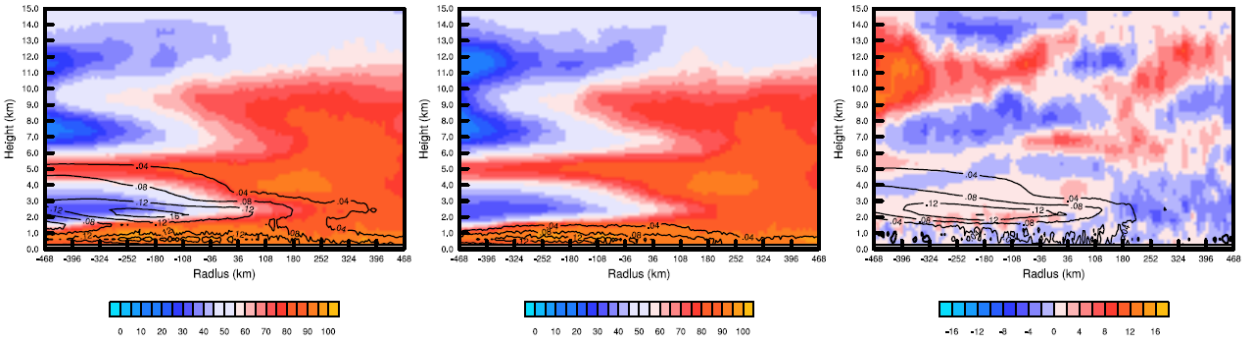
Height (km)
Radius (km)

(c)

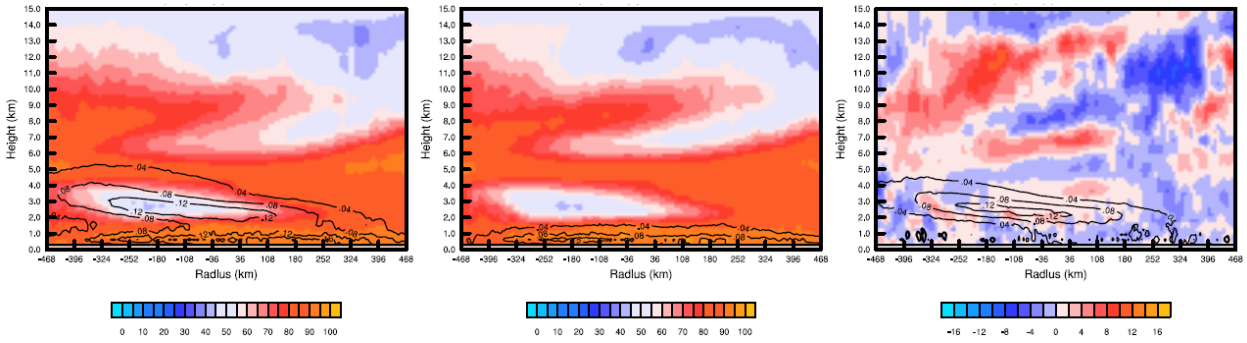
Height (km)
Radius (km)

(d)

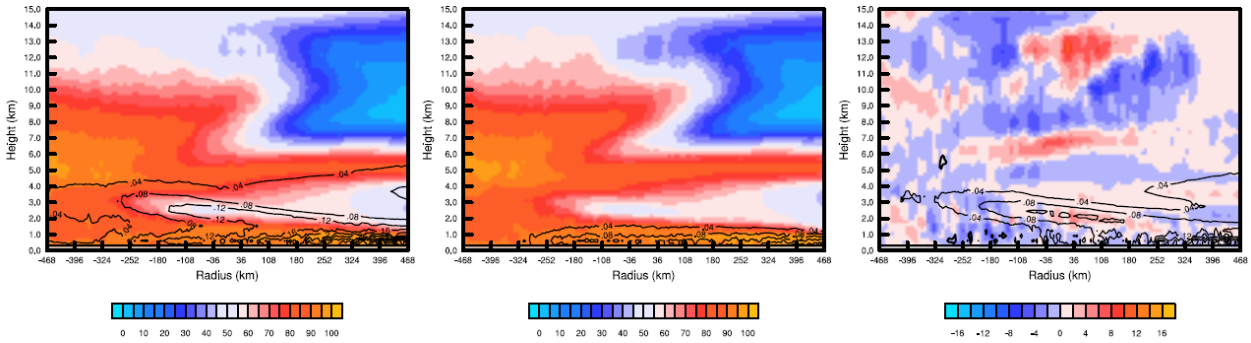

(e)

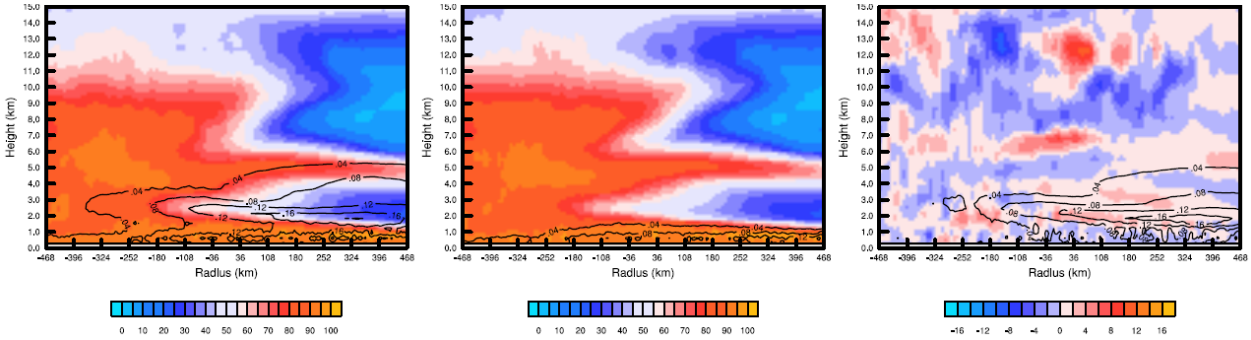

Figure 3-107. (a) The azimuthally averaged and time-averaged relative humidity (shading) and the extinction coefficient at 550nm (contour, units: km^{-1}). The time average is taken from 00UTC 24 August to 00UTC 25 August 2010. (b)-(e) are cross-sections in time average for the same variables. (b) Cross-section at 0°; (c) Cross-section at 45°; (d) Cross-section at 90°; (e) Cross-section at 135°. Their positions are indicated in Figure 3-104. (left) ExDO-H; (middle) ExDO-H-TurnoffDust; (right) ExDO-H minus ExDO-H-TurnoffDust (Solid contour lines indicate positive values and dashed contour lines indicate negative values).

(a)

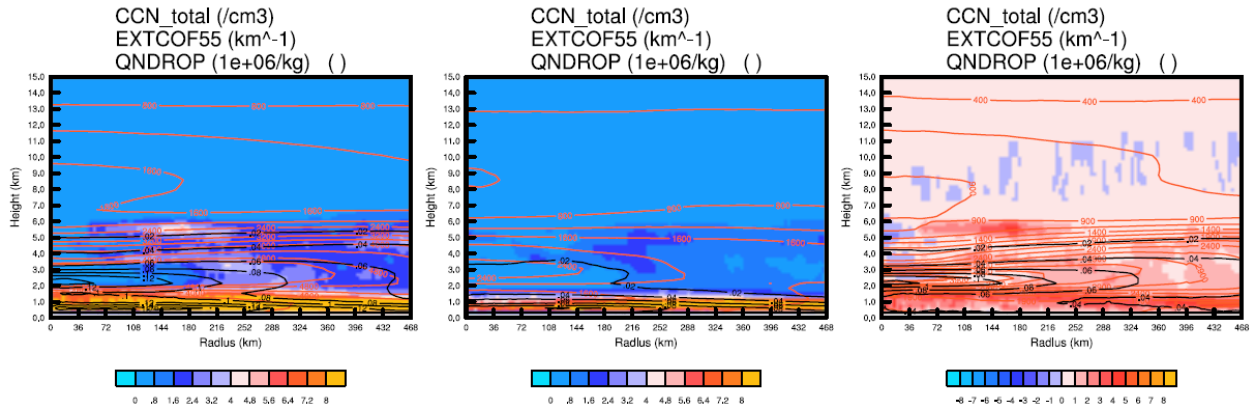
CCN_total (/cm3)
EXTCOF55 (km^-1)
QNDROP (1e+06/kg) ( )
CCN_total (/cm3)
EXTCOF55 (km^-1)
QNDROP (1e+06/kg) ( )
CCN_total (/cm3)
EXTCOF55 (km^-1)
QNDROP (1e+06/kg) ( )
Height (km)
Radius (km)

(b)

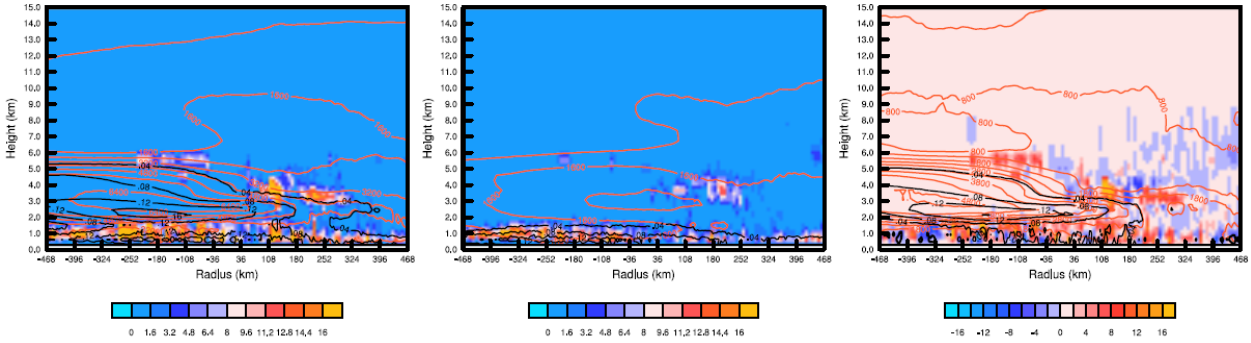
Height (km)
Radius (km)

(c)

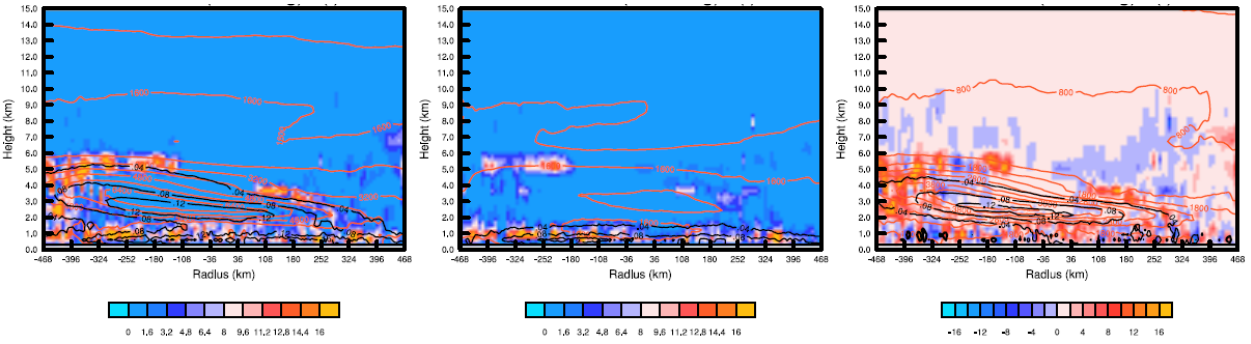
Height (km)
Radius (km)

(d)

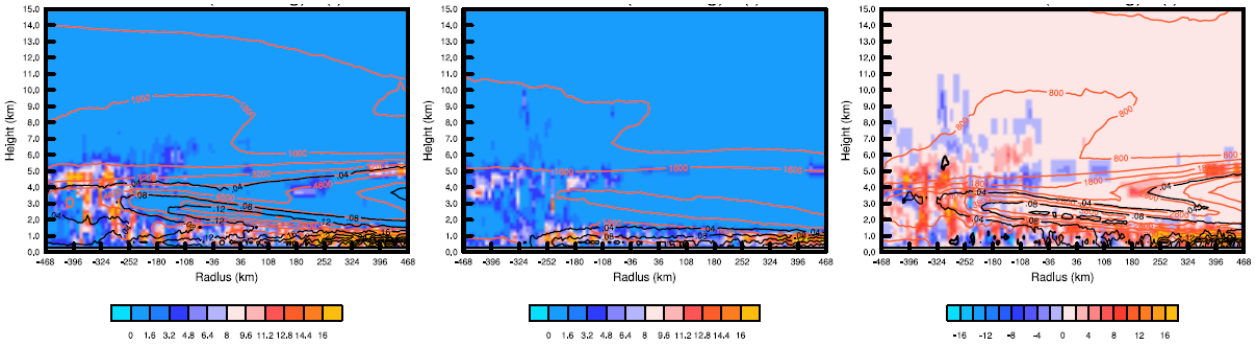

(e)

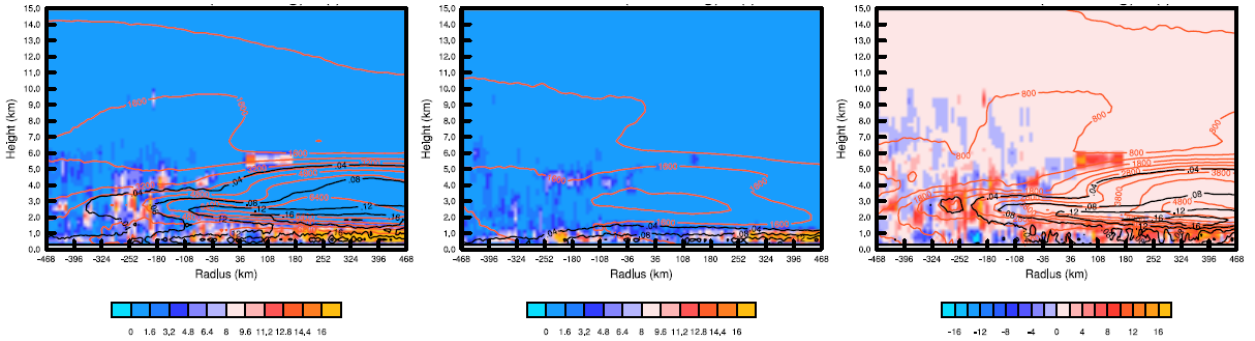

Figure 3-108. (a) The azimuthally averaged and time-averaged cloud droplets number (shading, units: 1e+06/kg), extinction coefficient at 550nm (black contour lines, units: km^{-1}), and CCN number (Red contour lines, units: cm^{-3}). Solid contour lines indicate positive values and dashed contour lines indicate negative values. The time average is taken from 00UTC 24 August to 00UTC 25 August 2010. (b)-(e) are cross-sections in time average for the same variables. (b) Cross-section at 0°; (c) Cross-section at 45°; (d) Cross-section at 90°; (e) Cross-section at 135°. Their positions are indicated in Figure 3-104. (left) ExDO-H; (middle) ExDO-H-TurnoffDust; (right) ExDO-H minus ExDO-H-TurnoffDust.

(a)

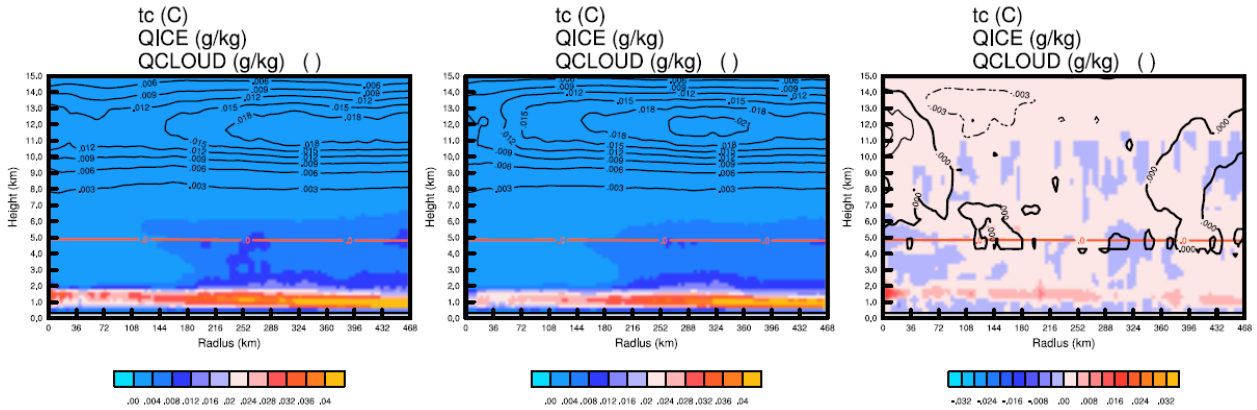
tc (C)
QICE (g/kg)
QCLOUD (g/kg) ( )
Height (km)
Radius (km)

(b)

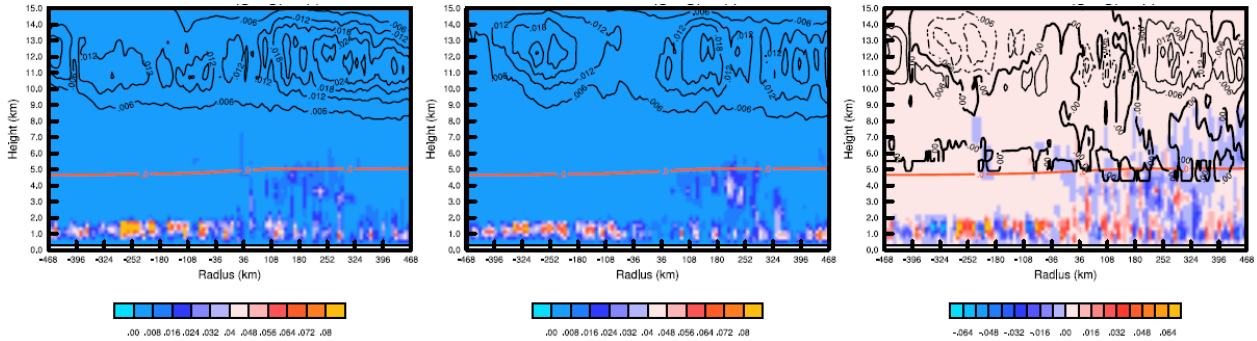
Height (km)
Radius (km)

(c)

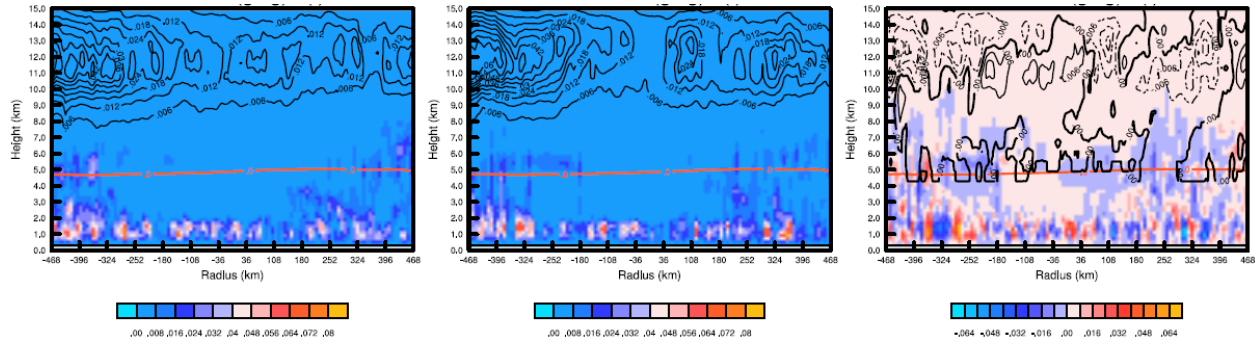
Height (km)
Radius (km)

(d)

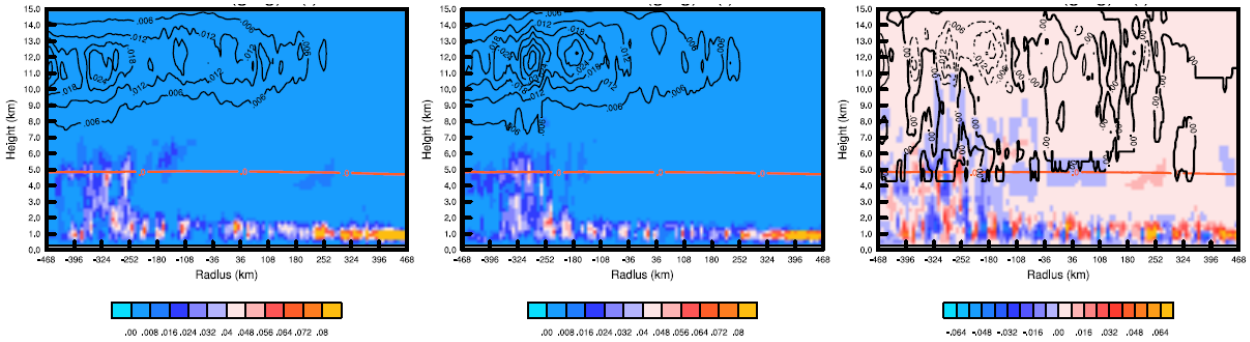

(e)

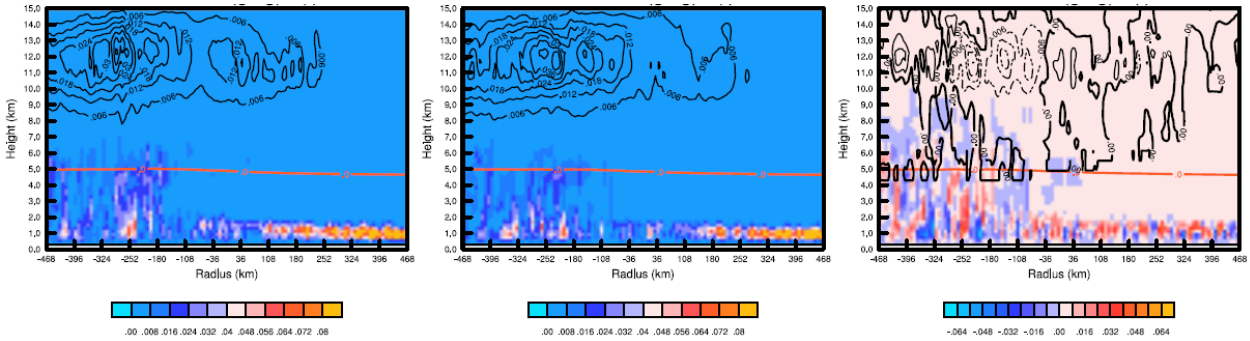

Figure 3-109. (a) The azimuthally averaged and time-averaged cloud mass mixing ratio (shading, units: g/kg) and the ice mass mixing ratio (contour, units: g/kg). The red solid line is zero isotherm. Solid contour lines indicate positive values and dashed contour lines indicate negative values. The time average is taken from 00UTC 24 August to 00UTC 25 August 2010. (b)-(e) are cross-sections in time average for the same variables. (b) Cross-section at 0°; (c) Cross-section at 45°; (d) Cross-section at 90°; (e) Cross-section at 135°. Their positions are indicated in Figure 3-104. (left) ExDO-H; (middle) ExDO-H-TurnoffDust; (right) ExDO-H minus ExDO-H-TurnoffDust.

(a)

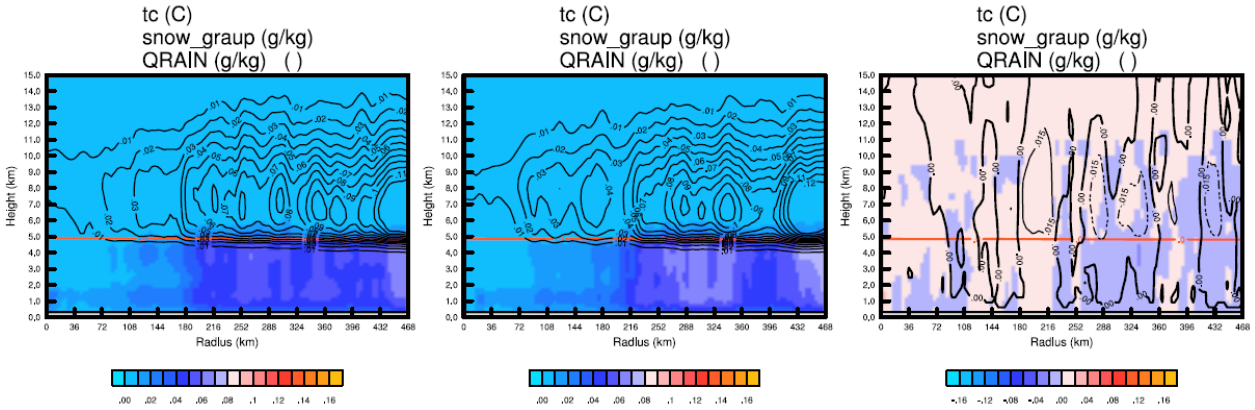
tc (C)
snow_graup (g/kg)
QRAIN (g/kg) ( )
Height (km)
Radius (km)

(b)

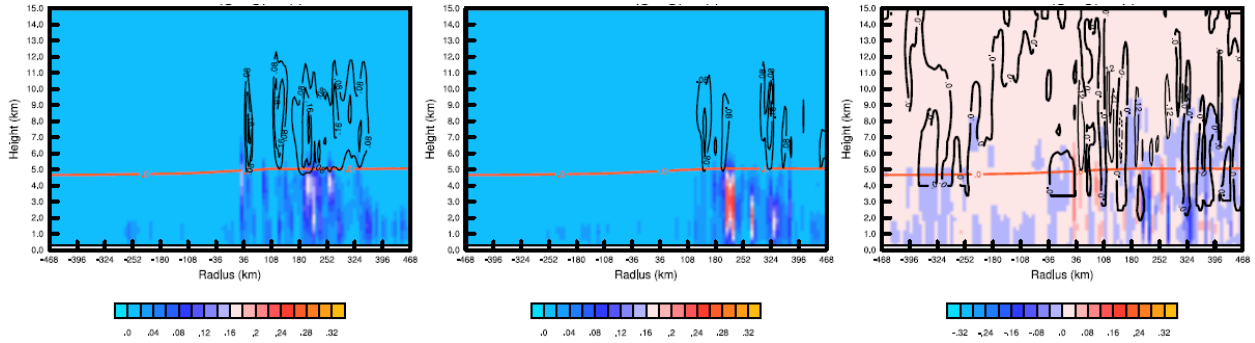
Height (km)
Radius (km)

(c)

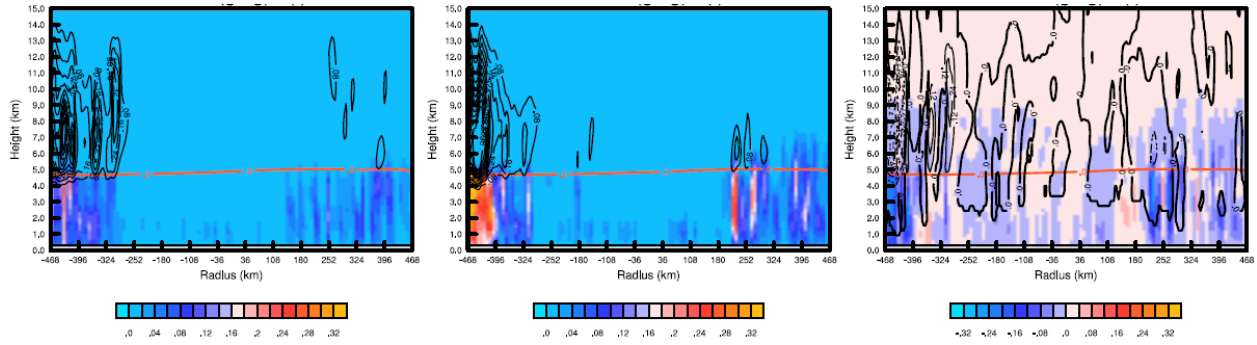
Height (km)
Radius (km)

(d)

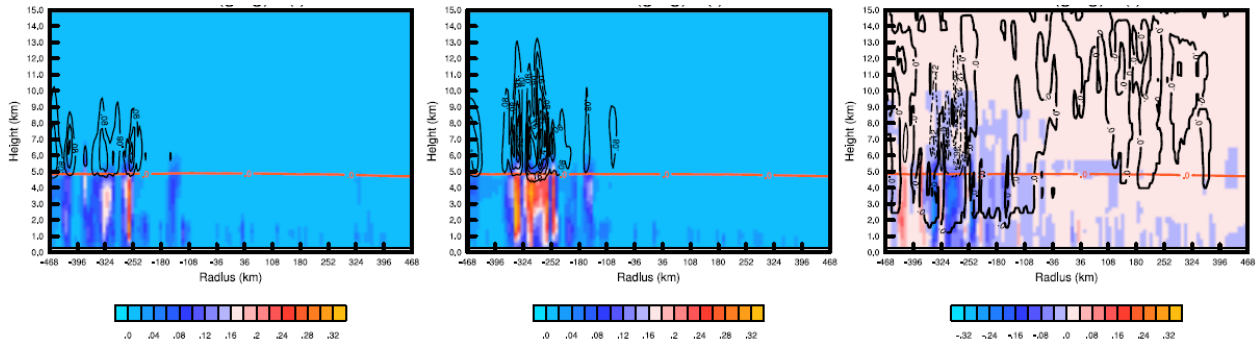

(e)

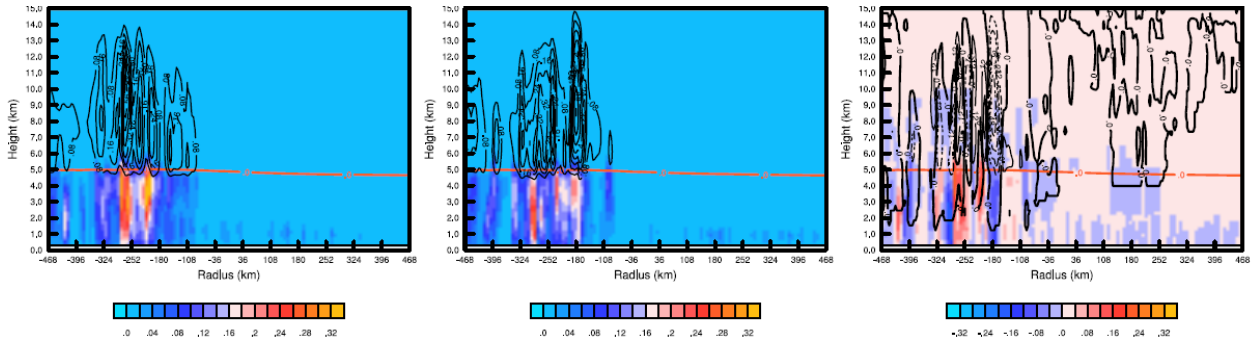

Figure 3-110. (a) The azimuthally averaged and time-averaged rain (shading, units: g/kg) and snow+ graupel (contour, units: g/kg). The red solid line is zero isotherm. Solid contour lines indicate positive values and dashed contour lines indicate negative values. The time average is taken from 00UTC 24 August to 00UTC 25 August 2010. (b)-(e) are cross-sections in time average for the same variables. (b) Cross-section at 0°; (c) Cross-section at 45°; (d) Cross-section at 90°; (e) Cross-section at 135°. Their positions are indicated in Figure 3-104. (left) ExDO-H; (middle) ExDO-H-TurnoffDust; (right) ExDO-H minus ExDO-H-TurnoffDust.

(a) (b) (c)

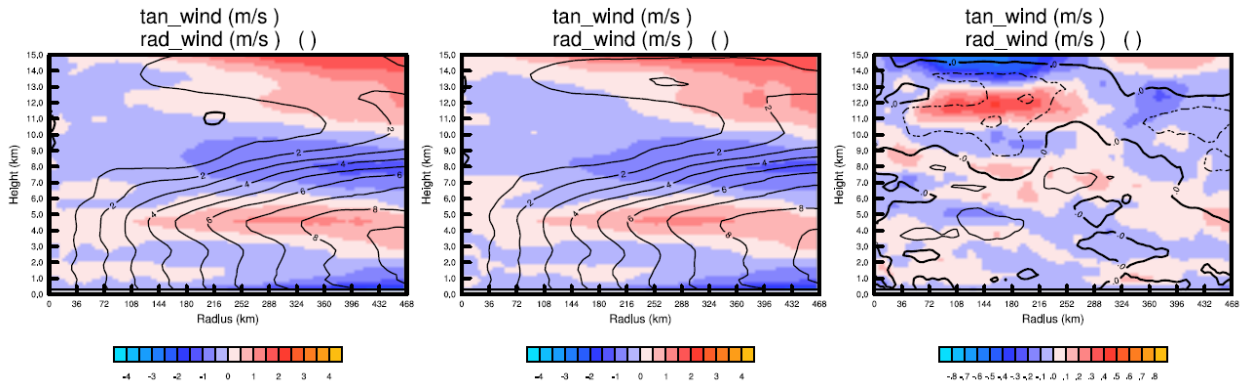

Figure 3-111. The azimuthally averaged and time-averaged radial wind (shading, units: m/s) and the tangential wind (contour, units: m/s). Positive values in the shading indicate outward direction. Solid contour lines indicate positive values and dashed contour lines indicate negative values. The time average is taken from 00UTC 24 August to 00UTC 25 August 2010. (a) ExDO-H; (b) ExDO-H-TurnoffDust; (c) ExDO-H minus ExDO-H-TurnoffDust.

(a) (b) (c)

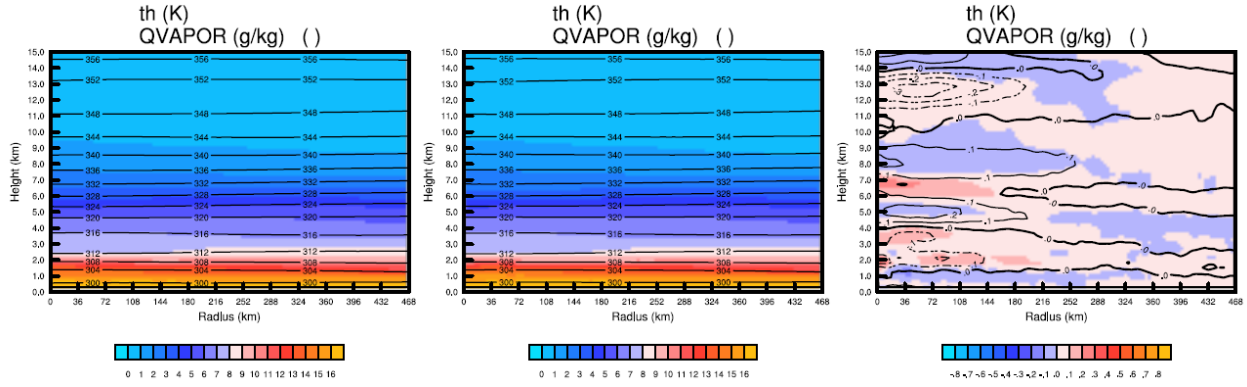

Figure 3-112. The azimuthally averaged and time-averaged water vapor mass mixing ratio (shading, units: g/kg) and potential temperature (contour, units: K). The time average is taken from 00UTC 24 August to 00UTC 25 August 2010. (a) ExDO-H; (b) ExDO-H-TurnoffDust; (c) ExDO-H minus ExDO-H-TurnoffDust (Solid contour lines indicate positive values and dashed contour lines indicate negative values).

(a) (b) (c)

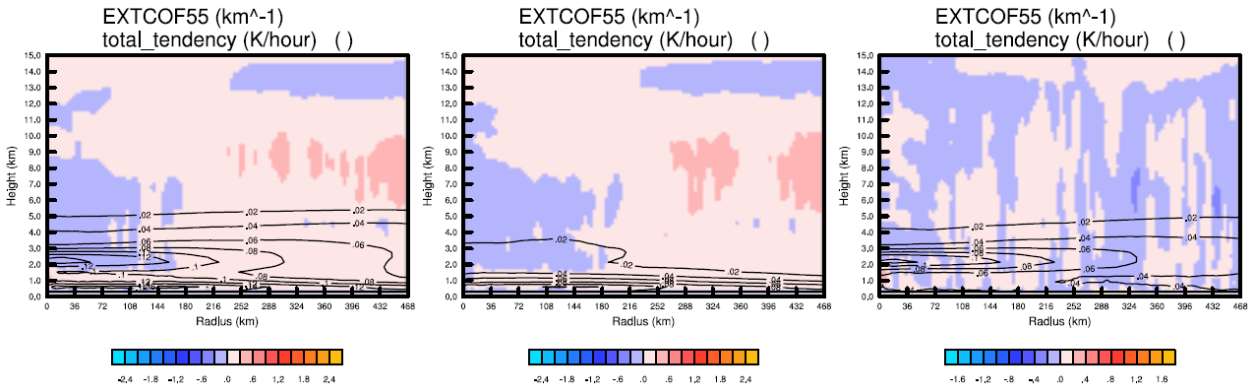

Figure 3-113. The azimuthally averaged and time-averaged total tendency (shading, units: K/hour) and extinction coefficient at 550nm (contour, units: km^{-1}). Total tendency includes shortwave radiative heating rate, longwave radiative heating rate, boundary heating rate, latent heating rate, and advection. The time-averaged is from 00UTC 24 August to 00UTC 25 August 2010. (a) ExDO-H; (b) ExDO-H-TurnoffDust; (c) ExDO-H minus ExDO-H-TurnoffDust (Solid contour lines indicate positive values and dashed contour lines indicate negative values).

C. Tropical depression stage

During the tropical depression stage, beginning from 01UTC 25 August 2010, the storm intensifies rapidly. Time-averaged and azimuthally averaged plots are produced to analyze the system. Contrary to the previous stage, the vertical velocity of the system at this stage is mainly positive around the center, with the strongest values above 6 km (Figure 3-114). The upward motion assists the growth of cloud droplets below 7 km and ice particles above 9 km (Figure 3-115). Above 9 km, cloud droplets turn into ice, and they release a large amount of latent heat which increases the upward motion. Accompanied by the upward motion around the center, the cloud, ice, rain, and snow all move towards the center (Figure 3-115, Figure 3-116, Figure 3-117). The

concentrations of the rain, snow, and graupel are much larger compared to the previous tropical low stage. The mixed rain process is stronger in which ice grows into snow, and snow melts into rain droplets below freezing level.

In the experiment ExDO-H which contains dust, on average, the vertical velocity is increased within 80-km radius while it is reduced between 80-km to 160-km radius (Figure 3-114). Because stronger vertical velocity helps cloud droplets grow to rain and snow, the change of precipitation (Figure 3-117c) matches the change of vertical velocity. In most of the areas, the number of cloud droplets and the cloud mass mixing ratio are increased in the dust experiment because adding dust increase CCN number (Figure 3-115c and Figure 3-116c).

The system has a stronger circulation compared to the previous stage. The tangential wind increases with a maximum of 10 m/s at around 300 km radius and 4 km height. (Figure 3-119). The near-surface radial inflow reaches about 2 m/s around the radius of maximum tangential wind. The radial inflows below 1 km and between 6 km and 8 km are enhanced after considering dust, in response to stronger ascent in the center. In a mature TC, such strengthened low-level inflow will increase low-level tangential wind. Here the enhanced radial inflow accelerates the mid-level vortex and moves it inward. But it decreases the tangential wind near the surface and moves closer to the center. This creates a stronger cyclonic shear that may favor the vortex development in the low level.

Adding dust also increases the moisture, especially at around 5-km height in the core region (Figure 3-120 and Figure 3-121). The relative humidity rises up by 10%. A possible reason for the moistening is the upward transport by stronger updrafts and evaporation in the downdrafts.

In summary, the dynamics at this stage is different from the previous stage. The vertical motion becomes stronger and concentrates around the center of the system. Stronger convection in

the center produces more cloud droplets, rain droplets, and ice particles. Once the upward motion can no longer support the weight of the hydrometers, they fall and generate precipitation. Since the convection is stronger in the center, it reduces the center pressure by warming up the mid-troposphere. Once center pressure is reduced, the stronger inflow from outside increases. They bring more mass and angular momentum inward, so that the tangential wind and vertical motion close to the center are both strengthened.

Adding dust increases the convection around the center inside 80 km radius. More ice, snow, and rain appear there. Since dust aerosols can be CCN, they increase the number of cloud droplets and cloud mass mixing ratio in most of the region. Rain, snow & graupel maxing ratios increase in the enhanced updraft region, but they are reduced in the weakened updraft region between 80 to 150 km.

(a) (b) (c)

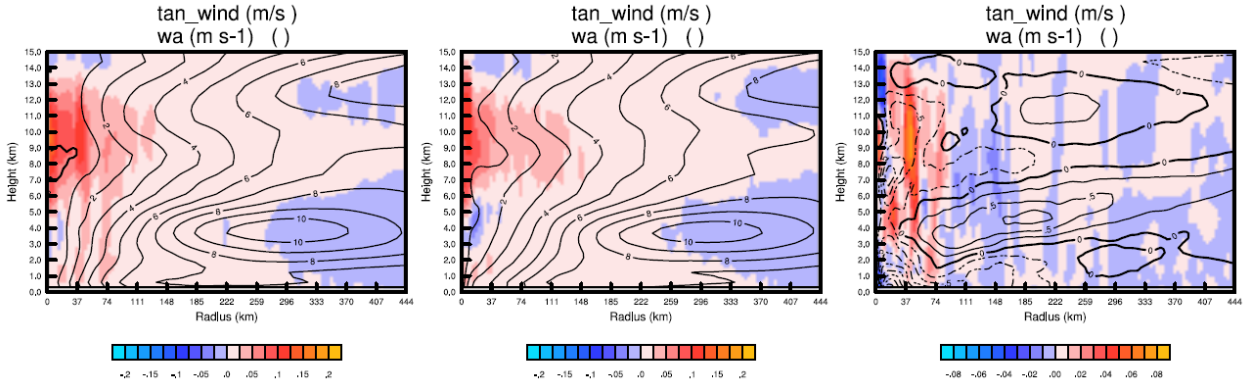

Figure 3-114. The azimuthally averaged and time-averaged vertical velocity (shading, units: m/s) and tangential wind (contour, units: m/s). Solid contour lines indicate positive values and dashed contour lines indicate negative values. The time average is taken from 00UTC 25 August to 00UTC 27 August 2010. (a) ExDO-H; (b) ExDO-H-TurnoffDust; (c) ExDO-H minus ExDO-H-TurnoffDust.

(a) (b) (c)

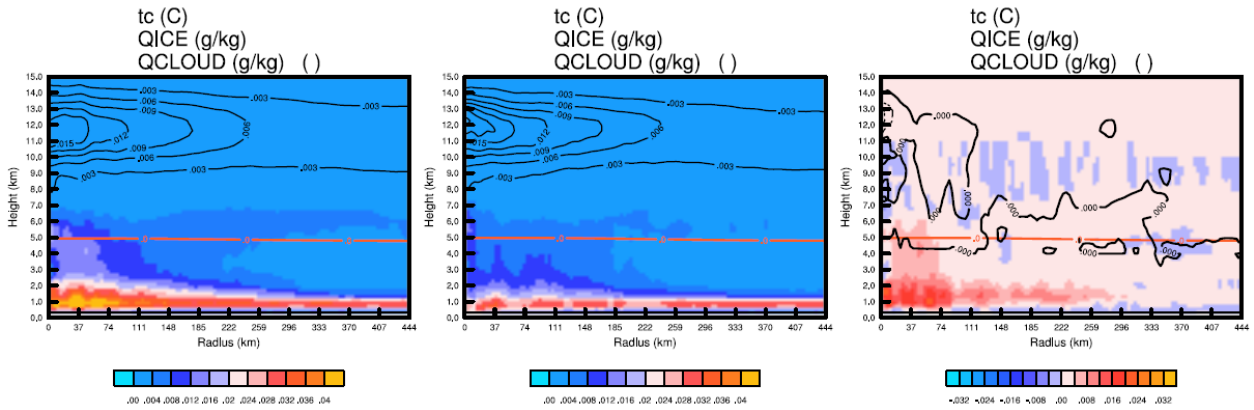

Figure 3-115. The azimuthally averaged and time-averaged cloud mass mixing ratio (shading, units: g/kg) and the ice mass mixing ratio (contour, units: g/kg). The red solid line is zero isotherm. The time average is taken from 00UTC 25 August to 00UTC 27 August 2010. (a) ExDO-H; (b) ExDO-H-TurnoffDust; (c) ExDO-H minus ExDO-H-TurnoffDust (Solid contour lines indicate positive values and dashed contour lines indicate negative values).

(a) (b) (c)

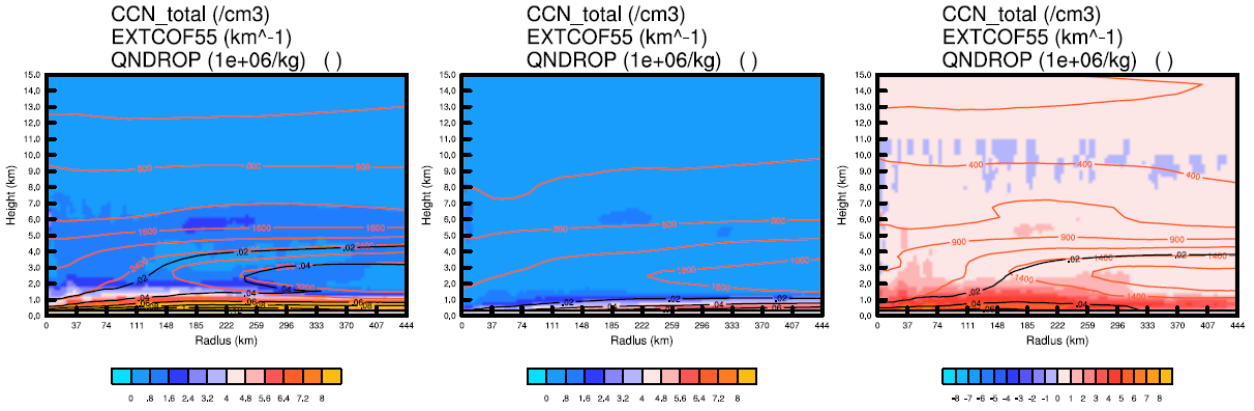

Figure 3-116. The azimuthally averaged and time-averaged cloud droplets number (shading, units: 1e+06/kg), extinction coefficient at 550nm (black contour lines, units: km^{-1}), and CCN number (Red contour lines, units: cm^{-3}). The time average is taken from 00UTC 25 August to 00UTC 27 August 2010. (a) ExDO-

H; (b) ExDO-H-TurnoffDust; (c) ExDO-H minus ExDO-H-TurnoffDust (Solid contour lines indicate positive values and dashed contour lines indicate negative values).

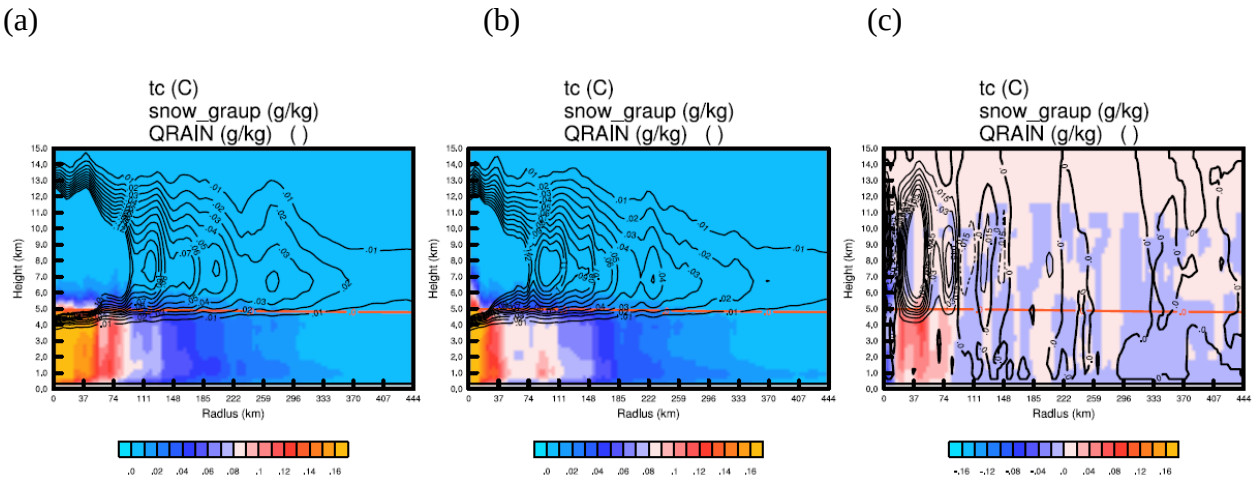

Figure 3-117. The azimuthally averaged and time-averaged rain (shading, units: g/kg) and snow+ graupel (contour, units: g/kg). The red solid line is 0° C freezing level. The time average is taken from 00UTC 25 August to 00UTC 27 August 2010. (a) ExDO-H; (b) ExDO-H-TurnoffDust; (c) ExDO-H minus ExDO-H-TurnoffDust (Solid contour lines indicate positive values and dashed contour lines indicate negative values).

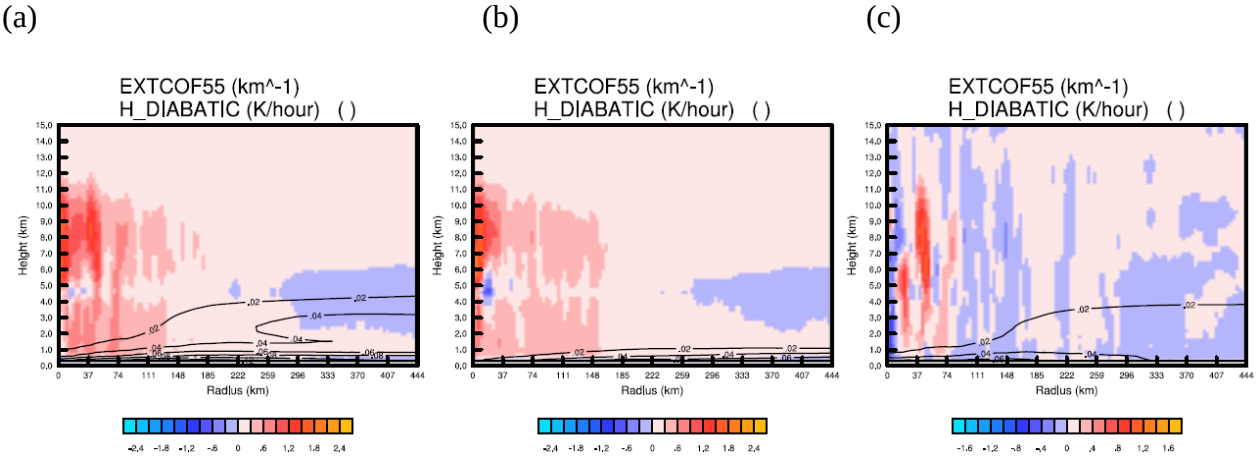

Figure 3-118. The azimuthally averaged and time-averaged latent heating rate (shading, units: K/hour) and extinction coefficient at 550nm (contour, units: km^{-1}). The time average is taken from 00UTC 25 August to

00UTC 27 August 2010. (a) ExDO-H; (b) ExDO-H-TurnoffDust; (c) ExDO-H minus ExDO-H-TurnoffDust (Solid contour lines indicate positive values and dashed contour lines indicate negative values).

(a) (b) (c)

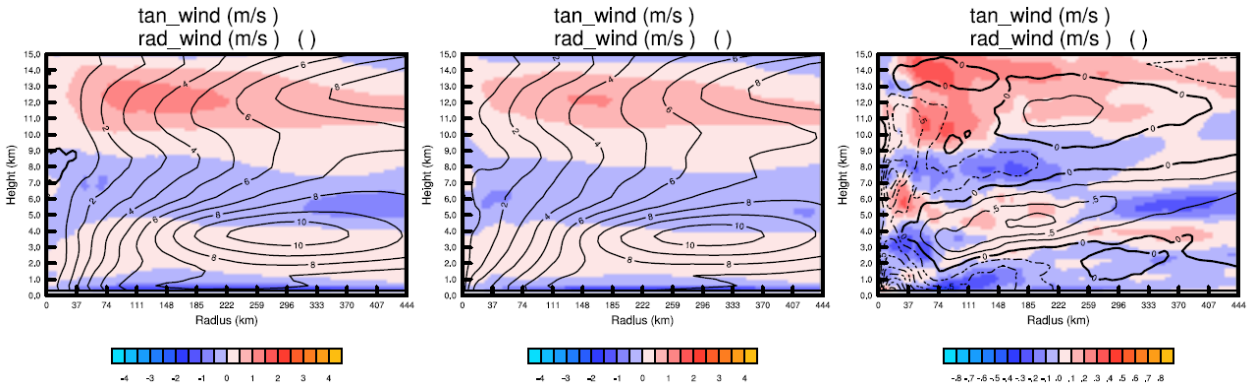

Figure 3-119. The azimuthally averaged and time-averaged radial wind (shading, units: m/s) and tangential wind (contour, units: m/s). Solid contour lines indicate positive values and dashed contour lines indicate negative values. The time average is taken from 00UTC 25 August to 00UTC 27 August 2010. (a) ExDO-H; (b) ExDO-H-TurnoffDust; (c) ExDO-H minus ExDO-H-TurnoffDust.

(a) (b) (c)

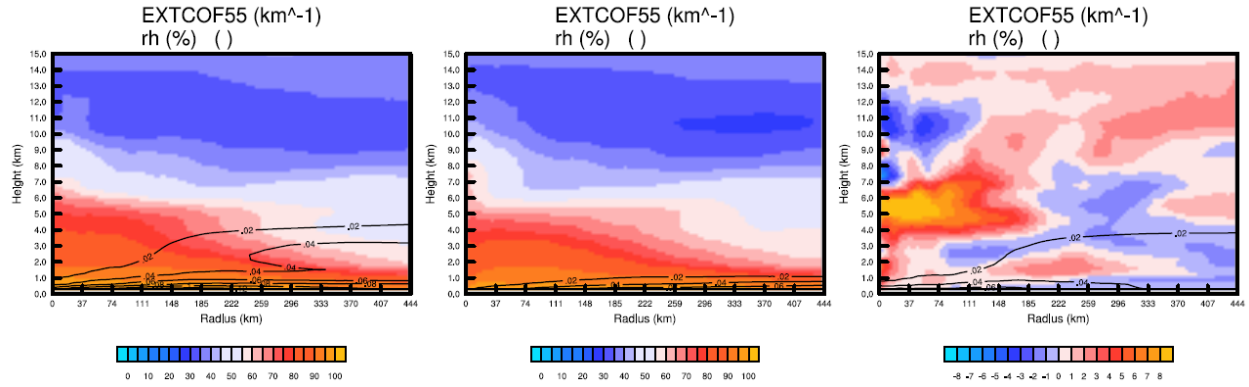

Figure 3-120. The azimuthally averaged and time-averaged relative humidity (shading) and the extinction coefficient at 550nm (contour, units: km^{-1}). The time-average is taken from 00UTC 25 August to 00UTC

27 August 2010. (a) ExDO-H; (b) ExDO-H-TurnoffDust; (c) ExDO-H minus ExDO-H-TurnoffDust (Solid contour lines indicate positive values and dashed contour lines indicate negative values).

(a) (b) (c)

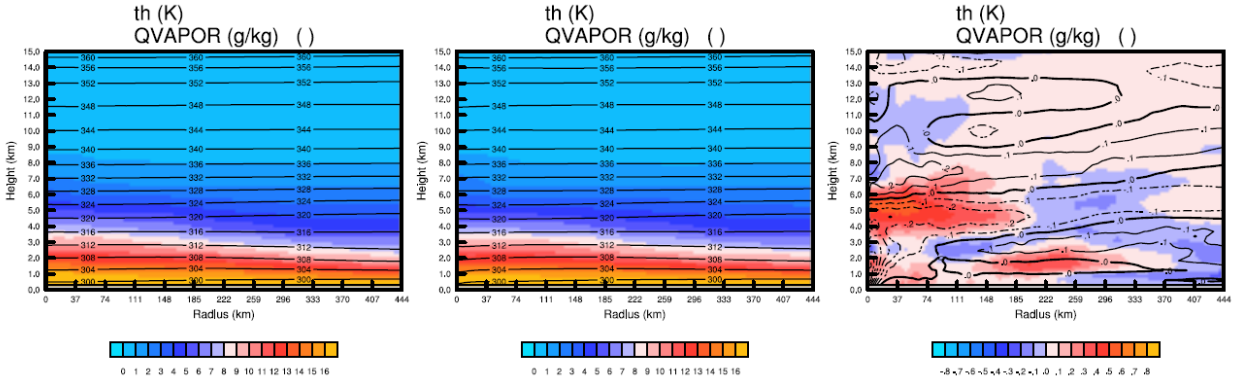

Figure 3-121. The azimuthally averaged and time-averaged water vapor mass mixing ratio (shading, units: g/kg) and potential temperature (contour, units: K). The time average is taken from 00UTC 25 August to 00UTC 27 August 2010. (a) ExDO-H; (b) ExDO-H-TurnoffDust; (c) ExDO-H minus ExDO-H-TurnoffDust (Solid contour lines indicate positive values and dashed contour lines indicate negative values).

(a) (b) (c)

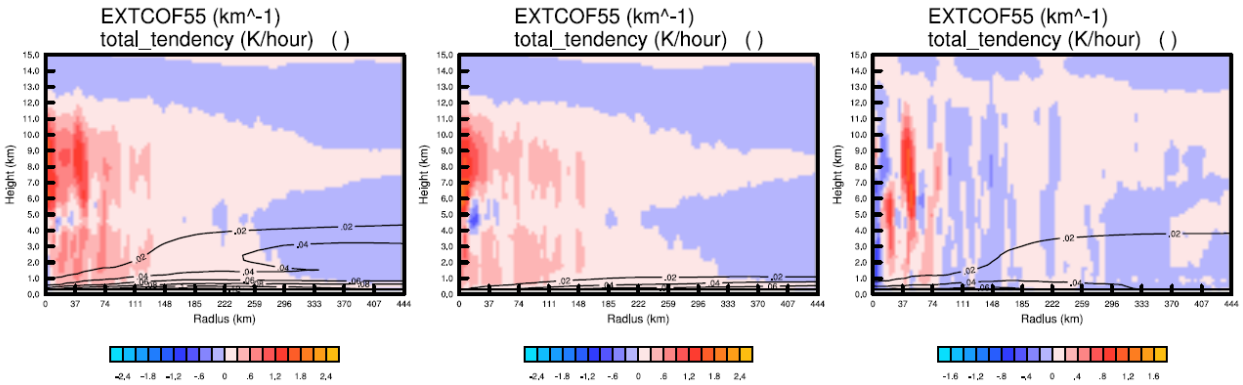

Figure 3-122. The azimuthally averaged and time-averaged total tendency (shading, units: K/hour) and extinction coefficient at 550nm (contour, units: km^{-1}). Total tendency includes shortwave radiative heating rate, longwave radiative heating rate, boundary heating rate, latent heating rate, and advection. The time

average is taken from 00UTC 25 August to 00UTC 27 August 2010. (a) ExDO-H; (b) ExDO-H-TurnoffDust; (c) ExDO-H minus ExDO-H-TurnoffDust (Solid contour lines indicate positive values and dashed contour lines indicate negative values).

4. Data assimilation

4.1 Data assimilation methods

Modern numerical weather forecasts use data assimilation to improve their accuracy. In this study, we want to examine how data assimilation improves the forecast of meteorological fields and aerosols.

Data assimilation is a method to combine information from models and observations. There are several data assimilation techniques: Optimal Interpolation(OI), three-dimensional variational analysis (3D-Var), four-dimensional variational data assimilation (4D-Var), Ensemble Kalman Filter (EnKF), etc.

EnKF is discussed here in detail since we use it in our experiments. Mathematically, data assimilation is an optimization problem. It is to find an optimal estimate of the current state given a first guess (which can be model forecast) and (previous or current) observations. Before EnKF was introduced, there were Kalman filter (Kalman 1960) for linear dynamic models and extended Kalman filter (EKF) for nonlinear dynamic models. EKF can be split into two alternative steps:

analysis step i,

$$
\begin{aligned}
K_i &= P_i^f \boldsymbol{H}_i^T [\boldsymbol{H_i} P_i^f \boldsymbol{H}_i^T + R]^{-1} \\
x_i^a &= x_i^f + K_i [y^o - \boldsymbol{H} x_i^f] \\
P_i^a &= [I - K_i \boldsymbol{H_i}] P_i^f
\end{aligned}
$$

forecast step i to i+1

$$
\begin{aligned}
x_{i+1}^f &= \boldsymbol{M}(x_i^a) \\
P_{i+1}^f &= \boldsymbol{M}_i P_i^a \boldsymbol{M}_i^T + Q_i
\end{aligned}
\qquad (4.1)
$$

Superscript a means analysis, f means forecast. Subscript i is the time index. K is a gain matrix, P is the error covariance matrix, it is continuously updated in an analysis and forecast cycle. $\boldsymbol{H}$ is observation operator, R is observational error covariance, x is the state vector, y^o is observation, Q is the model error covariance, M is the full nonlinear model, and $\boldsymbol{M_i}$ is a linearized model.

However, in nonlinear and high dimensional models such as atmospheric models, EKF has disadvantages: (1) storage and computational cost issue; for example, in the EKF scheme above, the dimensions of matrix P are large; (2) require linearization when deriving error covariance evolution equation.

To overcome the drawbacks of EKF, Evensen et al. (1994) proposed to use the ensemble to approximate and propagate the error covariance. Compared to EKF which explicitly forecasts the evolution of the complete forecast error covariance matrix using linear dynamics, EnKF estimates this matrix from a sample ensemble of fully nonlinear forecasts. The EnKF also addresses the computational difficulty of propagating and storing the forecast error covariance matrix, whose size equals to the square of the dimension of the forecast model (number of grid points times number of variables). Under assumptions of linearity of error growth and normality of observation and forecast errors, this scheme produces the correct background error covariances as ensemble size increases (Burgers et al. 1998). The ensemble Kalman filter (EnKF) was firstly applied in oceanography by Evensen et al., (1994) and in atmospheric research by Houtekamer & Mitchell (1998). Since then, EnKF has been widely used. There are several assumptions in this method: 1) Monte Carlo approximation to probability distribution functions; 2) Gaussian distributions used for computing update; 3) Localization in space: for each model grid point, only nearby observations are used to compute the analysis increment.

To implement EnKF in our experiments, we use the Data Assimilation Research Testbed (DART) developed at the National Center for Atmospheric Research (NCAR). It helps researchers to investigate data assimilation method in idealized models and high dimensional models easily. DART has several flavors of EnKF implemented. Here we choose the ensemble adjustment filter (Anderson 2001). The combination of DART and WRF has been used by many researchers for data assimilation and forecast of tropical cyclones (Torn and Torn 2010; Chen and Snyder 2007; Liu et al. 2012).

The data assimilation process can be demonstrated by the following diagram (Figure 4-1). The steps are:

(1) Use model to advance ensemble to time at which next observation becomes available.

(2) Get prior ensemble sample of observation, y=h(x), by applying forward operator h to each ensemble member.

(3) Get observed values and observational error distributions from the observing system.

(4) Find the increments for the prior observation ensemble.

(5) Use the ensemble samples of *y* and each state variable to linearly regress observation increments onto state variable increments.

(6) When all ensemble members for each state variable are updated, there is a new analysis that is integrated to the time of next observation.

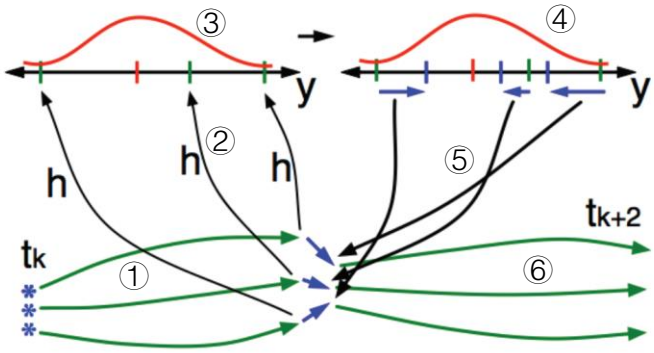

Figure 4-1. Data assimilation process. Adapted from DART website.

In this study, we modify the default WRF/DART:

(1) Replacing WRF by WRF-Chem to include chemistry;

(2) Adding required chemistry variables into the state variable vector;

(3) Adding the observation forward operator for MODIS AOD, which derives from the extinction coefficient at 550 nm from the WRF-Chem output;

(4) Implementing variable localization: MODIS AOD observation assimilation can only change AOD and AOD-related chemistry variables in the state vector, but not other meteorological fields. Meanwhile, assimilating meteorological observations can only change the meteorological fields but not the chemistry variables. Chemistry variables vary by the internal processes such as emission, transportation, and deposition in WRF-Chem;

(5) Data conversion tools are developed to convert MODIS AOD in HDF format to DART observation format.

4.2 Observation

Observations used in our study are conventional observations including radiosonde, aircraft communications addressing and reporting system(ACARS), Marine surface observations, and observations on land. Other observations are satellite wind, GPS refractivity, AIRS, and MODIS.

4.2.1 Conventional observations

A list of variables in a variety of conventional platforms is shown in Table 4-1. They are assimilated into the model by DART. Locations of the data in different platforms are shown in every 6 hours on 22 August 2010 (Figure 4-2 to Figure 4-5). Their locations are similar in other days. Radiosonde measurement has most of the data at 00UTC and 12UTC. They are mainly located on land and in the coastal region. Marine and ACARS observations cover the ocean. The plots shown here indicate the locations of the data before they are assimilated into the model. Some of them are rejected due to quality control in the data assimilation. The locations of the observations which are actually assimilated are not shown here.

Table 4-1. Variables in the conventional observations that were assimilated.

Data platform	Variables
Radiosonde	u wind component
	v wind component
	temperature
	surface altimeter

	relative humidity
Aircraft Communications Addressing and Reporting System (ACARS)	u wind component
	v wind component
	temperature
Marine	surface u wind component
	surface v wind component
	surface temperature
	surface altimeter
	surface relative humidity
Surface altimeter on land	altitude

(a) (b)

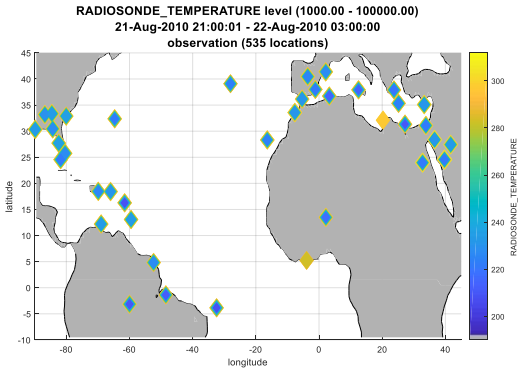

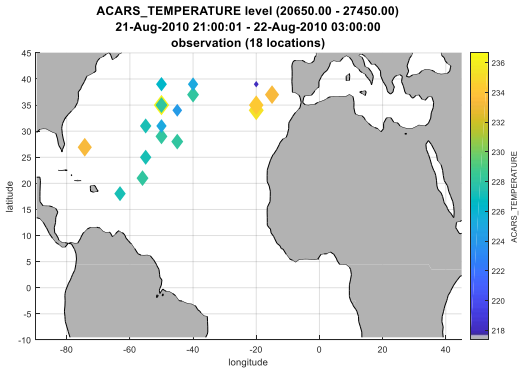

(c) (d)

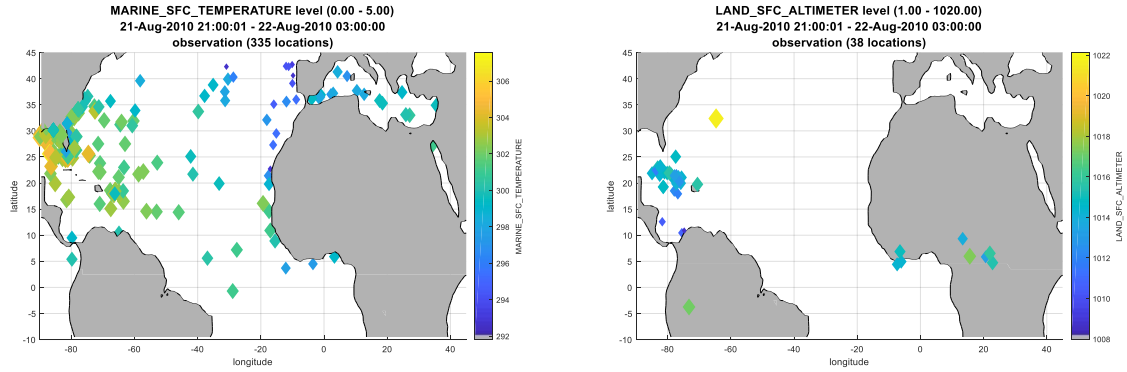

Figure 4-2. Locations of the conventional observations which are assimilated at 00UTC 22, August 2010. (a) Radiosonde; (b) ACARS; (c) Marine; (d) Land. Quality control value is no greater than 3 in DART.

(a) (b)

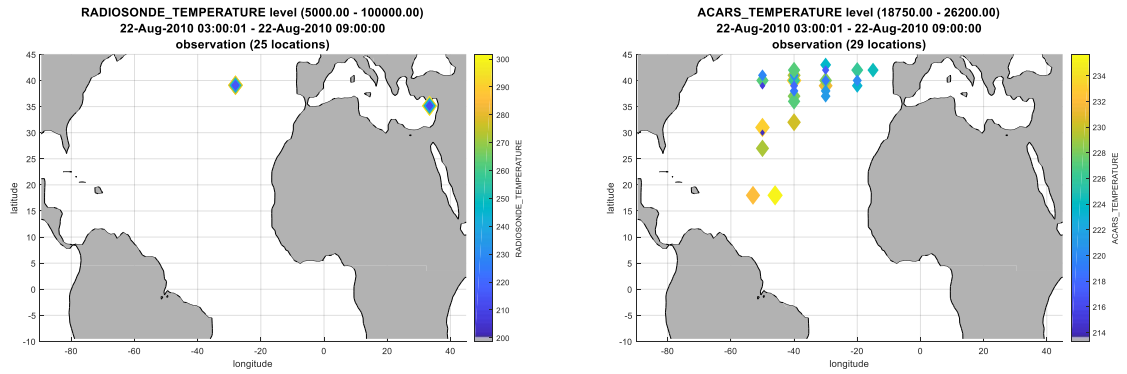

(c)

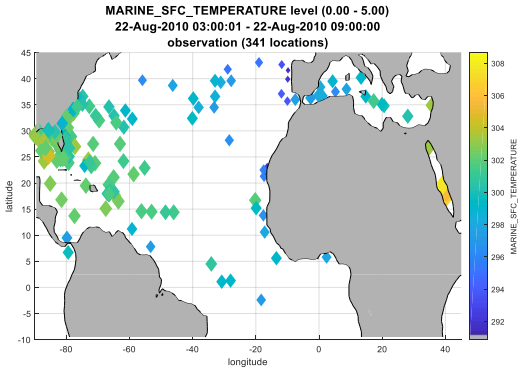

(d)

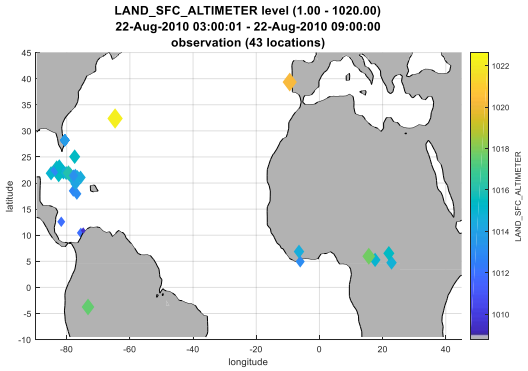

Figure 4-3. Same as Figure 4-2 but at 06UTC 22, August 2010.

(a)

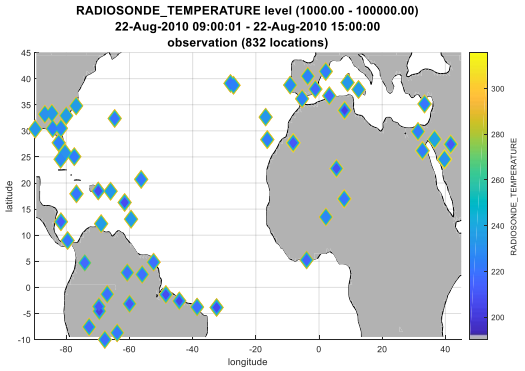

(b)

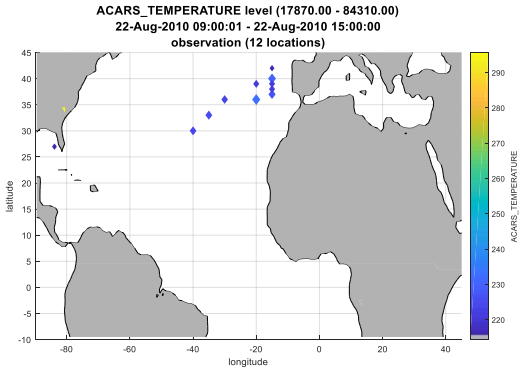

(c)

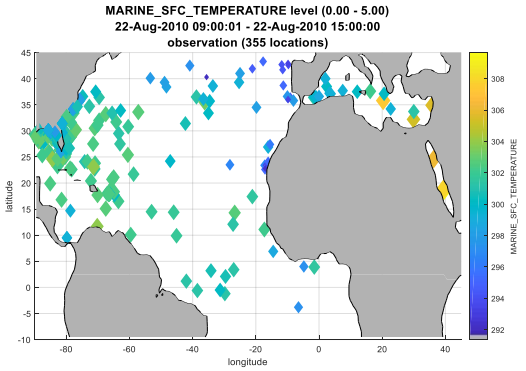

(d)

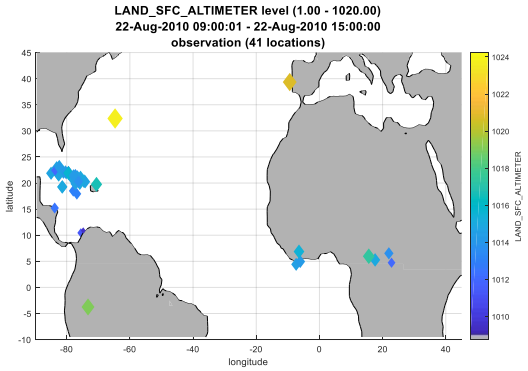

Figure 4-4. Same as Figure 4-2 but at 12UTC 22, August 2010.

(a)

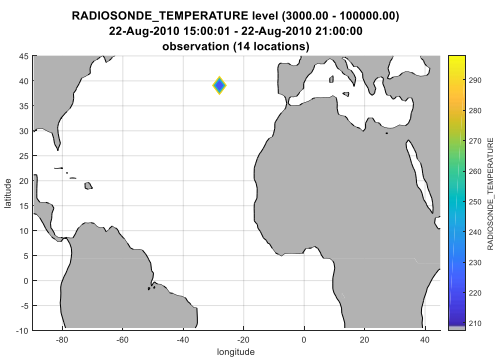

(b)

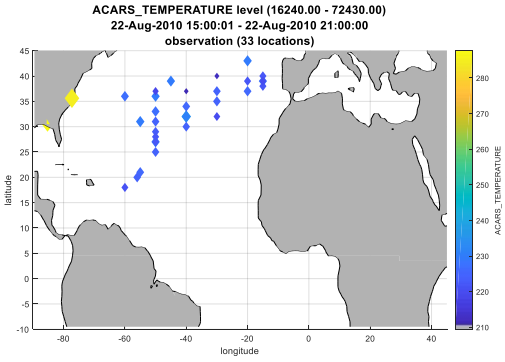

(c) (d)

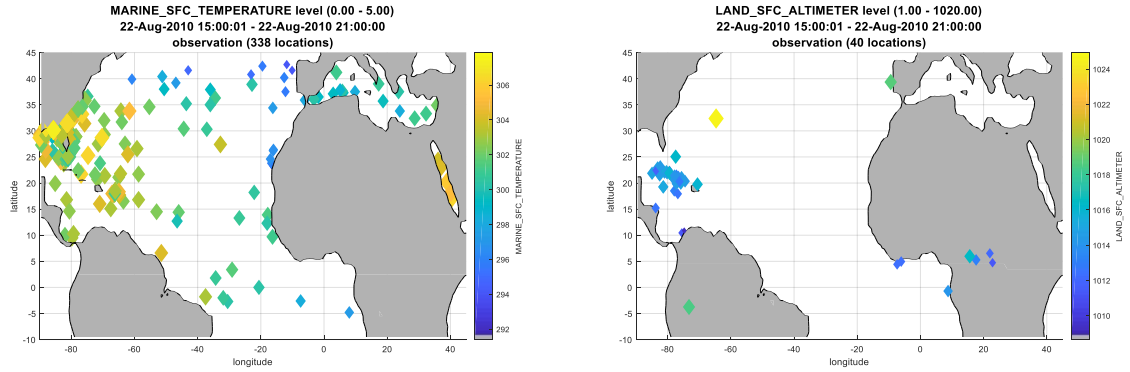

Figure 4-5. Same as Figure 4-2 but at 18UTC 22, August 2010.

4.2.2 Satellite wind

Satellite wind data are taken from the University of Wisconsin – CIMSS. The data coverage in our experiment is shown in Figure 4-6. Satellite data is useful in the data assimilation since it has much larger coverage compared to conventional observations.

(a)

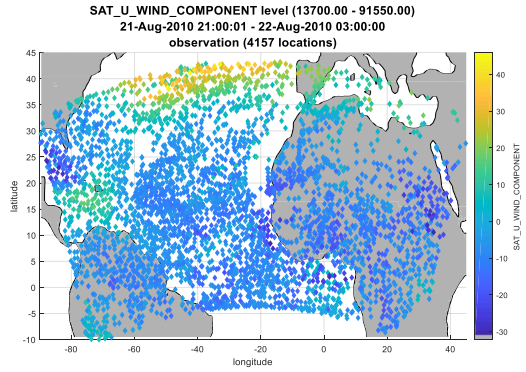

(b)

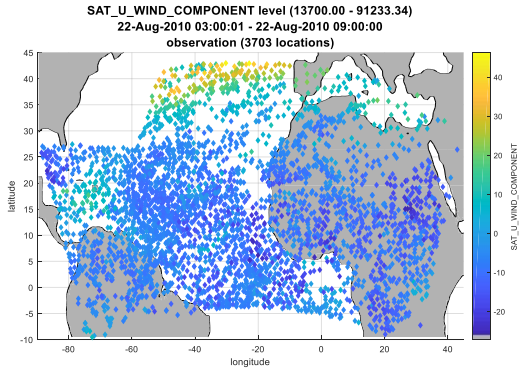

(c)

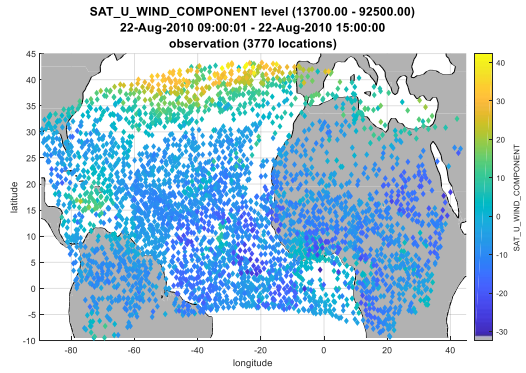

(d)

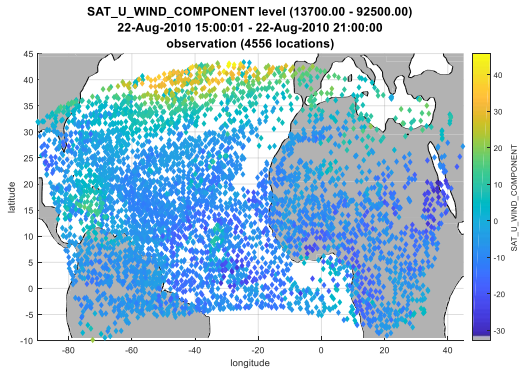

Figure 4-6. Locations of satellite wind data from CIMSS which are assimilated at (a) 00UTC 22; (b) 06UTC 22; (c) 12UTC 22; (d) 18UTC 22.

4.2.3 GPS refractivity

GPS Radio Occultation data are being returned from a series of satellites as part of the COSMIC project. The locations of the data are shown in Figure 4-7.

(a) (b)

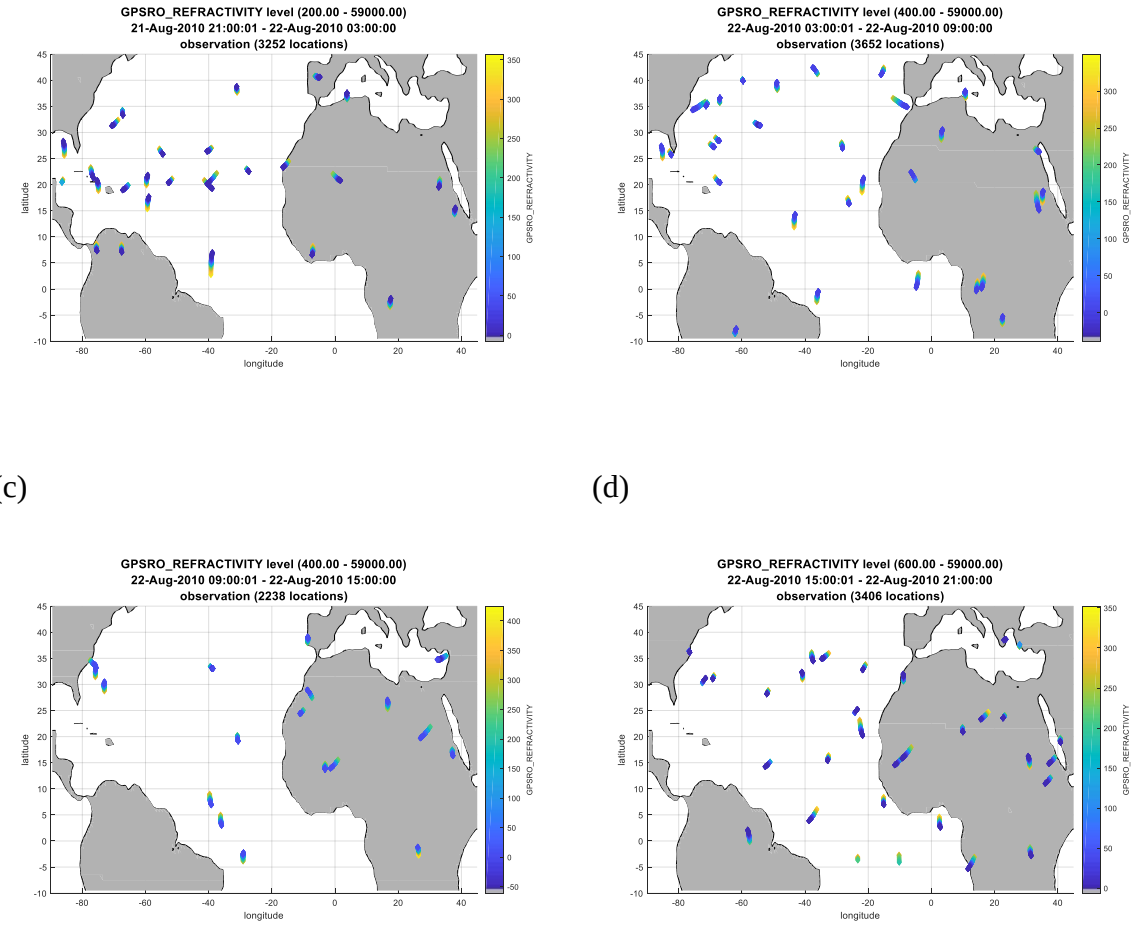

(c) (d)

Figure 4-7. Locations of GPS refractivity data from COSMIC which are assimilated at (a) 00UTC 22; (b) 06UTC 22; (c) 12UTC 22; (d) 18UTC 22.

4.2.4 MODIS AOD

AOD value can represent aerosol loadings in the atmosphere. Thus, assimilating AOD observation can correct aerosols in the model indirectly. MODIS AOD product provides abundant data which cover a large area. Assimilating MODIS AOD has been implemented into ECMWF

aerosol forecast (MACC-II product). There are a few other studies assimilated MODIS AOD as well. For example, Yin et al. (2016) used the Local Ensemble Transform Kalman Filter (only ten members) to assimilate MODIS AOD into an aerosol-coupled global model. 3DVAR data assimilation technique has been used to assimilate MODIS AOD into the WRF-Chem model (GOCART aerosol module) (Liu et al. 2011; Chen et al. 2017). They all result in an improved forecast of aerosols. However, very few people applied EnKF to assimilate MODIS AOD to investigate aerosol transport and its effects on the development of the tropical weather system. Because EnKF can provide flow-dependent background error covariance for the data assimilation, it is a good candidate for studying tropical convective system. We will apply this method in our study.

MODIS data are available from Aqua and Terra satellites. The MODIS instruments on Terra and Aqua image the same areas on Earth in approximately three hours apart. To maximize the availability of the data in our data assimilation experiment, both products are used.

There are mainly three aerosol algorithms in MODIS aerosol product: (1) Deep blue and Enhanced Deep Blue (DB/eDB) for land, (2) Dark Target (DT) for dark land, (3) Dark Target for the ocean (Table 4-2). Correspondingly, there are several datasets available: DB for land, DT for land, DT for the ocean, DT for both land and ocean, and merge version DB+DT for land and ocean. Since there are so many products can be chosen from, we need to have a plan to pick up some datasets to suit our experiments.

For MODIS AOD products over land, there are three types of datasets are available: DB, DT, and a merged version DB+DT. Beginning from the latest collection (version 6), Deep Blue product has been expanded from covering up only bright surface in the previous version to include vegetated region where it overlaps with Dart Target product. The correlation between DT and DB

is very high in the overlapping regions (Sayer et al. 2014). A merged version of them is also present in the current collection. All three products (DB, DT, and DB+DT) are suitable for quantitative applications (Sayer et al. 2014). However, only DB product has standard deviation provided directly in the data which is useful for data assimilation, while DT and DB+DT datasets do not have it. Only DB covers the desert region where we are interested in. Besides, DB also includes the region covered by DT. As a result, we only use Deep Blue product over land when we apply the data assimilation (Table 4-3).

In Deep blue product, quality assurance (QA) value ranges from 1 to 3, and the corresponding quality is from low to high. QA=1 is not recommended for scientific applications because the error may be underestimated due to cloud contamination (Hsu 2017). AOD with QA=3 in MODIS closely agrees with AERONET (Figure 4-8), while QA=2 has slightly higher uncertainty and should be suitable for most of the applications as well (Sayer et al. 2013). We only use data with QA equals to 2 and 3 (Table 4-3).

The expected error (EE) is provided in the deep blue product, which is one-standard deviation Gaussian confidence. It is estimated based on its comparison with AERONET data (Sayer et al. 2013). Higher AOD has a higher EE. EE value is used as the observation error in the data assimilation.

Table 4-2. Algorithm summaries for MODIS AOD, adapted from Sayer (2014).

Characteristic	e-Deep Blue (DB)	Dark Target (DT)	Ocean
Domain	Land	'Dark' (i.e. partly/fully vegetated) land	Dark (i.e. non-turbid/shallow) water
Averaging method	Retrieve then average	Average then retrieve	Average then retrieve
Aerosol optical model	Prescribed regionally/seasonally Sometimes retrieved	Fine model prescribed regionally/seasonally Coarse (dust analogue) model mixed in	Combination of 4 fine and 5 coarse modes 'Best' and 'average' solutions reported
Surface properties prescribed	Database or type-dependent dynamic, pseudo-Lambertian	Global dynamic relationship, pseudo-Lambertian	BRDF model incorporating glint, whitecaps, and fixed underlight
550 nm AOD uncertainty confidence envelope	~+/-(0.03+0.2*AOD_{MODIS}) (depends on geometric air mass)	+/-(0.05+0.15*$AOD_{AERONET}$)	+(0.04+0.1*$AOD_{AERONET}$) to -(0.02+0.1*$AOD_{AERONET}$)

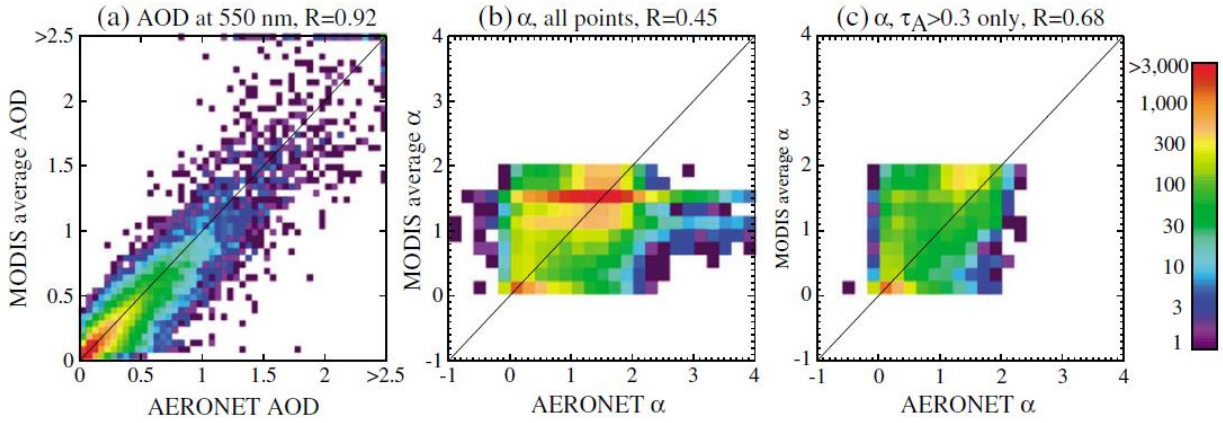

Figure 4-8. Scatter density histograms comparing AERONET and MODIS (a) AOD at 550 nm, (b) Angstrom exponent α, and (c) α for only those points where τ_A > 0.3. Only QA = 3 MODIS data are used. Adapted from Sayer et al. (2013)

Over the ocean, we use the DT product. MODIS AOD also matches AERONET well over the ocean (Figure 4-9). The expected error can be obtained from the value of AOD (τ), which is (-

0.02 τ - 10%), (+0.04 τ+10%) in collection 6.1. In the data assimilation, since we assume AOD follows a normal distribution which is symmetric, we use (+0.04 τ+10%) as the error.

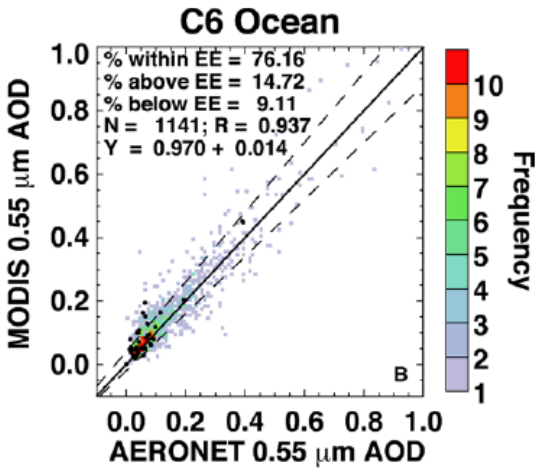

Figure 4-9. Frequency scatter plots for AOD at 0.55 μm over DT-ocean compared to AERONET (gray and color dots) and MAN (black dots), plotted from 6 months of Aqua (January and July; 2003, 2008 and 2010), computed with C6 algorithm. The one-one lines and EE envelopes (+(0.04 + 10 %), −(0.02 + 10 %), asymmetric) are plotted as solid and dashed lines. Collocation statistics are presented in the panel. Adapted from Levy et al. (2013).

Table 4-3. Datasets in MODIS that are used in the data assimilation.

	Dataset name	Data description	How to use
Land	Deep_Blue_Aerosol_Optical_Depth_550_Land_Best_Estimate	Deep Blue AOT at 0.55 micron for land with higher quality data (Quality flag=2,3)	
	Deep_Blue_Aerosol_Optical_Depth_550_Land_Estimated_Uncertainty	Estimated uncertainty (one-sigma confidence envelope) of Deep Blue AOT at 0.55 micron for land for all quality data (Quality flag=1,2,3)	
Ocean	Effective_Optical_Depth_Average_Ocean	Retrieved AOT for 'average' solution at 0.47, 0.55,0.66,0.86,1.24,1.63, 2.13 μm	Use 0.55μm
	Expected error for AOD over ocean	+(0.04 + 10 %), −(0.02 + 10 %)	+-(0.04 + 10 %)
	Land_Ocean_Quality_Flag	Quality Flag for Land and ocean Aerosol retrievals 0= bad; 1 = Marginal; 2= Good; 3=Very Good	Only use 2 and 3

The original resolution of MODIS AOD data is 10-km. Because our model horizontal resolution is 36-km, there are several MODIS AOD observations available in every model grid point. Since DART assimilates the observations sequentially, the model value at each grid point may be corrected by too many observations, which will over-correct the model value and makes the analysis too confident. Thus, we need to apply data thinning technique to the MODIS AOD data. The grid value from MODIS is selected in every 3 points. That leads to the average of 30-km resolution which is closer to the model resolution. By comparison of the data coverage, the distribution of the thinning data is similar to the distribution of the original data (figures not shown). MODIS AOD is usually available at 06UTC, 12UTC, and 18UTC for this domain, and most of the data are at 12UTC (Figure 4-10).

(a) (b)

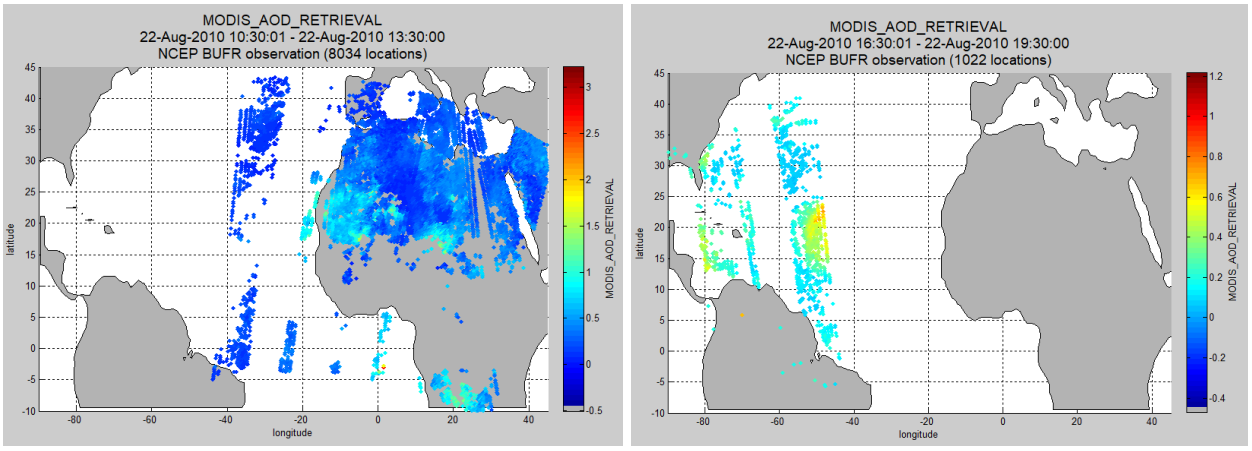

Figure 4-10. Locations of MODIS AOD which are assimilated at (a) 12UTC 22 and (b) 18UTC 22.

The data assimilation analysis step is performed every 6 hours at 00UTC, 06UTC, 12UTC, 18UTC. There is a time window at each analysis time. Data which have observation time within

the time window are assimilated. Different observations are given different time windows based on the data coverage, frequency, and common practice (Table 4-4).

Table 4-4. Assimilation window for different data products.

Observation platform	Assimilation window. units: hour
RADIOSONDE	± 1
ACARS	± 1
LAND	± 1
MARINE	± 0.5
CIMSS	± 1.5
COSMIC	± 2
MODIS	± 1.5

4.3 Model configuration

WRF-Chem used in previous chapters apply MOSAIC 8 bins module to treat aerosol processes. The dust process is treated by the GOCART dust scheme. Because running WRF-Chem with MOSAIC 8 bins module is computationally expensive, and EnKF data assimilation requires a set of ensemble runs, an aerosol module which is relatively fast and accurate enough is needed in our early study of using data assimilation to improve the aerosol forecast. Since dust is the main aerosol in our region, and other chemical processes are less important, we can choose another "simple GOCART" module available in WRF-Chem to deal with simple chemistry processes and dust process.

"Simple GOCART scheme" in WRF-Chem adapts the GOCART model. A detailed description of the GOCART model can be found in Chin et al. (2000a,b) and Ginoux et al. (2001). Originally, this is an "off-line" model which is driven by meteorological fields from other models. The GOCART algorithm is implemented in WRF-Chem, thus WRF/GOCART becomes an "on-line" model. The model has been evaluated by comparing between the ground-based measurements and satellite data with the model simulations in terms of aerosols size distributions and optical depth. The simulations generally agree with the observations (Chin et al. 2000a,b; Ginoux et al. (2001).

GOCART model contains several major aerosol types: dust, sulfate, organic carbon (OC), black carbon (BC), and sea salt. Dust and sea salt in GOCART are treated using the sectional approach, in which there are five bins for dust and four bins for sea salt. The size bins are based on dry physical diameter. In each bin, the particles are assumed to be spherical and internally mixed. On the contrary, OC and BC are treated using the bulk approach, in which mass mixing ratio is used.

GOCART dust process in this "simple GOCART scheme" is the same as the dust process in MOSAIC 8 bins module in our previous experiments except the number of bins is different. It only considers dust direct effect. The model has been used widely to study the dust direct effect (Chen et al. 2017).

In this experiment, the initial and boundary conditions are also obtained from MACC-II. The data conversion of dust, sea salt, OC and BC from MACC-II to the GOCART aerosols module in WRF-Chem is similar to previous experiments, except dust and sea salt have different bins.

Similar to the reason of modifying emission factors in MOSAIC module, we also tune the emission factors for dust and sea salt in this simple GOCART scheme to better match MODIS

AOD in test experiments. After the test, the emission factor for dust is changed from 1.0 to 0.5 (the same as MOSAIC 8 bins), and the emission factor for sea salt is changed from 1.0 to 0.4 (from 1.0 to 0.8 in MOSAIC 8 bins).

Table 4-5 lists all the experiment configurations. For simplicity, we name all observations except MODIS as conventional observations. They include Radiosonde, Marine, ACARS, Land, Satellite wind, and GPS. MODIS observation includes AOD.

In ExC, we run WRF without any chemistry. This is the same control experiment we conducted before.

In ExC+C, based on ExC, we assimilate conventional observations.

In ExDO, we use simple GOCART chemistry option in WRF-Chem. Dust and other aerosols are included in the model.

In ExDO+CM, based on ExDO, we assimilate conventional observations and MODIS AOD.

In the experiment ExC+C, the ensemble perturbations for meteorological initial and boundary conditions are generated by drawing spatially correlated noise from static background error covariance. The perturbations are added to the initial and boundary conditions of the control run to form the ensemble members. We run the ensemble models from the perturbed meteorological initial and boundary conditions at 12UTC 21 for six hours. From 18UTC 21, we assimilate conventional observations followed by another 6-h forecast before the next assimilation. The 6-h forecast and analysis cycle runs until 00UTC 27.

For the experiment ExDO+CM, we divide the data assimilation period into two stages:

(1) The initial ensemble generation is the same as ExC+C. Then from 18UTC 21 to 12UTC 22, we assimilate conventional observations but not MODIS AOD because we need to generate chemistry perturbations before assimilating MODIS AOD.

(2) MODIS AOD is assimilated began at 12UTC 22, and the data assimilation cycle is performed every 6 hours until 00UTC 27.

Table 4-5. Data assimilation set up.

Experiment name	Model	Aerosol module	Assimilate observations
ExC	WRF	None	None
ExC+C	WRF	None	Conventional observations (Radiosonde, Marine, ACARS, Land, Satellite wind, GPS)
ExDO	WRF-Chem	GOCART	None
ExDO+CM	WRF-Chem	GOCART	Conventional observations (Radiosonde, Marine, ACARS, Land, Satellite wind, GPS) and MODIS

4.4 Data assimilation results

Comparing ExC and ExC+C, data assimilation of conventional observations improves the storm track as it moves closer to the best track (Figure 4-11). The track error is reduced by 43%.

We see the similar improvement from ExDO to ExDO+CM, the track error is reduced by 48%. This indicates that although we assimilate both conventional observations and MODIS AOD at the same time, the major improvement for estimating the storm track mainly comes from assimilating conventional observations. In ExDO+CM, the model has a better meteorological background for the aerosol forecast.

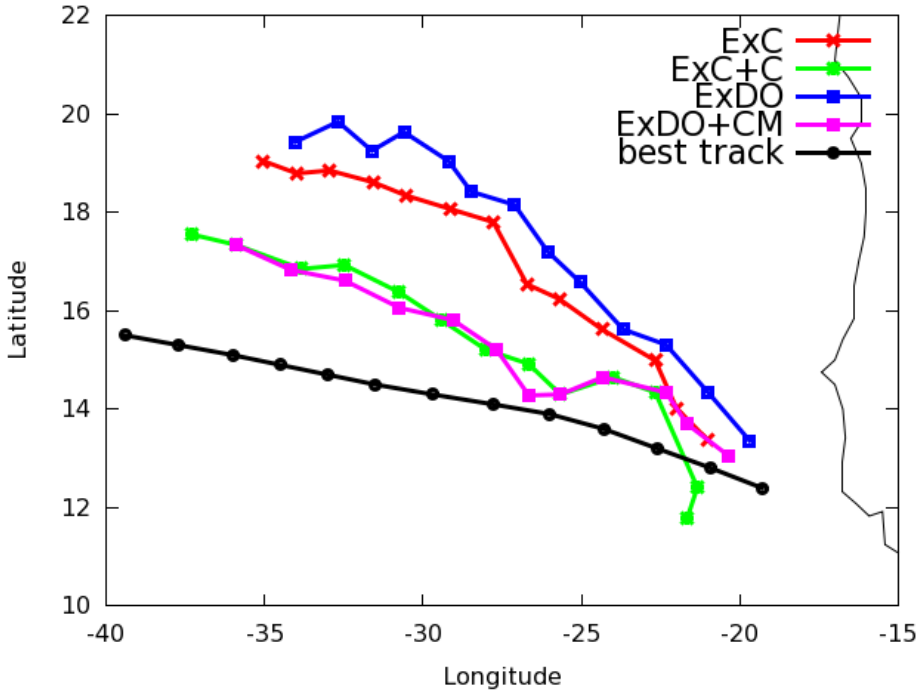

Figure 4-11. Simulated tracks and best track from 00UTC 24 to 00UTC 27 August 2010. The interval between neighboring dots is six hours.

In ExDO+CM, we want to first verify whether the assimilation of conventional observations is reasonable. For radiosonde temperature, both root mean square error (RMSE) and total spread

(the square root of the sum of the ensemble variance and the error variance associated with the observation) show reasonable values before data assimilation, and they are reduced after assimilating conventional observations. The averaged RMSE of radiosonde temperature in the prior is 1.385, and it is reduced to 1.2499 in the posterior (Figure 4-12a). The RMSE from 500 hPa to 700 hPa is about 1K in both the prior and the posterior, which is a reasonable value. The same conclusion can be drawn for the satellite wind (Figure 4-12b).

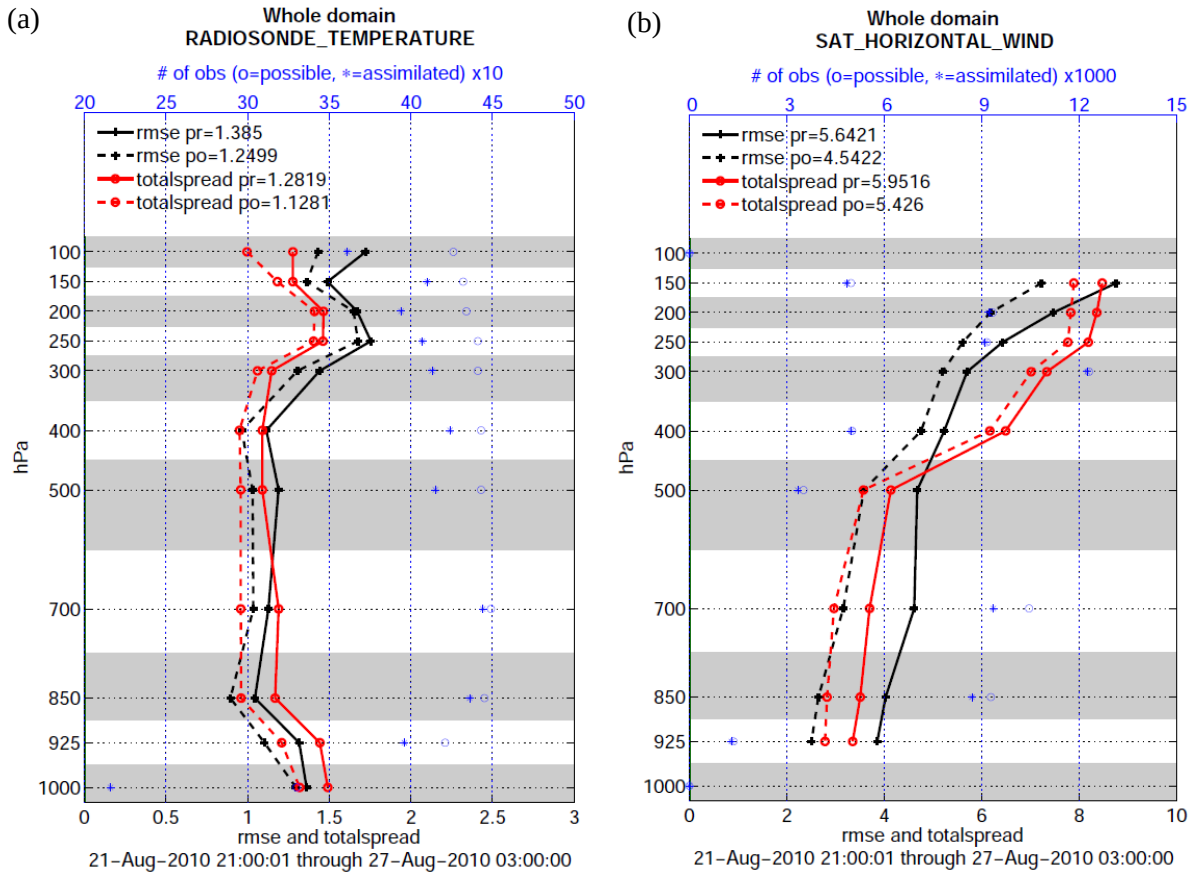

Figure 4-12. RMSE and total spread in prior and posterior from 00UTC 22 to 00UTC 27 August 2010 for (a) radiosonde temperature, (b) satellite horizontal wind.

In ExDO+CM, the model AOD in the forecast (prior) has a lower bias, especially comparing to high MODIS AOD values at the beginning of the assimilation (12UTC 22) (Figure 4-13a). The bias is reduced gradually as the model continues to assimilate data every 6 hours. The open circle in Figure 4-14 indicates the number of available MODIS AOD observations and the cross symbol indicates the number of MODIS AOD observations that are assimilated. They are close to each other. That means most of the data can be assimilated into the model because model AOD is not far away from MODIS AOD,

AOD RMSE is reduced after the data assimilation in every analysis time (Figure 4-14a). Although RMSE increases in the forecast when MODIS AOD observations are not available, RMSE has a decreasing trend. On average, RMSE is reduced from 0.14785 in the forecast to 0.10168 in the analysis. Figure 4-14b shows total spread. The total spread of model AOD in the analysis is close to the forecast after assimilating MODIS AOD (Figure 4-14b).

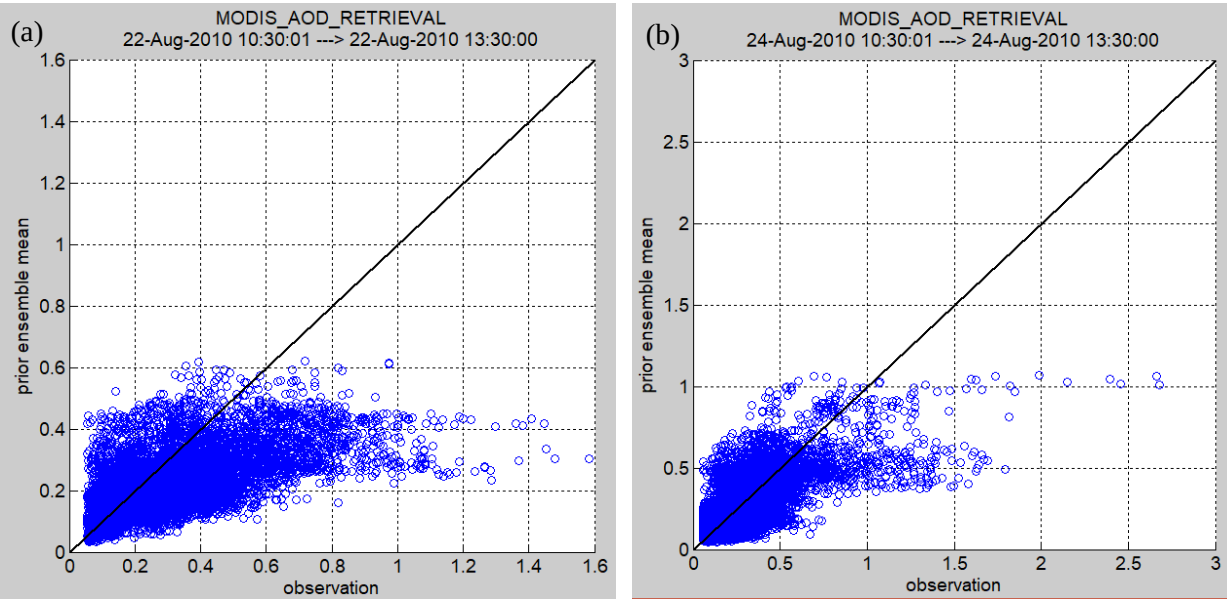

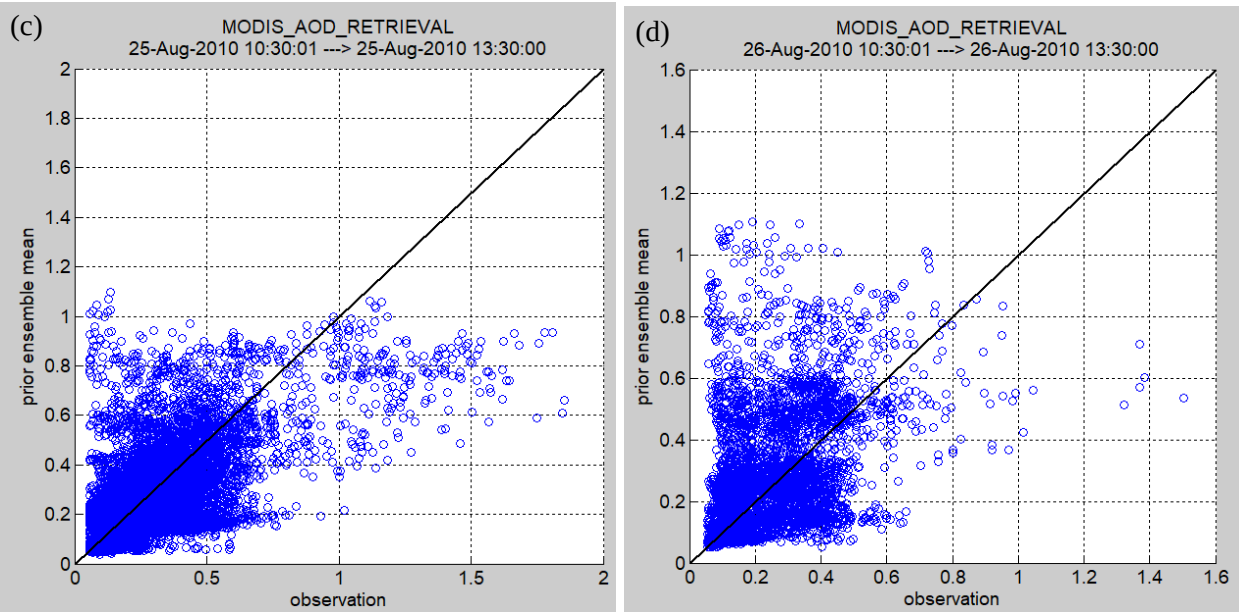

Figure 4-13. Ensemble mean in the prior (y axis) vs MODIS AOD (x axis) in August 2010. (a) 12UTC 22; (b) 12UTC 24; (c) 12UTC 25; (d) 12UTC 26.

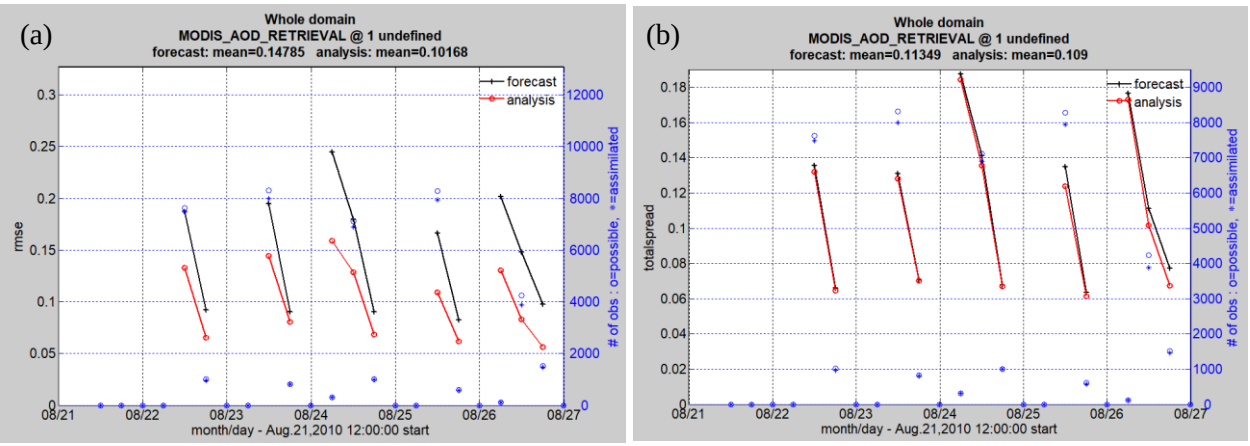

Figure 4-14. AOD diagnostics in the forecast and the analysis from 22 to 27 August 2010 from the experiment ExDO+CM. (a) RMSE; (b) total spread.

The horizontal distribution of the model AOD shows that relatively large differences in the forecast and analysis are on Sahara and on its west coast where MODIS observations are available

(Figure 4-15). At the beginning of the data assimilation period at 12UTC 22, the largest increment after the data assimilation is on the west coast of Africa. Because assimilating MODIS AOD corrects the model AOD gradually, the patterns in the forecast and in the analysis are getting closer with time.

We compare AOD before and after the data assimilation with AERONET AOD (Figure 4-16). We use the same method in section 3.3.2.2 to obtain AERONET AOD. During the data assimilation period, many stations in the domain reported missing data. Moreover, our experiment only does the analysis every 6 hours, but AERONET does not have many observations taken at the same analysis time. Thus, we only find two stations in the Sahel region, which can provide a decent amount of data for comparison.

At the Banizoumbou station, AOD values from ExDO (before the data assimilation) are generally larger than the AERONET AOD. Data assimilation lowers the model AOD values and moves them towards the AERONET AOD, although the AOD biases can be larger sometimes after the data assimilation. At the Zinder airport, model AOD is worse after the data assimilation compared to half of the AERONET observations. We then produce a composite plot for the Sahel region. Since Zinder airport is close to Banizoumbou station, when both Zinder airport and Banizoumbou station have observations at the same time, we take an average of AOD in these two stations to represent AOD in Sahel region. For the period when observations are only available from Zinder airport, we just use those observations. The composite plot shows that the error of the model AOD is reduced by 46% after the data assimilation.

In summary, data assimilation proves to be a good technique to improve the track forecast and the aerosol forecast. In spite of the usefulness of the data assimilation, we didn't use it before the sensitivity analyses in the previous chapters. The reasons are:

(1) Assimilating the meteorological variables include temperature will wipe out the effect from the dust. If we want to study the pure dust effect, we should avoid that.

(2) Assimilating only the MODIS AOD can indeed improve the dust forecast and provide a better background for analyses. However, because the model domain is large, the running speed of the aerosol scheme is slow, and EnKF requires an ensemble of models, we cannot afford to conduct such data assimilation before the sensitivity analyses at the moment. In the future, we can consider that and compare to our current results.

(a)

(b)

(c)

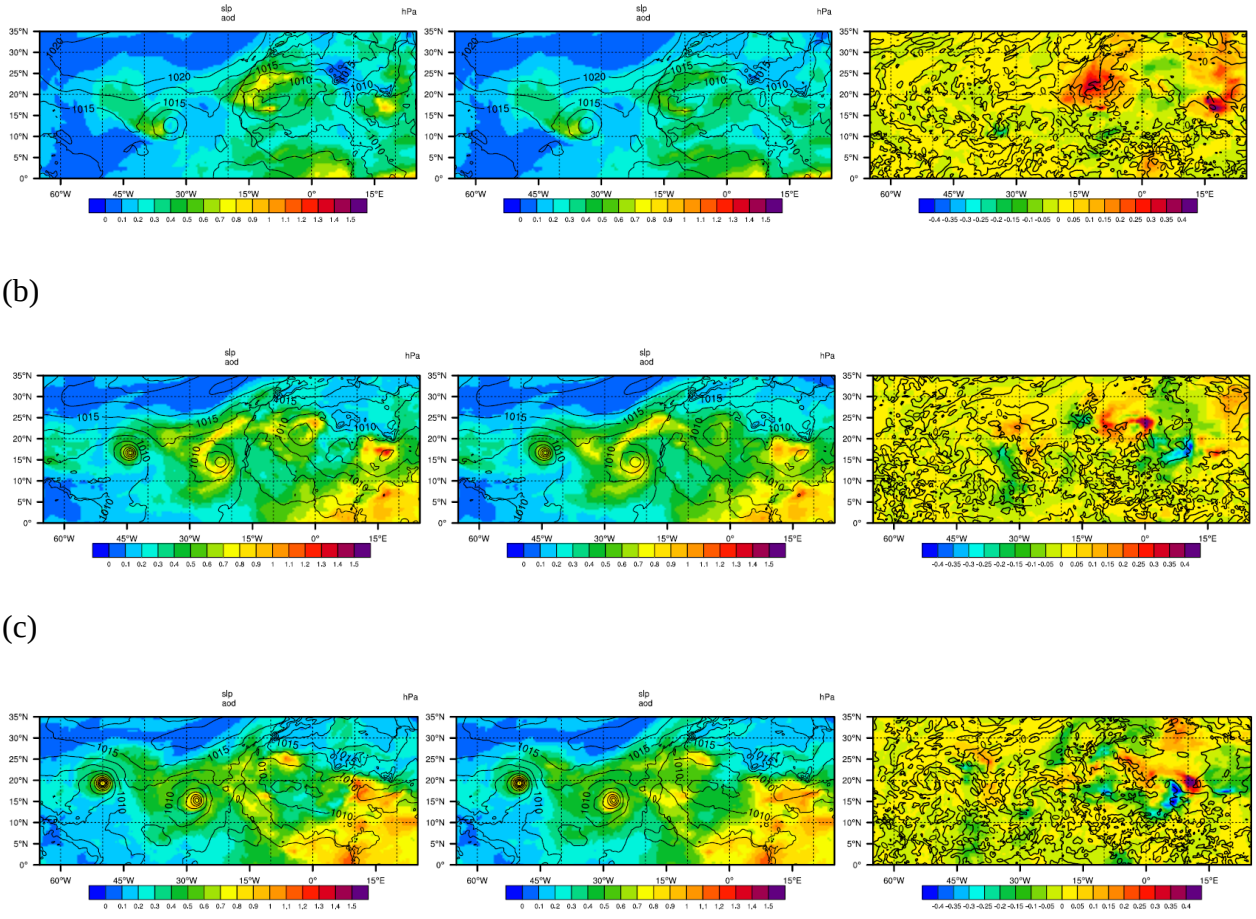

Figure 4-15. Model AOD (shading) and sea level pressure (contour, units: hPa) from the experiment ExDO+CM. (left) Model AOD after assimilating MODIS AOD, (middle) Model AOD before assimilating

MODIS AOD, (right) Difference (after assimilation – before assimilation) at (a) 12UTC 22, (b) 12UTC 24, (c) 12UTC 25.

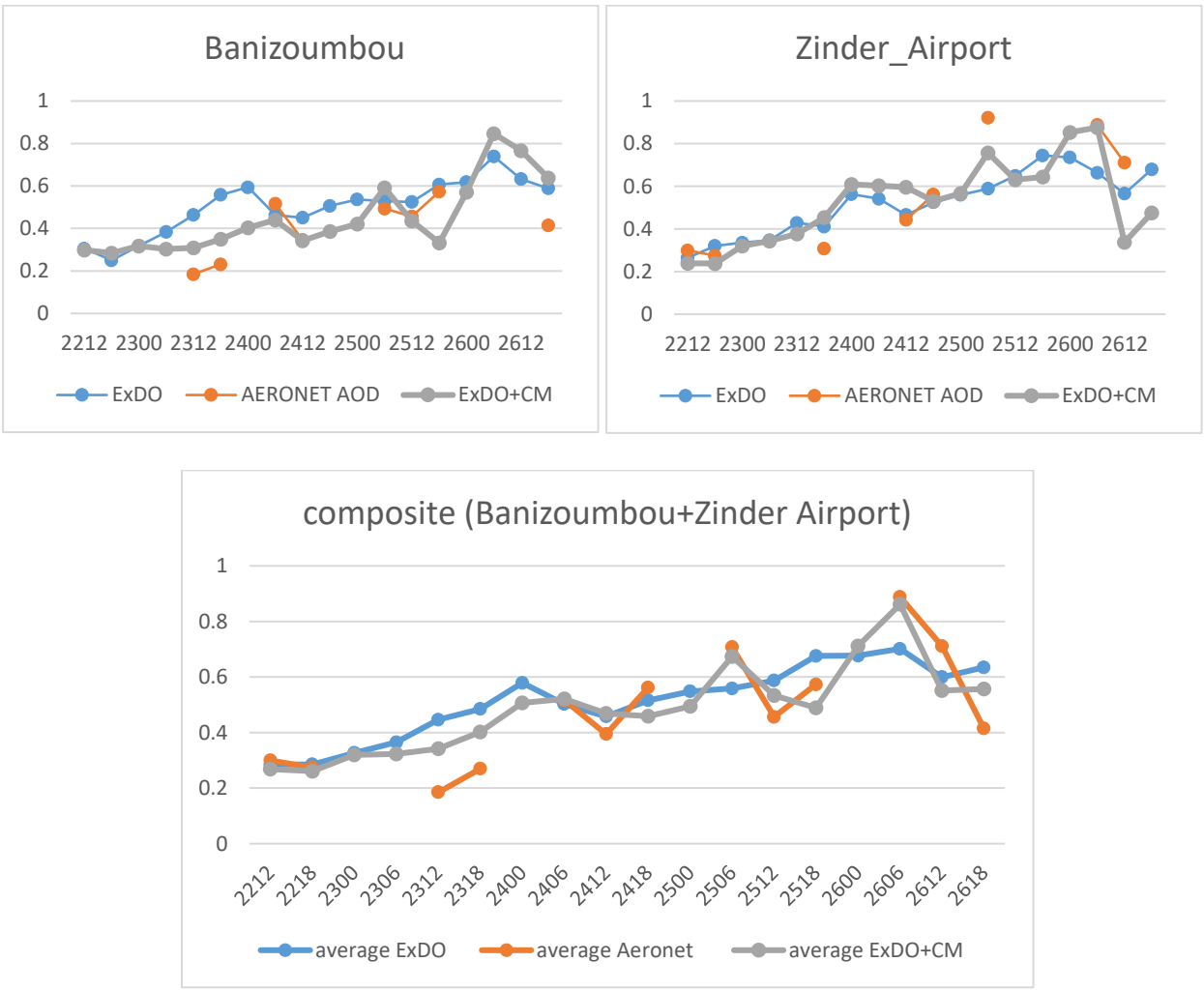

Figure 4-16. AOD from model and AERONET at the Banizoumbou and Zinder airport stations. The composite plot is the combination of AOD from two stations.

5. Conclusion and Future work

In this thesis, we investigate the impact of Saharan dust aerosols on the development of the tropical weather systems such as AEWs, the AEJ and tropical cyclones. The impact is quantified by studying the Hurricane Earl (2010) which developed from the AEW under the influence of SAL.

The WRF model coupled with online chemistry module (WRF-Chem), which includes aerosol-cloud interaction and radiative effect, is used to study this subject. We forecast the system from 12UTC 21 August 2010 to 00UTC 27 August 2010. The forecasts from some operational centers in this period have tracks biased to the north-east. Our model also produces biased tracks, but the biases are within a reasonable range compared to the operational forecasts. The AEWs, AEJ, and the surface low-pressure system in our simulations are stronger compared to the best track observation and reanalysis data. Model verification shows that the model can represent the SAL structure. The model can also forecast the distribution and the evolution of the aerosols reasonably well. We first study the dust effect by conducting two 36-km resolution simulations: one with all aerosols including dust (ExDO), and the other exclude dust (ExO).

At the surface, a surface low-pressure system is present while AEWs are existing in upper levels. When the low-pressure system is over North Africa, heating from the boundary during the daytime is the dominant heating source in the lower atmosphere. Dust has a direct radiative effect but not indirect effect because the region is free of clouds. Adding dust reduces the boundary heating in the daytime by reducing the surface temperature. The reduction of the surface temperature is a result of the reduction of shortwave radiation reaching the surface due to dust blocking partial incoming solar radiation. Although dust absorbs solar radiation and warms up the atmosphere, it cannot compensate for the loss of boundary heating. During the nighttime, longwave

radiative cooling is the dominant process. Adding dust increases such cooling effect. Overall, dust cools the column of the atmosphere. Because the low-pressure system is a warm core system in this region, the temperature cooling due to dust increases the surface center pressure. Therefore, the low-pressure system becomes weaker. However, the magnitude of the difference is minimal-less than 1 hPa on average.

The AEJ is generated and maintained by the horizontal temperature gradient and the thermal wind balance. Warmer temperature is located in the north where the atmosphere over Sahara is dry and hot. The AEJ is intensified in the south and weakened in the north when the simulation includes dust. It implies a slight southward shift of AEJ.

The AEW at 600 hPa associated with the surface low-pressure system decays gradually before it moves to the ocean. Then it intensifies as more moisture become available over the ocean. The intensity of the AEW at 850 hPa generally increases as it moves to the west due to more moisture available. The AEW at 600 hPa shifts to the south slightly after adding dust at the beginning. When dust is included, AEW intensity changes little at the beginning, then increases, and finally decreases. The AEWs at 850 hPa and 600 hPa merge when they move to the ocean, and they trigger tropical cyclogenesis. AEWs and low-pressure center at the surface are getting closer with time. The AEWs in the experiment containing dust are weaker than those without dust. Such difference grows larger with time.

When the system moves to the ocean, latent heat release by moist convection becomes the dominant heating and cooling sources. We conduct two additional higher resolution simulations (4-km resolution, ExDO-H includes dust and ExO-H excludes dust) which take the outputs from the previous two coarse resolution simulations (36-km resolution) to study dust microphysical effect. The simulations use double-moment microphysics scheme to study the interaction between

aerosols and microphysical processes. Increasing the model resolution reduces the intensity of the cyclone and brings the intensity closer to the observation. The error of the central pressure and the maximum surface wind speed are reduced by 58% and 46% respectively. However, the track forecast errors remain. The system is weaker in the simulation with dust, following the same trend as the coarse resolution simulations. Their difference can be traced back to the difference of the AEW developed over Africa.

These two high-resolution simulations do not separate the difference solely due to dust microphysics effect and the difference in the initial meteorological fields. Thus, we conduct one additional high resolution simulation (ExDO-H-TurnOffDust) in which we eliminate dust in the initial and boundary conditions in the experiment ExDO-H. We then compare them to understand how dust play a role when the system is over the ocean.

The tracks of the cyclone in these two experiments are almost identical (ExDO-H vs ExDO-H-TurnOffDust). The minimum sea-level pressure in the center in the experiment with dust is slightly lower than its counterpart. The difference is less than 1 hPa for most of the time. Thus, dust microphysics effect alone has a small impact on the dynamics of the cyclone.

In the tropical low stage, convection is more active in the southern periphery of the system. Convection promotes the formations of cloud, rain, snow, and graupel in the region. Downward motion around the center is not a result of the SAL; it is the large-scale descent motion from the mid and upper atmosphere. Dust increases the low-level cloud at 1-2 km height. It reduces rainfall in the outer edge of the SAL region between 250 km to 350 km radii, but increases rainfall in the inner edge at around 200 km. The associated latent heat release shifts the updraft radially inward. The dynamical consequence is the acceleration of tangential wind and the mid-level cyclogenesis.

The tropical depression stage has different dynamics than the tropical low stage. The system becomes stronger as the upward vertical motion intensifies and concentrates around the center of the system. Stronger convection in the center promotes cloud droplets growing into rain droplets and ice particles. Adding dust increases the convection around the center inside 80 km radius. More ice, snow, and rain appear there. Dust aerosols act as CCNs to increase the number of cloud droplets and cloud mass mixing ratio in most of the region. Rain, snow, and graupel mixing ratios increase in the enhanced updraft region, but they are reduced in the weakened updraft region between 80 to 150 km.

There is no simple relationship between the storm intensity and dust. Contrary to most previous studies which claim dust imposing a significant impact on tropical storms. In our case, the changes of the tropical storm, the AEJ, and the AEWs due to dust are smaller compared to many other studies. We believe those studies which found significant dust or SAL effects usually utilize simplified models or simple specifications of dust and/or SAL. Since our model includes more processes and applies an interactive aerosol module to study this subject, it is relatively more accurate, at least for this case. Our results suggest a pure meteorological model without complicated chemistry is sufficient for hurricane track and intensity forecast as long as the SAL is properly represented.

Finally, we use a simple chemistry model GOCART to forecast aerosols. Both conventional observations and MODIS AOD are assimilated using the EnKF data assimilation. Data assimilation improves the forecast for the storm and the aerosols.

The main contributions of this study to the scientific community are:

(1) After conducting a thorough overview of the literature, we compare the differences of their experiment designs and conclusions, and then identify the reasons behind the discrepancies.

(2) We try to overcome the limitations of the experiment designs in some previous studies. We use a coupled atmosphere and chemistry/aerosol model with better physical processes to investigate the sole impact of dust qualitatively and quantitatively. The initial and boundary conditions for the aerosols in our simulation are taken from the global aerosol models.

(3) We developed the method and tool to convert the aerosols from global aerosol forecast model to the WRF model.

(4) Our experiments include different stages of the tropical storm from the AEW to the tropical depression. The impact from dust to different stages of the system are evaluated, which are rarely done by many previous studies.

(5) We conduct the analysis in a variety of ways. The dust radiative and microphysical effects are both investigated.

(6) We use EnKF data assimilation to assimilation MODIS AOD to improve the aerosol forecast. According to the author's current knowledge, we are one of the few people to do that.

Although we conduct the experiments carefully, there are some limitations in our study as well. Since we just use one case in our study, our conclusions for this case may not apply to other cases. In the near future, we will select more cases to study this subject. Furthermore, we might also consider using global high-resolution models with aerosol forecasts to study the dust climatological effects on tropical weather systems.

Bibliography

AIRS Science Team/Joao Texeira, 2013: AIRS/Aqua L2 Standard Physical Retrieval (AIRS-only) V006. Greenbelt, MD, USA, Goddard Earth Sciences Data and Information Services Center (GES DISC), Accessed: 30 December 2012, 10.5067/Aqua/AIRS/DATA202

Anderson, J. L., 2001: An Ensemble Adjustment Kalman Filter for Data Assimilation. *Mon. Weather Rev.*, **129**, 2884–2903, doi:10.1175/1520-0493(2001)129<2884:AEAKFF>2.0.CO;2. http://journals.ametsoc.org/doi/abs/10.1175/1520-0493%282001%29129%3C2884%3AAEAKFF%3E2.0.CO%3B2.

Archer-Nicholls, S., and Coauthors, 2014: Gaseous chemistry and aerosol mechanism developments for version 3.5.1 of the online regional model, WRF-Chem. *Geosci. Model Dev.*, **7**, 2557–2579, doi:10.5194/gmd-7-2557-2014.

——, and Coauthors, 2015: Characterising Brazilian biomass burning emissions using WRF-Chem with MOSAIC sectional aerosol. *Geosci. Model Dev.*, **8**, 549–577, doi:10.5194/gmd-8-549-2015.

Ayash, T., S. Gong, C. Q. Jia, T. Ayash, S. Gong, and C. Q. Jia, 2008: Direct and Indirect Shortwave Radiative Effects of Sea Salt Aerosols. *J. Clim.*, **21**, 3207–3220, doi:10.1175/2007JCLI2063.1.

Bar??, R., and Coauthors, 2015: Sensitivity analysis of the microphysics scheme in WRF-Chem contributions to AQMEII phase 2. *Atmos. Environ.*, **115**, 620–629, doi:10.1016/j.atmosenv.2015.01.047.

Bierwirth, E., and Coauthors, 2009: Spectral surface albedo over Morocco and its impact on radiative forcing of Saharan dust. *Tellus, Ser. B Chem. Phys. Meteorol.*, **61**, 252–269, doi:10.1111/j.1600-0889.2008.00395.x.

Boers, R., J. R. Acarreta, and J. L. Gras, 2006: Satellite monitoring of the first indirect aerosol effect: Retrieval of the droplet concentration of water clouds. *J. Geophys. Res. Atmos.*, **111**, 1–13, doi:10.1029/2005JD006838.

Brammer, A., and C. D. Thorncroft, 2017: Spatial and Temporal Variability of the Three-Dimensional Flow around African Easterly Waves. *Mon. Weather Rev.*, **145**, 2879–2895, doi:10.1175/MWR-D-16-0454.1. http://journals.ametsoc.org/doi/10.1175/MWR-D-16-0454.1.

Braun, S. A., 2010: Reevaluating the Role of the Saharan Air Layer in Atlantic Tropical Cyclogenesis and Evolution. *Mon. Weather Rev.*, **138**, 2007–2037, doi:10.1175/2009MWR3135.1. http://journals.ametsoc.org/doi/abs/10.1175/2009MWR3135.1.

Braun, S. A., and J. A. Sippel, 2013: The Evolution and Role of the Saharan Air Layer during Hurricane Helene (2006). *Mon. Weather Rev.*, **141**, 4269–4295, doi:10.1175/MWR-D-13-00045.1.

Burgers, G., P. Jan van Leeuwen, and G. Evensen, 1998: Analysis Scheme in the Ensemble Kalman Filter. *Mon. Weather Rev.*, **126**, 1719–1724, doi:10.1175/1520-0493(1998)126<1719:ASITEK>2.0.CO;2. http://journals.ametsoc.org/doi/abs/10.1175/1520-0493%281998%29126%3C1719%3AASITEK%3E2.0.CO%3B2.

Burpee, R. W., 1972: The Origin and Structure of Easterly Waves in the Lower Troposphere of North Africa. *J. Atmos. Sci.*, **29**, 77–90, doi:10.1175/1520-0469(1972)029<0077:TOASOE>2.0.CO;2. http://journals.ametsoc.org/doi/abs/10.1175/1520-0469%281972%29029%3C0077%3ATOASOE%3E2.0.CO%3B2.

Cangialosi, J. P., 2011: *Tropical Cyclone Report Hurricane Earl*.

Carlson, T. N., 1969: Some remarks on African disturbances and their progress over the tropical Atlantic. *Mon. Weather Rev.*, **97**, 716–726, doi:http://dx.doi.org/10.1175/1520-0493(1969)097<0716:SROADA>2.3.CO;2. http://journals.ametsoc.org/doi/abs/10.1175/1520-0493(1969)097%3C0716:SROADA%3E2.3.CO;2%5Cnhttp://journals.ametsoc.org/doi/abs/10.1175/1520-0493(1969)097%3C0716:SROADA%3E2.3.CO%3B2.

CARLSON, T. N., 1969: Synoptic Histories of Three African Disturbances That Developed Into Atlantic Hurricanes. *Mon. Weather Rev.*, **97**, 256–276, doi:10.1175/1520-0493(1969)097<0256:SHOTAD>2.3.CO;2. http://journals.ametsoc.org/doi/abs/10.1175/1520-0493%281969%29097%3C0256%3ASHOTAD%3E2.3.CO%3B2.

Carrio, G. G., and W. R. Cotton, 2011: Investigations of aerosol impacts on hurricanes: Virtual seeding flights. *Atmos. Chem. Phys.*, **11**, 2557–2567, doi:10.5194/acp-11-2557-2011.

Chapman, E. G., W. I. Gustafson, R. C. Easter, J. C. Barnard, S. J. Ghan, M. S. Pekour, and J. D. Fast, 2008: Coupling aerosol-cloud-radiative processes in the WRF-Chem model: investigating the radiative impact of elevated point sources. *Atmos. Chem. Phys. Discuss.*, **8**, 14765–14817, doi:10.5194/acpd-8-14765-2008.

——, W. I. Gustafson, R. C. Easter, J. C. Barnard, S. J. Ghan, M. S. Pekour, and J. D. Fast, 2009: Coupling aerosol-cloud-radiative processes in the WRF-Chem model: Investigating the radiative impact of elevated point sources. *Atmos. Chem. Phys.*, **9**, 945–964, doi:10.5194/acp-9-945-2009.

Charney, J. G., and M. E. Stern, 1962: On the Stability of Internal Baroclinic Jets in a Rotating Atmosphere. *J. Atmos. Sci.*, **19**, 159–172, doi:10.1175/1520-0469(1962)019<0159:OTSOIB>2.0.CO;2. http://journals.ametsoc.org/doi/abs/10.1175/1520-0469%281962%29019%3C0159%3AOTSOIB%3E2.0.CO%3B2.

Chen, D., Z. Liu, C. Davis, and Y. Gu, 2017: Dust radiative effects on atmospheric thermodynamics and tropical cyclogenesis over the Atlantic Ocean using WRF-Chem coupled with an AOD data assimilation system. *Atmos. Chem. Phys.*, **17**, 7917–7939, doi:10.5194/acp-17-7917-2017.

Chen, S. H., S. H. Wang, and M. Waylonis, 2010: Modification of Saharan air layer and environmental shear over the eastern Atlantic Ocean by dust-radiation effects. *J. Geophys. Res. Atmos.*, **115**, 1–22, doi:10.1029/2010JD014158.

Chen, Y., and C. Snyder, 2007: Assimilating Vortex Position with an Ensemble Kalman Filter. *Mon. Weather Rev.*, **135**, 1828–1845, doi:10.1175/MWR3351.1. http://journals.ametsoc.org/doi/abs/10.1175/MWR3351.1.

Chin, M., and Coauthors, 2000a: Atmospheric sulfur cycle simulated in the global model GOCART: Comparison with field observations and regional budgets. *J. Geophys. Res. Atmos.*, **105**, 24689–24712, doi:10.1029/2000jd900385. http://www.scopus.com/inward/record.url?eid=2-s2.0-0006457375&partnerID=tZOtx3y1.

——, R. B. Rood, S.-J. Lin, J.-F. Müller, and A. M. Thompson, 2000b: Atmospheric sulfur cycle simulated in the global model GOCART: Model description and global properties. *J. Geophys. Res. Atmos.*, **105**, 24671–24687, doi:10.1029/2000JD900384. http://doi.wiley.com/10.1029/2000JD900384.

——, and Coauthors, 2002: Tropospheric Aerosol Optical Thickness from the GOCART Model and Comparisons with Satellite and Sun Photometer Measurements. *J. Atmos. Sci.*, **59**, 461–483, doi:10.1175/1520-0469(2002)059<0461:TAOTFT>2.0.CO;2. http://journals.ametsoc.org/doi/abs/10.1175/1520-0469%282002%29059%3C0461%3ATAOTFT%3E2.0.CO%3B2.

CIMSS/ University of Wisconsin-Madison, Saharan Air Layer (SAL).

Conant, W. C., and Coauthors, 2003: A model for the radiative forcing during ACE-Asia derived from CIRPAS Twin Otter and R/VRonald H. Browndata and comparison with observations. *J. Geophys. Res.*, **108**, 1–16, doi:10.1029/2002JD003260.

Davidi, A., A. B. Kostinski, I. Koren, and Y. Lehahn, 2012: Observational bounds on atmospheric heating by aerosol absorption: Radiative signature of transatlantic dust. *Geophys. Res. Lett.*, **39**, 1–5, doi:10.1029/2011GL050358.

Deepshikha, S., S. K. Satheesh, and J. Srinivasan, 2006: Dust aerosols over India and adjacent continents retrieved using METEOSAT infrared radiance
Part I: sources and regional distribution. *Ann. Geophys.*, **24**, 37–61, doi:10.5194/angeo-24-37-2006. http://www.ann-geophys.net/24/37/2006/.

Diongue, A., J. P. Lafore, J. L. Redelsperger, and R. Roca, 2002: Numerical study of a Sahelian synoptic weather system: Initiation and mature stages of convection and its interactions with the large-scale dynamics. *Q. J. R. Meteorol. Soc.*, **128**, 1899–1928, doi:10.1256/003590002320603467.

Dudhia, J. and Wang, J., 2014: *WRF Advanced Usage and Best Practices. 16th WRF Annual Workshop*.

Dunion, J. P., and C. S. Velden, 2004: The impact of the Saharan Air Layer on Atlantic tropical cyclone activity. *Bull. Am. Meteorol. Soc.*, **85**, 353–365, doi:10.1175/BAMS-85-3-353.

Dunstone, N. J., D. M. Smith, B. B. B Booth, L. Hermanson, and R. Eade, 2013: Anthropogenic aerosol forcing of Atlantic tropical storms The frequency of tropical storms in the North Atlantic region varies

markedly on decadal timescales. *Nat. Geosci.*, **6**, doi:10.1038/NGEO1854.

Emmons, L. K., and Coauthors, 2010: Description and evaluation of the Model for Ozone and Related chemical Tracers, version 4 (MOZART-4). *Geosci. Model Dev.*, **3**, 43–67, doi:10.5194/gmd-3-43-2010.

Evan, A. T., and S. Mukhopadhyay, 2010: African dust over the northern tropical Atlantic: 1955-2008. *J. Appl. Meteorol. Climatol.*, **49**, 2213–2229, doi:10.1175/2010JAMC2485.1.

——, J. Dunion, J. A. Foley, A. K. Heidinger, and C. S. Velden, 2006: New evidence for a relationship between Atlantic tropical cyclone activity and African dust outbreaks. *Geophys. Res. Lett.*, **33**, 1–5, doi:10.1029/2006GL026408.

——, G. R. Foltz, and D. Zhang, 2012: Physical response of the tropical-subtropical North Atlantic Ocean to decadal-multidecadal forcing by African dust. *J. Clim.*, **25**, 5817–5829, doi:10.1175/JCLI-D-11-00438.1.

Evensen, G., M. Carlo, and M. Carlo, 1994: with a nonlinear quasi-geostrophic model using Monte Carlo methods to forecast error statistics using alternative -- Dt Pt Dt Pt + • - Pt r / - • D •'. **99**.

Fast, J. D., W. I. Gustafson, R. C. Easter, R. A. Zaveri, J. C. Barnard, E. G. Chapman, G. A. Grell, and S. E. Peckham, 2006: Evolution of ozone, particulates, and aerosol direct radiative forcing in the vicinity of Houston using a fully coupled meteorology-chemistry-aerosol model. *J. Geophys. Res. Atmos.*, **111**, 1–29, doi:10.1029/2005JD006721.

Fast, J. D., and Coauthors, 2009: Evaluating simulated primary anthropogenic and biomass burning organic aerosols during MILAGRO: implications for assessing treatments of secondary organic aerosols. *Atmos. Chem. Phys. Discuss.*, **9**, 4805–4871, doi:10.5194/acpd-9-4805-2009.

Foltz, G. R., and M. J. McPhaden, 2008: Impact of Saharan dust on tropical North Atlantic SST. *J. Clim.*, **21**, 5048–5060, doi:10.1175/2008JCLI2232.1.

Forster, P., and Coauthors, 2007: Changes in Atmospheric Constituents and in Radiative Forcing Changes in Atmospheric Constituents and in Radiative Forcing Chapter 2. *Netherlands) G. Bodeker (New Zealand) Clim. Chang.*,.

Fowler, J. P., and T. J. Galarneau, 2017: Influence of Storm–Storm and Storm–Environment Interactions on Tropical Cyclone Formation and Evolution. *Mon. Weather Rev.*, **145**, 4855–4875, doi:10.1175/MWR-D-17-0131.1.

Ginoux, P., M. Chin, I. Tegen, J. M. Prospero, B. Holben, O. Dubovik, and S.-J. Lin, 2001a: Sources and distributions of dust aerosols simulated with the GOCART model. *J. Geophys. Res.*, **106**, 20255–20273, doi:10.1029/2000JD000053.

——, ——, ——, J. M. Prospero, B. Holben, O. Dubovik, and S.-J. Lin, 2001b: Sources and distributions of dust aerosols simulated with the GOCART model. *J. Geophys. Res. Atmos.*, **106**, 20255–20273, doi:10.1029/2000JD000053.

Giordano, L., and Coauthors, 2015: Assessment of the MACC reanalysis and its influence as chemical boundary conditions for regional air quality modeling in AQMEII-2. *Atmos. Environ.*, **115**, 371–388, doi:10.1016/j.atmosenv.2015.02.034.

Givati, A., D. Rosenfeld, A. Givati, and D. Rosenfeld, 2004: Quantifying Precipitation Suppression Due to Air Pollution. *http://dx.doi.org/10.1175/1520-0450(2004)043<1038:QPSDTA>2.0.CO;2*, doi:10.1175/1520-0450(2004)043<1038:QPSDTA>2.0.CO;2.

Grell, G. A., S. E. Peckham, R. Schmitz, S. A. McKeen, G. Frost, W. C. Skamarock, and B. Eder, 2005: Fully coupled "online" chemistry within the WRF model. *Atmos. Environ.*, **39**, 6957–6975, doi:10.1016/j.atmosenv.2005.04.027.

Grogan, D. F. P., T. R. Nathan, and S.-H. Chen, 2016: Effects of Saharan Dust on the Linear Dynamics of African Easterly Waves. *J. Atmos. Sci.*, **73**, 891–911, doi:10.1175/JAS-D-15-0143.1. http://journals.ametsoc.org/doi/10.1175/JAS-D-15-0143.1.

Gustafson, W. I., E. G. Chapman, S. J. Ghan, R. C. Easter, and J. D. Fast, 2007: Impact on modeled cloud characteristics due to simplified treatment of uniform cloud condensation nuclei during NEAQS 2004. *Geophys. Res. Lett.*, **34**, 1–5, doi:10.1029/2007GL030021.

Hansen, J., M. Sato, and R. Ruedy, 1997: Radiative forcing and climate response. *J. Geophys. Res. Atmos.*, **102**, 6831–6864, doi:10.1029/96JD03436.

Haywood, J., and O. Boucher, 2000: Estimates of the Direct and Indirect Radiative Forcing Due to Tropospheric Aerosols: A Review. *Rev. Geophys.*, **38**, 513–543.

Haywood, J., and Coauthors, 2003: Radiative properties and direct radiative effect of Saharan dust measured by the C-130 aircraft during SHADE: 1. Solar spectrum. *J. Geophys. Res. Atmos.*, **108**, 8577, doi:10.1029/2002JD002687.

Heald, C. L., D. A. Ridley, J. H. Kroll, S. R. H. Barrett, K. E. Cady-Pereira, M. J. Alvarado, and C. D. Holmes, 2014: Contrasting the direct radiative effect and direct radiative forcing of aerosols. *Atmos. Chem. Phys.*, **14**, 5513–5527, doi:10.5194/acp-14-5513-2014. http://www.atmos-chem-phys.net/14/5513/2014/.

Herbener, S. R., and Coauthors, 2014: Aerosol Indirect Effects on Idealized Tropical Cyclone Dynamics. *J. Atmos. Sci.*, **71**, 2040–2055, doi:10.1175/JAS-D-13-0202.1.

Hopsch, S. B., C. D. Thorncroft, and K. R. Tyle, 2010: Analysis of African Easterly Wave Structures and Their Role in Influencing Tropical Cyclogenesis. *Mon. Weather Rev.*, **138**, 1399–1419, doi:10.1175/2009MWR2760.1. http://journals.ametsoc.org/doi/abs/10.1175/2009MWR2760.1.

Hosseinpour, F., and E. M. Wilcox, 2014: Aerosol interactions with African/Atlantic climate dynamics. *Environ. Res. Lett.*, **9**, 075004, doi:10.1088/1748-9326/9/7/075004.

Houtekamer, P. L., and H. L. Mitchell, 1998: Data assimilation using an ensemble Kalman filter technique. *Mon. Weather Rev.*, **126**, 796–811, doi:10.1175/1520-0493(1998)126<0796:DAUAEK>2.0.CO;2.

Hsu, N. C., 2017: *CHANGES TO MODIS DEEP BLUE AEROSOL PRODUCTS BETWEEN COLLECTION 6 AND COLLECTION 6.1*.

Huang, J., Q. Fu, J. Su, Q. Tang, P. Minnis, Y. Hu, Y. Yi, and Q. Zhao, 2009: Taklimakan dust aerosol radiative heating derived from CALIPSO observations using the Fu-Liou radiation model with CERES constraints. *Atmos. Chem. Phys.*, **9**, 4011–4021, doi:10.5194/acp-9-4011-2009.

Inness, A., and Coauthors, 2013: The MACC reanalysis: An 8 yr data set of atmospheric composition. *Atmos. Chem. Phys.*, **13**, 4073–4109, doi:10.5194/acp-13-4073-2013.

IPCC, IPCC Fourth Assessment Report: Climate Change 2007.

Islam, M. N., and M. Almazroui, 2012: Direct effects and feedback of desert dust on the climate of the Arabian Peninsula during the wet season: A regional climate model study. *Clim. Dyn.*, **39**, 2239–2250, doi:10.1007/s00382-012-1293-4.

Ismail, S., and Coauthors, 2010: LASE Measurements of Water Vapor, Aerosol, and Cloud Distributions in Saharan Air Layers and Tropical Disturbances. *J. Atmos. Sci.*, **67**, 1026–1047, doi:10.1175/2009JAS3136.1.

Jenkins, G. S., A. S. Pratt, and A. Heymsfield, 2008: Possible linkages between Saharan dust and tropical cyclone rain band invigoration in the eastern Atlantic during NAMMA-06. *Geophys. Res. Lett.*, **35**, 1–7, doi:10.1029/2008GL034072.

Jiang, B., B. Huang, W. Lin, and S. Xu, 2016a: Investigation of the effects of anthropogenic pollution on typhoon precipitation and microphysical processes using WRF-Chem. *J. Atmos. Sci.*, 160114111241005, doi:10.1175/JAS-D-15-0202.1.

——, ——, ——, ——, B. Jiang, B. Huang, W. Lin, and S. Xu, 2016b: Investigation of the Effects of Anthropogenic Pollution on Typhoon Precipitation and Microphysical Processes Using WRF-Chem. *J. Atmos. Sci.*, **73**, 1593–1610, doi:10.1175/JAS-D-15-0202.1. http://journals.ametsoc.org/doi/10.1175/JAS-D-15-0202.1.

Jiang, H., G. Feingold, W. R. Cotton, P. G. Duynkerke, and M. S. Rams, 2001: Large-eddy simulations of entrainment of cloud condensation nuclei into the Arctic boundary layer : May 18 , 1998 , FIRE / SHEBA case study is a constant -3 below cloud to a peak of 250 cm -3 at the inversion in the sensitivity run show that droplet conce. **106**, 113–122.

Jin, Q., Z. L. Yang, and J. Wei, 2016: Seasonal responses of Indian summer monsoon to dust aerosols in the middle East, India, and China. *J. Clim.*, **29**, 6329–6349, doi:10.1175/JCLI-D-15-0622.1.

Johnson, B. T., K. P. Shine, and P. M. Forster, 2004: The semi-direct aerosol effect: Impact of absorbing aerosols on marine stratocumulus. *Q. J. R. Meteorol. Soc.*, **130**, 1407–1422, doi:10.1256/qj.03.61.

Johnson, D. B., and D. B. Johnson, 1982: The Role of Giant and Ultragiant Aerosol Particles in Warm Rain Initiation. *J. Atmos. Sci.*, **39**, 448–460, doi:10.1175/1520-0469(1982)039<0448:TROGAU>2.0.CO;2.

Jones, A., D. L. Roberts, and A. Slingo, 1994: A climate model study of indirect radiative forcing by anthropogenic sulphate aerosols. *Nature*, **370**, 450–453, doi:10.1038/370450a0. http://www.nature.com/doifinder/10.1038/370450a0.

Jones, C., N. Mahowald, and C. Luo, 2004: Observational evidence of African desert dust intensification of easterly waves. *Geophys. Res. Lett.*, **31**, 13–16, doi:10.1029/2004GL020107.

Jones, T. A., D. J. Cecil, and J. Dunion, 2007: The environmental and inner-core conditions governing the intensity of Hurricane Erin (2001). *Weather Forecast.*, **22**, 708–725, doi:10.1175/WAF1017.1.

Jury, M. R., and M. J. Santiago, 2010: Composite analysis of dust impacts on African easterly waves in the Moderate Resolution Imaging Spectrometer era. *J. Geophys. Res. Atmos.*, **115**, 1–11, doi:10.1029/2009JD013612.

Kalman, R. E., 1960: A New Approach to Linear Filtering and Prediction Problems. *Trans. ASME J. Basic Eng.*, **82**, 35–45, doi:10.1115/1.3662552.

Kalnay, E., and Coauthors, 1996: The NCEP/NCAR 40-year reanalysis project. *Bull. Am. Meteorol. Soc.*, **77**, 437–471, doi:10.1175/1520-0477(1996)077<0437:TNYRP>2.0.CO;2.

Kalverla, P. C., G. J. Duine, G. J. Steeneveld, and T. Hedde, 2016: Evaluation of the weather research and forecasting model in the durance valley complex terrain during the KASCADE field campaign. *J. Appl. Meteorol. Climatol.*, **55**, 861–882, doi:10.1175/JAMC-D-15-0258.1.

Karyampudi, V. M., and T. N. Carlson, 1988: Analysis and Numerical Simulations of the Saharan Air Layer and Its Effect on Easterly Wave Disturbances. *J. Atmos. Sci.*, **45**, 3102–3136, doi:10.1175/1520-0469(1988)045<3102:AANSOT>2.0.CO;2. http://dx.doi.org/10.1175/1520-0469(1988)045%3C3102:AANSOT%3E2.0.CO%5Cn2.

Karydis, V. A., P. Kumar, D. Barahona, I. N. Sokolik, and A. Nenes, 2011: On the effect of dust particles on global cloud condensation nuclei and cloud droplet number. *J. Geophys. Res. Atmos.*, **116**, doi:10.1029/2011JD016283.

Khain, A., B. Lynn, J. Dudhia, A. Khain, B. Lynn, and J. Dudhia, 2010: Aerosol Effects on Intensity of Landfalling Hurricanes as Seen from Simulations with the WRF Model with Spectral Bin

Microphysics. *J. Atmos. Sci.*, **67**, 365–384, doi:10.1175/2009JAS3210.1.

Kohler, H., and H. Kohler, THE NUCLEUS IN AND THE GROWTH OF HYGROSCOPIC DROPLETS.

Lamarque, J. F., J. T. Kiehl, P. G. Hess, W. D. Collins, L. K. Emmons, P. Ginoux, C. Luo, and X. X. Tie, 2005: Response of a coupled chemistry-climate model to changes in aerosol emissions: Global impact on the hydrological cycle and the tropospheric burdens of OH, ozone, and NOx. *Geophys. Res. Lett.*, **32**, 1–4, doi:10.1029/2005GL023419.

Lavaysse, C., J. P. Chaboureau, and C. Flamant, 2011: Dust impact on the west african heat low in summertime. *Q. J. R. Meteorol. Soc.*, **137**, 1227–1240, doi:10.1002/qj.844.

Lenny Bernstein, Peter Bosch, Osvaldo Canziani, Zhenlin Chen, Renate Christ, Ogunlade Davidson, William Hare, S., T. M. Huq, David Karoly, Vladimir Kattsov, Zbigniew Kundzewicz, Jian Liu, Ulrike Lohmann, Martin Manning, M. Bettina Menne, Bert Metz, Monirul Mirza, Neville Nicholls, Leonard Nurse, Rajendra Pachauri, Jean Palutikof, M. Parry, Dahe Qin, Nijavalli Ravindranath, Andy Reisinger, Jiawen Ren, Keywan Riahi, Cynthia Rosenzweig, R. S. Rusticucci, Stephen Schneider, Youba Sokona, Susan Solomon, Peter Stott, Ronald Stouffer, Taishi Sugiyama, and G. Y. Dennis Tirpak, Coleen Vogel, 2007: Climate Change 2007: Synthesis Report. doi:10.1256/004316502320517344.

Levin, Z., E. Ganor, and V. Gladstein, 1996: The Effects of Desert Particles Coated with Sulfate on Rain Formation in the Eastern Mediterranean. *J. Appl. Meteorol.*, **35**, 1511–1523, doi:10.1175/1520-0450(1996)035<1511:TEODPC>2.0.CO;2.

——, A. Teller, E. Ganor, and Y. Yin, 2005: On the interactions of mineral dust, sea-salt particles, and clouds: A measurement and modeling study from the Mediterranean Israeli Dust Experiment campaign. *J. Geophys. Res. D Atmos.*, **110**, 1–19, doi:10.1029/2005JD005810.

Levy, R. C., S. Mattoo, L. A. Munchak, L. A. Remer, A. M. Sayer, F. Patadia, and N. C. Hsu, 2013: The Collection 6 MODIS aerosol products over land and ocean. *Atmos. Meas. Tech.*, **6**, 2989–3034, doi:10.5194/amt-6-2989-2013.

Lin, C., S. H. I. Guang-yu, Z. Ling-zhi, and T. A. N. Sai-chun, 2009: Assessment of Dust Aerosol Optical Depth and Shortwave Radiative Forcing over the Northwest Pacific Ocean in Spring Based on Satellite

Observations. **2**, 224–229.

Liu, Y., J. Rui, D. Tie, X. Yongkun, and S. Guangyu, 2014: A Review of Aerosol Optical Properties and Radiative Effects. *J. Meteorol. Res.*, **28**, 1003–1028, doi:10.1007/s13351-014-4045-z.1.

Liu, Z., Q. Liu, H. C. Lin, C. S. Schwartz, Y. H. Lee, and T. Wang, 2011: Three-dimensional variational assimilation of MODIS aerosol optical depth: Implementation and application to a dust storm over East Asia. *J. Geophys. Res. Atmos.*, **116**, 1–19, doi:10.1029/2011JD016159.

——, C. S. Schwartz, C. Snyder, and S.-Y. Ha, 2012: Impact of Assimilating AMSU-A Radiances on Forecasts of 2008 Atlantic Tropical Cyclones Initialized with a Limited-Area Ensemble Kalman Filter. *Mon. Weather Rev.*, **140**, 4017–4034, doi:10.1175/MWR-D-12-00083.1. http://journals.ametsoc.org/doi/abs/10.1175/MWR-D-12-00083.1.

Lohmann, U., and J. Feichter, 2001: Can the direct and semi-direct aerosol effect compete with the indirect effect on a global scale? *Geophys. Res. Lett.*, **28**, 159–161, doi:10.1029/2000GL012051.

Ma, P. L., K. Zhang, J. J. Shi, T. Matsui, and A. Arking, 2012: Direct radiative effect of mineral dust on the development of African easterly waves in late summer, 2003-07. *J. Appl. Meteorol. Climatol.*, **51**, 2090–2104, doi:10.1175/JAMC-D-11-0215.1.

Ma, X., K. Von Salzen, and J. Li, 2008: Modelling sea salt aerosol and its direct and indirect effects on climate. *Atmos. Chem. Phys.*, **8**, 1311–1327, doi:10.5194/acp-8-1311-2008.

Mahowald, N. M., 2003: Mineral aerosol and cloud interactions. *Geophys. Res. Lett.*, **30**, 1475, doi:10.1029/2002GL016762. http://doi.wiley.com/10.1029/2002GL016762.

Messager, C., D. J. Parker, O. Reitebuch, A. Agusti-Panareda, C. M. Taylor, and J. Cuesta, 2010: Structure and dynamics of the Saharan atmospheric boundary layer during the West African monsoon onset: Observations and analyses from the research flights of 14 and 17 July 2006. *Q. J. R. Meteorol. Soc.*, **136**, 107–124, doi:10.1002/qj.469.

Miller, R. L., and I. Tegen, 1998: Climate response to soil dust aerosols. *J. Clim.*, **11**, 3247–3267, doi:10.1175/1520-0442(1998)011<3247:CRTSDA>2.0.CO;2.

——, and ——, 1999: Radiative Forcing of a Tropical Direct Circulation by Soil Dust Aerosols. *J. Atmos.*

Sci., **56**, 2403–2433, doi:10.1175/1520-0469(1999)056<2403:RFOATD>2.0.CO;2.

Mohalfi, S., H. S. Bedi, T. N. Krishnamurti, and S. D. Cocke, 1998: Impact of shortwave radiative effects of dust aerosols on the summer season heat low over Saudi Arabia. *Mon. Weather Rev.*, **126**, 3153–3168, doi:10.1175/1520-0493(1998)126<3153:iosreo>2.0.co;2.

Morcrette, J.-J., and Coauthors, 2009: Aerosol analysis and forecast in the European Centre for Medium-Range Weather Forecasts Integrated Forecast System: Forward modeling. *J. Geophys. Res.*, **114**, D06206, doi:10.1029/2008JD011235.

Morrison, H., J. a. Curry, M. D. Shupe, and P. Zuidema, 2005: A New Double-Moment Microphysics Parameterization for Application in Cloud and Climate Models. Part II: Single-Column Modeling of Arctic Clouds. *J. Atmos. Sci.*, **62**, 1678–1693, doi:10.1175/JAS3447.1.

NASA, CALIPSO. https://www.nasa.gov/mission_pages/calipso/main/index.html.

——, MODIS. https://modis.gsfc.nasa.gov/.

——, AERONET: aerosol robotic network. https://aeronet.gsfc.nasa.gov/.

NOAA, NHC Data Archive. https://www.nhc.noaa.gov/data/#hurdat.

Osborne, S. R., A. J. Baran, B. T. Johnson, J. M. Haywood, E. Hesse, and S. Newman, 2011: Short-wave and long-wave radiative properties of Saharan dust aerosol. *Q. J. R. Meteorol. Soc.*, **137**, 1149–1167, doi:10.1002/qj.771.

Otto, S., M. de Reus, T. Trautmann, A. Thomas, M. Wendisch, and S. Borrmann, 2007: Atmospheric radiative effects of an in-situ measured Saharan dust plume and the role of large particles. *Atmos. Chem. Phys. Discuss.*, **7**, 7767–7817, doi:10.5194/acpd-7-7767-2007.

Penner, J. E., and Coauthors, 2006: Model intercomparison of indirect aerosol effects. *Atmos. Chem. Phys.*, **6**, 3391–3405, doi:10.5194/acp-6-3391-2006.

Pytharoulis, I., and C. Thorncroft, 1999: The Low-Level Structure of African Easterly Waves in 1995. *Mon. Weather Rev.*, **127**, 2266–2280, doi:10.1175/1520-0493(1999)127<2266:TLLSOA>2.0.CO;2. http://journals.ametsoc.org/doi/abs/10.1175/1520-0493%281999%29127%3C2266%3ATLLSOA%3E2.0.CO%3B2.

Quaas, J., O. Boucher, N. Bellouin, and S. Kinne, 2008: Satellite-based estimate of the direct and indirect aerosol climate forcing. *J. Geophys. Res. Atmos.*, **113**, 1–9, doi:10.1029/2007JD008962.

Rasch, P. J., N. M. Mahowald, and B. E. Eaton, 1997: Representations of transport, convection and the hydrologic cycle in chemical transport models: Implications for the modeling of short lived and soluble species. *J. Geophys. Res.*, **102**, 28127–28138.

Reale, O., W. K. Lau, K.-M. Kim, and E. Brin, 2009: Atlantic Tropical Cyclogenetic Processes during SOP-3 NAMMA in the GEOS-5 Global Data Assimilation and Forecast System. *J. Atmos. Sci.*, **66**, 3563–3578, doi:10.1175/2009JAS3123.1. http://dx.doi.org/10.1175/2009JAS3123.1.

——, K. M. Lau, and A. da Silva, 2011: Impact of Interactive Aerosol on the African Easterly Jet in the NASA GEOS-5 Global Forecasting System. *Weather Forecast.*, **26**, 504–519, doi:10.1175/WAF-D-10-05025.1. http://journals.ametsoc.org/doi/abs/10.1175/WAF-D-10-05025.1.

Reale, O., K. M. Lau, A. Da Silva, and T. Matsui, 2014: Impact of assimilated and interactive aerosol on tropical cyclogenesis. *Geophys. Res. Lett.*, **41**, 3282–3288, doi:10.1002/2014GL059918.

Redelsperger, J. L., A. Diongue, A. Diedhiou, J. P. Ceron, M. Diop, J. F. Gueremy, and J. P. Lafore, 2002: Multi-scale description of a Sahelian synoptic weather system representative of the West African monsoon. *Q. J. R. Meteorol. Soc.*, **128**, 1229–1257, doi:10.1256/003590002320373274.

Reed, R. J., a. Hollingsworth, W. a. Heckley, and F. Delsol, 1988: An Evaluation of the Performance of the ECMWF Operational System in Analyzing and Forecasting Easterly Wave Disturbances over Africa and the Tropical Atlantic. *Mon. Weather Rev.*, **116**, 824–865, doi:10.1175/1520-0493(1988)116<0824:AEOTPO>2.0.CO;2.

Rosenfeld, D., Y. Rudich, and R. Lahav, 2001: Desert dust suppressing precipitation: A possible desertification feedback loop. *Proc. Natl. Acad. Sci.*, **98**, 5975–5980, doi:10.1073/pnas.101122798. http://www.pnas.org/cgi/doi/10.1073/pnas.101122798.

Rosenfeld, D., and Coauthors, 2012a: Aerosol Effects on Microstructure and Intensity of Tropical Cyclones. *Bull. Am. Meteorol. Soc.*, **93**, 987–1001, doi:10.1175/BAMS-D-11-00147.1.

——, W. L. Woodley, A. Khain, W. R. Cotton, G. Carrió, I. Ginis, and J. H. Golden, 2012b: Aerosol effects

on microstructure and intensity of tropical cyclones. *Bull. Am. Meteorol. Soc.*, **93**, 987–1001, doi:10.1175/BAMS-D-11-00147.1.

Ross, R. S., and T. N. Krishnamurti, 2007: Low-Level African Easterly Wave Activity and Its Relation to Atlantic Tropical Cyclogenesis in 2001. *Mon. Weather Rev.*, **135**, 3950–3964, doi:10.1175/2007MWR1996.1. http://journals.ametsoc.org/doi/abs/10.1175/2007MWR1996.1.

Rotstayn, L. D., and Y. Liu, 2005: A smaller global estimate of the second indirect aerosol effect. *Geophys. Res. Lett.*, **32**, 1–4, doi:10.1029/2004GL021922.

Rudich, Y., 2002: Treating clouds with a grain of salt. *Geophys. Res. Lett.*, **29**, 6–9, doi:10.1029/2002GL016055.

Saide, P. E., and Coauthors, 2012: Evaluating WRF-Chem aerosol indirect effects in Southeast Pacific marine stratocumulus during VOCALS-REx. **12**, 3045–3064. http://www.atmos-chem-phys.net/12/3045/2012/%5Cnpapers3://publication/doi/10.5194/acp-12-3045-2012.

San Jos??, R., and Coauthors, 2015: Sensitivity of feedback effects in CBMZ/MOSAIC chemical mechanism. *Atmos. Environ.*, **115**, 646–656, doi:10.1016/j.atmosenv.2015.04.030.

Sassen, K., P. J. DeMott, J. M. Prospero, and M. R. Poellot, 2003: Saharan dust storms and indirect aerosol effects on clouds: CRYSTAL-FACE results. *Geophys. Res. Lett.*, **30**, 1–4, doi:10.1029/2003GL017371.

Satheesh, S. K., and K. Krishna Moorthy, 2005: Radiative effects of natural aerosols: A review. *Atmos. Environ.*, **39**, 2089–2110, doi:10.1016/j.atmosenv.2004.12.029.

Sayer, A. M., N. C. Hsu, C. Bettenhausen, and M.-J. Jeong, 2013a: Validation and uncertainty estimates for MODIS Collection 6 “Deep Blue” aerosol data. *J. Geophys. Res. Atmos.*, **118**, 7864–7872, doi:10.1002/jgrd.50600.

——, ——, ——, and M. J. Jeong, 2013b: Validation and uncertainty estimates for MODIS Collection 6 “deep Blue” aerosol data. *J. Geophys. Res. Atmos.*, **118**, 7864–7872, doi:10.1002/jgrd.50600.

——, L. A. Munchak, N. C. Hsu, R. C. Levy, C. Bettenhausen, and M. J. Jeong, 2014: Modis collection 6 aerosol products: Comparison between aqua’s e-deep blue, dark target, and “merged” data sets, and

usage recommendations. *J. Geophys. Res.*, **119**, 13,965-13,989, doi:10.1002/2014JD022453.

Sayer, R. L. & A., 2014: *MODIS Aerosols Merged Dark Target / Deep Blue Product*.

Seinfeld, John H., and S. N. P., 2006: *Atmospheric chemistry and physics: from air pollution to climate change*. J. Wiley, Hoboken, N.J.,.

Shu, S., and L. Wu, 2009: Analysis of the influence of Saharan air layer on tropical cyclone intensity using AIRS/Aqua data. *Geophys. Res. Lett.*, **36**, 1–5, doi:10.1029/2009GL037634.

Sippel Jason A., S. A. B. C.-L. S., 2011: Environmental Influences on the Strength of Tropical Storm Debby (2006). *J. Atmos. Sci.*, **68**, 2557–2581, doi:10.1175/2011JAS3648.1.

Smoydzin, L., A. Teller, H. Tost, M. Fnais, and J. Lelieveld, 2012: Impact of mineral dust on cloud formation in a Saharan outflow region. *Atmos. Chem. Phys.*, **12**, 11383–11393, doi:10.5194/acp-12-11383-2012.

Sohn, B., T. Nakajima, H. Chun, and K. Aoki, 2007: More absorbing dust aerosol inferred from sky radiometer measurements at Anmyeon, Korea. *J. Meteorol. Soc. Japan*, **85**, 815–823, doi:10.2151/jmsj.85.815. http://apps.isiknowledge.com/full_record.do?&colname=WOS&search_mode=CitingArticles&qid=284&page=1&product=WOS&SID=4EFKc8PFMICDdEbE3K9&doc=1.

Sokolik, I. N., O. B. Toon, and R. W. Bergstrom, 1998: Modeling the radiative characteristics of airborne mineral aerosols at infrared wavelengths. *J. Geophys. Res. Atmos.*, **103**, 8813–8826, doi:10.1029/98JD00049.

Sun, D., K. M. Lau, and M. Kafatos, 2008: Contrasting the 2007 and 2005 hurricane seasons: Evidence of possible impacts of Saharan dry air and dust on tropical cyclone activity in the Atlantic basin. *Geophys. Res. Lett.*, **35**, 1–5, doi:10.1029/2008GL034529.

——, W. K. M. Lau, M. Kafatos, Z. Boybeyi, G. Leptoukh, C. Yang, and R. Yang, 2009: Numerical simulations of the impacts of the Saharan air layer on Atlantic tropical cyclone development. *J. Clim.*, **22**, 6230–6250, doi:10.1175/2009JCLI2738.1.

Takemura, T., and Coauthors, 2002: Single-Scattering Albedo and Radiative Forcing of Various Aerosol

Species with a Global Three-Dimensional Model. *J. Clim.*, **15**, 333–352, doi:10.1175/1520-0442(2002)015<0333:SSAARF>2.0.CO;2.

Tan, F., H. S. Lim, K. Abdullah, T. L. Yoon, and B. Holben, 2015: Monsoonal variations in aerosol optical properties and estimation of aerosol optical depth using ground-based meteorological and air quality data in Peninsular Malaysia. *Atmos. Chem. Phys.*, **15**, 3755–3771, doi:10.5194/acp-15-3755-2015.

Tang, Y., and Coauthors, 2009: The impact of chemical lateral boundary conditions on CMAQ predictions of tropospheric ozone over the continental United States. *Environ. Fluid Mech.*, **9**, 43–58, doi:10.1007/s10652-008-9092-5.

Tegen, I., and I. Fung, 1994: Modeling of mineral dust in the atmosphere' transport, and optical thickness. *J. Geophys. Res.*, **99**, 22897–22914, doi:10.1029/94JD01928.

——, and A. A. Lacis, 1996: Modeling of particle size distribution and its influence on the radiative properties of mineral dust aerosol. *J. Geophys. Res. Atmos.*, **101**, 19237–19244, doi:10.1029/95JD03610.

——, ——, and I. Fung, 1996: The influence on climate forcing of mineral aerosols from disturbed soils. *Nature*, **380**, 419–422, doi:10.1038/380419a0. http://www.nature.com/doifinder/10.1038/380419a0.

Texeira, J., 2013: *AIRS/Aqua L2 Standard Physical Retrieval (AIRS+AMSU) V006*. Greenbelt, MD, USA,.

The COMET program/ UCAR, 2017: The COMET Program.

Thorncroft, C., and K. Hodges, 2001: African easterly wave variability and its relationship to Atlantic tropical cyclone activity. *J. Clim.*, **14**, 1166–1179, doi:10.1175/1520-0442(2001)014<1166:AEWVAI>2.0.CO;2.

Thorncroft, C. D., and M. Blackburn, 1999: Maintenance of the African easterly jet. *Q. J. R. Meteorol. Soc.*, **125**, 763–786, doi:10.1002/qj.49712555502. http://doi.wiley.com/10.1002/qj.49712555502.

Thorncroft, C. D., C. D. Thorncroft, B. J. Hoskins, and B. J. Hoskins, 1994: An Idealized Study of African Easterly Waves .1. a Linear View. *Q. J. R. Meteorol. Soc.*, **120**, 953–982.

Tompkins, A. M., C. Cardinali, J. J. Morcrette, and M. Rodwell, 2005: Influence of aerosol climatology on forecasts of the African Easterly Jet. *Geophys. Res. Lett.*, **32**, 1–4, doi:10.1029/2004GL022189.

Torn, R. D., and R. D. Torn, 2010: Performance of a Mesoscale Ensemble Kalman Filter (EnKF) during the NOAA High-Resolution Hurricane Test. *Mon. Weather Rev.*, **138**, 4375–4392, doi:10.1175/2010MWR3361.1.

Twohy, C. H., 2015: Measurements of Saharan Dust in Convective Clouds over the Tropical Eastern Atlantic Ocean*. *J. Atmos. Sci.*, **72**, 75–81, doi:10.1175/JAS-D-14-0133.1. http://journals.ametsoc.org/doi/10.1175/JAS-D-14-0133.1.

——, and Coauthors, 2009: Saharan dust particles nucleate droplets in eastern Atlantic clouds. *Geophys. Res. Lett.*, **36**, 1–6, doi:10.1029/2008GL035846.

Vizy, E. K., and K. H. Cook, 2009: Tropical Storm Development from African Easterly Waves in the Eastern Atlantic: A Comparison of Two Successive Waves Using a Regional Model as Part of NASA AMMA 2006. *J. Atmos. Sci.*, **66**, 3313–3334, doi:10.1175/2009JAS3064.1.

Wang, K., Y. Zhang, K. Yahya, S. Y. Wu, and G. Grell, 2015: Implementation and initial application of new chemistry-aerosol options in WRF/Chem for simulating secondary organic aerosols and aerosol indirect effects for regional air quality. *Atmos. Environ.*, **115**, 716–732, doi:10.1016/j.atmosenv.2014.12.007. http://dx.doi.org/10.1016/j.atmosenv.2014.12.007.

Wang, Y., K.-H. Lee, Y. Lin, M. Levy, and R. Zhang, 2014: Distinct effects of anthropogenic aerosols on tropical cyclones. *Nat. Clim. Chang.*, **4**, 368–373, doi:10.1038/nclimate2144. http://www.nature.com/doifinder/10.1038/nclimate2144.

Wild, O., X. Zhu, and M. J. Prather, 2000: Fast-J: Accurate Simulation of In- and Below-Cloud Photolysis in Tropospheric Chemical Models. *J. Atmos. Chem.*, **37**, 245–282, doi:10.1023/A:1006415919030.

William C. Skamarock, E., *A Description of the Advanced Research WRF Version 3*.

Wisconsin-Madison, C. U. of, Tropical Cyclones: A Satellite Perspective CIMSS TC Webpage Product Archive. http://tropic.ssec.wisc.edu/#.

Wong, S., and A. E. Dessler, 2005: Suppression of deep convection over the tropical North Atlantic by the Saharan Air Layer. *Geophys. Res. Lett.*, **32**, 1–4, doi:10.1029/2004GL022295.

Wu, L., S. A. Braun, J. J. Qu, and X. Hao, 2006: Simulating the formation of Hurricane Isabel (2003) with

AIRS data. *Geophys. Res. Lett.*, **33**, 18–21, doi:10.1029/2005GL024665.

Wu, M. L. C., O. Reale, S. D. Schubert, M. J. Suarez, R. D. Koster, and P. J. Pegion, 2009: African easterly jet: Structure and maintenance. *J. Clim.*, **22**, 4459–4480, doi:10.1175/2009JCLI2584.1.

Xia, X., and X. Zong, 2009: Shortwave versus longwave direct radiative forcing by Taklimakan dust aerosols. *Geophys. Res. Lett.*, **36**, 1–5, doi:10.1029/2009GL037237.

Xinyong, S., J. Xiaocen, and L. Di, 2017: Simulations of Anthropogenic Aerosols Effects on the Intensity and Precipitation of Typhoon Fitow (1323) Using WRF-Chem Model. *Chinese J. Atmos. Sci. (in Chinese)*, **41**, 960–974, doi:10.3878/j.issn.1006-9895.1703.16216.

Yin, Y., S. Wurzler, Z. Levin, and T. G. Reisin, 2002: Interactions of mineral dust particles and clouds: Effects on precipitation and cloud optical properties. *J. Geophys. Res. Atmos.*, **107**, 1–14, doi:10.1029/2001JD001544.

Yoshioka, M., N. M. Mahowald, A. J. Conley, W. D. Collins, D. W. Fillmore, C. S. Zender, and D. B. Coleman, 2007: Impact of desert dust radiative forcing on sahel precipitation: Relative importance of dust compared to sea surface temperature variations, vegetation changes, and greenhouse gas warming. *J. Clim.*, **20**, 1445–1467, doi:10.1175/JCLI4056.1.

Yu, S., R. Mathur, J. Pleim, D. Wong, R. Gilliam, K. Alapaty, C. Zhao, and X. Liu, 2014: Aerosol indirect effect on the grid-scale clouds in the two-way coupled WRF-CMAQ: Model description, development, evaluation and regional analysis. *Atmos. Chem. Phys.*, **14**, 11247–11285, doi:10.5194/acp-14-11247-2014.

Zaveri, R. A., and L. K. Peters, 1999: A new lumped structure photochemical mechanism for large-scale applications. *J. Geophys. Res. Atmos.*, **104**, 30387–30415, doi:10.1029/1999JD900876. http://doi.wiley.com/10.1029/1999JD900876.

——, R. C. Easter, J. D. Fast, and L. K. Peters, 2008: Model for Simulating Aerosol Interactions and Chemistry (MOSAIC). *J. Geophys. Res. Atmos.*, **113**, 1–29, doi:10.1029/2007JD008782.

Zhang, H., G. M. McFarquhar, S. M. Saleeby, and W. R. Cotton, 2007: Impacts of Saharan dust as CCN on the evolution of an idealized tropical cyclone. *Geophys. Res. Lett.*, **34**, 1–6,

doi:10.1029/2007GL029876.

——, ——, W. R. Cotton, and Y. Deng, 2009: Direct and indirect impacts of Saharan dust acting as cloud condensation nuclei on tropical cyclone eyewall development. *Geophys. Res. Lett.*, **36**, 1–6, doi:10.1029/2009GL037276.

Zhang, J., 2003: Longwave radiative forcing of Saharan dust aerosols estimated from MODIS, MISR, and CERES observations on Terra. *Geophys. Res. Lett.*, **30**, 1–4, doi:10.1029/2003GL018479.

Zhao, C., X. Liu, L. R. Leung, B. Johnson, S. A. McFarlane, W. I. Gustafson, J. D. Fast, and R. Easter, 2010: The spatial distribution of mineral dust and its shortwave radiative forcing over North Africa: Modeling sensitivities to dust emissions and aerosol size treatments. *Atmos. Chem. Phys.*, **10**, 8821–8838, doi:10.5194/acp-10-8821-2010.

——, ——, L. R. Leung, and S. Hagos, 2011: Radiative impact of mineral dust on monsoon precipitation variability over West Africa. *Atmos. Chem. Phys.*, **11**, 1879–1893, doi:10.5194/acp-11-1879-2011.

Zhu, A., V. Ramanathan, F. Li, and D. Kim, 2007: Dust plumes over the Pacific, Indian, and Atlantic oceans: Climatology and radiative impact. *J. Geophys. Res. Atmos.*, **112**, 1–20, doi:10.1029/2007JD008427.

AIRS data description from JPL.

Appendix A: Conversion from MACC-II to MOSAIC

1. Convert dust

The dust in MACC-II and MOSAIC is bin model, but they have different bin sizes. The diameters for dust bins in MACC-II are 0.03-0.55, 0.55-0.9, 0.9-20. Units: μm.

The diameters for dust bins in MOSAIC are: 0.039-0.078, 0.078-0.156, 0.156-0.312, 0.312, 0.625, 0.625-1.25, 1.25-2.5,2.5-5, 5-10. Units: μm.

We will use the following deduction to explain how to convert dust from MACC-II to MOSAIC 8 bins model.

The volume differential

$$dV = n_V^e(lnD_p)dlnD_p \quad (1)$$

where $n_V^e(lnD_p)$ is aerosol volume lognormal distribution

if density ρ is uniform among different sizes of particles

$$\rho dV = \rho n_V^e(lnD_p)dlnD_p \quad (2)$$

$$d\rho V = \rho n_V^e(lnD_p)dlnD_p \quad (3)$$

The mass differential

$$dM = n_M^e(lnD_p)dlnD_p \quad (4)$$

where $n_M^e(lnD_p)$ is aerosol mass lognormal distribution

$$Thus, \frac{dM}{dlnD_p} = n_M^e(lnD_p) \quad (5)$$

In bin mode, we assume mass distribution function is uniform in each bin, thus,

$$\frac{dM}{dlnD_p} = n_M^e(lnD_p) = \frac{\Delta M}{\Delta lnD_p} \quad (6)$$

For every model grid in MACC-II model, we define the total mass of particles within each bin are M_1, M_2, M_3; the ranges of these three bins are D_0~D_1, D_1~D_2, D_2~D_3, as shown in the following figure

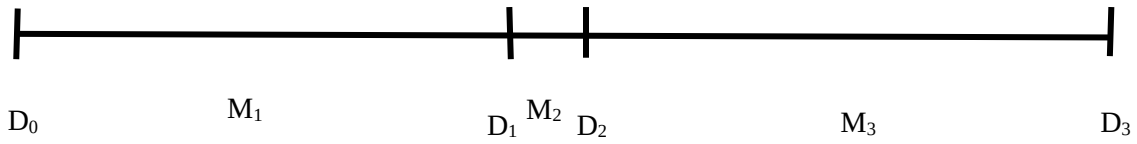

Aerosol mass lognormal distribution $n_M^e(lnD_p)$ for each bin in MACC-II model will be:

MACC-II bin1: $n_{M,1}^e(lnD_p) = \frac{\Delta M}{\Delta lnD_p} = \frac{M_1}{lnD_1 - lnD_0}$ (7)

MACC-II bin2: $n_{M,2}^e(lnD_p) = \frac{\Delta M}{\Delta lnD_p} = \frac{M_2}{lnD_2 - lnD_1}$

MACC-II bin3: $n_{M,3}^e(lnD_p) = \frac{\Delta M}{\Delta lnD_p} = \frac{M_2}{lnD_3 - lnD_2}$

MACC-II bin1 contains the first three MOSAIC bins (d_0~d_1, d_1~d_2, d_2~d_3) and part of the fourth bin (d_3~ D_1), as figure shows below

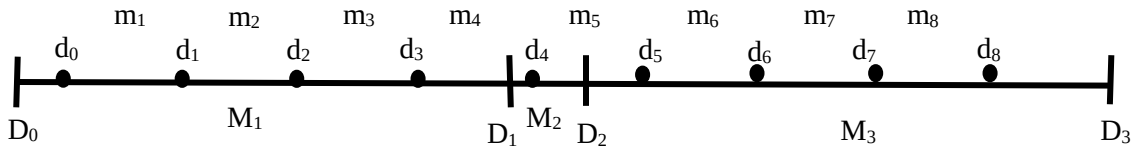

m_1 ~m_8 are total mass of particles within each bin in MOSAIC, d_0~d_8 are diameters for bins.

For MOSAIC bin1(d_0~d_1), because it is within MACC-II bin1, it uses the same mass distribution function as MACC-II. Thus, for MOSAIC bin1, its mass distribution function

$$n_{m,1}^{e}(lnD_p) = n_{M,1}^{e}(lnD_p) = \frac{M_1}{lnD_1 - lnD_0} \quad (8)$$

The mass of MOSAIC bin1 is the integration of the mass distribution function

$$m_1 = \int_{lnd_0}^{lnd_1} n_{m,1}^{e}(lnD_p)\, dlnD_p, \quad (9)$$

however, to keep the mass conserved, we extend the lower boundary in the integration

$$m_1 = \int_{lnD_0}^{lnd_1} n_{m,1}^{e}(lnD_p)\, dlnD_p \quad (10)$$

Since the distribution function $n_{m,1}^{e}(\ln D_p)$ is uniform from D_0 to D_1, the integration can be expressed as

$$m_1 = n_{m,1}^{e}(lnD_p) \times (lnd_1 - lnD_0) \quad (11)$$

$$= \frac{M_1}{lnD_1 - lnD_0} \times (lnd_1 - lnD_0)$$

Similarly,

$$m_2 = n_{m,2}^e(lnD_p) \times (lnd_2 - lnd_1) = n_{M,1}^e(lnD_p) \times (lnd_2 - lnd_1) = \frac{M_1}{lnD_1 - lnD_0} \times (lnd_2 - lnd_1) \quad (12)$$

$$m_3 = n_{m,3}^e(lnD_p) \times (lnd_3 - lnd_2) = n_{M,1}^e(lnD_p) \times (lnd_3 - lnd_2) = \frac{M_1}{lnD_1 - lnD_0} \times (lnd_3 - lnd_2) \quad (13)$$

Whenever the MOSAIC bin expands two MACC-II bins, for example, MOSAIC bin4, its calculation is separated into two parts.

First, calculate the mass of the particles which are within the first MACC-II bin,

$$m_{4,1} = n_{m,4,1}^e(lnD_p) \times (lnD_1 - lnd_3) = n_{M,1}^e(lnD_p) \times (lnD_1 - lnd_3) = \frac{M_1}{lnD_1 - lnD_0} \times (lnD_1 - lnd_3) \quad (14)$$

Second, get the mass of the particles which are within the second MACC-II bin

$$m_{4,2} = n_{m,4,2}^e(lnD_p) \times (lnd_4 - lnD_1) = n_{M,2}^e(lnD_p) \times (lnd_4 - lnD_1) = \frac{M_2}{lnD_2 - lnD_1} \times (lnd_4 - lnD_1) \quad (15)$$

$$m_4 = m_{4,1} + m_{4,2} = \frac{M_1}{lnD_1 - lnD_0} \times (lnD_1 - lnd_3) + \frac{M_2}{lnD_2 - lnD_1} \times (lnd_4 - lnD_1) \quad (16)$$

By applying the similar methods, the mass of all other bins will be

$$m_{5,1} = n^{e}_{m,5,1}(lnD_p) \times (lnD_2 - lnd_4) = n^{e}_{M,2}(lnD_p) \times (lnD_2 - lnd_4) = \frac{M_2}{lnD_2 - lnD_1} \times (lnD_2 - lnd_4) \quad (17)$$

$$m_{5,2} = n^{e}_{m,5,2}(lnD_p) \times (lnd_5 - lnD_2) = n^{e}_{M,3}(lnD_p) \times (lnd_5 - lnD_2) = \frac{M_3}{lnD_3 - lnD_2} \times (lnd_5 - lnD_2) \quad (18)$$

$$m_6 = n^{e}_{m,6}(lnD_p) \times (lnd_6 - lnD_5) = n^{e}_{M,3}(lnD_p) \times (lnd_6 - lnD_5) = \frac{M_3}{lnD_3 - lnD_2} \times (lnd_6 - lnD_5) \quad (19)$$

$$m_7 = n^{e}_{m,7}(lnD_p) \times (lnd_7 - lnD_6) = n^{e}_{M,3}(lnD_p) \times (lnd_7 - lnD_6) = \frac{M_3}{lnD_3 - lnD_2} \times (lnd_7 - lnD_6) \quad (20)$$

$$m_8 = n^{e}_{m,8}(lnD_p) \times (lnD_3 - lnd_7) = n^{e}_{M,3}(lnD_p) \times (lnD_3 - lnd_7) = \frac{M_3}{lnD_3 - lnD_2} \times (lnD_3 - lnd_7) \quad (21)$$

Sea salt is also a bin mode in MACC-II, it follows similar conversion method as dust. However, sea salt from MACC-II has a high bias in our case. Some studies also found the same situation (Giordano et al. 2015). Thus, sea salt initial and boundary conditions are excluded from

the conversion. Instead, sea salt in the atmosphere can be generated by emission from the sea by sea salt parameterization in the model.

2. Convert Black carbon, organic carbon, and sulfate

For Black carbon, organic carbon and sulfate, they follow a log-normal distribution.

Their parameters are given in the following table1, which is adapted from table 6 from Emmons et al. (2010).

Table1. Bulk aerosol parameters used in calculation of surface area: number distribution mean diameter $\overline{D_p}$, geometric standard deviation σ_g and density ρ

Aerosol	$\overline{D_p}$ (μm)	σ_g(μm)	ρ (g/cm^3)
BC1, BC2	0.0236	2.00	1.0
OC1, OC2	0.0424	2.20	1.8
Sulfate	0.139	2.03	1.7

The volume distribution function is

$$n_V(D_p) = \frac{(\frac{\pi}{6})N_t}{(2\pi)^{1/2} D_p ln\sigma_g} exp(3ln\overline{D_{pg}} + \frac{9}{2} ln^2\sigma_g) \times exp(-\frac{[lnD_p - (ln\overline{D_{pg}} + 3ln^2\sigma_g)]^2}{2ln^2\sigma_g}) \quad (22)$$

(8.52 from Seinfeld, John H. 2006)

D_p *is particle diameter*

N_t *is the total number of particles*

σ_g *is* geometric standard deviation, its value is given in table1

$\overline{D_{pg}}$ is median diameter

$\overline{D_{pgv}}$ is volume median diameter, its relation to number median diameter is

$$ln\overline{D_{pgv}} = ln\overline{D_{pg}} + 3ln^2\sigma_g \quad \text{(8.53 from Seinfeld, John H. 2006)} \tag{23}$$

$ln\overline{D_{pgv}}$ can be expressed using the given valuse by the following steps

Because

$$\overline{D_p} = \overline{D_{pg}}\exp(\frac{ln^2\sigma_g}{2}), \tag{24}$$

Where $\overline{D_p}$ is mean diameter （8.44 from Seinfeld, John H. 2006)

Thus, $\overline{D_{pg}}=\overline{D_p}/\exp(\frac{ln^2\sigma_g}{2})$ (25)

formula (2) will be

$$ln\overline{D_{pgv}} = ln\overline{D_{pg}} + 3ln^2\sigma_g = \ln\left(\frac{\overline{D_p}}{\exp\left(\frac{ln^2\sigma_g}{2}\right)}\right) + 3ln^2\sigma_g \tag{26}$$

$\overline{D_p}$, σ_g are given in the table1. $ln\overline{D_{pgv}}$ can be calculated

let $A=\frac{\pi}{6}exp(3ln\overline{D_{pg}} + \frac{9}{2}ln^2\sigma_g)$ (27)

which is a constant number for specific type of aerosol

Formula (1) becomes

$$n_V(D_p) = \frac{AN_t}{(2\pi)^{1/2} D_p ln\sigma_g} \times exp(-\frac{[lnD_p - ln\overline{D_{pgv}}]^2}{2ln^2\sigma_g}) \quad (28)$$

In which $ln\overline{D_{pgv}} = \ln\left(\frac{\overline{D_p}}{\exp\left(\frac{ln^2\sigma_g}{2}\right)}\right) + 3ln^2\sigma_g$

Aerosol number distribution

$$n_V(D_p) = \frac{N_t}{(2\pi)^{1/2} D_p ln\sigma_g} \times exp(-\frac{(lnD_p - ln\overline{D_{pg}})^2}{2ln^2\sigma_g})$$ *(8.34* from Seinfeld, John H. 2006) (29)

can be transformed into cumulative distribution function

$$N(D_p) = \frac{N_t}{2} + \frac{N_t}{2}\text{erf}(\frac{\ln(D_p) - ln\overline{D_{pg}}}{\sqrt{2}ln\sigma_g})$$ *)* (8.39 from Seinfeld, John H. 2006) (30)

Defining the normalized cumulative distribution

$$\widetilde{N}(D_p) = \frac{N(D_p)}{N_t} = \frac{1}{2} + \frac{1}{2}\text{erf}(\frac{\ln(D_p) - ln\overline{D_{pg}}}{\sqrt{2}ln\sigma_g})$$ (8.46 from Seinfeld, John H. 2006) (31)

Similarly, volume distribution (3) can also be written as volume cumulative distribution function

$$V(D_p) = \frac{AN_t}{2} + \frac{AN_t}{2}\mathrm{erf}(\frac{\ln(D_p) - ln\overline{D_{pgv}}}{\sqrt{2}ln\sigma_g}) \quad (32)$$

Defining the normalized volume cumulative distribution

$$\tilde{V}(D_p) = V(D_p)/AN_t$$

$$\tilde{V}(D_p) = \frac{1}{2} + \frac{1}{2}\mathrm{erf}(\frac{\ln(D_p) - ln\overline{D_{pgv}}}{\sqrt{2}ln\sigma_g}) \quad (33)$$

Given $D_{p,1}$ as the lower boundary of one bin, the value of the volume cumulative distribution function:

$$\widetilde{V_1}(D_p) = \frac{1}{2} + \frac{1}{2}\mathrm{erf}(\frac{\ln(D_{p,1}) - ln\overline{D_{pgv}}}{\sqrt{2}ln\sigma_g}) \quad (34)$$

$D_{p,2}$ as the upper boundary of the bin, the value of the volume cumulative distribution fuction

$$\widetilde{V_2}(D_p) = \frac{1}{2} + \frac{1}{2}\mathrm{erf}(\frac{\ln(D_{p,2}) - ln\overline{D_{pgv}}}{\sqrt{2}ln\sigma_g}) \quad (35)$$

The volume of all the particles within the bin will be the difference between the cumulative distribution function value

$$\Delta\tilde{V} = \widetilde{V_2}(D_p) - \widetilde{V_1}(D_p) = \frac{1}{2}\mathrm{erf}\left(\frac{\ln(D_{p,2}) - ln\overline{D_{pgv}}}{\sqrt{2}ln\sigma_g}\right) - \frac{1}{2}\mathrm{erf}(\frac{\ln(D_{p,1}) - ln\overline{D_{pgv}}}{\sqrt{2}ln\sigma_g}) \quad (36)$$

$ln\overline{D_{pgv}}$ can be obtained using formular : $ln\overline{D_{pgv}} = \ln\left(\frac{\overline{D_p}}{\exp\left(\frac{ln^2\sigma_g}{2}\right)}\right) + 3ln^2\sigma_g$,

σ_g for different aerosols are given in the table1

Since $\widetilde{V}$ is normalized, $\Delta\widetilde{V}$ value is between 0 and 1, which is the percentage of the total volume of all bins.

Because the density is uniform among different particle sizes, $\Delta\widetilde{V}$ is also the mass percentage of the total mass of all bins. Thus, for black carbon, organic carbon and sulfate, the mass ratio in each of all 8 bins can be obtained using the above formula (5)

3. Programing

(1) NCL

Horizontal regrid from MACC rectilinear grid to WRF curvilinear grid, using the bilinear method

Vertical interpolation from MACC model level to WRF model level

Output netCDF files

(2) Python

Read netCDF file

Redistribution bins aerosol and bulk aerosol, using the formulas above

Calculate the tendency for boundary

Replace wrfinput_d01 and wrfbdy_d01